Polymer-Derived Microporous Ceramics for Membranes and Sensors for High Temperature Hydrogen Purification and Sensing

---

Ph.D. Dissertation by Ravi Mohan Prasad, FG Disperse Feststoffe, FB Material- und Geowissenschaften, Technische Universität Darmstadt, Germany

TECHNISCHE
UNIVERSITÄT
DARMSTADT

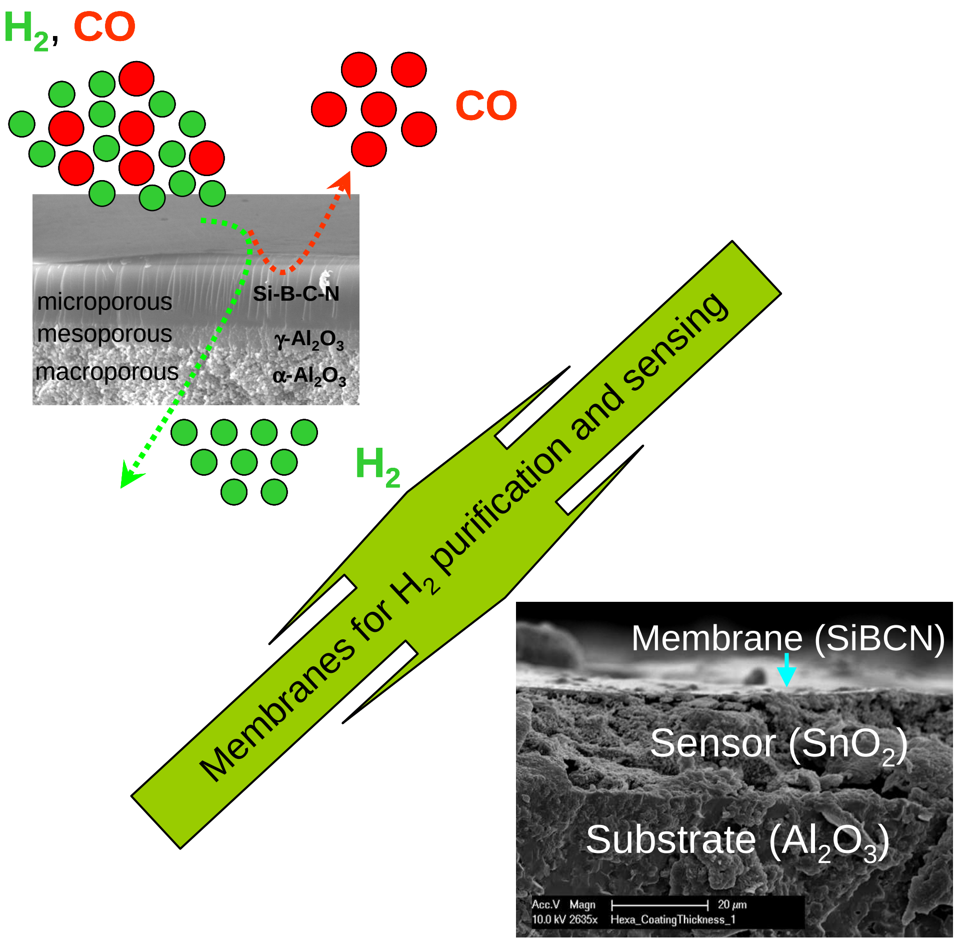

Polymer-Derived Microporous Ceramics for Membranes and Sensors for High Temperature Hydrogen Purification and Sensing

Vom Fachbereich Material- und Geowissenschaften
der Technischen Universität Darmstadt

zur

Erlangung des akademischen Grades eines
Doktor-Ingenieurs
(Dr. -Ing)
genehmigte Dissertation

von

M. Tech. Ravi Mohan Prasad
aus Jamshedpur, Indien

Berichterstatter:	Prof. Dr. Ralf Riedel
Mitberichterstatter:	Prof. Dr. Christina Roth
Prüfer (FB 11):	Prof. Dr. Wolfgang Ensinger
Prüfer (extern):	Prof. Dr. Jörg Schneider
Tag der Einreichung:	26.04.2012
Tag der mündlichen Prüfung:	11.06.2012

Darmstadt 2012
D 17

Acknowledgements

I wish to express my sincere gratitude to those who supported my endeavors during my PhD work:

Firstly, I express my sincere gratitude towards **Prof. Dr. Ralf Riedel,** my PhD advisor**,** for allowing me to be a part of his research group, offering me a fair work bench, his valuable time and closely following my work during the course of my doctoral thesis. I appreciate his constant motivation throughout this period and his support.

I am indebted to **PD Dr. Aleksander Gurlo** for his supervision, advice, and invaluable time he gave in discussing various issues throughout my work and to read this thesis and giving critical comments about it. His truly scientist intuition has exceptionally inspired me and enriched my growth as a student, a researcher and a scientist. I am also thankful to him for his moral support in hard phase of this period, without which, it would have been difficult for me to arrive at this stage. In any amount I appreciate his help, it is not enough.

I would also like to acknowledge the financial support from the German Research Foundation (DFG) for my PhD work. This work has been performed within the framework of the project “Thermoresistant ceramic membrane with integrated gas sensor for high temperature separation and detection of hydrogen and carbon monoxide” of the priority program “Adapting surfaces for high temperature applications” (DFG-SPP 1299, www.spp-haut.de).

It is a pleasure to pay my sincere appreciation to the collaborators. A special thanks goes to Prof. Y. Iwamoto (Nagoya Institute of Technology, Japan) for supplying porous supports and giving useful tips during the realization of gas permeance set-up. I greatly appreciate Dr. Michael Hübner, Dr. N. Barsan, and Prof. U. Weimar (University of Tübingen) for working in a very productive collaboration and helping with gas sensing measurements. I would like to thank Janka Ihring, Dr. Nadine Kaltenborn, and Dr. I. Voigt (IKTS, Hermsdorf) for supporting single gas permeance measurements during the second phase of DFG project.

I am very thankful to Dr. Koji Morita, Dr. Stefan Lauterbach, Mathis M. Müller and Prof. Dr. H.-J. Kleebe for TEM measurements and for the fruitful discussion.

I am very grateful to Dr. Gabriela Mera for her interest and helping in NMR, IR and Raman characterization.

I would like to thank Riza Iskander and Prof. J. Mayer (RWTH-Aachen University, Germany) for their unconditional support for measuring cross-sectional TEM images of membrane coated supports.

In addition, there were many people supported my work, I would like to recognize in particular:

- Dr. Emanuel Ionescu for introducing me to work with Schlenk lines, for fruitful disccusion related to various polymers, and for his considerable support and impetus.
- Claudia Fasel for STA measurements.
- Dr. H. Breitzke (TU Darmstadt) and Dr. F. Poli (Universität Stuttgart) for solid state NMR characterization.
- Dr. Aitana Tamayo for her great support in performing measurements at synchrotron and post-measurement data analysis.
- Irene Mieskes for helping with Hg-porosimetry measurements.
- Jean-Christophe Jaud for assisting in XRD measurements.

Collective and individual acknowledgments are also owed to all my present and former colleagues at the FG Disperse Feststoffe, FB Material- und Geowissenschaften, TU Darmstadt: Liviu, Dima, Magdalena, Sandra, Carmen, Ricardo, Ilaria, Benjamin, Christoph, Miria, Mahdi, Mirabbos, Maged, Mirko, Jan, Yan, Shrikant, Sarabjeet, Jia, Cristina, Wenji, and others for the pleasant and friendly working atmosphere during my PhD.

My special acknowledgement and mention goes to my Master's thesis supervisors Prof. S.K. Pabi (IIT Kharagpur, India), Prof. H. Hahn (TU Darmstadt, Germany) and Dr. Maximilian Fichtner (FZK, Germany) for their encouragement and support. Working with them was the real source of interest that inspired me to go for the PhD studies in the field of energy.

I am very grateful to my parents and all my family members for their support and faith, and my wife, Anjana, for her encouragement and patience while I was working and writing my thesis until late evenings.

Finally, I would like to thank everybody who was important to the successful realization of thesis.

Table of Contents

I Basics

II Experimental

III Results and discussion

Abstract

The growing interest in the use of hydrogen as main fuel has increased the need for pure hydrogen (H_2) production and purification. There are several by-products (CO, H_2O, CO_2) associated with the production of hydrogen which might damage the production rate. Therefore, separation of hydrogen from other gases is an important step in the hydrogen production process. If H_2 can be selectively removed from the product side during hydrogen production in membrane reactors, then it would be possible to achieve complete CO conversion in a single-step under high temperature conditions.

The main goal of the present work is the high temperature H_2 purification and sensing by applying polymer-derived ceramics. To prove the concept, the microporous SiBCN, Si_3N_4 and SiCN ceramic membranes have been synthesized by the polymer-pyrolysis route and their performance for the hydrogen separation have been evaluated in tubular membranes as well as in planar chemiresistors.

The synthesis of amorphous SiBCN ceramics has been realized through pyrolysis of poly(organoborosilazanes) in argon. Multilayered amorphous SiBCN/γ-Al_2O_3/α-Al_2O_3 membranes with gradient porosity have been realized and assessed with respect to the thermal stability, pore-size distribution and H_2/CO permeance. N_2-adsorption measurement indicates micropores in the range of 0.68-0.73 nm for three-fold SiBCN/γ-Al_2O_3/α-Al_2O_3 membrane. SEM characterization of three-fold SiBCN/γ-Al_2O_3/α-Al_2O_3 membrane shows the thickness of SiBCN membrane layer is 2.8 μm; gas permeance measurements of the membrane shows H_2/CO selectivity of about 10.5 and the H_2 permeance of about 1.05×10^{-8} mol m^{-2} s^{-1} Pa^{-1}. The observed gas permeation properties point out that the transportation of gas molecules through the membrane is governed by both activated and Knudsen diffusion.

The stability and sensing characteristics of SnO_2 sensors coated with amorphous microporous SiBCN layers have been studied in oxygen-free atmospheres. The SiBCN layers coated on SnO_2 sensors are amorphous, crack-free and microporous. The diameter of micropores (about 0.70 nm) is larger than the kinetic diameter of H_2 (0.289 nm) and CO (0.376 nm) molecules, allowing in this way their diffusion towards the bottom SnO_2 sensing layer. Transient response characteristics and sensor signals of uncoated SnO_2, three-fold and five-fold SiBCN-coated SnO_2 sensors exposed to CO (10, 20 and 120 ppm) and H_2 (40, 400 and 900 ppm) in nitrogen at 350 and 530 °C are obtained. Uncoated SnO_2 sensor is reduced at 530 °C in H_2 to tin while SiBCN-coated SnO_2 sensors show reversible resistance changes while exposed to CO and H_2.

Si_3N_4-ceramics have been synthesized via a dry ammonia pyrolysis of commercially available polysilazane (KiON HTT 1800). Amorphous microporous-Si_3N_4 ceramic layers deposited on the top of GaN sensing layer followed by dry ammonia treatment leads to the improved H_2 to CO selectivity of Si_3N_4/GaN sensors in the oxygen-free atmosphere. Transient response of the uncoated-, three-fold Si_3N_4 coated- and ammonia treated-GaN sensors exposed to CO (10, 20 and 120 ppm) and H_2 (40, 400 and 900 ppm) in pure nitrogen at 350 and 530 °C are investigated. The results indicate that uncoated-GaN sensor shows high response towards both CO and H_2 whereas for microporous Si_3N_4 coated- and ammonia treated-GaN gas sensors the sensitivity towards the interfering gas CO is significantly reduced.

High-surface area micro- and mesoporous carbon-rich SiCN ceramics have been obtained by controlled thermolysis of a carbon-rich poly(diphenylsilylcarbodiimide) precursor under argon. The formation of porous SiCN ceramics is due to the carbothermal reaction of amorphous silicon nitride phase with excess carbon, which leads to materials with high specific surface area of about 500-600 $m^2\ g^{-1}$. High-resolution Transmisson Electron Microscopy indicates that pores are embedded only in the free carbon phase. The transformation from micro- to mesoporous ceramics after heat treatment between 1600 and 1700 °C, due to the organization of graphene-like free carbon phase, is discussed.

Zusammenfassung

Durch das wachsende Interesse an der Verwendung von Wasserstoff als Brennstoff ist der Bedarf an reinem Wasserstoff (H_2) gestiegen. Während der Produktion von Wasserstoff entstehen verschiedene Nebenprodukte wie CO, CO_2 und H_2O, die den Umsatz verringern. Daher ist die Trennung des Wasserstoffs von den anderen Gasen ein wichtiger Schritt in dessen Produktion. Wenn Wasserstoff selektiv von der Produktseite in Membranreaktoren entfernt werden kann, dann wäre eine vollständige CO-Konvertierung in einem Schritt bei hohen Temperaturen möglich.

Das Hauptziel der vorliegenden Arbeit ist die Reinigung von Wasserstoff bei hohen Temperaturen und Detektion durch Verwendung polymer-abgeleiteter Keramiken. Um das Potential dieses Konzeptes aufzuzeigen, wurden mikroporöse SiBCN, Si_3N_4 und SiCN Keramik-Membranen über die Polymer-Pyrolyse-Route synthetisiert und ihre Leistungsfähigkeit hinsichtlich der Separation von Wasserstoff in Rohrmembranen sowie in planaren Chemieresistoren evaluiert.

Die Synthese der amorphen SiBCN Keramik erfolgte durch Pyrolyse von Poly-(organylborosilazanen) in Argon. Mehrschichtige, amorphe SiBCN/γ-Al_2O_3/α-Al_2O_3 Membranen mit einem Porositätsgradienten wurden hergestellt und hinsichtlich ihrer thermischen Stabilität, Porengrößenverteilung und H_2/CO Durchlässigkeit untersucht. Stickstoffadsorptionsmessungen der dreischichtigen SiBCN/γ-Al_2O_3/α-Al_2O_3 Membran zeigten, dass Mikroporen mit einer Größe von 0,68–0,73 nm vorliegen. Die Charakterisierung der Membran mittels Rasterelektronenmikroskopie (REM) zeigt, dass die Dicke der amorphen SiBCN-Schicht 2,8 μm beträgt. Messungen der Gasdurchlässigkeit an der Membran weisen eine H_2/CO Selektivität von ca. 10,5 und eine Durchlässigkeit für Wasserstoff von $1,05\times10^{-8}$ mol m^{-2} s^{-1} Pa^{-1} auf. Die gemessenen Gaspermabilitäten deuten darauf hin, dass der Transport der Gasmoleküle durch die Membran sowohl durch aktivierte als auch durch Knudsen-Diffusion erfolgt.

Die thermische Stabilität und die sensorischen Eigenschaften von SnO_2 basierten Sensoren, die mit einer mikroporösen SiBCN Schicht beschichtet worden sind, wurden in sauerstofffreier Atmosphäre untersucht. Die SiBCN-Schichten sind amorph, rissfrei und mikroporös. Der mittlere Durchmesser der Mikroporen (etwa 0,70 nm) ist größer als der kinetische Durchmesser von H_2 (0,289 nm) und CO (0,376 nm), so dass beide Gase durch die Membran auf den Sensor diffundieren können. Das Ansprechverhalten der unbeschichteten und der drei- und fünfach mit SiBCN beschichteten SnO_2 basierenden Sensoren auf CO (10, 20 und 120 ppm) und H_2 (40, 400 und 900 ppm) wurde in Stickstoff bei 350 und 530 °C untersucht, und die erhaltenen Kurzzeitsignale wurden interpretiert. Während der unbeschichtete SnO_2 basierte Sensor bei 530 °C durch den Wasserstoff zu elementaren Zinn reduziert wird, zeigt das SiBCN-beschichtete Sensorsystem eine reversible Widerstandsänderung bei Anwesenheit von H_2 und CO.

Die Si_3N_4 basierten, keramischen Schichten wurden durch Pyrolyse von kommerziell erhältlichem Polysilazan (KiON HTT 1800) in trockenem Ammoniak synthetisiert. Die Abscheidung von amorphen, mikroporösen Si_3N_4-Schichten auf die Oberfläche einer GaN-basierten Sensorschicht, gefolgt von einer Pyrolyse in trockenem Ammoniak, führt zu einer verbesserten H_2 zu CO Selektivität in sauerstofffreier Atmosphäre. Auch in diesem system wurde das Ansprechverhalten der unbeschichteten als auch der dreifach mit Si_3N_4 beschichteten und anschließend in Ammoniak behandelten GaN-basierenden Sensoren auf CO (10, 20 und 120 ppm) und H_2 (40, 400 und 900 ppm) in Stickstoff bei 350 und 530 °C untersucht. Es zeigt sich, dass der unbeschichtete GaN basierte Sensor ein hohes Ansprechverhalten auf CO und H_2 aufweist, während der mit Si_3N_4 beschichtete und anschließend in Ammoniak pyrolysierte GaN-basierte Sensor über ein verringertes Ansprechverhalten für CO verfügt.

Durch Thermolyse kohlenstoffreicher Poly(diphenylcarbodiimide) unter Argon wurden mikro- und mesoporöse SiCN-Keramiken mit hohem Kohlenstoffgehalt und großer

Oberfläche erhalten. Die Ursache der Porosität ist die carbothermische Reaktion des Siliciumnitrids mit freiem Kohlenstoff, die zu SiCN-Keramiken mit hoher spezifischer Oberfläche von ca. 500–600 m^2 g^{-1} führt. Hochauflösende Transmissionselektronenmikroskopie (HRTEM)-Aufnahmen zeigen, dass die Poren ausschließlich in der freien Kohlenstoffphase eingebettet sind. Nach thermischer Auslagerung zwischen 1600 und 1700 °C erfolgt eine Umwandlung der mikroporösen SiCN-Keramik zu einem mesoporösen System. Die Änderung der Porengröße ist eine Folge der Reorganisation der freien Kohlenstoffphase unter der hoher Einfluß Temperaturen.

Introduction and motivation

The present world is running on fossil fuel economy. Automobiles, trains, and planes are mostly fueled by gasoline and diesel. Most of the power plants use oil, coal, and natural gas for their fuel. Since decades fossil fuels have played a crucial role in the socio-economic development of our society that we see today. However, big problems are associated with fossil fuels: (i) *air pollution* – this is caused by the burning of the fuel to carbon monoxide and nitrogen oxides, (ii) *global warming* – carbon dioxide that comes out of fossil fuel fired power plant and automobile's tailpipe is a greenhouse gas that is slowly raising the planet temperature. The problems associated with fossil fuels are shifting the interest of the world towards the "hydrogen economy." The hydrogen economy is considered as a potentially unlimited renewable source of fuel that promises to solve all of the problems of using fossil fuel as well as energy crisis. It is a clean technology as the by-product is water; hydrogen adds no greenhouse gases to the environment. However, the shift towards hydrogen economy cannot be achieved until the challenges and technological hurdles – cost effective hydrogen production from fossil fuels with carbon sequestration, separation and purification of hydrogen gas post-production and subsequent storage systems – are resolved. One of the important factors that determine the economics of hydrogen production is the efficiency of hydrogen purification. Large-scale production of hydrogen which is used for processes in various industries, such as metallurgical, chemical, etc., requires a large investment for the separation and purification processes.

Hydrogen production from fossil fuels involves two main steps: (i) steam reforming of methane (CH_4) to hydrogen (H_2) and carbon monoxide (CO) at high temperature, (ii) CO is subsequently converted to carbon dioxide (CO_2) at lower temperature. The presence of impurities (like sulfur compounds) in the feedstock can produce mixtures of H_2, CO, CO_2, H_2O, hydrocarbons, sulfur and nitrogen compounds etc. Therefore, gas separation is required to obtain high purity of H_2 for final applications. For example, reformation reactions are often not complete, leaving small concentrations (≈ 1%) of CO in the fuel stream. CO is known to act as a poison for the polymer electrolyte membrane (PEM) fuel cell catalysts. As a consequence, fuel cell performance degrades when CO is present in the fuel even at few ppm levels.

Hydrogen can be purified by three main methods: pressure swing adsorption (PSA), cryogenic distillation, and membrane separation. PSA and cryogenic distillation methods involves energy intensive operations; therefore, economically these two methods are not superior for using hydrogen as a fuel against petroleum fuels. Membrane separation method is considered to be the most promising gas separation method because of low energy consumption, possibility of continuous operation, lower capital investment, and relatively easy to operate and control. Over the last two decades, researchers have explored the possibilities of using various types of membranes, such as polymer, dense palladium (Pd), and porous ceramic membranes for hydrogen purification. Although Pd-based membranes exhibit excellent hydrogen selectivity, they are susceptible to poison by sulfur, form pinholes and cracks due to hydrogen embrittlement, and are also very expensive. Ceramic membranes are very promising due to their chemical and thermal stability and inertness; therefore, they can be regenerated and decontaminated at high temperatures. Polymer-derived ceramics are found to be excellent candidates for high temperature application as they exhibit excellent thermal and chemical stability. Polymer-derived ceramic membranes with pore-diameters less than 1 nm are believed to be promising candidates for high temperature H_2 separation.

The research presented in this thesis is focused on:

(i) *synthesis and characterization of microporous ceramic materials applying the polymer-pyrolysis route*;

(ii) *integration of microporous polymer-derived ceramics into gas separation membranes as well as in chemiresistors*;

(iii) *high-temperature separation of H_2 and CO applying multilayered ceramic membranes*;

(iv) *H_2 and CO sensing in harsh reducing conditions with membrane/sensor combinations*.

This thesis is organized as follows:

Chapter 1 gives an overview of methods of hydrogen production and purification. Various membrane types applied so far for hydrogen purification as well as their performances and limitations are described. The main problems of gas sensors based on semiconducting materials, so called chemiresistors, are discussed.

Chapter 2 presents the experimental procedure used for the synthesis of ceramic membranes and gas sensors and also briefly describes various characterization methods applied in this work.

Chapter 3 describes the design and operation principle of a laboratory-scale gas permeance set-up which has been realized during the present research work.

Chapter 4 is dedicated to the engineering multilayered ceramic membranes with a gradient porosity. The concept of multilayered membranes, the structure, pore-size characteristics and the thermal stability of porous supports and intermediate layers are described in this chapter.

Chapter 5 describes the synthesis and characterization of polymer-derived SiBCN ceramic membranes and their performance in terms of hydrogen separation. The integration of a SiBCN membrane with a SnO_2 gas sensor for the protection of the sensor is also reported and discussed.

Chapter 6 presents the synthesis and characterization of a microporous Si_3N_4 membrane by the ammonolysis of a polysilazane precursor. Microporous Si_3N_4 coated- and ammonia treated-GaN sensors for selective H_2 detection are reported.

Chapter 7 reports on an unconventional route to synthesize tunable micro- and mesoporous ceramic materials with a high specific surface area by the thermal decomposition of carbon-rich polymer-derived SiCN ceramics.

Chapter 8 summarizes the present study and underlines its prospective future by evaluating the obtained results in terms of permeance and selectivity as well as sensor activity of the synthesized integrated ceramic membrane systems.

Part I

Basics

Chapter 1. Literature survey

1.1. Hydrogen purification methods

Hydrogen is the simplest and most abundant element on earth known to us. It has the highest energy content per unit of weight of any known fuel. It is chemically active and is always found in combination with other elements such as oxygen (in water), carbon (in methane) etc. Hydrogen is an energy carrier rather than an energy source. For hydrogen to be used as a fuel, it must first be separated from other elements through electrolysis, gasification (high temperature heating in the absence of oxygen), or reforming (high temperature heating through a catalyst). We see hydrogen as an alternative fuel but it has its own drawbacks. One of the biggest impediments in hydrogen fuel is its purification. Current methods of hydrogen purification are not so efficient and effective.

1.1.1 Hydrogen production and purification needs

The important aspect of “hydrogen economy” is the production of hydrogen, the total energy consumed and CO/CO_2 emitted in the process. Realization of “hydrogen economy” and utilization of hydrogen as an energy carrier will require increasing the hydrogen production by more than an order of magnitude over the current production levels. About 50 million metric tons of hydrogen was produced world wide in 2003, which was equivalent to only 2% of the world energy demand [1]. The demand for hydrogen will intensify even more if hydrogen is used as an energy carrier for power generation applications. For successful transition to hydrogen economy, hydrogen must also be affordable.

Hydrogen can be produced from five different methods namely: (i) *Steam reforming* – a reaction of natural gas (methane) or other light hydrocarbons (ethane or propane) in the presence of catalyst, (ii) *Ammonia dissociation* – the breaking of ammonia into its simpler components, namely hydrogen and nitrogen, (iii) *Partial oxidation* – a reaction of hydrocarbons (such as natural gas, petroleum coke or coal) with oxygen to produce hydrogen and carbon monoxide, (iv) *Electrolysis of water* – a process which transforms water into its elements through the use of an electric current, and (v) *Photocatalytic water splitting* – splitting of water into hydrogen and oxygen using photocatalysts under solar light is a potentially clean and renewable source for hydrogen fuel. Among all of these methods used to produce hydrogen the steam reforming of natural gas method is still the most popular method for commercial hydrogen production but with a side waste of greenhouse gas emission.

The steam reforming of natural gas to produce hydrogen is the most common method of producing bulk hydrogen as well as the hydrogen used in the industrial synthesis of ammonia (Figure 1.1). It is also the least expensive method. At high temperature (700–1100 °C) and in the presence of a metal-based catalyst (nickel), steam reacts with methane to yield CO and H_2. The reaction equation is given as:

$$CH_4 + H_2O \leftrightarrow CO + 3H_2 \quad (1.1)$$

Additional hydrogen can be recovered by lower temperature gas-shift reaction with the CO produced (water-gas shift (WGS) reaction):

$$CO + H_2O \leftrightarrow CO_2 + H_2 \quad (1.2)$$

In order to obtain high purity hydrogen from either syngas (mixture of CO and H_2) or the products of water-gas shift reaction, the separation of H_2 from CO or CO_2 is necessary.

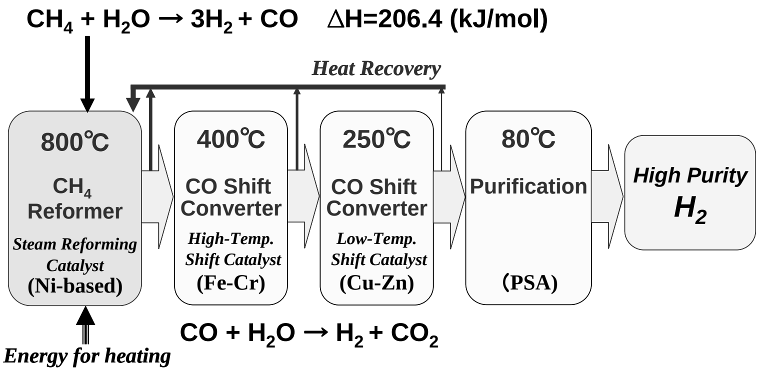

Figure 1.1. Conventional steam methane reforming process (adapted from reference [2]). PSA – Pressure swing adsorption.

Large-production of H_2 for the processes in metallurgical, chemical, petrochemical, pharmaceutical, and textiles industries often requires large capital investment for the separation and purification of H_2. Currently, H_2 can be purified through one or a combination of three major processes: (i) pressure swing adsorption (PSA), (ii) cryogenic distillation, or (iii) membrane separation. Each of these processes is based on a different separation principle, and consequently, the process characteristics differ significantly. Selecting the appropriate hydrogen purification technology depends not only on the investments, but also on process flexibility, reliability, and ease of scalability.

1.1.2 Pressure swing adsorption (PSA)

Pressure swing adsorption is the most widely used separation technique. The PSA process is based on the fact that under pressure, gases tend to be attracted on solid surfaces, or "adsorbed." The higher the pressure, the more gas is adsorbed; when the pressure is reduced, the gas is released, or desorbed. This property is applied to separate gases in a mixture because different gases tend to be attracted to different solid surfaces more or less strongly.

Typical adsorbent materials (zeolite, activated carbon, silica gel and alumina) are capable of adsorbing impurities (in the syngas stream) at a higher gas-phase partial pressure than at a lower partial pressure. The impurities are adsorbed in a fixed-bed adsorber at high pressure and then expelled as the system pressure “swings” to a lower level. Multiple beds are utilized simultaneously so that a continuous stream of hydrogen at purities up to 99.9% may be produced. Hydrogen is essentially not adsorbed and is available close to feed pressure: the typical pressure drop between the feed and product limits is less than 0.689 bars.

PSA process is mainly divided into five steps [3]: (i) *adsorption* – contaminated feedstock gas is pumped at high adsorption pressure, impurities are adsorbed, and pure hydrogen is withdrawn as product. When adsorber has reached its adsorption capacity, it is taken offline, and a fresh adsorbed is brought in the feed; (ii) *cocurrent depressurization* – the adsorber is depressurized from the product side to recover the hydrogen trapped in the adsorbent void spaces and high-purity hydrogen is collected; (iii) *counter current depressurization* – the bed is partially regenerated by depressurizing towards the feed end, and the desorbed impurites are rejected; (iv) *purge at low pressure* – the adsorbent is purge with high-purity hydrogen (taken from another adsorber on cocurrent depressurization) to further regenerate the bed; and (v) *countercurrent pressurization* – the adsorber is repressurized with hydrogen, provided from the cocurrent depressurization, before being returned to the feed side. The amount of hydrogen recovered is dependent on inlet pressure, purge gas pressure, level of impurites, and hydrogen concentration.

Separating efficiency of a typical PSA process is about 85%, and about 99.9% pure hydrogen output can be achieved. In this process the pressure of desired product (hydrogen) is generally kept at close to the input pressure to save recompression costs if the product is required at elevated pressure. An important advantage of PSA process is that all undesirable materials are removed. However, with the increase in concentration levels of non-hydrogen compounds, the effectiveness of PSA systems drops dramatically. PSA systems are usually employed for gases with more than 70% hydrogen by volume because the amount of material to be removed is so great.

1.1.3 Cryogenic distillation

The cryogenic process is a low temperature separation process which uses the difference in boiling temperatures (relative volatilities) of the feed components to effect the separation [4]. The hydrogen-rich syngas stream is compressed, and through controlled expansion of the contaminant gases, the temperature is reduced, and the contaminant gases liquefy and separate from the hydrogen. Hydrogen liquefies at 20 K. The only gas that liquefies at lower temperature is helium. Thus, all other elements liquefy before hydrogen, which permits high purity separation. If the feed contains significant amounts of CO and CO_2, a methane wash column is required to reduce the level of these gases [4]. This column uses liquid methane to wash the impurities from the hydrogen product stream. It is necessary if CO is to be reduced to ppm levels in the hydrogen product. Cryogenic separation becomes competitive for extremely large process applications where high purity is required. From the thermodynamic point of view, cryogenic separation is the most efficient method for hydrogen purification; however, capital cost is disproportionately high for all but the largest applications.

1.1.4 Membrane separation techniques

Conventional separation techniques, PSA and cryogenic distillation, are commercially available. However, these techniques are not cost effective and are quite energy intensive for hydrogen purification. Therefore, innovative separation technologies with higher efficiency and lower cost need to be developed for the economic production of hydrogen at large scale.

Membrane-related processes are considered to be one of the most promising technologies for the production of high-purity hydrogen [1]. It can provide an attractive alternative to PSA and cryogenic distillation, depending upon the purity and scale of production. Differently from conventional separation processes, membrane gas separation does not require a phase change [1]. It is considered to be the most promising gas separation process because of low energy consumption, possibility of continuous operation, lower investment cost, relatively easy to operate and control, mild process conditions, and possibility to combine with other separation technologies. In the last few years, significant efforts have been made in the direction of development of inorganic H_2-selective membranes because of their operation in high temperature and high pressure conditions [6-7]. These inorganic membranes possess high thermal resistance and mechanical strength. Use of membrane separation processes is growing at a slow but steady rate. It is estimated that the market of membrane gas separation technology in year 2020 will be five times of that of year 2000 [2].

1.2. Gas-selective membranes for hydrogen purification

A membrane is a physical barrier that permits selective transport of mass between two phases. It is called “selective” because some components can pass through the membrane more easily than others. Membrane applications are very diverse, ranging from reverse osmosis (to produce clean water) to micro filtration (to filter bacteria). Metal membranes have been used to purify hydrogen as early as 1965. The first commercially significant gas separation membrane “PRISM” based on polysulfone membrane material was introduced in late 1979 by Monsanto and is currently available from Air products and Chemicals Incorporation [9]. In the last 20 years a large range of gas separation membranes has been developed. In the following sections gas separation membranes have been discussed in great detail.

1.2.1 Membrane nomenclature and classification

The nomenclature used for gas selective membranes is shown in Figure 1.2. The two sides of the membrane are called feed and permeate. The feed is separated into two streams, i.e. the retenate and permeate streams. Either the retenate or the permeate could be the products stream, depending upon types of membranes used and the feed system. In general, feed side and permeate side are chosen such that the permeation of the relevant species takes place from the feed to permeate. The permeate stream is the product stream, if the solvent is purified by removing solutes using a membrane which allows the permeation of solvent and retain the permeation of solutes.

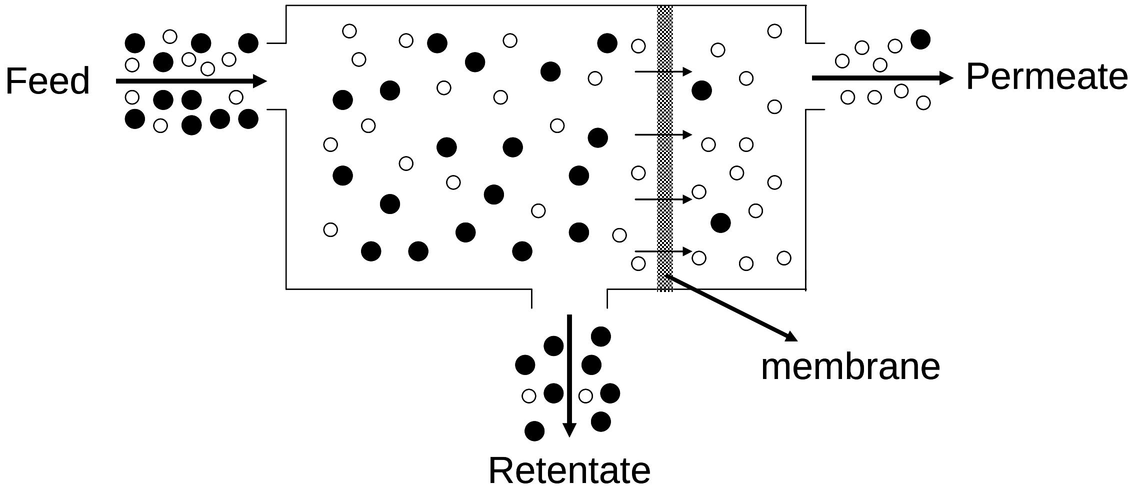

Figure 1.2. A cartoon illustrating a membrane separation process: feed stream is divided into retentate and permeate.

Performance and efficiency of membranes are usually measured in terms of flow (permeance or flux) through the membrane and membrane selectivity towards mixtures. Some of the important parameters commonly used for evaluating the membrane separation performance are as follows [10]:

$$\text{flux } (J),\ J = \frac{Q}{At} \tag{1.3}$$

where Q is the amount of gas permeated through the membrane area A in a time period of t.

$$\text{permeance } (P_m),\ P_m = \frac{J}{\Delta P} \tag{1.4}$$

where ΔP is the partial pressure difference between the feed and permeate side, $\Delta P = P_f - P_p$, P_f and P_p are the partial pressures on the feed and permeate side, respectively.

$$\text{selectivity } (S_{i/j}),\ S_{i/j} = \frac{(y_i / y_j)}{(x_i / x_j)} \tag{1.5}$$

where $S_{i/j}$ is the selectivity of component i over component j in a mixture, x and y are the molar compositions in the feed side and the permeate side of the membrane, respectively.

$$\text{permselectivity } (S^o_{i/j}),\ S^o_{i/j} = \frac{(P_{m,i})_{pure}}{(P_{m,j})_{pure}} \tag{1.6}$$

where $(P_{m,i})_{pure}$ is the permeance of pure gas i.

Separation factor of component i ($\alpha_{i/j}$), $\alpha_{i/j} = \dfrac{y_i/(1-y_i)}{x_i/(1-x_i)}$ (1.7)

If the separation factor is equal to one, then there is no separation. The higher the separation factor, the more selective the membrane is to certain species (which is usually a desirable membrane property).

Membranes can be classified in terms of their properties: (i) *based on materials they are made of* – polymeric, inorganic (glass, metal, ceramics) (ii) *membrane structure* – symmetric membranes have a homogeneous structure, whereas asymmetric membranes consist of several layers with different characteristics, (iii) *the way in which gas transport through membrane takes place* – in porous membranes gas transport takes place through their pores, whereas dense membranes allow transport through the bulk of the membrane material.

According to membrane pore size, membranes can be divided into microfiltration (MF), ultrafiltration (UF), nanofiltration (NF) and gas separation membranes. According to the definition of IUPAC in terms of the pore size [11], the MF, UF and NF membranes correspond to macroporous (pore diameter d_p>50 nm), mesoporous (2 nm<d_p<50 nm) and microporous (0<d_p<2 nm) membranes, respectively.

Ceramic membranes are usually composite ones consisting of several layers of one or more different ceramic materials. They generally have a macroporous support, one or two mesoporous intermediate layers and a microporous (or a dense) top layer. As shown in Figure 1.3, the bottom layer provides mechanical support, while the intermediate layers bridge the pore size differences between the macroporous support and the top separation layer where the actual separation takes place.

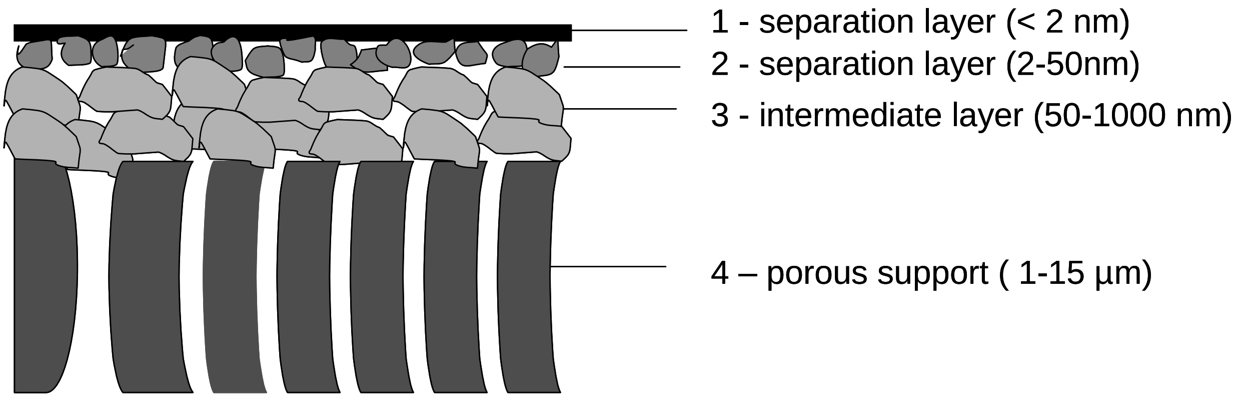

Figure 1.3. Schematic representation of an asymmetric membrane (adapted from reference [12]). The values given in bracket are typical thickness of different layers in the membrane.

1.2.2 Gas separation mechanisms

The gas separation mechanisms in porous membranes depend on the interactions between permeating molecules and the membrane pore surface, the membrane pore size, the feed composition, and the operating pressure and temperature. With respect to hydrogen separation, separation mechanisms can be through one or a combination of five separation mechanisms [7]: (i) Knudsen diffusion, (ii) surface diffusion, (iii) capillary condensation, (iv) molecular sieving, and (v) solution diffusion. Separation mechanisms differ for porous membranes and dense (nonporous) ones. Transport and separation mechanisms in porous membranes are Knudsen diffusion, surface diffusion, capillary condensation and molecular sieving. In dense membranes the transport is by solution diffusion. In the following sections, aforementioned five mechanisms are described.

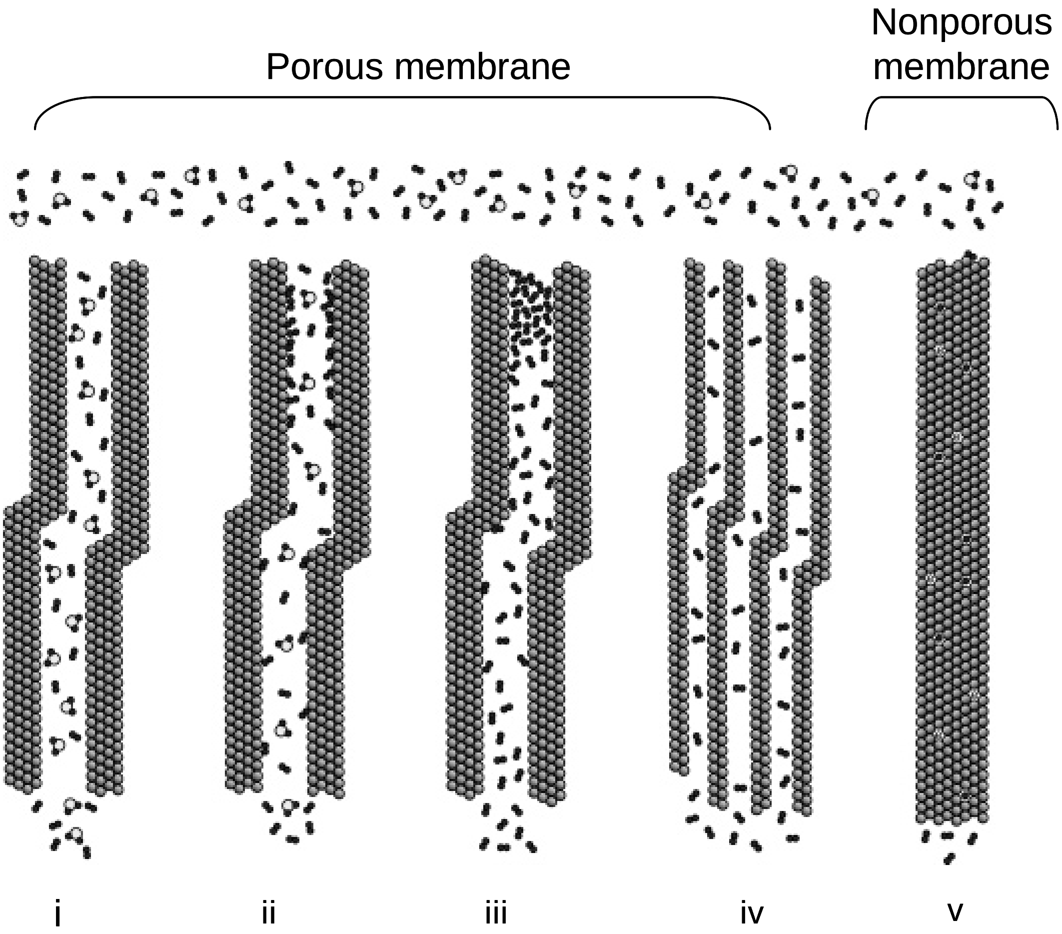

Figure 1.4. Hydrogen separation mechanisms in porous/non-porous membranes of: (i) Knudsen diffusion, (ii) surface diffusion, (iii) capillary condensation, (iv) molecular sieving, and (v) solution diffusion (reprinted with the permission from reference [7]. Copyright 2007, American Chemical Society).

1.2.2.1 Knudsen diffusion

Knudsen diffusion occurs when the mean free path of the diffusing gas molecules is much larger than the pore size. In mesoporous materials the mean free path of a gas molecule is larger than the size of the pore. Therefore, the interaction between gas molecule and pore wall is more important than the molecule-molecule interaction. The Knudsen number K_n is a characteristic parameter defined as the ratio of the mean free path of gas molecules [13]. Its value is given by $K_n = \lambda/d_p$, where λ being the average free path of the gas molecules and d_p is the pore diameter. When $\lambda >> d_p$ the movement of molecules inside the narrow pore channels takes place through collisions of diffusing molecules with the wall rather than with each other. In the regime of Knudsen diffusion the permeance (P_K) is given by following equation [14]:

$$P_K = \frac{\varepsilon d_P}{\tau L}\left(\frac{8}{9\pi MRT}\right)^{\frac{1}{2}}, \tag{1.8}$$

where ε is the porosity of the membrane, d_P is the pore diameter, τ is the tortuosity, L mean membrane thickness, R is the gas constant, T is the temperature, and M is the molecular weight of the diffusing gas.

Since the driving force for transport is the partial pressure of the gas species, Knudsen transport can occur either by concentration gradients or by pressure gradients. The relative permeation rate of each component is inversely proportional to the square root of its molecular weight. Selectivity can be calculated with the square root of the ratio of the molar masses of gases involved (based on equation 1.6). For example, the selectivity of H_2 with respect to CO_2 by Knudsen diffusion will be 4.7. Hence, separation by Knudsen diffusion has a limited selectivity and depends on the molecular masses of gases and is therefore only applied for the separation of light gases from heavier ones. However, fluxes through the membrane are high.

1.2.2.2 Surface diffusion

Gas molecules can interact with the surface, adsorb on surface sites and be mobiles on the surface. In the surface diffusion mechanisms, the diffusing species adsorb on the walls of the pore, and then readily transport across the surface in the direction of decreasing surface concentration. Molecules with larger molecular weight and with larger polarity and polarizability are selectively adsorbed on the membrane surface [15]. The adsorbed species on the membrane pores can also drastically reduce or eliminate the transport of non-selectively adsorbed molecules across the pore by reducing the size of accessible void space through the pore [15]. This hindrance effect introduces non-adsorptive separation selectivity for the adsorbed species when the pore size is between 2 to 3 molecular diameters of the adsorbed species. The concentration of adsorbed species depends upon the temperature, pressure, and the nature of the surface. The effect of surface diffusion is pronounced at moderate temperatures. At higher temperatures, adsorption decreases and therefore surface diffusion will be less pronounced at higher temperatures. In order to employ surface diffusion as an effective separation mechanism, the pores should be very small (pore radius < 3 nm) and the temperature should be kept low (< 300 °C), due to the necessary physical adsorption of the gas [16].

1.2.2.3 Capillary condensation

In porous system at the temperature below the critical temperature point of the diffusing gas, the increase of pressure first leads to multilayer adsorption until finally all pores are filled with liquid. This phenomenon is called capillary condensation [17]. The unique aspect of capillary condensation is that vapor condensation occurs below the saturation vapor pressure, P_{sat}, of the pure liquid. If the pores are completely filled with condensed phase, only the species soluble in the condensed phase can permeate through the membrane. Fluxes and selectivities are generally high for capillary condensation. Although this separation mechanism appears to be effective, it is limited by the need for a condensable component. This restricts its applicability range due to the temperature and pressure range needed for capillary condensation.

1.2.2.4 Molecular sieving and activated diffusion

When the pore sizes in membranes become quite small (< 2 nm), molecular sieving can be used to separate molecules. The pore size becomes so small that only smaller molecules can permeate through the membrane. High selectivity and permeability for the small gas molecules in a mixture can be obtained from molecular sieving, but a very fine-tuning of the membrane pore sizes is required to achieve the desired separation efficiency [18]. One of the most important characteristics of microporous membranes, which results in very high separation factors, is the activated gas transport. It has been found that the permeance (P_{MS}) through microporous materials increases as function of temperature [19] according to equation 1.9.

$$P_{MS} = P_o \exp\left(-\frac{E_a}{RT}\right), \tag{1.9}$$

where P_o is pre-exponential factor, E_a is activation energy, R is gas constant, and T is temperature.

1.2.2.5 Solution diffusion

In dense membranes, there is no pore available for gas diffusion using the above mentioned mechanisms. The most common model to describe gas transport through dense membranes is the solution diffusion mechanism. Gases are soluble in the membrane matrix to a certain extent. Due to differences in solubility and diffusivity of gases in the membrane, separation occurs [13]. A gas molecule is adsorbed on one side of the membrane, dissolves in the membrane, diffuses through the membrane and desorbs on the other side of the membrane. When diffusion through the membrane takes place in the form of ions and electron or as atoms, the molecules first split up after adsorption and recombine after diffusing through the membrane. Separation through polymeric membranes is based on this mechanism as well as in dense inorganic membranes. Selectivity by solution diffusion mechanism is quite high, but the flux is quite low, in comparison to that is observed in porous membranes.

1.2.3 Materials

Gas selective membranes can be broadly categorized into four types: polymeric (organic), metallic, carbon and ceramic (the latter three are named as inorganic). Much work has been done in the development of polymeric membranes compared to inorganic membranes due to relatively lower cost of the polymer. Interest in the field of inorganic membranes development has grown rapidly in the last two decades due to their ability to be operated under higher temperature than polymeric membranes and their relatively higher chemical stability. Table 1.1 presents selected properties (operational temperature range, hydrogen selectivity, hydrogen flux, chemical stability, etc.) of the hydrogen separation membranes and their general characteristics. In the following section state-of-the art and developments in different types of microporous membranes for gas separation has been described.

Table 1.1. Properties of selected hydrogen separation membranes [20].

	Membrane types				
	dense polymer	**microporous ceramic**	**dense metallic**	**porous carbon**	**dense ceramic**
T range, °C	< 100	200-600	300-600	500-900	600-900
H_2 selectivity	Low	5-139	> 1000	4-20	> 1000
H_2 flux	Low	60-300	60-300	10-200	6-80
Stability	Swelling	Stability in H_2O	Phase transition	Brittle	Stability in CO_2
Poisoning	HCl, SO_x	-	H_2S, HCl, CO	Strong adsorbing vapors	H_2S
Materials	Polymers	Silica,alumina, zirconia, titania, zeolites	Pd and its alloys	Carbon	Proton-conducting ceramics
Transport mechanism	Solution-diffusion	Molecular sieving, activated diffusion	Solution-diffusion	Surface diffusion, molecular sieving	Solution-diffusion

1.2.3.1 Metals and alloys

Metallic materials are of great interest for hydrogen-selective membranes. The fundamental mechanism governing the performance of dense metallic membranes is quite different from porous membranes. In a dense metallic membrane, H_2 permeates through the solid material via the solution diffusion mechanism that involves a total of seven steps [7]: (i) arrival of a mixture of H_2 and undesired gas stream to the feed end of the membrane; (ii) dissociation of chemisorbed H_2 into H^+ ions and electrons (e^{-1}); (iii) adsorption of H^+ ions into the membrane bulk; (iv) diffusion of H^+ ions and electrons through the membrane; (v) desorption of H^+ ions and the electrons into discrete molecules of H_2; (vi) reassociation of the H^+ ions and the electrons into H_2 molecules; and (vii) diffusion of the H_2 from the permeate-end of the membrane. The diffusive flux of hydrogen through a bulk metal membrane of thickness L is generally described by Sievert's law [21]:

$$J = \frac{-k(\sqrt{P_f} - \sqrt{P_p})}{L}, \tag{1.10}$$

where J is diffusive flux (molm^{-2}s^{-1}), k is the hydrogen permeability of the metal (molm^{-1}s^{-1}Pa$^{-0.5}$), L is the membrane thickness (m), P_f and P_p are the hydrogen partial pressures (Pa) on the feed side and permeate side of the membrane surface. The square-root proportionality of hydrogen flux with respect to the partial pressure driving force is indicative of the bulk phase diffusion as the rate-limiting step [22]. As hydrogen is transported through a unique dissociated atomic form through the metal, the metal membranes are 99.9% selective to hydrogen and allow the permeation of undesired gas species through pin-holes and defects in the metal membrane.

High-purity hydrogen could be available through dense metallic membranes especially through Pd and its alloys. Hydrogen selectivity is typically very high in these systems, since the dense structure prevents the passage of large atoms and molecules such as CO, CO_2, O_2, N_2, etc. This high selectivity translates to very high purity hydrogen and the increased thermal stabilities allow higher operating temperatures. The metals which are most suitable for H_2 separation membranes typically have high H_2 permeabilities [23], high diffusivities or solubilities [24], and good thermal stability elevated temperatures [25]. Metallic membranes for hydrogen separation could be of many types, such as (i) pure metals: Pd, V, Ta, Nb, and Ti; (ii) binary alloys of Pd: Pd-Cu, Pd-Ag, Pd-Y etc.; (iii) complex alloys: Pd alloyed with more than two other metals; (iv) amorphous alloys: typically Group IV and Group V metals;

and (v) coated metals: Pd over Ta, V, etc. The permeability of H_2 through these types of membranes is a function of the lattice structure and various types of lattice defects (vacancies, dislocation) and reactivity towards H_2. Body centered cubic (BCC) metals such as Fe, V, Nb, and Ta exhibit high H_2 permeabilities [23-24] than face centered cubic (FCC) metals such as Pd and Ni [26]. Pd possessing significantly higher H_2 permeability than Ni. H_2 permeability decreases with increasing temperature in the case of Nb, V, and Ta. This is due to the decrease of hydrogen solubility more rapidly that the increase of the diffusion coefficient. Although Nb, V, and Ta have higher permeabilities (10–15 times greater than Pd), these metals form oxide layers and are difficult to use as hydrogen separation membranes [26].

Historically, H_2 separations were performed with Pd-based membranes, since they naturally catalyze the surface dissociation/reassociation processes and are highly permeable to hydrogen. Extensive research works have been done in the field of Pd-based membranes [27-33]. Pd is the most widely researched material since it is highly permeable to the H_2, resistant to ambient conditions of air, oxygen and moisture, and is able to rapidly dissociate H_2 molecules into atoms on the surface. Pd alloy membrane can be used to produce H_2 for practical purposes with a purity of up to 99.99%. Earlier in United States and former Soviet Union, relatively thick-walled tubes of Pd were employed. The nearly perfect hydrogen permselectivity of thicker Pd membranes enables them to provide very high purity H_2 for use in semiconductor manufacturing industry. But monolithic Pd foils and tubes are very costly and hence prohibitive for most purposes. Therefore, to produce economic means of H_2 separation on an industrial scale, a thin layer of about < 20 µm, adherent and durable Pd film must be applied to a hydrogen-permeable support [34]. Kikuchi and Uemiya have done an extensive work on Pd composites that uses porous membranes as supports [35-38]. Over the last decade, composite Pd membranes coupled with high permselectivity and reasonable H_2 fluxes have been fabricated using a range of deposition methods and supports. Composite membranes consist of a thin layer of Pd on H_2 permeable support so that Pd films with micron thicknesses or less are attainable. Very high H_2 permselectivity is possible if a defect-free Pd can be deposited onto the membrane support. In addition, the membrane can be operated at high transmembrane pressure differentials because the substrate provides mechanical supports for the thin Pd film.

A major limitation of the Pd membrane is the high cost of this metal and difficulty of fabricating defect free membranes with films of the order of microns or less. There are several other problems that impede the use of Pd membrane technology. Additionally, Pd may undergo a phase transition ($\alpha \rightarrow \beta$) in the presence of H_2 at temperature below 300 °C [39-40]. This leads to an increase in lattice size as it absorbs H_2, leading to wraping and embrittlement. To avoid metal embrittlement and resulting membrane cracking or distortion, pure Pd should not be exposed to H_2 at temperatures below 300 °C. Pd is also susceptible to contamination/poisoning by common industrial constituents such as hydrogen sulfide, chlorine, carbon monoxide, and hydrocarbons. Long-term stability at high temperature, above 450 °C, has been a problem, mainly deactivation by carbon under reaction conditions in a membrane reactor [41-43]. To increase resistance to embrittlement, Pd is alloyed with other metals such as Ag and Cu. In addition to providing thermal stability, alloying Pd with other metals also increases its resistance to chemical contaminants. Pd-Ag alloy is found to maximize the hydrogen permeability. Alloying of Pd with Cu has been reported to offer significant tolerance to the presence of hydrogen sulfide in the hydrogen gas stream [44-45]. Several other alloying elements, such as Au, Y, and Ce have been identified with significant increase in hydrogen permeability [46]. Ternary alloy compositions (Pd-Cu-transition metal) are also being investigated for maximizing membrane permeability and stability.

For Pd membranes to be economically attractive in H_2 separations one must try to increase their flux by a factor of 2–4. Hence, research is focused on the preparation of thin metallic films. Thin membranes would reduce the cost as well as increase the H_2 flux. Thin Pd membranes are deposited on porous supports. Two supports were widely used, such as porous

Vycor (silica glass), and porous alpha-alumina [26]. These supports are used because of their smooth surface. However, fitting ceramics to metals gives the mechanical stability. Therefore, stainless steel could be used as a support material because of its mechanical stability, its thermal expansion coefficient close to that of Pd, and its ease of sealing. Generally there are three methods for coating thin metallic films onto supports: electroless-plating, chemical vapour deposition (CVD), and physical sputtering [47]. Under controlled conditions all these methods produce good quality membranes with high hydrogen selectivity. Table 1.2 presents some of the selected metallic membranes, substrate used for coatings, and their hydrogen permeance and selectivity.

Table 1.2. Selected metallic membranes for hydrogen separation.

Method (material)	**Support**	**H_2 Permeance (10^{-6} molm^{-2}s^{-1}Pa^{-1})**	**Selectivity**
CVD (Pd)	γ-Al_2O_3	0.1–0.2 at 773 K [2]	200–300 (H_2/He)
electroless (Pd)	TiO_2	6.3 at 773 K [49]	1140 (H_2/N_2)
electroless (Pd)	stainless steel	0.22 at 623 K [50]	110 (H_2/N_2)
electroless (Pd-Cu)	γ-Al_2O_3/ZrO_2	0.023 at 723 K [44]	1150 (H_2/N_2)
electrodeposition (Pd-Cu)	Ni-porous stainless steel	8.4 at 723K [51]	3000 (H_2/N_2)
electrodeposition (Pd-Ni)	stainless steel	6.7 at 723 K [52]	10000 (H_2/N_2)
electrodeposition (Pd-Ag)	silicon wafer	45 at 723 K [53]	4000 (H_2/N_2)

1.2.3.2 Polymer

Gas separation from polymer membranes is used industrially for hydrogen separation from gaseous mixtures that consist of N_2, CO, or hydrocarbons. In the past decades, a considerable amount of attention has been paid to polymeric membranes for gas separation applications. Polymeric membranes such as UOP Polysep membrane systems and Monsanto PRISM membrane systems are currently used to recover hydrogen from refinery, petrochemical, and chemical process streams [54].

Polymeric membranes are generally used in lower-temperature hydrogen-recovery. Operating temperatures are limited to 90–100 °C [55]. These membranes are less expensive, easier to process, and more mechanically tunable than their inorganic counterparts. Good ability to cope with high pressure drops and low costs are key advantages of polymer membranes. However, limited mechanical strength, relatively high sensitivity to swelling and compaction, and susceptibility to chemicals such as HCl, SO_x, and CO_2 make them less attractive.

Polymer membranes are dense type and can be further divided into *glassy* (prepared at temperature below the glass transition temperature) and *rubbery* (prepared at temperature below the glass transition temperature) polymeric membranes. Glassy membranes have higher selectivity and lower flux, whereas rubbery membranes have higher flux but lower selectivity [55]. Glassy polymers are dominated by diffusivity selectivity and thus are often employed to remove lighter gases such as H_2, whereas rubbery polymers are dominated by solubility selectivity and are used to remove heavier gases like CO_2. Polymer membrane used for gas separation processes follow solution-diffusion mechanism. Some of the polymers which have been tested with respect to hydrogen permeation are polysulfone, polystyrene, polymethyl methacrylate, polyvinylidene fluoride [20]. Polysterene shows the best combination of H_2 permeability and selectivities over N_2, CH_4, and CO_2 [1], with H_2/N_2 and H_2/CO_2 selectivity of about 39.7 and 2.3, respectively.

As we have seen in previous sub-sections (1.2.3.1 and 1.2.3.2), metal and alloys membranes are sensitive to gases such as CO or H_2S, ceramic membranes which are inert to these poisonous gases would be of better choice for H_2 purification. In microporous ceramic membranes, the flux is directly proportional to the pressure, where as in Pd membranes, it is proportional to the square root of the pressure. Hence, microporous ceramic membranes become more attractive options when systems are operated at higher pressures. Also, in microporous inorganic membranes permeance increase with temperatures. Therefore, microporous ceramic membranes can be operated at higher pressures and temperatures. In the following two sub-sections silica and zeolite based membranes are described.

1.2.3.3 Silica

Silica ceramic membranes have shown great potential for the hydrogen separation and production application in the last decade. Amorphous silica contains irregular pores with a mean pore size of about 3 Å. These membranes are selective to small molecules such as H_2 and He. These membranes have shown exceptional H_2 selectivities, H_2/N_2 ~10000 [57-58]. Typical H_2 permeance through silica membranes are of 10^{-9}–10^{-10} mol m^{-2} s^{-1} Pa^{-1} at 500 °C, which is very low and not sufficient for practical applications. To increase the permeance of the silica membranes, they should be deposited on porous supports as a thin film. Ultrathin membranes have been developed on porous substrates by sol-gel coating [59] or CVD techniques [60-61]. Silica polymeric sols are formed by acid-catalyzed hydrolyis and the polymerization of tetraethylothosilicates (TEOS) or methyltriethoxysilane (MTES) under controlled reaction conditions of pH, temperature, and duration. In a CVD technique, silica particles may be formed by chemical reactions, e.g., gas-phase silane hydrolysis or thermal decomposition of precursors.

Although silica membranes are hydrogen-selective at high temperatures, it is also known to be reactive with water, hence, degradation of separation performance over time in the presence of steam at high temperatures. The interaction of the water molecules with the silica surface depends on the type of the functional groups, which are mainly hydroxyl-groups in case of silica. Prolonged exposure of silica in humid air above 400 °C causes rapid densification [62]. Owing to low selectivity and concerns about hydrothermal stability in the synthesis gas environment containing steam porous silica membranes are not suitable for hydrogen separation. In order to improve hydrothermal stability of silica membranes researchers have added metal [63], inorganic oxides [64-66] etc., into silica. Metals-doped silica membranes exhibited separation properties similar to the pure silica membranes but the hydrothermal stability of metal-doped silica was significantly improved. Duke et al. improved hydrothermal stability of silica membranes by modifying the surface with carbon [67]. They applied a novel carbonized template into the silica micropores which provided hydrothermal stability at 200 °C without any loss in the membrane performance after 200 hours of continuous operation. Table 1.3 presents H_2 separation performances of some selected silica membranes synthesized by different methods.

Table 1.3. Performance of H_2 selective silica membranes derived by different methods/modifications.

Method/materials	**H_2 Permeance (10^{-8} mol m^{-2} s^{-1} Pa^{-1})**	**Selectivity**
sol-gel	36 at 543 K [68]	150 (H_2/N_2)
sol-gel	200 at 473 K [69]	> 500 (H_2/CH_4)
sol-gel	0.4 at 423 K [70]	< 100 (H_2/N_2)
CVD	0.06 at 700 K [71]	160 (H_2/N_2)
CVD	0.02 at 873 K [60]	4200 (H_2/CH_4)
ZrO_2 doped	8.9 at 773 K [64]	190 (H_2/N_2)
NiO doped	20 at 773 K [65]	400 (H_2/N_2)
NbO doped	3.9 at 473 K [66]	46 (H_2/CO_2)

1.2.3.4 Zeolite

Zeolites are crystalline aluminosilicates materials that have uniform, molecular-sized pores. Zeolite structure is made up of TO_2 units, where T is a tetrahedral framework atom (Si, Al, B, Ge, etc.) [7]. Since the development of first zeolite membrane in 1987 [72], significant progress has been made to improve membrane quality. Today more than 14 zeolite structures, including MFI, LTA, MOR, DDR, and FAU have been employed as hydrogen separation membranes. Among various types of zeolite membranes available, the 10-membrane ring MFI structure (silicalite-1 and ZSM-5) is the most extensively studied for gas separation. MFI membranes with high Si/Al ratios possess outstanding thermal and chemical stabilities. Highly siliceous DDR-type zeolite consists of cages connected by narrow elliptical windows of 8-member ring openings [10]. Molecular transport through DDR-type zeolite is mainly controlled by the narrow windows which have dimensions of 3.6×4.4 Å^2 [10]. The DDR zeolite has excellent thermal stability allowing high temperature operations in moist atmosphere.

Zeolite materials are commonly prepared by precipitation under hydrothermal conditions in the presence of a template that dictates the zeolite structure during crystal growth. Generally tetrapropyl ammonium hydroxide (TPAOH) is used as a common template, which is burned off after zeolite crystal growth. In the secondary growth (template-free method), a zeolite seed layer is dip-coated on the support followed by the growth of seeds into continuous zeolite layer [73].

Mechanism of gas permeation through the MFI-type zeolite membrane depends on the gas adsorption properties on the zeolite. Nonadsorbing gas molecules may directly enter the zeolite pores. Permeation of strongly adsorbing gases through MFI membrane is controlled by either adsorption or activated diffusion, or both. In MFI zeolites, H_2 selectivities over other gases were observed to be rather moderate at higher temperatures because gas transport through the 5.6 Å diameter MFI channels is governed by Knudsen-type diffusion. Dong et al. obtained a H_2/CH_4 selectivity of 2 with H_2 permeance of about 10^{-7} mol m^{-2} s^{-1} Pa^{-1} [57]. All the MFI type membranes exhibited ideal H_2/CO_2 selectivities below the theoretical Knudsen diffusion selectivity ~4.69. This low H_2 selectivity was attributed to the existence of nonselective membrane defects, such as, pinholes and sealing leakage as well as possible chemical interactions between the molecules and the chemical impurities in the zeolites structure. DRR-type zeolite membranes having an effective pore-size of 4 Å was expected to offer high H_2 selectivities over gases such as CO_2, CO, CH_4, etc. The DDR zeolite membranes achieved H_2/CO_2 ideal selectivity slightly greater than the Knudsen factor at 500 °C, but the selectivity was far lower than that was expected [74]. Also, the H_2 permeance was lower than that in the MFI membranes by an order of magnitude because of the relatively large membrane thickness (~10 µm). Low H_2 selectivity in DDR membranes has been attributed to the presence of intercrystalline paths in the membranes [10], as shown in Figure 1.5.

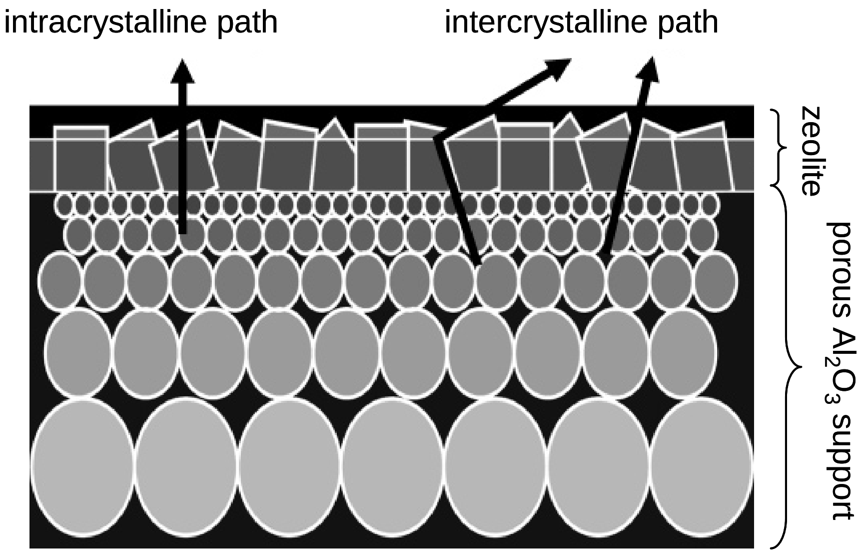

Figure 1.5. A general representation of a zeolite membrane deposited on a porous Al_2O_3 support, showing possible gas permeation pathways either through inter- or intrazeolite crystals (adapted with the permission from reference [7]. Copyright 2007, American Chemical Society).

To improve the performace of zeolite membranes, surface modification techniques have been employed by different research groups. To enhance the H_2 selectivity, MFI membranes must be modified to reduce the intercrystalline pore size as well as to minimize the non-selective intercrystalline pores. In case of DDR-type membranes, improvements are needed to eliminate the intercrystalline pores and to significantly reduce membrane thickness to enhance H_2 permeance. Masuda et al. [75] modified zeolite membranes by catalytic cracking of silanes molecules (methyldiethoxysilane) preadsorbed at the active sites. After calcination, mono-SiO_2 units formed in the zeolite channels that reduced the effective MFI pore-size. H_2 separation factor for H_2/N_2 mixture was increased by more than 50 times at 110 °C but the H_2 permeance was reduced by an order of magnitude from 2.8×10^{-7} to 2×10^{-7} mol m^{-2} s^{-1} Pa^{-1}. Zheng et al. [76] used the counterdiffusion CVD technique to modify the intercrystalline pore in an in situ made DDR zeolite membrane (thickness ~10 µm). They used TEOS as silica precursor. H_2/CO_2 permeselectivity of the membrane was increased from 2.6 to 32.7 after modification. However, H_2 permeance was decreased from about 10^{-6} to 10^{-8} mol m^{-2} s^{-1} Pa^{-1}. Enhancement in H_2/CO_2 selectivity for the modified DDR membrane was attributed to the reduction in intercrystalline pore.

One of the main hurdles to the industrial applications of zeolite membranes is the high cost associated with the time-consuming, energy intensive membranes preparation processes. Another challenge in zeolite membrane development is the minimization of intercrystal pores formed in polycrystalline zeolite films. The existence of intercrystal pores with sizes large than the zeolitic pores is the major cause for decline in molecular separation efficiency. Presently the zeolite membrane development is at a laboratory scale. For commercial applications, greater H_2 flux and selectivity needs to be demonstrated.

1.2.3.5 Carbon

Carbon membranes are prepared in both forms: unsupported and supported. Generally carbon membranes are produced by pyrolysis of polymeric films, such as, polyimide, polyfurfuryl alcohl, polyvinylidene chloride, phenolic resin etc., on a macroporous support in an inert atmosphere with temperatures in the range of 773–1173 K (carbonization). Among the supported membranes, capillary tubes or hollow fibers are prepared. Generally these membranes are several microns thick; the permeance of CMS is low due to fine pore size and low porosity. Because carbon has a natural affinity for adsorption of heavier hydrocarbon species and polar molecules, CMS membranes are used at high temperature to eliminate interference due to adsorption. The permeation characteristics of the carbon molecular sieve (CMS) membranes are strongly dependent on the pyrolysis conditions of temperature and duration [77] — gas permeance through membranes is decreased with an increase in pyrolysis temperature because membranes become denser and pore size is decreased. Hatori et al. prepared CMS membranes from polyimide precursor and found very high H_2/CO selectivity over 1000 at 50 °C [78]. The H_2/CO_2 selectivity was relatively lower, which is thought to be due to the greater adsorption of CO_2 compared to CO. Wang and Hong [79] reported the H_2/N_2 selectivity of about 100 for CMS membranes with very high permeance around 2×10^{-6} mol m^{-2} s^{-1} Pa^{-1}. Carbon membranes are resistant to contaminants such as H_2S and thermally stable and can be used at higher temperatures compared to the polymeric membranes.

Selective surface flow (SSF) membranes were introduced by Rao and Sircar in 1993 [80]. These membranes were synthesized by coating a macorporous graphite disc with layers of polyvinyl chloride-acrylate terpolymer latex polymer followed by pyrolysis at 1000 °C. The permeability of H_2 in a mixture with hydrocarbons was reduced by several orders of magnitude over that of pure H_2, indicating hydrocarbon-selective adsorption hindered pore diffusion of H_2 which makes these membranes promising for H_2 separation. Gas separation process in this membrane works opposite to other inorganic membranes. Since adsorption occurs on the high-pressure side, the partial pressure of the component to be adsorbed can be low. The partial pressure gradient across the membrane does not need to be high to attain separation, since the driving force for mass transfer across the membrane is the difference in the concentration of the adsorbed species. Separation process in SSF membranes are based on the adsorption properties of the components, and larger/polar species can be separated from the mixture. Another advantage of SSF membranes is — adsorption capacity and selectivity increase with decreasing temperature which reduces operational cost.

Although carbon membranes have shown promising applications in the field of H_2 separation, they still have some drawbacks before being introduced in the market. They are very brittle and fragile [79], which requires more careful handling. Furthermore, carbon membranes are still expensive. Processing cost is expensive — it requires a prepurifier for removing traces of strongly adsorbing vapors, which can clog the pores. This problem is avoided by operating at sufficiently high temperatures.

1.2.3.6 Polymer-derived ceramics (PDC)

Since the last few decades ceramics derived from preceramic polymers have attracted great attention due to their advantages over traditional ceramic processing methods. The traditional method to prepare SiC and Si_3N_4 ceramics is the powder technology, which requires sintering additives and very high temperature (1700–2000 °C) [81-82]. Polymer-derived ceramics (PDCs) offer an easier route to synthesize ceramic fibers, thin layer or composites materials which in principle cannot be produced using powder technology [83]. Furthermore, the relatively low temperature (1000–1300 °C) to produce Si-based ceramics is of enormous economical interest. PDCs exhibit exceptional properties, such as, thermal, chemical and oxidation stability up to 1500 °C and above [84].

The first synthesis of the non-oxide ceramic 'SiC' via molecular organosilicon compounds was reported by Fritz in 1956 [85] and later by Yajima in 1975 [86]. However, the production of these ceramics starting from polymeric precursors was reported for the first time in the early 1960s. Later the first practical application — manufacturing of small-diameter Si_3N_4/SiC fibers for high-temperature applications — from polyorganosilicon compounds (polysilazanes, polysiloxanes, and polycarbosilanes) to Si-based ceramics was reported by Verbeek and Winter [87-88]. Different classes of preceramic precursors (polysilazane, polycarbosilane, polycarbosiloxanes, polysiloxanes, etc.) which are generally used for the synthesis of PDCs are illustrated in Figure 1.6.

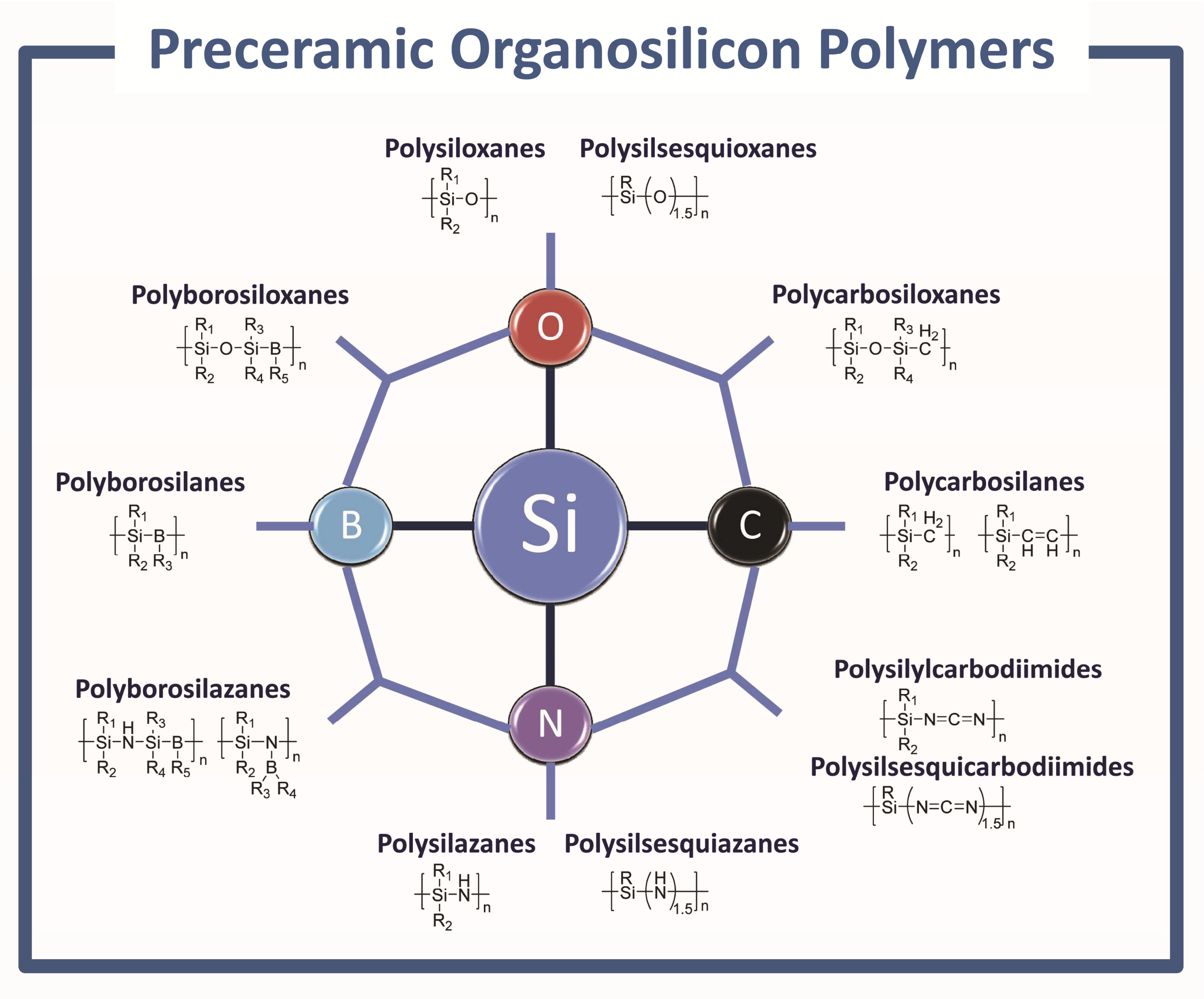

Figure 1.6. Main classes of Si-based polymers for ceramics: polysilazanes, polyborosilazanes, polyborosilanes, polyborosiloxanes, polysiloxanes, polycarbosiloxanes, polysilylcarbodiimides etc. (reproduced from reference [89] with the permission of John Wiley and Sons).

These polymers are characterized by an inorganic backbone and organic substituents. The backbone provides thermal resistance and the substituents can possess the ability to modify properties, such as, solubility, hydrophobicity/hydrophilicity. These substituents also affect the cross-linking ability between polymeric chains. The molecular structure of preceramic polymer influences — the composition, number of phases and phase distribution, microstructure of the final ceramic materials.

Formation of PDCs consists of three main steps [90]: (i) synthesis of the preceramic polymer; (ii) cross-linking of the polymer at moderate temperatures to get organic/inorganic network; (iii) ceramization process of the cross-linked polymer – polymers are converted to inorganic amorphous/crystalline materials depending on the pyrolysis temperature between 800 °C to 1800 °C. One of the main advantages of using the PDCs route is the control over the final composition of the ceramic by using different preceramic polymeric precursors, cross-linking and pyrolysis conditions.

Chlorosilanes R_xSiCl_{4-x} (x=0, 1, 2, 3) are the most common starting materials used for the synthesis of above shown different preceramic organosilicon polymers (Figure 1.6). The monomers used in the synthesis of organosilicon polymers contain active sites such as Si-H, Si-Cl, Si-C=C, which allows polymerization by means of elimination, substitution or addition reactions. These polymers are generally produced in large scale by the Müller-Rochow process — involving the reaction of gaseous methyl chloride with silicon, containing copper as catalyst in a fluidized-bed reactor at 250-300 °C. Different synthesis routes of organochlorosilicon polymers are shown in Figure 1.7.

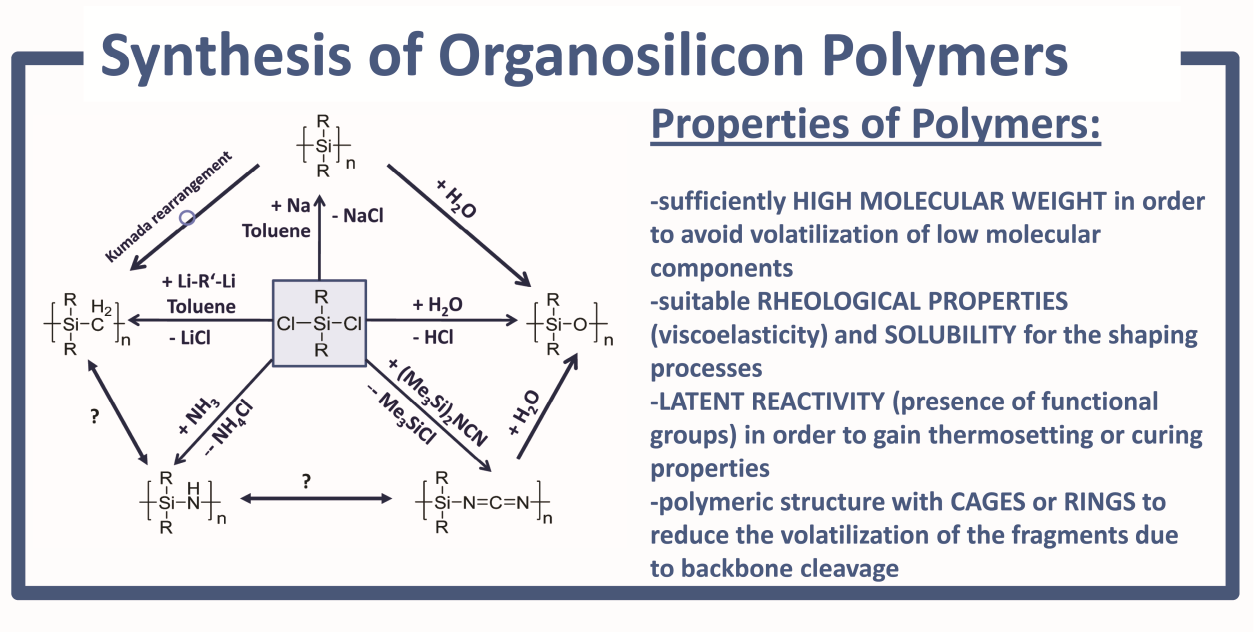
Synthesis of Organosilicon Polymers

Properties of Polymers:

-sufficiently HIGH MOLECULAR WEIGHT in order to avoid volatilization of low molecular components

-suitable RHEOLOGICAL PROPERTIES (viscoelasticity) and SOLUBILITY for the shaping processes

-LATENT REACTIVITY (presence of functional groups) in order to gain thermosetting or curing properties

-polymeric structure with CAGES or RINGS to reduce the volatilization of the fragments due to backbone cleavage

Figure 1.7. Synthesis routes of most representative classes of Si-based preceramic polymers from organochlorosilanes (reproduced from reference [89] with the permission of John Wiley and Sons).

As already mentioned above, the second critical step in the processing of PDCs is the cross-linking process. During this step the polymeric precursors are converted into organic/inorganic hybrid materials at low temperatures (100–300 °C). This transformation prevents the loss of low molecular weights of components (monomers) of the precursors, and thus increases the ceramic yield. Various possible reactions occurring during cross-linking are illustrated in Figure 1.8, in case for polysilazanes:

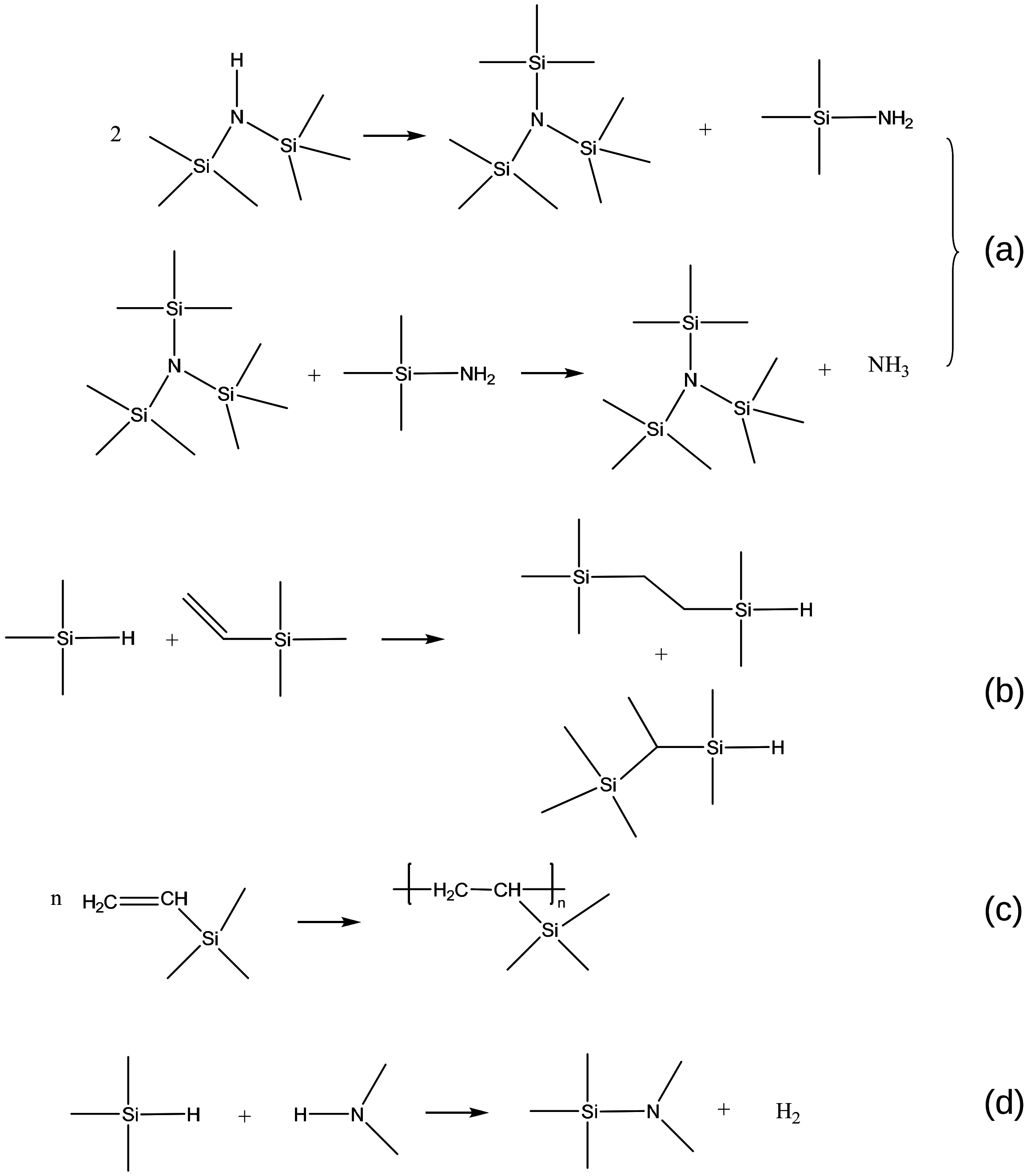

Figure 1.8. Cross-linking reactions of polysilazanes: (a) transamination, (b) hydrosilylation, (c) vinyl polymerization, (d) dehydrocoupling (adapted from reference [90]).

Cross-linking of polysilazanes occurs via four major reactions: transamination, dehydrocoupling, vinyl polymerization and hydrosilylation. *Hydrosilylation* reaction occurs for the precursors containing Si-H and vinyl groups, which leads to the formation of Si-C-Si and Si-C-C-Si bonds. This is a fast reaction which can even occur starting from 100-120 °C. Higher ceramic yields as well as higher carbon contents can be achieved in the final ceramic due to hydrosilylation reaction [91]. *Dehydrocoupling* of Si-H/N-H or Si-H/Si-H leads to Si-N and Si-Si bond formation and hydrogen evolution. This reaction generally starts at 300 °C. *Vinyl polymerization* occurs at higher temperatures with no mass loss. *Transamination* reactions (200–400 °C) are associated with the evolution of amines, ammonia etc. and hence mass loss occurs. This reaction leads to a decrease in the nitrogen content.

During the last step, polymer-to-ceramic conversion, thermal decomposition of the basic organosilicon polymer occurs, namely the so called ceramization process [90]. The ceramization process of cross-linked precursors involves thermolysis and volatilization of organic fragments and hydrogen in the temperature range between 600 and 1000 °C, which finally results in the formation of mostly amorphous ceramics. Investigation of the volatile species and fragments of the decomposition products during the organic/inorganic transformation is monitored by simultaneous thermal analysis coupled by mass spectrometry (TGA) and/or FTIR spectroscopy. *During the polymer-to-ceramic transformation, evolution of gases, such as, CH_4, NH_3, H_2, etc., leads to generation of pores in the ceramic matrix. This process of pore generation can be utilized for the development of microporous ceramic membranes by depositing polymeric precursor on a porous support followed by a pyrolysis process.* The thermal decomposition behavior of different organosilicon polymers is illustrated in Figure 1.9. After the thermal treatment above 800 °C different preceramic polymers like polycarbosilanes, polysiloxanse and polysilazanes/polysilylcarbodiimides are transformed into amorphous SiC, $Si_xC_yO_z$ and $Si_xC_yN_z$ ceramics, respectively.

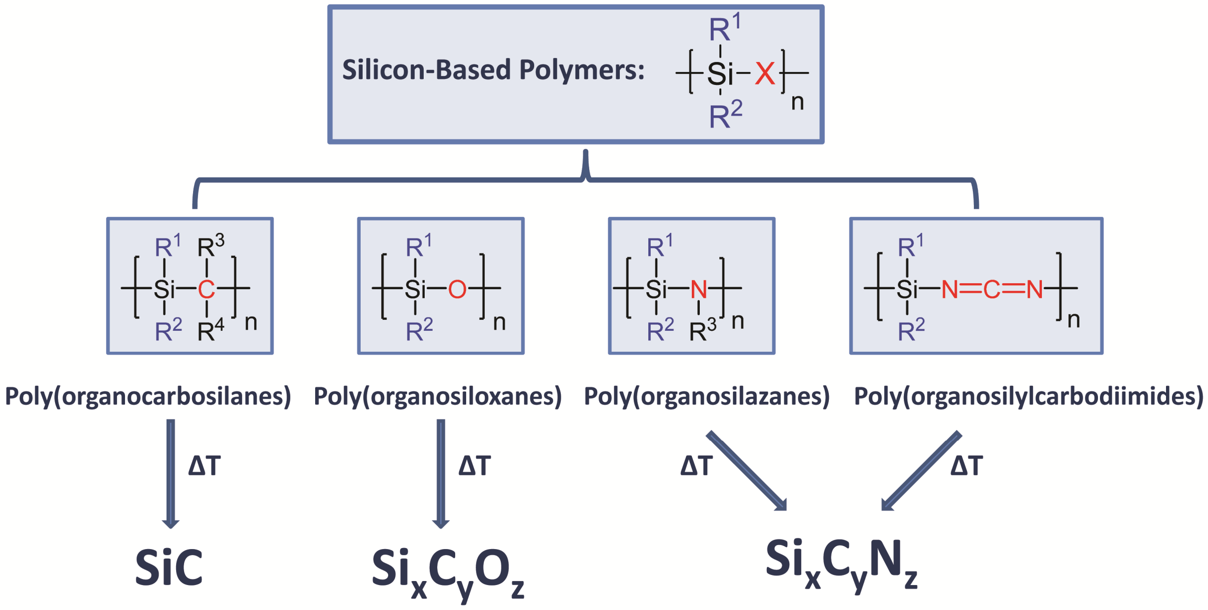

Figure 1.9. Thermal decomposition of silicon-based polymers. Polymer-derived silicon carbide (SiC), silicon oxycarbide ($Si_xC_yO_z$) and silicon carbonitride ($Si_xC_yN_z$) ceramics are obtained after the thermal treatment of polycarbosilane, polysiloxane and polysilazanes/polysilylcarbodiimides, respectively, at T ≥ 800 °C under inert atmosphere (Ar or N_2) (reproduced from reference [89] with the permission of John Wiley and Sons).

Very few works have been reported in the field of hydrogen separation using polymer-derived ceramic membranes and are summarized in Table 1.4. H_2-permselective amorphous SiOC membranes were synthesized by curing of polycarbosilane or polydimethylsilane in air at 373 K and subsequent pyrolysis at 573–1223 K in argon [92-94]. An amorphous SiO_2 membrane was synthesized by the thermal conversion of a polysilazane in air on a Si_3N_4 porous support at 873 K [1]. This polysilazane-derived SiO_2 membrane exhibited a H_2/N_2 selectivity of 141 at 573 K. Thermally stable amorphous microporous SiC membranes were synthesized from polycarbosilane by a cross-linking/pyrolysis process in argon [96-97]. Novel SiCN and SiBCN forming polymers have been synthesized and were studied for the applications as high-temperature hydrogen separation membrane [98-99].

Table 1.4. Gas permeation properties of polymer-derived ceramics (data taken from reference [90] and references therein).

Precursors: Ceramics	**Pyrolysis Temperature**	**H_2 Permeance (10^{-8} mol m^{-2} s^{-1} Pa^{-1})**	**Selectivity**
PCS: SiOC	723 K under Ar	55.0 at 673 K [92]	7.2 (H_2/N_2)
PCS: SiOC	1223 K under Ar	1.0 at 673 K [93]	18-63 (H_2/N_2)
PDS: SiOC	573 K under Ar	8.9 at 473 K [94]	100 (H_2/N_2)
PSZ: SiO_2	873 K in Air	1.3 at 573 K [1]	141 (H_2/N_2)
PCS: SiC	1073 K under Ar	8.1 at 873 K [96]	11.6 (H_2/N_2)
PCS: SiC	973 K under Ar	8.0 at 373 K [97]	100 (H_2/N_2)
PCS-PVS: SiOC	1123 K under Ar	0.3 at 523 K [100]	206 (H_2/N_2)

PCS: Polycarbosilane, PDS: Polydimethylsilane, PSZ: Polysilazane, PVS: Polyvinylsilane.

1.2.4 Membrane properties required for efficient gas separation

The five performance targets for H_2 separation set forth by the U.S. Department of Energy reflect the present capabilities and highlight the distinct research and development opportunities which are necessary to fully realize the “hydrogen economy” [7]. These target values are listed in Table 1.5.

Table 1.5. Current status and future H_2 membrane performance targets [7].

property	**2003**	**2007**	**2010**	**2015**
cost (USD/ft^2)	178	150	100	< 100
operating T (°C)	300–600	400–700	300–600	250–1000
operating ΔP (MPa)	0.69	1.38	≤ 2.75	2.75–6.90
H_2 recovery (% gas processes)	60	70	80	90
H_2 purity (% of dry gas)	> 99.9	> 99.9	> 99.95	99.99
durability (years)	< 1	1	3	> 5

To set long-term targets for membrane technology Verweij et al. [73] has provided a number of interrelated goals for inorganic membranes: (i) gas permeance > 10^{-5} mol m^{-2} s^{-1} Pa^{-1} with selectivity > 100, (ii) < 50% degradation in these properties over > 10000 hours of operation, (iii) production yield > 90%; reproducibility > 90%, (iv) regeneration and/or in situ repair capability to restore > 90% of the original transport properties.

Aforementioned goals indicate the basic and important properties are selectivity and permeance. High permeance and selectivity are most likely met with thin microporous membrane layers because of their porous and selective structure. In the absence of defects, the selectivity is a function of the material properties at given operating conditions. The productivity is a function of the material properties as well as the thickness of the membrane film, and the lower the thickness, the higher the productivity. Materials with relative high fluxes require that the effective thickness of the membrane to be made as small as possible without introducing defects. Highly permeable membrane are not in thick membrane form to minimize overall material cost. The permselectivity should be as high as possible to allow flexibility in setting transmembrane pressure difference. Unfortunately, high permselectivity often correlate with low membrane permeance, and this presents a compromise between productivity and selectivity of the membrane.

Membrane long-term operational stability is related to the occurrence of unwanted chemical reactions, phase transformation, and diffusion processes. For example, reaction of Pd based membranes with sulfur components [101], reaction of silica membranes with high pressure steam [102], aqueous dissolution of mesoporous γ-Al_2O_3 [103], etc. This degradation can be suppressed by selecting more stable compositions. For aqueous environments the choice of stable meso-porous structures is limited to TiO_2, ZrO_2, CeO_2, and SnO_2.

Development in inorganic membranes has been seriously restrained by poor yields on a lab scale and related low reproducibility. The most viable synthesis and manufacturing routes for supported inorganic membranes are based on consolidation of ceramic, polymers followed by thermal processing [104]. Dry powders are often poorly defined with broad size distribution, impurities, and irregular agglomeration. Shaping these powders into plates/tubes by dry pressing/extrusion generally results in low relative densities and major defects in the packing structure and the external surface [105]. Bulk inhomogeneity increases during thermal processing while surface defects propagate into subsequent intermediate and membrane layers. In gas separation a small amount of surface defects can significantly degrade overall selectivity of supported membrane. The quality of ceramic powder is steadily improving, and α-Al_2O_3 particles with a narrow size distribution are readily available. Large agglomerates and contaminations are removed by size-selective techniques like ultra-sound assisted screening [105]. Substantial progress has been made in the preparation of flat multilayer supports. On the other hand, high-quality tubular multilayer supports for high-performance gas separation are yet to be developed. Layer homogeneity and smoothness, which results in less localized stress formation, have a favorable effect on operational stability.

1.2.5 Membrane reactor concept

As already mentioned in section 1.1.1, hydrogen is mainly produced via steam reforming of hydrocarbons in conventional systems. This reaction goes through different intermediate stages to convert CO into CO_2 and H_2. Moreover, in this reaction high temperature energy supply is needed for complete conversion. Hence, research is focused to search for alternative ways of high efficient H_2 production system. In this respect “membrane reactor (MR)” seems to be a possible solution where both reaction and separation occurs simultaneously. Due to the integration of reaction and separation processes, chemical processes become simpler which leads to much lower processing cost. Moreover, membrane reactors are capable of promoting a reaction by selectively removing one of products from the reaction zone through membrane which shifts the reaction equilibrium to the products side. This increases the yield of the desired product. Thus selectivity is also improved by suppressing other undesired reactions. In other words, if H_2 can be selectively removed from the products side during hydrogen production in membrane reactors, thermodynamic equilibria of the reactions (steam methane-reforming and water-gas shift) are shifted to the product side, and higher conversions of CH_4 to H_2 and CO/CO_2 can be achieved and at even lower temperatures. Calculation done by Shu et al. [106] shows, membrane separation can result in the significant conversion improvement on the methane steam-reforming in a lower temperature range of 500-600 °C.

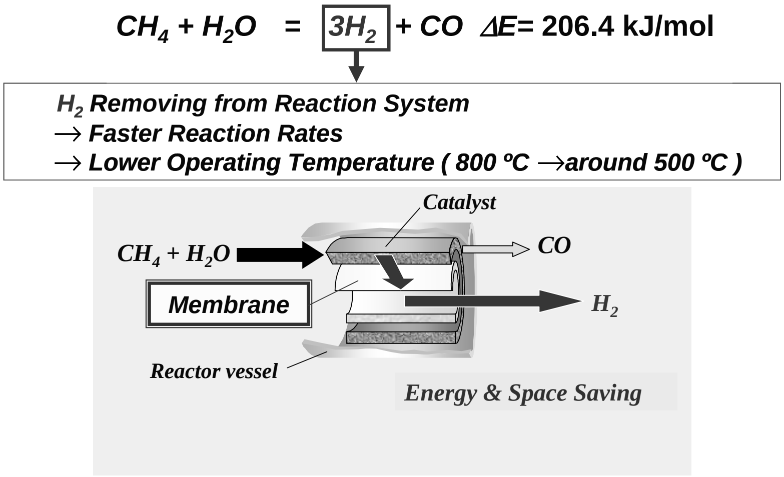

Figure 1.10. A novel membrane reactor for hydrogen production and purification (adapted from reference [2]).

The most common configuration of a MR consists of a membrane developed over a porous support, as shown in Figure 1.10. Depending on the catalytic activity of membrane, a MR can be classified as inert membrane reactor, where the catalyst is located out of the membrane and the membrane is exclusively used as a separator or as catalytic membrane reactor, with a catalytically active membrane [107]. Catalytic activity in a membrane can be introduced by three ways: (i) the catalyst is coated in the form of paste on the membrane, (ii) the membrane itself could be catalytically active, and (iii) by impregnating catalyst into the pores of a microporous materials.

1.3. Metal-oxide based gas sensors

According to the definition of a gas sensor, given by the International Union of pure and Applied Chemisty (IUPAC), “a chemical sensor is a device that transforms chemical information, ranging from the concentration of a specific sample component to total composition analysis, into analytically useful signal. The chemical information, mentioned above, may originate from a chemical reaction of the analyte or from a physical property of the system investigated" [108]. Gas sensors are constructed by combining two functions- first to recognize gas molecules and second to transduce the recognition into a signal output, as shown in Figure 1.11. Gas recognition is usually carried out through the interaction (adsorption, reaction) of gas molecules with the chosen material (receptor). The interaction exerts physical or chemical effects on or around the receptors, such as formation of reaction products, heat generation, changes in mass or dimension of receptor. Any of these effects can be converted into electrical or optical signals through chosen material properties (transducers).

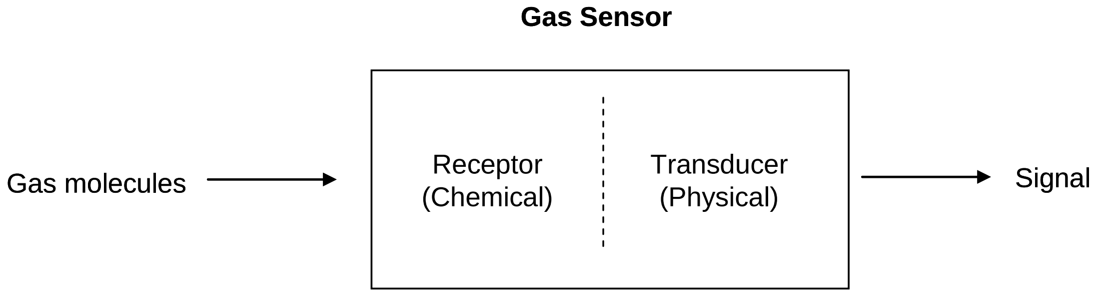

Figure 1.11. Construction of gas sensors with receptor and transducer (adapted from reference [109]).

In order to monitor different gases, varieties of gas sensors have been developed and many are commercially available. Semiconductors, ionic conductors, piezoelectric crystals, optical fibers, and other functional materials have been introduced as gas sensors. Various gas sensors which are presently commonly used are shown in Figure 1.12. Semiconductor gas sensors are divided into two main groups using metal oxide and Si, for which sensor devices are constructed in form of resistor and MISFET (Metal-Insulator-Semiconductor Field-Effect Transistor), respectively [109]. The former group is currently dominating in the field of gas sensors. Semiconducting metal-oxide based gas sensors have attracted attention among users and scientists in gas sensing. These sensors are also known as chemiresistor, metal-oxide-based gas sensor (MOX), gas-sensitive resistors, or semiconductor gas sensors. A sensor element generally comprises a sensitive layer which is deposited over a substrate provided with electrodes for the measurement of the electrical signal. The device is generally heated by heater separated from the sensing layer and electrodes by an electrical insulating layer.

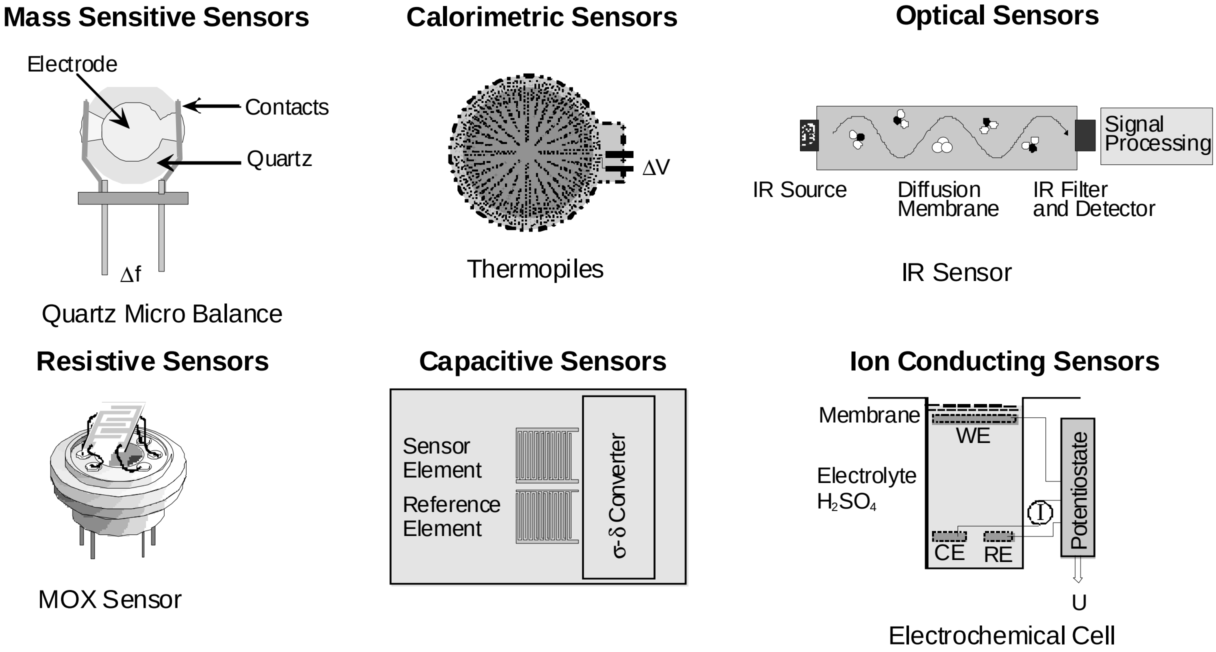

Figure 1.12. A selection of available gas sensor types (adapted from reference [110]).

Among these sensor types, semiconductor-based chemiresistor sensors are widely used for detection of toxic and combustible gases owing to their low cost and simplicity. A chemiresistive gas sensor works on the principle of a change in electrical resistance due to an interaction between the semiconductor and the gas. The electrical resistance of a chemiresistive sensor changes (increase or decrease) when exposed to analyzing gases. Increase or decrease in resistance depends on the nature of sensor material (n-type or p-type) and gas type (reducing or oxidizing), as shown in Figure 1.13. They usually operate between 100 and 500 °C in real atmospheric conditions (in oxygen and moisture).

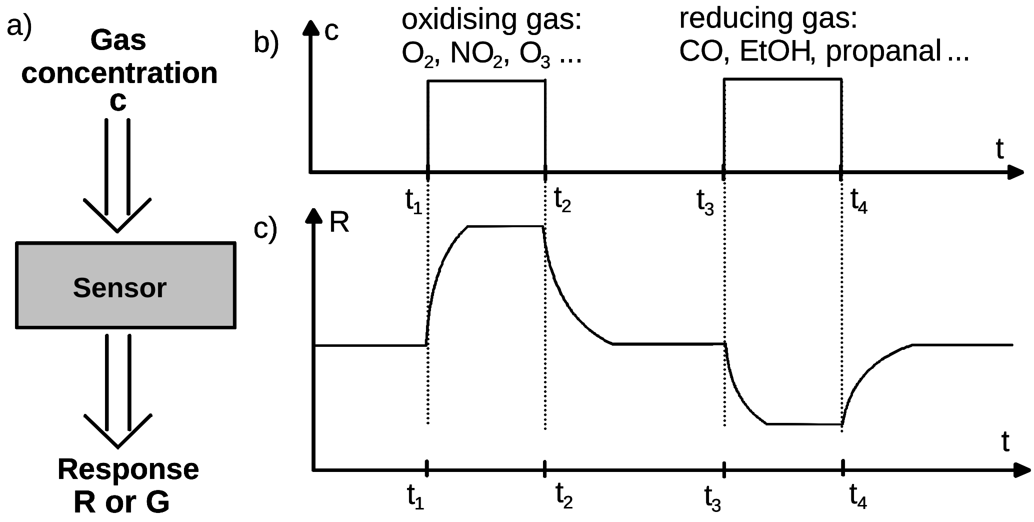

Figure 1.13. Sensor principle (a) principle functioning of a metal-oxide-based gas sensor, (b) the gas is applied at t1, t3 and removed at t2, t4, (c) which lead to changes in the resistance R or conductance G of the sensor (reproduced from reference [111] with the permission of John Wiley and Sons).

The most important characteristics of gas sensors are [109]:

- **Sensitivity**: *response to small concentration change of gases*. The sensitivity of a sensor is expressed in terms of sensor signal S which is defined as a ratio of resistance in air to that in gas, $S = R_{air}/R_{gas}$ or $S = R_{gas}/R_{air}$ for reducing or oxidizing gases, respectively.
- **Response time**: This is the time interval over which resistance attains a fixed percentage (usually 90%) of final value when the sensor is exposed to full-scale concentration of the gas. It is represented as T90, T80 etc. A T90 of 45 sec implies that the sensor exhibits 90% of the saturation value of resistance in 45 sec. A small value of response time is indicative of a good sensor.
- **Recovery time**: This is the time interval, usually referred as T10, over which sensor resistance reduces to 10% of the saturation value when the sensor is exposed to full-scale concentration of the gas.
- **Selectivity**: *strong response to selective gases.* Sensors are normal sensitive to more than one gas species and hence, show cross-sensitivities. The selectivity or specifity of

a sensor towards a particular gas is expressed in terms of dimension that compares the concentration of the corresponding interfering gas that produces the same sensor signal. Selectivity = Sensitivity of the sensor for interfering gas/Sensitivity towards the desired gas.

- **Stability**: *signal reproducibility over time*. This is the ability of the sensor to maintain its properties when operated continuously for long time under extreme conditions. A good sensor should work for several years without showing significant degradation in the performance.

The history of semiconducting metal-oxides sensors began in 1962, when Seiyama et al. [112] reported for the first time the change in conductivity of ZnO thin films when heated to 300 °C in the presence of traces of reactive gases present in the air. In the same year, similar properties were reported for SnO_2 by Taguchi [113] which he patented later known as TGS – Taguchi Gas sensor. Subsequently various oxides, such as, WO_3, In_2O_3, V_2O_5, MoO_3, NiO, CuO, $BaTiO_3$ etc., have been studied. Table 1.6 presents a list of various materials used as metal-oxide gas sensors. But SnO_2 based gas sensors have remained the most commonly used and the best-understood prototype material for commercial use [114].

Besides oxides, III-nitrides such as GaN [115-116], InN [117], and gallium oxonitride [118] have also shown chemical gas sensing application for the detection of H_2, O_2, NH_3 etc.

Table 1.6. Various metal-oxide based chemiresistive materials, additives and the analyzing gases which can be detected (data taken from [109] and references therein).

Base metal-oxides	**Additives**	**Analyzing gas**
Al_2O_3	Al, SiO_2/Si	Humidity, CH_4, NH_3
Bi_2O_3	Sb_2O_3	Smoke, CO, NO
CdO	$ZnFe_2O_4$	Ethanol
Cr_2O_3	TiO_2	NO_2, O_2, NH_3, Humidity
Co_3O_4	SiO_2	NH_3, CO_2, CH_4, C_3H_8, H_2, NO_2, Cl
CuO	SnO_2	CO, Ethanol, H_2S
Fe_2O_3	Au, Zn (Pt, Pd, RuO_2)	Methane, propane, Benzene, Toulene, CO_2, NO_2, Methanol, Acetone
Ga_2O_3	SnO_2, Pd, Ta_2O_5, WO_3, NiO	O_2, CO_2, NO, NH_3
In_2O_3	MoO_3, Au, Al, SnO_2	O_3, NO_2, H_2, CO, C_3H_8, H_2S, Cl_2, CO_2, SO_2, NH_3, Ethanol, Acetone
MoO_3	Ti	NH_3, CO_2, NO_2
Nb_2O_5	SnO_2	NH_3, CO_2, C_2H_5OH, H_2
NiO	Li, TiO_x	H_2, HCHO, CH_4, CH_3, COOH, CO, NO_2
Ta_2O_5	-	Humidity
SnO_2	Pt, Ag, Pd, Os, Fe, Au, In, Ru, Bi_2O_3, CeO_2, CuO	CO, CH_4, SO_2, N_2O, CO_2, NO_2, CH_3OH, C_2H_5OH, C_3H_8, H_2, LPG, H_2S, NH_3, C_nH_{2n+2}
TiO_2	La, Pt, Cr_2O_3, WO_3	CH_3OH, C_2H_5OH, C_3H_7OH, O_2, H_2, NH_3, NO_2
WO_3	Mg, Zn, Mo, Re, Au, Pd	NO_2, NH_3, C_2H_5OH, Butylamines, Propanaol, Toulene
ZnO	Al, Sn, Cu, Pd, Fe_2O_3	NH_3, H_2, NO_2, LPG, CH_4, CO, H_2S, CH_3OH, C_2H_5OH, C_3H_7OH

1.3.1 Basic mechanisms of gas sensing in semiconductors

A simple model to explain the resistance change in a metal-oxide based gas sensors is that, in air, oxygen adsorbs on the surface (to form oxygen ion), where the electron on the oxygen is extracted from the conduction band of the semiconductor. This electron extraction tends to increase the resistance for an n-type semiconductor, such as SnO_2. This model is known as "*Ionosorption model*". At lower temperature of adsorption (150–200 °C) oxygen adsorbs on SnO_2 nondissociately to form molecular oxygen ion ($O_2^-{}_{(ads)}$) and at higher temperature between 200–400 °C, it dissociates to atomic oxygen ion ($O^-{}_{(ads)}$) [119-121]. Combustible gas like H_2 reacts with the adsorbed O^- to form water, and the electron is send-back to the semiconductor which tends to decrease resistance. These competitive processes are illustrated by the following equations:

$$O_{2\,(ads)} + e^- \rightarrow O_2^-{}_{(ads)} \qquad (1.11)$$

$$O_2^-{}_{(ads)} + e^- \rightarrow 2\,O^-{}_{(ads)} \qquad (1.12)$$

$$H_2 + O^-{}_{(ads)} \rightarrow H_2O + e^- \qquad (1.13)$$

In the case of reducing gases such as CO in the presence of oxygen, the oxidation of CO into CO_2 by reaction with ionosorbed oxygen is responsible for the decrease in electrical resistance by generating delocalized electrons:

$$CO + O^-{}_{(ads)} \rightarrow CO_2 + e^- \qquad (1.14)$$

In the absence of oxygen, CO acts as electron donor: it is adsorbed as a CO^+ ion, thus inserting an electron into the conduction band [120], according to the following equation:

$$CO \rightarrow CO^+ + e^- \qquad (1.15)$$

1.3.2 Selectivity problem

Successful development of gas sensors for commercial purpose should possess three important characteristics: sensitivity, selectivity and stability [122]. Metal oxide gas sensors in general show high sensitivity but poor selectivity if pure sensor materials are used. Sensitivity is often improved by impregnating noble catalyst particles. Reproducible performance may be improved by using very stable materials, which may be operated at quite high temperature, but this can not solve the selectivity problem. Among the well-known gas sensitive materials (SnO_2, ZnO, TiO_2, WO_3 and In_2O_3), SnO_2 is most commonly used and often doped with noble metals such as Pt and Pd to enhance sensing performance. These sensors behave more or less similar to various reducing gases (H_2, CO etc.) and this could lead to false alarm and error in the concentrations measured by the detector due to difficulty in separating the effects of different gases.

Figure 1.14 shows results obtained with commercial thick film SnO_2 based gas sensors [114]. SnO_2 based sensors show good sensitivity for many reducing gases, resulting in a poor selectivity. One can observe that the effects of the different gases are very difficult to separate. Another general example is the effect of humidity because its presence in various amounts can significantly affect the sensor signal, causing an uncertainty in interpreting sensor data [123].

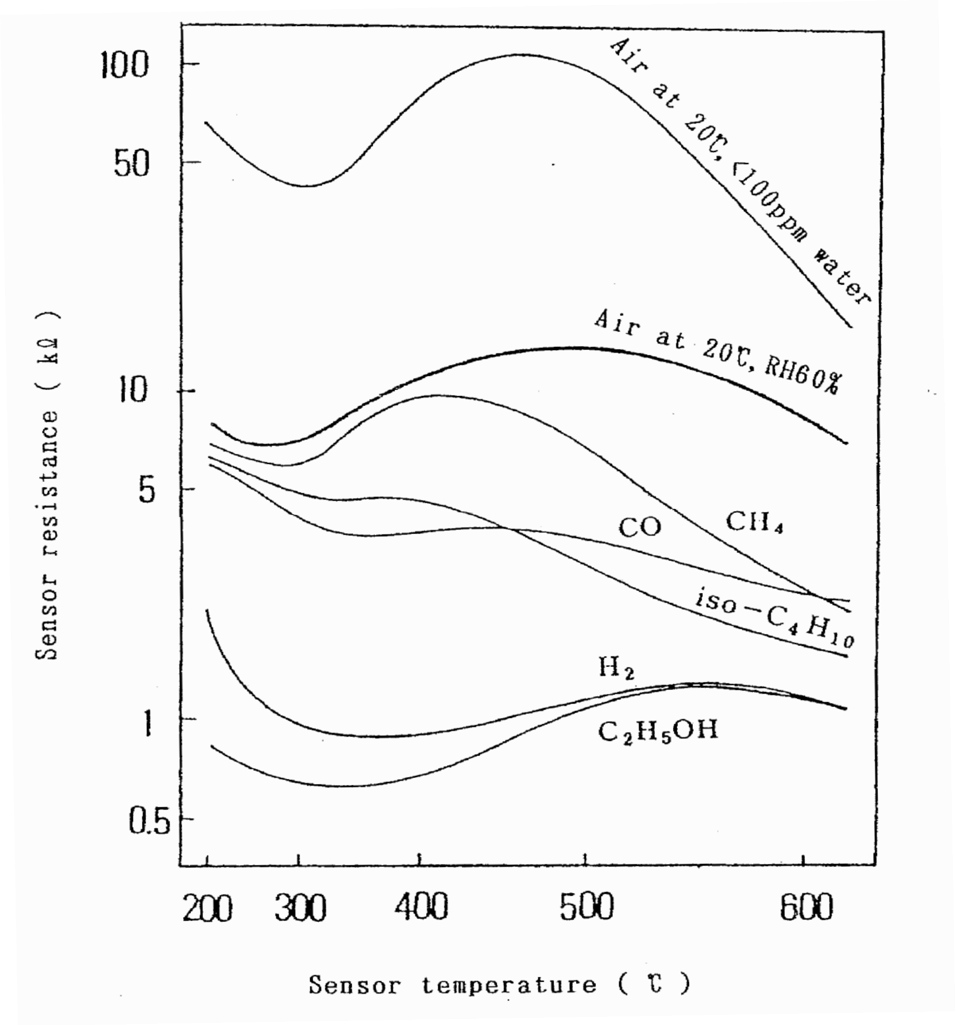

Figure 1.14. SnO_2 sensor response to different gases (1000 ppm) [114] indicating difficulty in separating effects of different gases.

It is evident from the above details that metal-oxide gas sensors suffer most seriously from the problem of poor selectivity. Researchers have worked in the last decades on the enhancements of the gas sensors selectivity in different ways [121, 123-136]. In general there are four ways of obtaining selectivity in semiconductor gas sensors [124]: (i) the use of catalysts and promoters, (ii) the use of temperature control, (iii) the use of specific surface additives, and (iv) the use of physical or chemical filters on the top of the sensing material. By doping CuO, SnO_2 becomes selective to H_2S [125]; while at high temperatures the selectivity for NH_3 gets enhanced [109]. One of the effective ways of transforming a sensor to a highly selective and sensitive sensor is to apply a filter directly on the sensing layer as shown in

Figure 1.15. A physical filter with well defined pore size hinders the interfering gas (bigger molecules) from reaching the sensing layer but allows the gas to be detected to reach sensors surface. Dense [126-127] or mesoporous [128] SiO_2, zeolites [129] and charcoal [130] are few of the examples. These filters are included as sensor add-ons, e.g. in the housing above the sensor element, and there are many commercial sensors that are offered in such forms. Chemical filters eliminate interfering gases via a chemical reaction [131] or preferentially transform the target gas into a more active species [132]. Such a catalytic filter can be a porous thick film of ceramic (Al_2O_3, SiO_2 etc.) [133-134] or doped SnO_2 on sensing films [135-136]. Additionally, noble metals can be used as filter layers, either incorporated in an oxide [137] or as a metallic film [138]. These filter layers are often deposited directly on top of the sensing layers or are realized by mixing with the sensing material before coating.

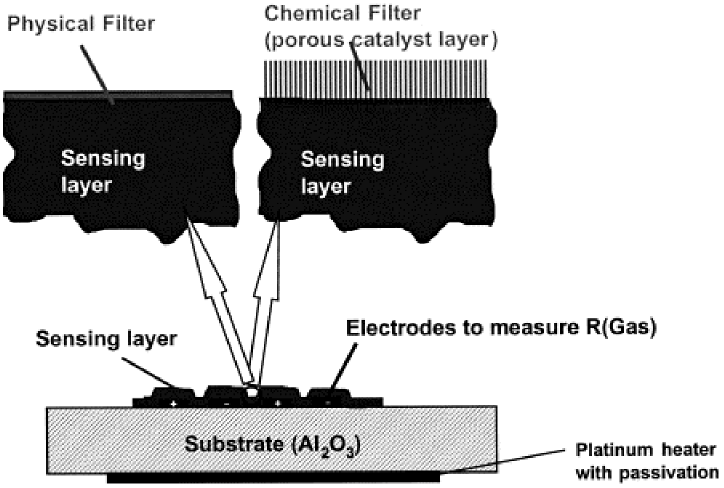

Figure 1.15. Schematic cross-section of a high-temperature operated metal-oxide gas sensor with a gas filter located directly at the surface of the sensing materials (reproduced from reference [131] with the permission of Elsevier).

The detection of H_2 and CO in oxygen free conditions is of interest for several emerging applications; the on-line control of the performance of hydrogen fuel cells is only one example out of many. As mentioned above, most of the hydrogen is produced through steam reforming of methane which is the main constituent of natural gas [139]. The methane reformation and water gas shift reactions are not complete, leaving small concentrations (≈ 50 ppm) of CO in the fuel stream. CO is known to be an extremely effective poison for the Pt-based catalysts; accordingly, even a few ppm of CO causes a substantial degradation in the fuel cell performance [139]. Therefore, if the hydrogen from steam reforming is used as a fuel in fuel cells, the residual CO concentration in the fuel should be precisely controlled [140]. Previous works on filter/sensor integration have neither been focused on separation of small molecules such as H_2 and CO, nor studied amorphous ceramic materials, nor applied filter/sensor combination in the oxygen free conditions. Accordingly, one of the goals of the present work is to investigate the suitability of polymer-derived ceramics for their application as gas separation filters integrated with chemiresistors. The main feature of polymer-derived ceramics is their chemical and thermal stability and tunable porosity allowing for their application in harsh reducing conditions.

1.4. References

[1] I.E.A., "Moving to a hydrogen economy: dreams and realities," IEA/SLT(2003)5, 2003.

[2] Y. Iwamoto, "Precursors Derived Ceramic Membranes," *E-MRS Spring Meeting*, Strasbourg, 2004.

[3] S. Sircar, T.C. Golden, "Purification of hydrogen by pressure swing adsorption," *Separation Science and Technology*, 35 (2000) 667-687.

[4] A.B. Hinchliffe, K.E. Porter, "A comparison of membrane separation and distillation," *Chemical Engineering Research & Design*, 78 (2000) 255-268.

[5] S.A. Stern, "Polymers for gas separations - the next decade," *Journal of Membrane Science*, 94 (1994) 1-65.

[6] T.M. Nenoff, R.J. Spontak, C.M. Aberg, "Membranes for hydrogen purification: An important step toward a hydrogen-based economy," *MRS Bulletin*, 31 (2006) 735-741.

[7] N.W. Ockwig, T.M. Nenoff, "Membranes for hydrogen separation," *Chemical Reviews,* 107 (2007) 4078-4110.

[8] R.W. Baker, "Future directions of membrane gas separation technology," *Industrial & Engineering Chemistry Research*, 41 (2002) 1393-1411.

[9] W.A. Bollinger, D.L. Maclean, R.S. Narayan, "Separation systems for oil refining and production," *Chemical Engineering Progress*, 78 (1982) 27-32.

[10] J. Dong, Y.S. Lin, M. Kanezashi, Z. Tang, "Microporous inorganic membranes for high temperature hydrogen purification," *Journal of Applied Physics,* 104 (2008) 121301.

[11] W.J. Koros, Y.H. Ma, T. Shimidzu, "Terminology for membranes and membrane processes (Reprinted from Pure & Appl Chem, vol 68, pg 1479-1489, 1996)," *Journal of Membrane Science,* 120 (1996) 149-159.

[12] K. Li, *Ceramic Membranes for Separation and Reaction,* Wiley, Chichester, 2007.

[13] R.R. Bhave, *Inorganic Membranes: Synthesis, Characteristics and Applications,* Van Nostransd Reinhold, New York, 1991.

[14] M. Knudsen, "The Law of the molecular flow and viscosity of gases moving through tubes," *Ann. Phys.*, 28 (1909) 1909.

[15] M.B. Rao, S. Sircar, "Performance and pore characterization of nanoporous carbon membranes for gas separation," *Journal of Membrane Science*, 110 (1996) 109-118.

[16] R.J.R. Uhlhorn, "Ceramic membranes for gas separation: synthesis and gas transport properties," University of Twente, Enschede, 1990.

[17] A.J. Burggraaf, L. Cot, *Fundamentals of Inorganic Membrane Science and Technology,* Elsevier, 1996.

[18] M.B. Rao, A. Sircar, "Nanoporous carbon membranes for separation of gas mixtures by selective surface flow " *Journal of Membrane Science,* 85 (1993) 252-264.

[19] A.J. Burggraaf, "Single gas permeation of thin zeolite (MFI) membranes: theory and analysis of experimental observations," *Journal of Membrane Science*, 155 (1999) 45-65.

[20] S. Adhikari, S. Fernando, "Hydrogen membrane separation techniques," *Industrial & Engineering Chemistry Research*, 45 (2006) 875-881.

[21] T.L. Ward, T. Dao, "Model of hydrogen permeation behavior in palladium membranes," *Journal of Membrane Science*, 153 (1999) 211-231.

[22] A. Damle, *Hydrogen Separation and Purification, Hydrogen Fuel,* CRC Press, 2008, pp. 283-324.

[23] R.E. Buxbaum, A.B. Kinney, "Hydrogen transport through tubular membranes of palladium-coated tantalum and niobium," *Industrial & Engineering Chemistry Research,* 35 (1996) 530-537.

[24] H. Wipf, "Solubility and diffusion of hydrogen in pure metals and alloys," *Physica Scripta,* T94 (2001) 43-51.

[25] F.A. Lewis, "Solubility of hydrogen in metals," *Pure and Applied Chemistry,* 62 (1990) 2091-2096.

[26] S. Uemiya, "Brief review of steam reforming using a metal membrane reactor," *Topics in Catalysis*, 29 (2004) 79-84.

[27] P.P. Mardilovich, Y. She, Y.H. Ma, M.H. Rei, "Defect-free palladium membranes on porous stainless-steel support," *Aiche Journal*, 44 (1998) 310-322.

[28] Y.H. Ma, B.C. Akis, M.E. Ayturk, F. Guazzone, E.E. Engwall, I.P. Mardilovich, "Characterization of intermetallic diffusion barrier and alloy formation for Pd/Cu and Pd/Ag porous stainless steel composite membranes," *Industrial & Engineering Chemistry Research*, 43 (2004) 2936-2945.

[29] A.E. Ayturk, I.P. Mardilovich, E.E. Engwall, Y.H. Ma, "Synthesis of composite Pd-porous stainless steel (PSS) membranes with a Pd/Ag intermetallic diffusion barrier," *Journal of Membrane Science*, 285 (2006) 385-394.

[30] D.S. Sholl, Y.H. Ma, "Dense metal membranes for the production of high-purity hydrogen," *MRS Bulletin*, 31 (2006) 770-773.

[31] Y.H. Ma, I.P. Mardilovich, E.E. Engwall, "Thin composite palladium and palladium/alloy membranes for hydrogen separation," *Advanced Membrane Technology*, 984 (2003) 346-360.

[32] S. Uemiya, "State-of-the-art of supported metal membranes for gas separation," *Separation and Purification Methods*, 28 (1999) 51-85.

[33] H.Y. Gao, Y.S. Lin, Y.D. Li, B.Q. Zhang, "Chemical stability and its improvement of palladium-based metallic membranes," *Industrial & Engineering Chemistry Research*, 43 (2004) 6920-6930.

[34] A.J. Derosset, "Diffusion of Hydrogen through Palladium Membranes," *Industrial and Engineering Chemistry*, 52 (1960) 525-528.

[35] S. Uemiya, T. Matsuda, E. Kikuchi, "Hydrogen permeable palladium silver alloy membrane supported on porous ceramics," *Journal of Membrane Science*, 56 (1991) 315-325.

[36] S. Uemiya, N. Sato, H. Ando, T. Matsuda, E. Kikuchi, "Steam reforming of methane in a hydrogen-permeable membrane reactor," *Applied Catalysis*, 67 (1991) 223-230.

[37] S. Uemiya, Y. Kude, K. Sugino, N. Sato, T. Matsuda, E. Kikuchi, "A palladium porous-glass composite membrane for hydrogen separation," *Chemistry Letters*, (1988) 1687-1690.

[38] S. Uemiya, N. Sato, H. Ando, Y. Kude, T. Matsuda, E. Kikuchi, "Separation of hydrogen through palladium thin-film supported on a porous-glass tube," *Journal of Membrane Science*, 56 (1991) 303-313.

[39] A.S. Darling, "The diffusion of hydrogen through palladium " *Platinum Metals Review*, 2 (1958) 16-22.

[40] T. Maruno, H. Tsuji, R. Otsuka, "Hydrogen embrittlement of Pd-Ag binary-alloys," *Journal of the Japan Institute of Metals*, 47 (1983) 768-775.

[41] K.L. Yeung, R. Aravind, J. Szegner, A. Varma, "Metal composite membranes: Synthesis, characterization and reaction studies," *11th International Congress on Catalysis - 40th Anniversary*, 101 (1996) 1349-1358.

[42] J.P. Collins, R.W. Schwartz, R. Sehgal, T.L. Ward, C.J. Brinker, G.P. Hagen, C.A. Udovich, "Catalytic dehydrogenation of propane in hydrogen permselective membrane reactors," *Industrial & Engineering Chemistry Research*, 35 (1996) 4398-4405.

[43] H.C. Foley, A.W. Wang, B. Johnson, J.N. Armor, "Effect of a model hydrogenation on a catalytic palladium membrane," *ACS Symposium Series*, 517 (1993) 168-184.

[44] F. Rao, J.D. Way, R.L. McCormick, S.N. Paglieri, "Preparation and characterization of Pd-Cu composite membranes for hydrogen separation," *Chem. Eng. J.*, 93 (2003) 11-22.

[45] P. Kamakoti, B.D. Morreale, M.V. Ciocco, B.H. Howard, R.P. Killmeyer, A.V. Cugini, D.S. Sholl, "Prediction of hydrogen flux through sulfur-tolerant binary alloy membranes," *Science*, 307 (2005) 569-573.

[46] A.G. Knapton, "Palladium alloys for hydrogen diffusion membranes - A REVIEW OF HIGH PERMEABILITY MATERIALS," *Platinum Metals Review*, 21 (1977) 44-50.

[47] G.Q. Lu, J.C.D. da Costa, M. Duke, S. Giessler, R. Socolow, R.H. Williams, T. Kreutz, "Inorganic membranes for hydrogen production and purification: A critical review and perspective," *Journal of Colloid and Interface Science*, 314 (2007) 589-603.

[48] G. Xomeritakis, Y.S. Lin, "CVD synthesis and gas permeation properties of thin palladium/alumina membranes," *Aiche Journal*, 44 (1998) 174-183.

[49] L.Q. Wu, N.P. Xu, J. Shi, "Preparation of a palladium composite membrane by an improved electroless plating technique," *Industrial & Engineering Chemistry Research*, 39 (2000) 342-348.

[50] K.S. Chou, S.M. Wang, "Studies on the preparation of Pd/alumina/porous stainless steel membranes for hydrogen separation," *Journal of the Chinese Institute of Chemical Engineers*, 31 (2000) 499-506.

[51] S.E. Nam, K.H. Lee, "Hydrogen separation by Pd alloy composite membranes: introduction of diffusion barrier," *Journal of Membrane Science*, 192 (2001) 177-185.

[52] S.E. Nam, K.H. Lee, "A study on the palladium/nickel composite membrane by vacuum electrodeposition," *Journal of Membrane Science*, 170 (2000) 91-99.

[53] H.D. Tong, F.C. Gielens, J.G.E. Gardeniers, H.V. Jansen, C.J.M. van Rijn, M.C. Elwenspoek, W. Nijdam, "Microfabricated palladium-silver alloy membranes and their

application in hydrogen separation," *Industrial & Engineering Chemistry Research*, 43 (2004) 4182-4187.

[54] Committee on Alternatives and Strategies, National Research Council, National Academy of Engineering, "The Hydrogen Economy: Opportunities, Costs, Barriers, and R&D Needs," *National Academy Press*, Washington, DC, 2005.

[55] S.C.A. Kluiters, "Status review on membrane systems for hydrogen separation," Energy Center of Netherlands: petten, The Netherlands, 2004.

[56] C.J. Orme, M.L. Stone, M.T. Benson, E.S. Peterson, "Testing of polymer membranes for the selective permeability of hydrogen," *Separation Science and Technology*, 38 (2003) 3225-3238.

[57] J.H. Dong, Y.S. Lin, W. Liu, "Multicomponent hydrogen/hydrocarbon separation by MFI-type zeolite membranes," *Aiche Journal*, 46 (2000) 1957-1966.

[58] M. Nomura, K. Ono, S. Gopalakrishnan, T. Sugawara, S.I. Nakao, "Preparation of a stable silica membrane by a counter diffusion chemical vapor deposition method," *Journal of Membrane Science*, 251 (2005) 151-158.

[59] C.J. Brinker, T.L. Ward, R. Sehgal, N.K. Raman, S.L. Hietala, D.M. Smith, D.W. Hua, T.J. Headley, "Ultramicroporous silica-based supported inorganic membranes," *Journal of Membrane Science*, 77 (1993) 165-179.

[60] A.K. Prabhu, S.T. Oyama, "Development of a hydrogen selective ceramic membrane and its application for the conversion of greenhouse gases," *Chemistry Letters*, (1999) 213-214.

[61] A.K. Prabhu, S.T. Oyama, "Highly hydrogen selective ceramic membranes: application to the transformation of greenhouse gases," *Journal of Membrane Science*, 176 (2000) 233-248.

[62] S. Giessler, L. Jordan, J.C.D. da Costa, G.Q. Lu, "Performance of hydrophobic and hydrophilic silica membrane reactors for the water gas shift reaction," *Separation and Purification Technology*, 32 (2003) 255-264.

[63] M. Kanezashi, T. Fujita, M. Asaeda, "Nickel-doped silica membranes for separation of helium from organic gas mixtures," *Separation Science and Technology*, 40 (2005) 225-238.

[64] K. Yoshida, Y. Hirano, H. Fujii, T. Tsuru, M. Asaeda, "Hydrothermal stability and performance of silica-zirconia membranes for hydrogen separation in hydrothermal conditions," *Journal of Chemical Engineering of Japan*, 34 (2001) 523-530.

[65] M. Kanezashi, M. Asaeda, "Hydrogen permeation characteristics and stability of Ni-doped silica membranes in steam at high temperature," *Journal of Membrane Science*, 271 (2006) 86-93.

[66] V. Boffa, D.H.A. Blank, J.E. ten Elshof, "Hydrothermal stability of microporous silica and niobia-silica membranes," *Journal of Membrane Science*, 319 (2008) 256-263.

[67] M.C. Duke, J.C.D. da Costa, G.Q. Lu, M. Petch, P. Gray, "Carbonised template molecular sieve silica membranes in fuel processing systems: permeation, hydrostability and regeneration," *Journal of Membrane Science*, 241 (2004) 325-333.

[68] S. Kitao, M. Asaeda, "Separation of organic-acid water mixtures by thin porous silica membrane," *Journal of Chemical Engineering of Japan*, 23 (1990) 367-370.

[69] R.M. de Vos, H. Verweij, "High-selectivity, high-flux silica membranes for gas separation," *Science*, 279 (1998) 1710-1711.

[70] J.C.D. da Costa, G.Q. Lu, V. Rudolph, Y.S. Lin, "Novel molecular sieve silica (MSS) membranes: characterisation and permeation of single-step and two-step sol-gel membranes," *Journal of Membrane Science*, 198 (2002) 9-21.

[71] S.C. Yan, H. Maeda, K. Kusakabe, S. Morooka, Y. Akiyama, "Hydrogen-permselective SiO_2 membrane formed in pores of alumina support tube by chemical-vapor-deposition with tetraethyl orthosilicate," *Industrial & Engineering Chemistry Research*, 33 (1994) 2096-2101.

[72] H. Suzuki, "Composite membrane having a surface layer of an ultrathin film of cage-shaped zeolite and processes for production thereof ,", U.S. Patent 4699892, 1987.

[73] H. Verweij, Y.S. Lin, J.H. Dong, "Microporous silica and zeolite membranes for hydrogen purification," *MRS Bulletin*, 31 (2006) 756-764.

[74] M. Kanezashi, J. O'Brien-Abraham, Y.S. Lin, K. Suzuki, "Gas permeation through DDR-type zeolite membranes at high temperatures," *Aiche Journal*, 54 (2008) 1478-1486.

[75] T. Masuda, N. Fukumoto, M. Kitamura, S.R. Mukai, K. Hashimoto, T. Tanaka, T. Funabiki, "Modification of pore size of MFI-type zeolite by catalytic cracking of silane and application to preparation of H_2-separating zeolite membrane," *Microporous and Mesoporous Materials*, 48 (2001) 239-245.

[76] Z. Zheng, A.S. Hall, V.V. Guliants, "Synthesis, characterization and modification of DDR membranes grown on alpha-alumina supports," *Journal of Materials Science*, 43 (2008) 2499-2502.

[77] A.F. Ismail, L.I.B. David, "A review on the latest development of carbon membranes for gas separation," *Journal of Membrane Science*, 193 (2001) 1-18.

[78] H. Hatori, H. Takagi, Y. Yamada, "Gas separation properties of molecular sieving carbon membranes with nanopore channels," *Carbon*, 42 (2004) 1169-1173.

[79] L.J. Wang, F.C.N. Hong, "Carbon-based molecular sieve membranes for gas separation by inductively-coupled-plasma chemical vapor deposition," *Microporous and Mesoporous Materials*, 77 (2005) 167-174.

[80] M.B. Rao, S. Sircar, "Nanoporous carbon membranes for separation of gas mixtures by selective surface flow " *Journal of Membrane Science*, 85 (1993) 253-264

[81] W. Bocker, H. Landfermann, H. Hausner, "Sintering of alpha-silicon carbide with additions of aluminum," *Powder Metallurgy International*, 11 (1979) 83-85.

[82] G. Ziegler, J. Heinrich, G. Wotting, "Relationships between processing, microstructure and properties of dense and reaction-bonded silicon-nitride," *Journal of Materials Science*, 22 (1987) 3041-3086.

[83] R. Riedel, G. Passing, H. Schonfelder, R.J. Brook, "Synthesis of dense silicon-based ceramics at low-temperatures," *Nature*, 355 (1992) 714-717.

[84] R. Riedel, A. Kienzle, W. Dressler, L. Ruwisch, J. Bill, F. Aldinger, "A silicoboron carbonitride ceramic stable to 2000°C," *Nature*, 382 (1996) 796-798.

[85] G. Fritz, B. Raabe, "Bildung siliciumorganischer verbindungen .5. die thermische zersetzung von $Si(CH_3)_4$ Und $Si(C_2H_5)_4$," *Zeitschrift Fur Anorganische Und Allgemeine Chemie*, 286 (1956) 149-167.

[86] S. Yajima, J. Hayashi, M. Omori, "Continuous silicon-carbide fiber of high-tensile strength," *Chemistry Letters*, (1975) 931-934.

[87] W. Verbeek, "Production of shaped articles of homogeneous mixtures of silicon carbide and nitride," Bayer AG, German Patent Number 2218960, 1973.

[88] G. Winter, W. Verbeek, M. Mansmann, "Formkoerper aus homogenen mischungen von siliciumcarbid und siliciumnitrid und verfahren zu ihrer herstellung," Bayer AG, German Patent Number 2243527, 1974.

[89] P. Colombo, G. Mera, R. Riedel, G.D. Soraru, "Polymer-derived ceramics: 40 years of research and innovation in advanced ceramics," *Journal of the American Ceramic Society*, 93 (2010) 1805-1837.

[90] P. Colombo, R. Riedel, G.D. Soraru, H.J. Kleebe, *Polymer Derived Ceramics: From Nano-Structure to Applications*, DEStech Publications, Inc., Lancaster, Pennsylvania 17602 USA, 2010.

[91] N.S.C.K. Yive, R.J.P. Corriu, D. Leclercq, P.H. Mutin, A. Vioux, "Silicon carbonitride from polymeric precursors - thermal cross-linking and pyrolysis of oligosilazane model compounds," *Chemistry of Materials*, 4 (1992) 141-146.

[92] K. Kusakabe, Z.Y. Li, H. Maeda, S. Morooka, "Preparation of supported composite membrane by pyrolysis of polycarbosilane for gas separation at high-temperature," *Journal of Membrane Science*, 103 (1995) 175-180.

[93] Z.Y. Li, K. Kusakabe, S. Morooka, "Preparation of thermostable amorphous Si-C-O membrane and its application to gas separation at elevated temperature," *Journal of Membrane Science*, 118 (1996) 159-168.

[94] L.L. Lee, D.-S. Tsai, "A hydrogen-permselective silicon oxycarbide membrane derived from polydimethylsilane," *Journal of the American Ceramic Society*, 82 (2004) 2796-2800.

[95] Y. Iwamoto, K. Sato, T. Kato, T. Inada, Y. Kubo, "A hydrogen-permselective amorphous silica membrane derived from polysilazane," *Journal of the European Ceramic Society*, 25 (2005) 257-264.

[96] T. Nagano, K. Sato, T. Saitoh, Y. Iwamoto, "Gas permeation properties of amorphous SiC membranes synthesized from polycarbosilane without oxygen-curing process," *Journal of the Ceramic Society of Japan*, 114 (2006) 533-538.

[97] H. Suda, H. Yamauchi, Y. Uchimaru, I. Fujiwara, K. Haraya, "Preparation and gas permeation properties of silicon carbide-based inorganic membranes for hydrogen separation," *Desalination*, 193 (2006) 252-255.

[98] K.W. Volger, R. Hauser, E. Kroke, R. Riedel, Y.H. Ikuhara, Y. Iwamoto, "Synthesis and characterization of novel non-oxide sol-gel derived mesoporous amorphous Si-C-N membranes," *Journal of the Ceramic Society of Japan*, 114 (2006) 567-570.

[99] R. Hauser, S. Nahar-Borchard, R. Riedel, Y.H. Ikuhara, Y. Iwamoto, "Polymer-derived SiBCN ceramic and their potential application for high temperature membranes," *Journal of the Ceramic Society of Japan*, 114 (2006) 524-528.

[100] R.A. Wach, M. Sugimoto, M. Yoshikawa, "Formation of silicone carbide membrane by radiation curing of polycarbosilane and polyvinylsilane and its gas separation up to 250 degrees C," *Journal of the American Ceramic Society*, 90 (2007) 275-278.

[101] A. Kulprathipanja, G.O. Alptekin, J.L. Falconer, J.D. Way, "Pd and Pd-Cu membranes: inhibition of H_2 permeation by H_2S," *Journal of Membrane Science*, 254 (2005) 49-62.

[102] G.P. Fotou, Y.S. Lin, S.E. Pratsinis, "Hydrothermal stability of pure and modified microporous silica membranes," *Journal of Materials Science*, 30 (1995) 2803-2808.

[103] T. Kuzniatsova, M.L. Mottern, K. Shqau, D. Yu, H. Verweij, "Micro-structural optimization of supported gamma-alumina membranes," *Journal of Membrane Science*, 316 (2008) 80-88.

[104] M.L. Mottern, K. Shqau, J.Y. Shi, D. Yu, H. Verweij, "Thin supported inorganic membranes for energy-related gas and water purification," *International Journal of Hydrogen Energy*, 32 (2007) 3713-3723.

[105] L. Zhang, I.-S. Park, K. Shqau, W. Winston Ho, H. Verweij, "Supported inorganic membranes: Promises and challenges," *Journal of the Minerals, Metals and Materials Society*, 61 (2009) 61-71.

[106] J. Shu, B.P.A. Grandjean, S. Kaliaguine, "Methane steam reforming in asymmetric Pd-Ag and Pd-Ag/porous SS membrane reactors," *Applied Catalysis A-General*, 119 (1994) 305-325.

[107] E. Mallada, M. Menéndez, "Inorganic membranes: Synthesis, characterization and applications," Elsevier Science, 2008.

[108] A. Hulanicki, S. Glab, F. Ingman, "Chemical sensors definitions and classification," *Pure and Applied Chemistry*, 63 (1991) 1247-1250.

[109] D.K. Aswal, S.K. Gupta, "Science and technology of chemiresistor gas sensors," Nova Science Publishers, Inc., New York, 2007.

[110] J. Kappler, *Characterization of high-performance* SnO_2 *gas sensors for CO detection by in-situ techniques (Ph.D. Thesis, University of Tübingen)*, Shaker Verlag, Aachen, 2001.

[111] A. Gurlo, N. Barsan, U. Weimar, *Gas sensors based on semiconducting metal oxides*, J.L.G.Fierro (Ed.) *Metal Oxides: Chemistry and Applications*, CRS Press, Boca Raton, 2006, pp. 683-738.

[112] T. Seiyama, A. Kato, K. Fujiishi, M. Nagatani, "A new detector for gaseous components using semiconductive thin films," *Analytical Chemistry*, 34 (1962) 1502-&.

[113] N. Taguchi, "Gas-Detecting Device," *Jpn Pat 45-38200*, (1962).

[114] K. Ihokura, J. Watson, *Stannic Oxide Gas Sensors, Principles and Applications*, CRC Press, Boca Raton, 1994.

[115] F. Yun, S. Chevtchenko, Y.T. Moon, H. Morkoc, T.J. Fawcett, J.T. Wolan, "GaN resistive hydrogen gas sensors," *Applied Physics Letters*, 87 (2005) -.

[116] C.-Y. Chang, G.-C. Chi, W.-M. Wang, L.-C. Chen, K.-H. Chen, F. Ren, S. Pearton, "Electrical transport properties of single GaN and InN nanowires," *Journal of Electronic Materials*, 35 (2006) 738-743.

[117] G. Koley, C. Zhihua, "InN nanowire based sensors," *IEEE Sensors 2008*, 2008, pp. 118-121.

[118] M. Kerlau, O. Merdrignac-Conanec, P. Reichel, N. Barsan, U. Weimar, "Preparation and characterization of gallium (oxy)nitride powders - Preliminary investigation as new gas sensor materials," *Sensors and Actuators B: Chemical*, 115 (2006) 4-11.

[119] A. Gurlo, "Interplay between O_2 and SnO_2: Oxygen ionosorption and spectroscopic evidence of adsorbed oxygen," *Chemphyschem*, 7 (2006) 2041-2052.

[120] A. Gurlo, R. Riedel, "In situ and operando spectroscopy for assessing mechanisms of gas sensing," *Angewandte Chemie-International Edition*, 46 (2007) 3826-3848.

[121] N. Barsan, U. Weimar, "Conduction model of metal oxide gas sensors," *Journal of Electroceramics*, 7 (2001) 143-167.

[122] C.O. Park, S.A. Akbar, J. Hwang, "Selective gas detection with catalytic filter," *Materials Chemistry and Physics*, 75 (2002) 56-60.

[123] N. Barsan, U. Weimar, "Understanding the fundamental principles of metal oxide based gas sensors; the example of CO sensing with SnO_2 sensors in the presence of humidity," *Journal of Physics-Condensed Matter*, 15 (2003) R813-R839.

[124] S.R. Morrison, "Selectivity in semiconductor gas sensors," *Sensors and Actuators*, 12 (1987) 425-440.

[125] V.R. Katti, A.K. Debnath, K.P. Muthe, M. Kaur, A.K. Dua, S.C. Gadkari, S.K. Gupta, V.C. Sahni, "Mechanism of drifts in H_2S sensing properties of SnO_2: CuO composite thin film sensors prepared by thermal evaporation," *Sensors and Actuators B: Chemical*, 96 (2003) 245-252.

[126] G. Tournier, C. Pijolat, "Selective filter for SnO_2-based gas sensor: application to hydrogen trace detection," *Sensors and Actuators B: Chemical*, 106 (2005) 553-562.

[127] C.H. Kwon, D.H. Yun, H.-K. Hong, S.-R. Kim, K. Lee, H.Y. Lim, K.H. Yoon, "Multi-layered thick-film gas sensor array for selective sensing by catalytic filtering technology," *Sensors and Actuators B: Chemical*, 65 (2000) 327-330.

[128] A. Cabot, J. Arbiol, A. Cornet, J.R. Morante, F.L. Chen, M.L. Liu, "Mesoporous catalytic filters for semiconductor gas sensors," *Thin Solid Films*, 436 (2003) 64-69.

[129] O. Hugon, M. Sauvan, P. Benech, C. Pijolat, F. Lefebvre, "Gas separation with a zeolite filter, application to the selectivity enhancement of chemical sensors," *Sensors and Actuators B: Chemical*, 67 (2000) 235-243.

[130] M. Schweizer-Berberich, S. Strathman, U. Weimar, R. Sharma, A. Seube, A. Peyre-Lavigne, W. Gopel, "Strategies to avoid VOC cross-sensitivity of SnO_2-based CO sensors," *Sensors and Actuators B: Chemical*, 58 (1999) 318-324.

[131] M. Fleischer, S. Kornely, T. Weh, J. Frank, H. Meixner, "Selective gas detection with high-temperature operated metal oxides using catalytic filters," *Sensors and Actuators B: Chemical*, 69 (2000) 205-210.

[132] J. Hubalek, K. Malysz, J. Prasek, X. Vilanova, P. Ivanov, E. Llobet, J. Brezmes, X. Correig, Z. Sverak, "Pt-loaded Al_2O_3 catalytic filters for screen-printed WO_3 sensors highly selective to benzene," *Sensors and Actuators B: Chemical*, 101 (2004) 277-283.

[133] T. Suzuki, K. Kunihara, M. Kobayashi, S. Tabata, K. Higaki, H. Ohnishi, "A micromachined gas sensor based on a catalytic thick film/SnO_2 thin film bilayer and thin film heater - Part 1: CH_4 sensing," *Sensors and Actuators B: Chemical*, 109 (2005) 185-189.

[134] S. Tabata, K. Higaki, H. Ohnishi, T. Suzuki, K. Kunihara, M. Kobayashi, "A micromachined gas sensor based on a catalytic thick film/SnO_2 thin film bilayer and a thin film heater - Part 2: CO sensing," *Sensors and Actuators B: Chemical*, 109 (2005) 190-193.

[135] F. Menil, C. Lucat, H. Debeda, "The thick-film route to selective gas sensors," *Sensors and Actuators B: Chemical*, 25 (1995) 415-420.

[136] G.G. Mandayo, E. Castano, F.J. Gracia, A. Cirera, A. Cornet, J.R. Morante, "Built-in active filter for an improved response to carbon monoxide combining thin- and thick-film technologies," *Sensors and Actuators B: Chemical*, 87 (2002) 88-94.

[137] G. Sberveglieri, "Classical and Novel Techniques for the Preparation of Sno2 Thin-Film Gas Sensors," *Sensors and Actuators B: Chemical*, 6 (1992) 239-247.

[138] J. Wollenstein, H. Bottner, M. Jaegle, W.J. Becker, E. Wagner, "Material properties and the influence of metallic catalysts at the surface of highly dense SnO_2 films," *Sensors and Actuators B: Chemical*, 70 (2000) 196-202.

[139] B. Sørensen, *Hydrogen and Fuel Cells: Emerging Technologies and Applications*, Academic Press, New York, 2005.

[140] S. Wieland, T. Melin, A. Lamm, "Membrane reactors for hydrogen production," *Chemical Engineering Science*, 57 (2002) 1571-1576.

Part II

Experimental

Chapter 2. Experimental procedures

This chapter presents the experimental methods and devices employed in this thesis work. Section 2.1 describes methods used for synthesizing polymers and intermediate mesoporous layers, their deposition on as-received porous supports and thermolysis conditions to obtain unsupported and supported membranes. Section 2.2 briefly deals with the synthesis of sensing materials used and procedures applied to get sensor data. Various characterization techniques/tools applied in this work are listed in section 2.3.

2.1. Membranes

2.1.1 Macroporous support

The as-received porous alumina supports were cleaned with acetone to remove any dirt, oil that may have occurred post-production and during packaging them. After cleaning supports with acetone they were heated in an oven for 5 h to remove any moisture present on the support surface. These cleaned supports were used for structural characterizations and for the deposition of membranes. The thermal stability of as-received porous supports was examined under three different atmospheres (air, argon and ammonia) by heating to the desired temperature with a heating rate of 100 °C h^{-1}, held for 5 h and cooled down to room temperature with a rate of 100 °C h^{-1}.

2.1.2 Intermediate mesoporous layer

Gamma-alumina (γ-Al_2O_3): Unsupported γ-Al_2O_3 powder was obtained by calcination of boehmite colloidal dispersion (Alfa Aesar, 4 wt. % in H_2O) at and above 500 °C up to the desired calcination temperature. To investigate the thermal stability of γ-Al_2O_3 powder (obtained after calcinations at 800 °C), the powder was treated under air, argon and ammonia atmospheres by heating to 800 °C with a heating rate of 100 °C h^{-1}, held for 3 h and cooled down to room temperature with a rate of 100 °C h^{-1}.

$MgAl_2O_4$ spinel: Based on the work of Pflanz et al. [1] $MgAl_2O_4$ was synthesized. 4.138 g of magnesium isopropoxide, $MgAl_2(^iOPr)_8$ (Alfa Aesar, 99.95%) was taken in a Schlenk flask and then 100 ml of dry isopropanol was introduced in the flask and mixed for 30 min under argon atmosphere. Thereafter, 30 ml of distilled water was added and mixed for 30 min. The solution was divided into four parts and precipitate was separated by centrifugation (3000 rpm, 10 min). Each centrifuged part was mixed with 10 ml of distilled water and mixed manually with a glass rod. Nitric acid solution (6.5 wt.% in water) was added drop-wise in each of the four parts to get ratios of $c(NO_3^-)$ to $c(Mg^{2+})$ of 0.15, 0.20, 0.25, and 0.30. The selection of the concentration ratios was done based on the range which showed smallest particle size (20–40 nm) in the work of Pflanz et al. [1]. These four solutions were mixed overnight using magnetic stirring. Each part was dried at 100 °C in an oven and further calcined at 800 °C. Pore-size measurements of these calcined powders were done using nitrogen-sorption method. Spinel obtained from the solution with $c(NO_3^-)/c(Mg^{2+})$ ~0.20 showed the highest BET surface area with narrower pore size distribution and this powder was chosen for further characterization. To determine the thermal stability the powder was calcined at 800, 1000 and 1200 °C.

2.1.3 Precursors synthesis and thermolysis conditions to obtain ceramics

SiBCN ceramic: Polyborosilazanes are synthesized by ammonolysis and aminolysis of chlorosilylboranes. To avoid long and difficult filtration processes for separation of solid by-products such as NH_4Cl, a novel salt-free synthetic approach was used, i.e. a hydroboration reaction where the vinyl group containing cyclosilazanes were treated with borane dimethyl sulphide. This synthesis method provides the advantage of avoiding time-consuming separation of the synthesized polymer from ammonium salts formed as by-products. In addition, it allows for using commercially available cyclosilazanes.

Two different cyclosilazanes were used as monomer for the synthesis of polyborosilazanes, i.e. 1,3,5-trivinyl-1,3,5-trimethyl-cyclosilazane and 1,3,5,7-tetravinyl-1,3,5,7-tetramethyl-cyclosilazane. The synthesis of the pre-ceramic polymers was carried out under argon using the Schlenk technique. To synthesize polyborotrisilazane, a solution of 5.4 ml of 1,3,5-trivinyl-1,3,5-trimethyl-cyclotrisilazane (ABCR chemicals) in 25 ml of anhydrous toluene was cooled under stirring to 0 °C. Then 2.8 ml of borane dimethylsulfide dissolved in 25 ml toluene was added drop wise to the cyclotrisilazane solution. The mixture was stirred for 2 hours at 0 °C. After heating up to room temperature, the solution was stirred until solution was converted to gel. To obtain solid materials for the structural characterization, the solvent was evaporated under vacuum. In the synthesis of polyborotetrasilazane, a solution of 5.04 ml of 1,3,5,7-tetravinyl-1,3,5,7-tetramethyl-cyclotetrasilazane in 25 ml of toluene was cooled under stirring to 0 °C. Then 2.78 ml of borane dimethylsulfide dissolved in 25 ml toluene was added drop wise to the cyclotetrasilazane solution. For the structural characterization the polymer obtained by removing the solvent under vacuum was used. Dried polymers were pyrolyzed at two temperatures (800 °C and 1000 °C) under flowing argon atmosphere to obtain ceramic powder for further characterizations. The polymers were heated to the required temperatures (T_r) with a heating rate of 100 °C h^{-1}, hold for 2 h at T_r, and cooled to room temperature at a rate of 100 °C h^{-1}.

Si_3N_4 ceramic: Unsupported membranes of Si_3N_4 were synthesized by the ammonolysis of commercially available polysilazane (KiON HTT 1800) in dry ammonia at 800 and 1000 °C. To obtain ceramic powder, polysilazane was heated up to 200 °C with a rate of 50 °C min^{-1}, hold for 2 h at 200 °C to facilitate cross-linking, further heated to the required temperature (T_r), hold for 2 h at T_r and then cooled to room temperature at a rate of 50 °C min^{-1}. To get a thin layer of membrane on porous support polysilazane HTT 1800 was diluted (60 by vol. % in dry toluene).

Carbon-rich SiCN ceramic powder: The precursor used for the synthesis of C-rich SiCN was poly(diphenylsilylcarbodiimide). The synthesis of the precursor and the derived ceramics was carried out in purified argon atmosphere as described in reference [15]. Bis(trimethylsilyl)carbodiimide (0.047 mol) was mixed under stirring with a catalytic amount of pyridine (0.024 mol). Afterwards, the substituted dichlorosilane $PhHSiCl_2$ (0.047 mol) was added and the reaction mixture was kept under reflux at 66 °C for 6 h (b.p. $PhHSiCl_2$ ~65–66 °C) and then at 120 °C for another 12 h. After completion of the reaction, the by-product trimethylchlorosilane was removed by distillation. To obtain C-rich SiCN ceramic thermolysis of synthesized poly(diphenylsilylcarbodiimide) was done in two steps. In the first step synthesized polymer was taken in a quartz boat and heated under flowing argon to 1100 °C with a rate of 100 °C min^{-1}, hold for 2 h, and cooled to room temperature at a rate of 100 °C min^{-1}. To obtain ceramics at temperatures above 1100 °C, pre-pyrolyzed powder (obtained at 1100 °C) was put in a SiC boat which was placed in a carbon crucible and heated in an Astro furnace with a heating rate of 5 °C min^{-1} under argon atmosphere to the required thermolysis temperature, hold for desired time, and finally cooled to room temperature at a rate of 10 °C min^{-1}.

2.1.4 Membrane deposition on porous supports

Two different dimensions of tubular porous α-Al_2O_3 supports (provided by Noritake Co. Ltd., Japan and IKTS, Hermsdorf, Germany) were used for the deposition of membranes. Membranes were coated on the outer wall of the supports received from Noritake whereas for the supports received from IKTS membrane deposition was done on the inner wall of the supports. Two different methods were used for coating these supports with polymer.

Intermediate γ-Al_2O_3 layer was developed on the outer surface of the tubular supports (Noritake Co. Ltd, outer diameter (OD): 6 mm, inner diameter (ID): 4 mm) by dipping them in a boehmite colloidal dispersion (Alfa Aesar, 4 wt. % in H_2O) with subsequent calcination at

800 °C in air for 2 h. To obtain crack-free γ-Al_2O_3 layer on porous support 1 wt.% of PVA (Alfa Aesar) was added in boehmite colloidal dispersion. The deposition of the SiBCN membranes on the outer surface of alumina supports with the intermediate mesoporous γ-Al_2O_3 layers was performed by dip-coating of the tubular supports in solutions containing the pre-ceramic polymer followed by the subsequent pyrolysis in argon at 800 ºC for 2 h (as described in section 2.1.3). For multiple layer of membrane deposition on support, precursor coated support was pyrolyzed at 800 ºC before depositing successive layers. The applied dip-coating method to coat supports with intermediate layer or pre-ceramic solutions is shown in Figure 2.1. To do this, both ends of hollow tubular porous Al_2O_3-support were sealed with silicon rubber before dip-coating. Porous supports were dipped in boehmite sol for 0.5 min and in polymeric solution for 3–4 min and taken out with a speed of 2 cm min^{-1}.

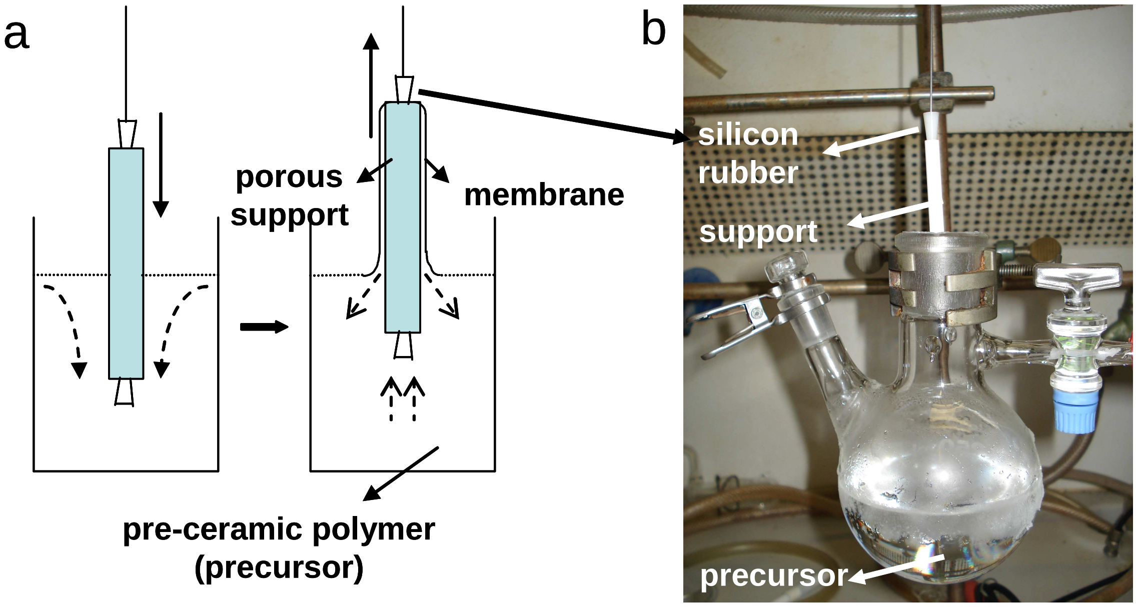

Figure 2.1. Dip-coating process applied for the deposition of membranes on porous supports: (a) Schematic, (b) snap shot of a real deposition process.

The tubular supports received from IKTS (OD: 10 mm, ID: 7 mm) were coated with polymers on the inner wall of supports in a different way. One end of tubular porous support was tightly gripped with FEP tube (inner wall of FEP tube fastened securely to the outer wall of support) and the support was clamped. Then polymer filled syringe was tightened on the other end of the FEP tube. Subsequently, polymer was injected through the FEP tube such that inner volume of support was filled with the polymer. After 3–4 minutes polymer was slowly withdrawn using Syringe from the porous support. Thereafter, FEP tube was carefully removed from the support and polymer coated support was pyrolyzed.

2.1.5 Gas permeance measurements

Gas permeance measurement method used in this thesis work is described in chapter 3 (section 3.3.4) along with the definition of relevant terms used for the understanding of permeance measurement set-up.

2.2. Gas sensors

2.2.1 Sensor material synthesis and its deposition on sensor supports

Coating of sensing materials on sensor supports was done at the Institute of Physical and Theoretical Chemistry, University of Tuebingen, Germany and used as-received. Sensing materials synthesis methods are described in the following:

SnO_2 synthesis: A detailed description of the synthesis procedure and the full characterization of as-prepared powders are given in reference [2]. SnO_2 powders were obtained by wet chemistry method, starting by dropwise addition of ammonia to an aqueous $SnCl_4$ solution, followed by washing in distilled water to remove chlorine contamination. The formed precipitate was subsequently dried in normal atmosphere for 12 h (80 °C) and then calcined in the air at 1000 °C for 8 h which led to a particle size of SnO_2 around 200 nm.

GaN synthesis: GaN as sensing material was obtained by conventional nitridation of commercial gallium oxide β-Ga_2O_3 (Alfa Aesar, 99.99%) at 900°C over 24 h [3]. Commercial GaN powder (Sigma-Aldrich, 99.99 %) was also used in this study.

Screen-printing process: The substrate used for the deposition of sensing material is consisting of planar Al_2O_3 substrate with Pt-electrodes on the front side for measuring the sensor resistance and a Pt-heater on the backside to heat the sensor at the temperature of interest (Figure 2.2). The electrodes have an interdigited structure to allow measuring resistances on a small area. To obtain a continuous sensing layer on the substrate, synthesized powder (SnO_2 or GaN) was mixed with an organic compound (1,2-propanediol) and then ball-milled to obtain homogenous paste. The paste was pressed through the holes of a screen onto the alumina substrate. After screen printing the substrate coated with powder was kept at room temperature for 12 h. The final thermal treatment was performed in a moving belt oven (400–600°C) under dry nitrogen flow.

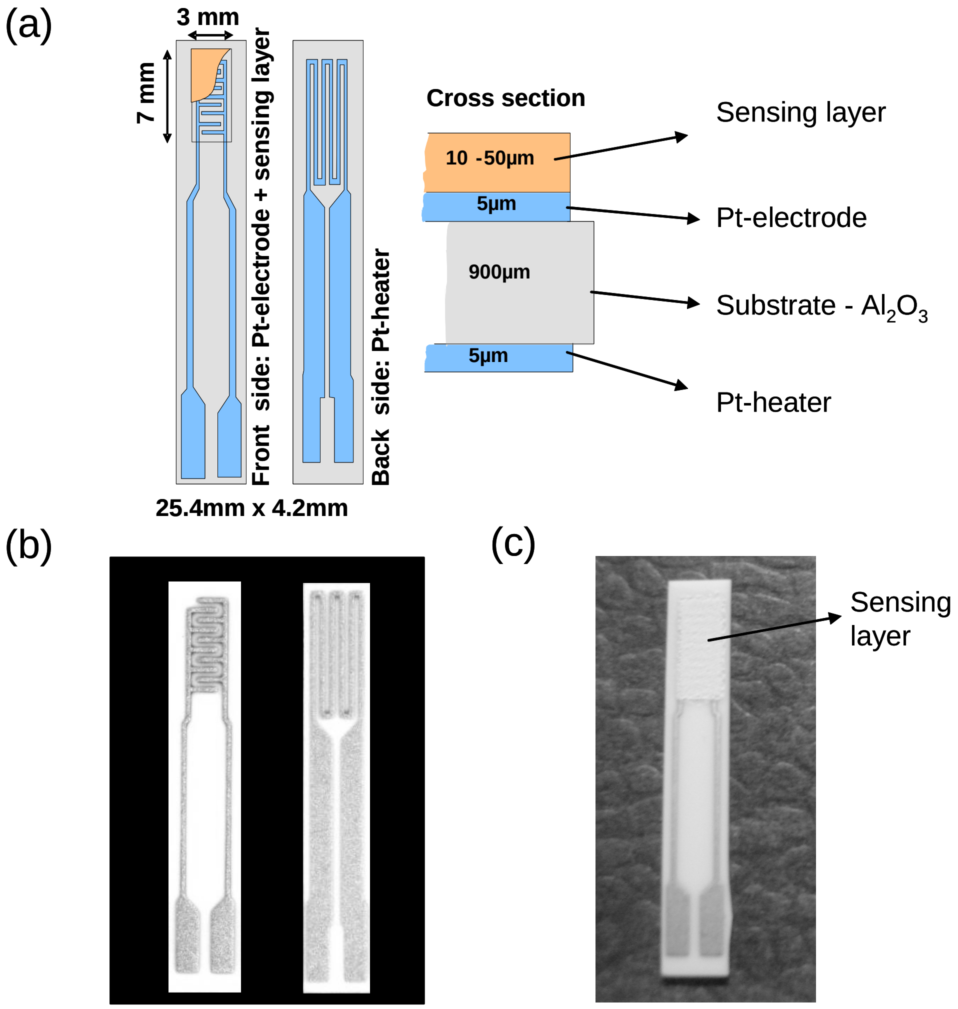

Figure 2.2. Gas sensor supports: (a) layout of planar alumina substrate with Pt-electrodes on the front side and Pt-heater on the backside, (b) actual sensor support, (c) SnO_2 layer (screen-printed) on the front side of support.

2.2.2 Membrane deposition on sensor supports

The sensors (received from the University of Tuebingen) were coated with pre-ceramic polymer precursor by dip-coating method in a similar way used for porous supports (section 2.1.4) as shown schematically in Figure 2.3. The Pt-heater on the back-side of sensor support was protected in a special way — using cellotape during polymer coating and then carefully removed before pyrolysis.

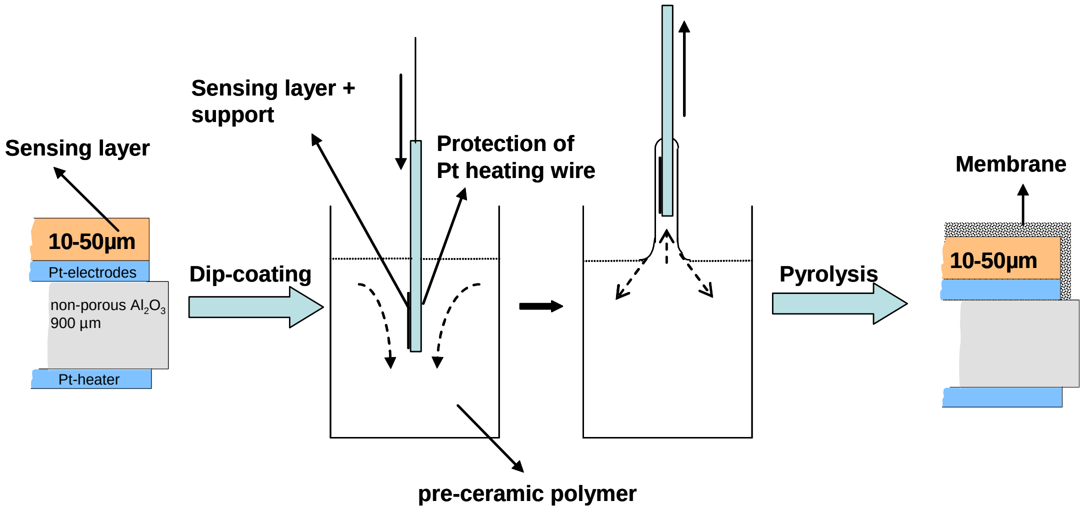

Figure 2.3. Schematic of membrane deposition on gas sensors.

2.2.3 Gas sensing measurement procedure and data collection

DC-resistance measurements were performed to characterize the sensor performance using digital multimeter (Keithley DMM199). The actual oxygen concentration (below 4 ppm) was controlled on-line with an electrochemical oxygen gas analyzer based on YSZ (Zirox SGM400). The response of sensors during exposure to CO and H_2 in nitrogen (Type 5.5) with a flow of 500 ml min^{-1} at 350 and 530 °C was measured. To keep the sensors at the operating temperature a power supply was used to ensure a constant voltage drop over the platinum on the back side of the alumina substrate (Figure 2.2). All measurements were repeated for each gas and temperature to check the reproducibility. The sensor data during the measurement by the sensor system is transferred to the external computer via RS232 connections.

2.3. Characterization techniques

2.3.1 Attenuated total reflection infrared (ATR-IR) spectroscopy

Attenuated total reflection (ATR) spectra for air-sensitive polymers (polyborotrisilazane and polyborotetrasilazane) were measured using the Golden Gate single-reflection ATR accessory at a Perkin Elmer FT-IR Series 1600 spectrometer with spectral range from 4000 and 600 cm^{-1} with a spectral resolution of 1 cm^{-1}. Measurements were performed under argon atmosphere.

2.3.2 Nuclear magnetic resonance (NMR) spectroscopy

^{1}H, ^{13}C and ^{29}Si liquid state Nuclear Magnetic Resonance (NMR) spectra were recorded on a Bruker DRX 500 MHz spectrometer using a 5 mm BBO rotor diameter using C_6D_6 as solvent. Spectra were referenced to tetramethylsilane (TMS) as the internal reference.

Solid state Magic Angle Spinning NMR (MAS NMR) measurements were performed on a Bruker CXP 300 MHz spectrometer operating at a static magnetic field of 7.05 T and using a 4 mm magic angle spinning (MAS) probe. Cross polarization (cp) $^{29}Si\{^{1}H\}$ and ^{13}C $\{^{1}H\}$ spectra were acquired at the spinning speed of 5 kHz, using contacts time of 5 ms, pulse lengths of 4 μs and recycle delays of 5 s. The number of scans was 2000. For the acquisition of ^{11}B spectra a simple one pulse excitation was applied. The spectra were recorded at a spinning speed of 14 kHz using a 45° pulse length of 1.1 μs and recycle delays of 10 s. The number of scans was 400. ^{29}Si and ^{13}C chemical shifts were determined relative to the external standards Q_8M_8 and adamantane, respectively, and are given with respect to the standard TMS ($\delta = 0$ ppm). ^{11}B spectra were calibrated using a solution of boric acid H_3BO_3 as secondary standard.

2.3.3 Simultaneous thermal analysis (STA)

Simultaneous Thermal Analysis (STA) measurements were carried out using a Simultaneous thermoanalyzer Netzsch STA 449C Jupiter coupled with a Quadrupole mass spectrometer

QMS 403C Aëolos, Netzsch Gerätebau GmbH, Selb/Bayern. The polymeric samples were heated to 1400 °C with a heating rate of 5 °C min^{-1} in argon or helium atmosphere at flow rate of 25 ml min^{-1}, while simultaneously measuring the mass loss and the gases released via mass spectrometry (Quadrupole Mass Spectrometer QMA 400, Blazers). High temperature thermogravimetry (HT TG) was performed in He 5.0, 75 ml min^{-1}, with a heating rate of 2 °C min^{-1}.

Thermo-gravimetric (TG) analysis of the polymer under ammonia was performed in the following way. Ammonolysis of polymer was done between 100 and 1000 °C, at intervals of 100 °C. For each measurement 0.1 g of polymer was taken. The difference in mass before and after ammonolysis was calculated at each temperature to get the yield at each temperature and plotted at different temperatures to get TG profile.

2.3.4 X-ray diffraction (XRD)

X-ray powder diffraction (XRD) measurement was performed in flat-sample transmission geometry on a STADI P X-ray diffractometer (STOE & Cie GmbH, Germany) with Ge(111) monochromator using Mo Kα radiation at a scanning speed of 1° min^{-1} in the 2θ range of 10-50° and on a D8 Advance diffractometer (Bruker, USA) with Cu Kα radiation under reflection scanning mode in the 2θ range of 10-70°. The structures were identified using the program STOE WinXPOW and MDI Jade 5.0 software.

2.3.5 Elemental analysis

The amount of carbon in the pyrolyzed samples was determined by C-analyzer (Leco C-200). The probe material was weighed and mixed with tungsten and iron and is put in an Al_2O_3 crucible. Then crucible was placed in high frequency electric field, and burned up in oxygen stream. Carbon contained in the sample is completely oxidized to CO_2 gas before passing it through an IR-cell. Quantification of carbon content is done based on Lambert Beer’s law, where the absorption is proportional to the carbon content. Standards used were steel and SiC.

The nitrogen and oxygen contents were measured with N/O analyzer (Leco, Type TC-436) using a hot extraction method. The powder sample was packed in a tin capsule and then placed in a nickel basket. The powdered samples were burned in a graphite crucible at about 2700 °C under helium atmosphere. Oxygen in the sample reacts with carbon forming carbon monoxide which is oxidized to CO_2 using CuO catalyst. CO_2 formed was quantitatively analyzed by IR absorption spectroscopy. Thermally released nitrogen was measured by thermal conductivity measurement. Oxygen anlaysis was accomplished in an IR-cell as CO_2. Formed CO can be oxidized using Pt/SiO_2 catalyzer. N,O contents in the sample were compared with calibration standards like steel, Ti-steel or TiN, WO_3.

Si and B were calculated based on initial Si and B molar ratio present in the precursor and by subtracting the amounts of C, N and O.

2.3.6 Scanning electron microscopy (SEM)

The morphologies of the powdered and bulk samples were examined using a XL30 FEG scanning electron microscope (Philips, The Netherlands) with an acceleration voltage of 10–25 kV. To measure the thickness of membrane layers (membrane coated supports) samples were cut/broken such that membrane cross-section was visible for taking SEM images. Before the SEM observation, the samples were sputtered with a thin gold layer to avoid charging.

2.3.7 Transmission electron microscopy (TEM)

Transmission electron microscopy (TEM) measurements were performed on powdered samples using an FEI CM20STEM instrument (FEI, Eindhoven, the Netherlands) operating at an acceleration voltage of 200 kV (wavelength λ=2.51 pm) in order to distinguish the crystal structure and particle size. For the TEM sample preparation, the ceramic powders were dispersed in an ultrasonic bath (high purity methanol 99.8%, Sigma-Aldrich Co.) and a small droplet of the suspension was placed on holey carbon (Cu) grit. Upon drying, the samples were lightly coated with carbon to avoid charging under the electron beam.

2.3.8 Raman spectroscopy

Raman spectra were recorded from 100 to 4000 cm^{-1} on a confocal Horiba HR800 micro-Raman spectrometer (Horiba Jobin Yvon, Germany) with excitation laser wavelengths of 488, 514 and 633 nm. All measurements were performed in air at room temperature.

2.3.9 Mercury-porosimetry

Pore-size distributions of the as-received α-Al_2O_3 support and those treated under various atmospheres (air, argon, and ammonia) were measured by mercury porosimetry method (Micromeritics, Pore Sizer 9320). The operation of a mercury porosimeter is based on the physical principle that a non-reactive liquid (in this case, mercury), which does not wet the surface of the material onto which it is applied, does not penetrate into the pores until such a pressure is applied that it forces the liquid into the pores. The ratio between the applied pressure and the size of the pores is defined by Washburn’s equation, where the pore diameter is inversely proportional to the applied pressure: the higher the pressure, the smaller are the pores into which it is possible to intrude the liquid.

2.3.10 Nitrogen-sorption measurements

The porous properties of the samples were investigated by determining their N_2 adsorption and desorption isotherms at 77 K. The samples were preheated at 150 °C for 24 h under vacuum before the measurement. The specific surface area (S_{BET}) values were calculated by the Brunauer, Emmett and Teller (BET) method [4] from the linear portion of the adsorption isotherm. Pore size distribution (PSD) was calculated by the Barrett, Joyner and Halenda (BJH) method [5] from the desorption isotherm. The total pore volume was calculated from the maximum amount of nitrogen gas adsorption at partial pressure (P/P_0) = 0.99.

Pore-size distribution and BET surface area of unsupported γ-Al_2O_3 were measured by N_2 sorption analysis (Quantachrome Autosorb-3B, Quantachrome, USA). Pore volume and pore-size distribution of SiBCN membrane coated on α-Al_2O_3 supports was done by N_2 adsorption isothermal analysis (Model Autosorb-1-MP, Quantachrome Instruments, USA). Microporosity of SiBCN membrane was evaluated by Saito-Foley (SF) method.

2.3.11 Small-angle X-ray scattering (SAXS)

As scattering technique, SAXS is generally applied to study structures in the size range 1 to 100 nm by measuring the intensity of the scattering, I(q), as a function of the scattering vector, q

$$|q| = \frac{4\pi \sin\theta}{\lambda} \qquad (2.1)$$

where λ being the incident wavelength and θ is half of scattering angle. X-ray scattering occurs due to electron density inhomogeneities in the sample and remains essentially unaffected when electrons shifts within a particle by distances which are small compared to the overall particle dimensions, as in amorphous aggregates. In an isotropic medium, the SAXS intensity is a function of the modulus of the scattering vector. Considering a system of N independent particles scattering independently, or so called diluted system, the SAXS intensity is given by Guinier's Law:

$$I(q) = N(\Delta\rho)^2 V^2 \exp\left(-\frac{R_g{}^2 q^2}{3}\right) \qquad (2.2)$$

where R_g is the gyration radius of the particles of volume V, electronic difference between the particles and the matrix is represented by $\Delta\rho$. The R_g formally corresponds to the radius of inertia in mechanics; it is the root mean square of the distances of all the electrons from their center of gravity. It depends on both pore-size and shape [5-6]. In a polydispersed system, only an average value of R_g can be obtained from the slope of log-log plot of equation 2.2, $\ln[I(q)] = m + nq^2$.

SAXS measurements (scattering vector, q: 0.1-10 nm^{-1}) were carried out to investigate the microporosity distribution in the amorphous SiBCN ceramic powders at 7T-WLS-μspot beamline (synchrotron radiation source BESSY II, Germany) using a two-dimensional MarMosaic CCD detector (Mar 225, Mar, Evanston, U.S.A.). The sample to detector distance was set to 1.012 meter. Unsupported ceramic membrane materials were ground into powder and introduced in quartz capillary (Hilgenberg GmbH, Germany) and the measurements were performed in transmission mode. Data were processed and converted into diagrams of scattered intensities versus scattering vector q by employing the computer program FIT2D. SAXS data which is obtained after subtracting background and normalization process were analyzed using Igor Pro/Irena package.

2.4. References

[1] K.B. Pflanz, R. Riedel, H. Chmiel, "Preparation of Spinel Ultrafiltration Membranes," *Advanced Materials*, 4 (1992) 662-665.

[2] A. Dieguez, A. Romano-Rodriguez, J.R. Morante, J. Kappler, N. Barsan, W. Gopel, "Nanoparticle engineering for gas sensor optimisation: improved sol-gel fabricated nanocrystalline SnO_2 thick film gas sensor for NO_2 detection by calcination, catalytic metal introduction and grinding treatments," *Sensors and Actuators B: Chemical*, 60 (1999) 125-137.

[3] M. Kerlau, O. Merdrignac-Conanec, P. Reichel, N. Barsan, U. Weimar, "Preparation and characterization of gallium (oxy)nitride powders - Preliminary investigation as new gas sensor materials," *Sensors and Actuators B: Chemical*, 115 (2006) 4-11.

[4] S. Brunauer, P.H. Emmett, E. Teller, "Adsorption of gases in multimolecular layers," *Journal of the American Chemical Society*, 60 (1938) 309-319.

[5] E.P. Barrett, L.G. Joyner, P.P. Halenda, "The determination of pore volume and area distributions in porous substances. I. computations from nitrogen isotherms," *Journal of the American Chemical Society*, 73 (1951) 373-380.

[6] G. Laudisio, R.K. Dash, J.P. Singer, G. Yushin, Y. Gogotsi, J.E. Fischer, "Carbide-derived carbons: A comparative study of porosity based on small-angle scattering and adsorption isotherms," *Langmuir*, 22 (2006) 8945-8950.

[7] Y. Gogotsi, A. Nikitin, H.H. Ye, W. Zhou, J.E. Fischer, Y. Bo, H.C. Foley, M.W. Barsoum, "Nanoporous carbide-derived carbon with tunable pore size," *Nature Materials*, 2 (2003) 591-594.

Part III

Results and discussion

Chapter 3. Design and realization of the experimental set-up for the determination of permeance characteristics

The design and operation principle of a laboratory-scale system — which has been newly constructed within the framework of this thesis work — for characterization of gas permeance is described in this chapter. Section 3.1 defines important basic terminologies which are used in the field of gas separation membranes. General principles of permeance measurements are explained in the section 3.2. Finally, the experimental set-up realized in this work is described in the sections 3.3.

3.1. Definitions

Basic definition of relevant terms related to membrane based gas separation process is already defined in chapter 1 (section 1.2.1) and schematic of a membrane separation process showing feed, retentate, and permeate is shown in Figure 1.2.

The performance of membranes are described in terms of flux (or permeance) and selectivity (permselectivity and actual membrane selectivity). The flux is the total transport of material through the membrane and is expressed as mass or mole per unit time per unit area. Permeance is defined as the flux per unit pressure difference between feed and permeate sides. The selectivity is defined as the permeance ratio of two gases: (i) permselectivity: the ratio of single gas permeances; (ii) actual membrane selectivity: the ratio of the gas permeances, measured for mixtures. These functional characteristics of a membrane which are calculated in terms of flux, permeance and selectivity and are listed in Table 3.1.

Table 3.1. Parameters describing the performance of the membranes.

Flux, F_i [mol/m^{2}s]:	$F = \frac{V/SRT}{\Delta t/\Delta p_2}$	V - S -	The total volume of the buffer tank and gas line, [m^3]. This is highlighted as red in Figure 3.3. The membrane area [m^2]
Permeance, P_i [mol/m^{2}sPa]:	$P_i = \frac{FM_i^p}{p_1 M_i^f - p_2 M_i^p}$	R - T - Δp_2 -	Gas constant [J/Kmol]] Temperature [K] Pressure difference at permeate side
Selectivity, P_i/P_j:	$\alpha_{i/j} = \frac{P_i}{P_j}$	p_1 - p_2 - M_i^f and M_i^p -	The feed gas pressure The logarithmical average of p(Permeate-start) and p(Permeate-end), start and end are two points of linear pressure increase as shown in Figure 3.. Molar fractions of gas i on the feed side and permeate side, respectively.

3.2. Choice of permeance measurement method

Two experimental methods for the measurements of permenace rates and for the determination of steady-state gas permeances are standardized by American Society of Testing Methods (ASTM) as the ASTM method D1434–82 [1]. They are (i) the manometric (also variable-pressure, constant volume manometric or pressure increase) method and (ii) the volumetric (variable-volume) method. The variable-pressure and variable-volume methods use the same basic principle: one side of the membrane is exposed to the gas to be studied (feeding side). In the pressure increase method, a gas permeates through a membrane into a closed constant-volume chamber that is pre-evacuated and the pressure rise in this chamber is recorded as a function of time. In the volumetric method, the permeance chamber expands against a low constant pressure (usually atmospheric) and the volume increase is recorded as a function of time.

To determine the gas concentrations, the permeating gas is swept away with a carrier gas (usually nitrogen) and fed into a detector/sensor. The detector is often specific to the permeating species. The permeance of the membrane is determined from the amount of permeation and experimental parameters such as time, membrane area, pressure difference, concentrations etc. Permeation measurements depend on differences in concentration of the permeating species on either side of the membrane to provide the 'potential difference' that drives the permeating species. The increase in concentration of permeating species is determined either through a general method such as pressure changes, mass changes or by using a detector specific to the species being studied. Figure 3.1 illustrates a typical permeation curve, characterizing permeation through pressure change. The feed side is exposed (at $t = t_0$) to the permeant and the amount permeating through the sample is measured through an increase in pressure/concentration at the permeating side.

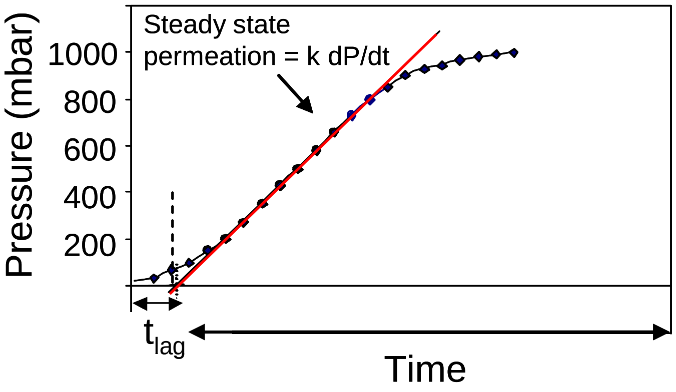

Figure 3.1. Illustrative permeation curve: pressure increase over time, where k is proportional constant.

There is a short delay in detecting an increase in pressure, characterized by the "time-lag" t_{lag}, while the first molecules diffuse through the membrane. The pressure and rate of change of pressure continues to increase as further gas molecules permeate through the sample. The rate of increase in pressure levels off when the concentration in the sample reaches equilibrium. The linear portion of the curve is called steady state permeation. *It is important* *to note that a permeation experiment can be performed as long as a pressure gradient of the gas component to be measured across the membrane is maintained.*

Following four parameters were taken into account for constructing lab-scale experimental set-up considering the main goal, i.e. separation of H_2 and CO:

Firstly, as the use of pure H_2 and CO for single gas permeance measurements was not possible due to safety reasons in the university (single gas permeance measurements of H_2 and CO_2 were done at HITK described in Chapter 6), the permeance characteristics should be measured using diluted H_2 and CO (gas mixtures with N_2). This requires use of micro-gas chromatograph for knowing the gas concentrations/partial pressure after permeance through membrane. Permeance calculation formula listed in Table 3.1 indicates that single gas permeance measurement does not require mole fraction of the gas on the feed and permeating side. Therefore, single gas permeance of pure gases such as He, Ne, Ar, CO_2, and N_2 could be easily measured.

Secondly, one of the most important points need to keep in mind while designing permenace measurement set-up is — the total volume of the buffer tank and gas line on permeate side. The smaller the total volume, the faster the measurement. When a buffer tank of very small volume is used, pressure increase on permeate side occurs very fast and the time during which pressure increases could not be noted accurately. Buffer tank of about 1 liter is optimized in our case.

Thirdly, in microporous membrane, flux through the membrane is directly proportional to the applied transmembrane pressure (ΔP_T) at a particular temperature [2].

$$\Delta P_T = (\frac{p_F + p_R}{2}) - p_{PR} \tag{3.1}$$

p_F: feed side pressure
p_R: retentate end pressure
p_{PR}: permeate side pressure

The general dependence of flux on transmembrane pressure is shown in Figure 3.2. Both feed side and retentate end pressures were optimized to be 1 bar where as permeate side pressure was optimized in the range of 30–100 mbars.

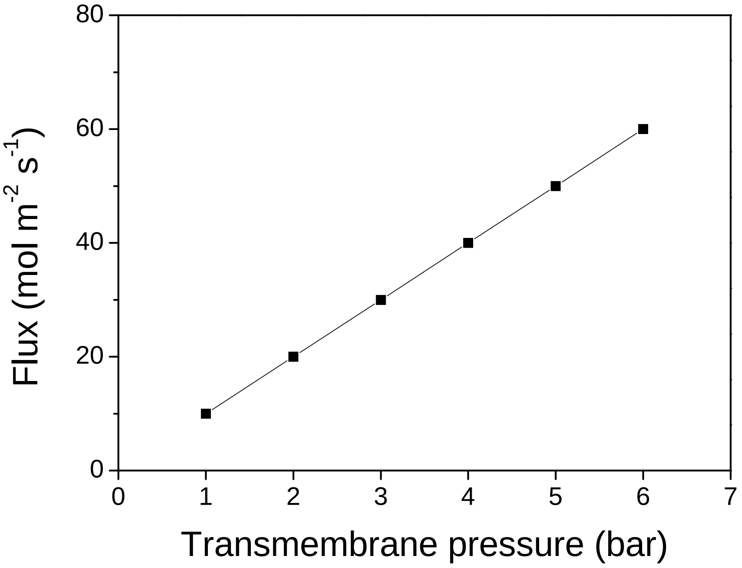

Figure 3.2. A model flux vs. transmembrane pressure relationship for a microporous membrane.

Fourthly, the permeance through a microporous membrane also increases dramatically as the temperature is increased. Therefore, microporous membranes have the potential to produce higher fluxes at elevated temperatures and pressures. A higher value of flux will reduce the membrane area requirements and can result in a lower overall cost. In some situation, the increased energy costs associated with the higher operating temperature have to be considered to achieve an optimum balance between the increased operating costs and lower capital costs. The temperature optimized for our set-up was 400–500 °C.

Taking into consideration the factors/reasons described above, pressure increase method was selected for the realization of permeance measurement set-up.

3.3. Experimental realization

Schematic of the experimental set-up which has been constructed and used for the determination of permeance characteristics is shown in Figure 3.3A. The set-up consists of the following parts:

(i) gas flow and pressure regulation systems: gas cylinders, pressure regulators, mass flow controllers (MFC), pressure gauges, valves, tubing, measurement and controlling units, vacuum pump

(ii) measurement cell which consists of gas tight sealed alumina tube and ceramic membrane

(iii) micro gas chromatograph (micro GC) to measure the concentration of gases on the permeate side

The experimental set-up has been realized according to the schematic set-up illustrated in Figure 3.3A and is shown in Figure 3.3B. Different parts of the set-up are described in the following sections.

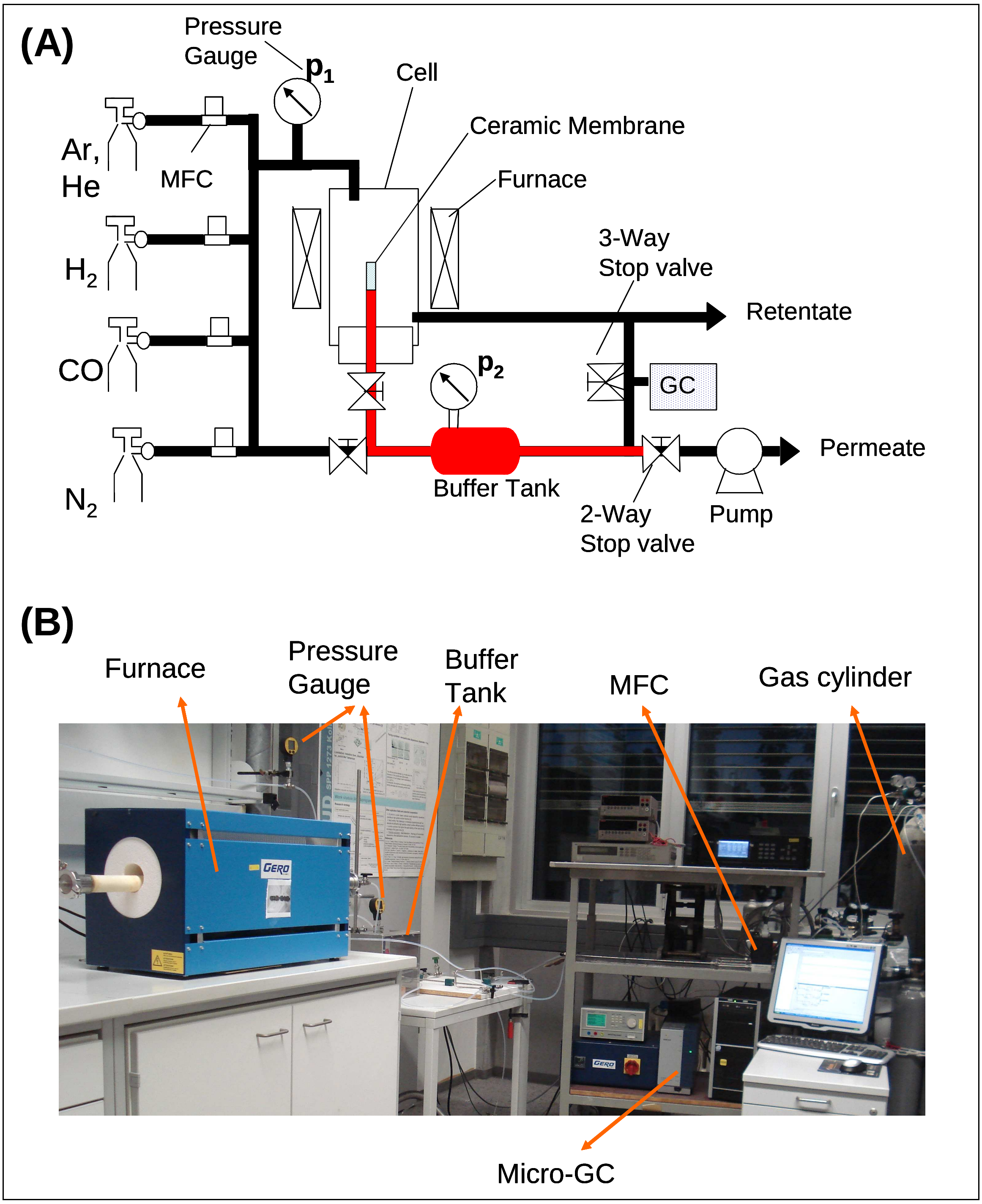

Figure 3.3. (A) Schematic representation of experimental set-up for gas permeation measurement. Red part represents buffer tank with pipelines where gas permeated through membrane is collected and sent to micro GC for the analysis; p_1 and p_2 indicates pressure at feed- and retentate-side, respectively, (B) The set-up for gas permeation measurements that has been realized at Disperse Feststoffe, Fachbereich Material-und Geowissenschaften, Technische Universitaet Darmstadt. It includes gas mixing facility (MKS Instruments), rotary pump, high temperature gas sealed tube oven (Gero GmbH, Germany, Type Sr 70-500/12) and micro GC (Varian CP 4900 with three chromatographic columns to analyze H_2, CO, N_2 and CO_2).

3.3.1 Gas mixing bench

In order to perform permeance measurement, a gas mixture facility is needed. To make the gas mixtures, gas mixing bench is employed. The gas mixing bench consists of four mass flow controllers (MFCs), as shown in Figure 3.4.

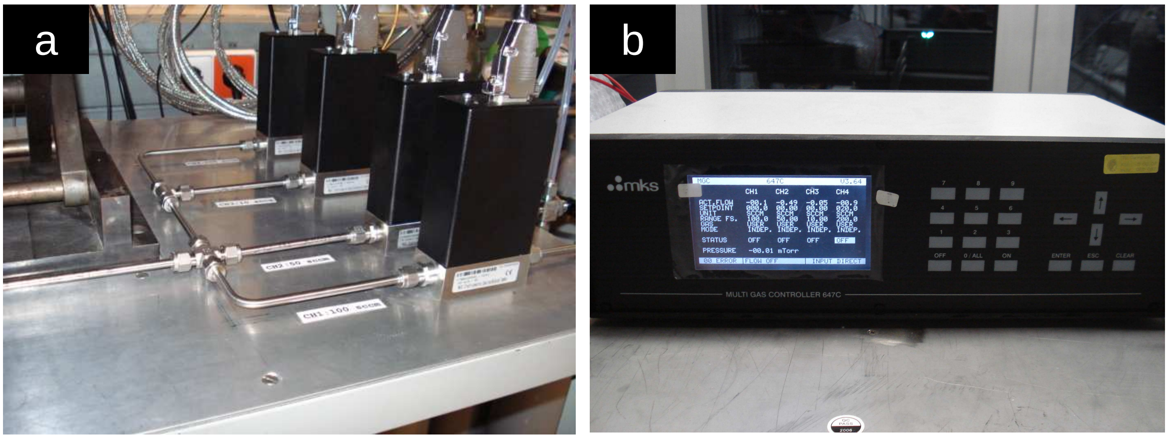

Figure 3.4. Gas-mixing bench consisting of four-channel gas mixing station having (a) mass flow controller, (b) multi gas controller (MGC).

Four mass flow controllers (Type 1179B, MKS Instruments GmbH, Germany) are fixed on test bench. Maximum flow rates through these four flow controllers are 10, 50, 100 and 200 cm^3 min^{-1}. The external control of MFCs is controlled by multi gas controller (MGC, type 647C, MKS Instruments GmbH, Germany). MFCs are connected via RS-232 interface to MGC. In order to control the flow through individual channels and to work more efficiently and user friendly, the gas mixing bench is operated by LabVIEW software program which is written indegineously.

The gas channels are interconnected by Swagelok stainless steel tubings. The concentrations of different gases in the final gas mixture (for feed side) are adjusted by controlling the ratio of test gas flow to total gas flow according to equation 3.2.

$$C_{g,1} = C_{g0,1} \times \frac{GFR_1(\mathrm{sccm})}{GFR_T(\mathrm{sccm})} \tag{3.2}$$

where
sccm: standard cubic centimetre per minute
$C_{g,1}$: gas concentration flowing through channel-1 in the final mixture
$C_{g0,1}$: gas concentration as supplied in the gas cylinder
GFR_1: gas glow rate through channel-1
GFR_T: total gas flow rate

3.3.2 Permeation system

The gas mixture that is made using gas mixing bench is fed at feed-side of the furnace (GERO GmbH, Germany, Type Sr 70-500/12) accompanied with the membrane coated support. After permeating through membrane, the gases come out from the permeate-end and are collected in a buffer tank (made of borosilicate glass). Rest of the gases go to exhaust from the retentate-end.

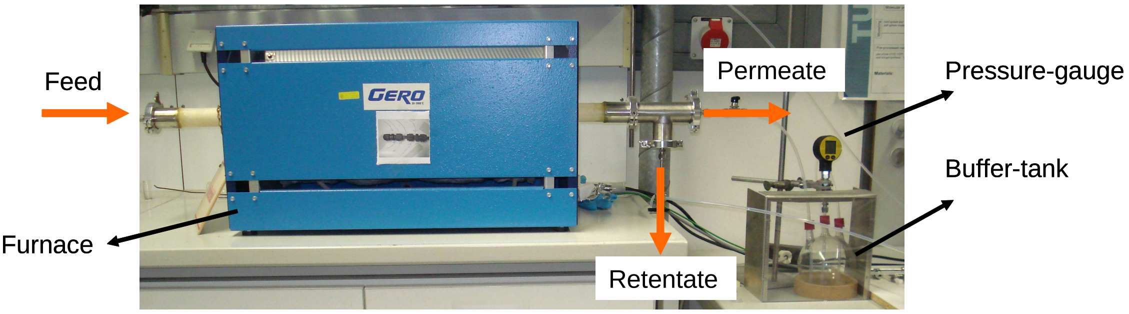

Figure 3.5. Permeation system showing feed-, permeate- and retenate-ends of permeation cell along with buffer-tank.

Permeation system should be tightly sealed from the external environment in order to prevent extraneous transfer of material to permeation cell. The materials used in the construction of the cell should not react with gases which are used for permeation measurement. Stainless steel is a suitable material for making gas-tight permeation system. In the very first measurements it is found that our porous supports are not able to withstand pressure induced by stainless steel ferrules while making supports gas-tight with Swagelok connections using stainless steel ferrules. An elegant technical solution is found to solve this problem by applying graphite based ferrules as illustrated in Figure 3.6. However, the use of graphite ferrules limits the maximum temperature for permeance measurements to 450 °C.

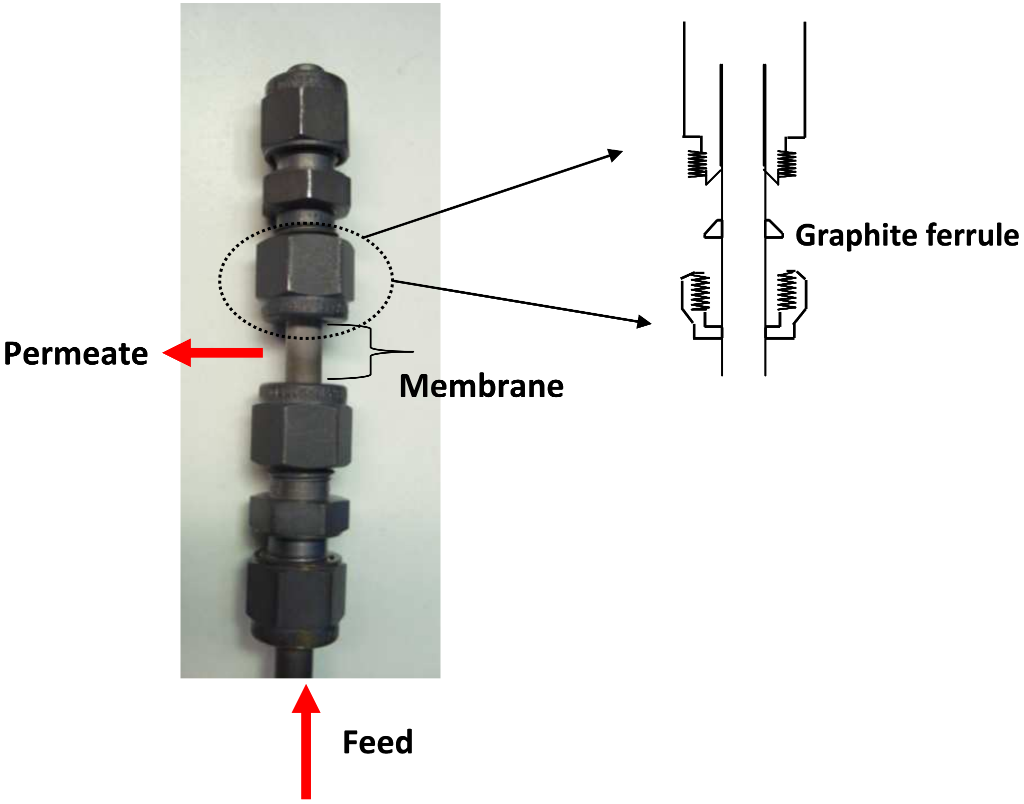

Figure 3.6. Membrane connected with Swagelok parts using graphite ferrules. Graphite ferrules are used for gas-tight connection for gas permeation measurements which are stable up to 450 °C.

3.3.3 Gas analysis system

In order to determine the performance characteristics of membranes, concentration of permeated gases has to be measured. This is done with the help of micro GC (Varian CP-4900) using RS-232 as the method of communication for instrument control. The CP-4900 micro GC uses TCP/IP (Transmission Control Protocol / Internet Protocol) to communicate over the Ethernet network and needs to be given a static IP address to identify and is controlled by Varian Galaxie software. Figure 3.7a is the front view and Figure 3.7b with the cover removed showing GC channels.

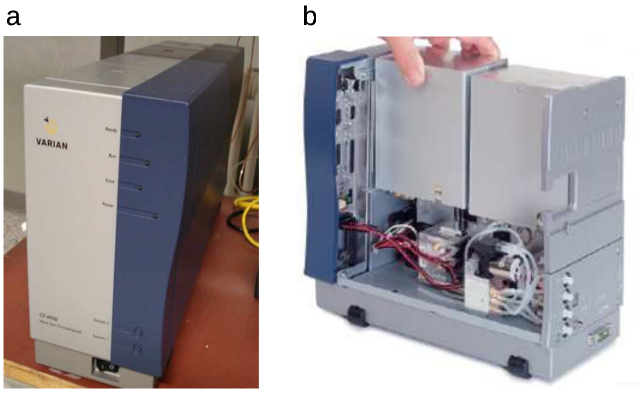

Figure 3.7. CP-4900 Micro GC: (a) Front view and (b) GC-channels (www.varianinc.com).

Varian CP-4900 is a three channel system. Two channels contain Molsieve (MS-5A) columns while the third channel uses a Poraplot Q (PPQ) column. Each channel is equipped with a thermal conductivity detector (TCD). The Molsieve columns are operated at 50 °C and at pressure of 200 kPa (channel 1) and 250 kPa (channel 2) to separate H_2, CO, CO_2, N_2, O_2. PPQ column is operated at 70 °C and 200 kPa to separate CO_2, C_2, C_3 components. Ar is used as the carried gas for channel 1 and He as a carrier gas for both second and third channels. The input pressure of the carrier gases should be maintained at 5.5 bars during the whole GC operation. The columns are housed in an oven that can be set to temperatures ranging from ambient to 180 °C. The column is where gases are separated as they are swept away through the column by the carrier gas. A screen-shot of the process during operation of GC is shown in Figure 3.8.

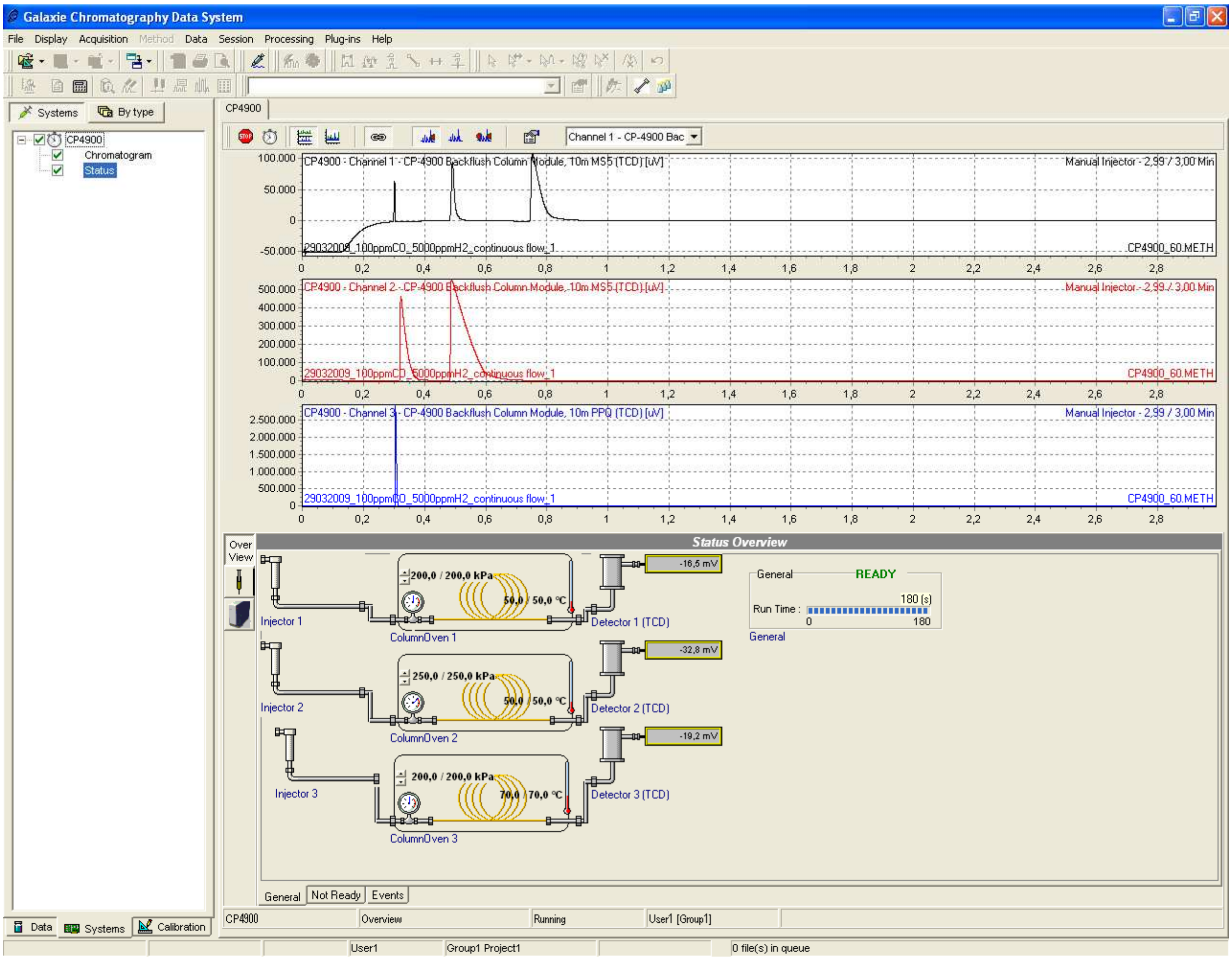

Figure 3.8. Screen-shot of Galaxie window showing peaks of gases separated in different GC columns.

The CP-4900 uses a gas sample loop that is etched into a silicon wafer. The internal volume of the loop is 10 µl. Sample volumes of 1 to 10 µl can be selected using the Galaxie software. The sample is drawn into the CP-4900 by an internal sampling pump. The pump can be programmed to run for any length of time. Generally pumptime of 1 to 2 minutes is used to ensure the sample transfer line is thoroughly purged. When the sampling pump stops, the CP-4900 injects the sample and system runs for 3 minutes.

Before performing permeation measurements to measure concentration of permeated gases, micro GC is calibrated with respect to different gases (H_2, CO, CO_2) for different concentration range as shown in Figure 3.9 and are listed in Table 3.2. The calibrations of gases are done under continuous gas flow mode. Channel 1, channel 2 and channel 3 are optimized for the aforementioned concentration ranges of hydrogen, carbon monoxide and carbon dioxide, respectively. Sometimes micro GC fails to detect some peaks. The common reason for this failure is contamination. Even though CP-4900 is designed to protect the main column and detectors from contamination, after a few days of continuous use some contaminants will inevitably make it through the precolumns and onto the main columns. When this happens, micro GC will produce irregular signal and peak shapes. When contamination of the main column occurs, the CP-4900 must be cleaned. The cleaning procedure involves setting the oven temperature to 160 °C for each of the three channels. The channels are maintained at this temperature for one night. During this time contaminants are swept away from the columns by the carrier gases.

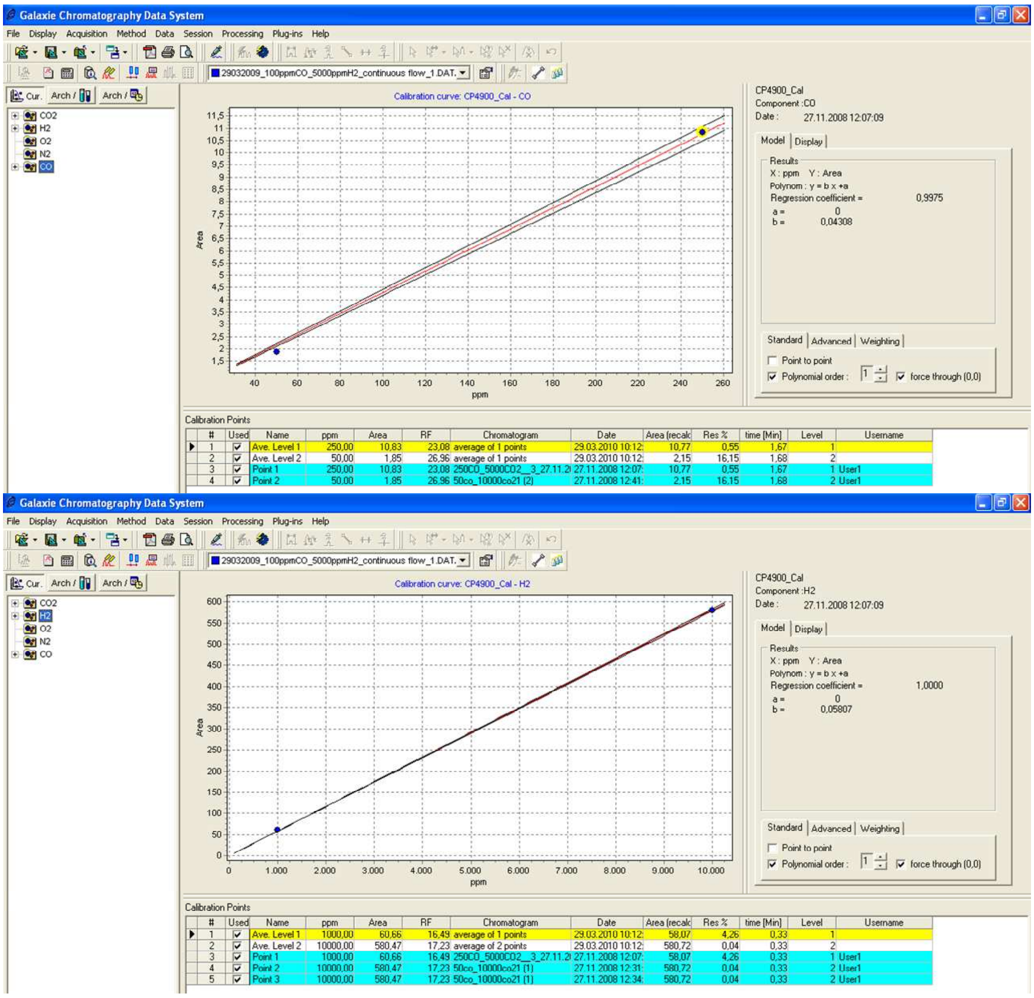

CP4900_Cal
Component :CO
Date : 27.11.2008 12:07:09

Results
X : ppm Y : Area
Polynom : y = b x +a
Regression coefficient = 0,9975
a = 0
b = 0,04308

☐ Point to point
☑ Polynomial order : 1 ☑ force through (0,0)

Calibration Points

#	Used	Name	ppm	Area	RF	Chromatogram	Date	Area (recalc	Res %	time [Min]	Level	Username
1	☑	Ave. Level 1	250,00	10,83	23,08	average of 1 points	29.03.2010 10:12:	10,77	0,55	1,67	1	
2	☑	Ave. Level 2	50,00	1,85	26,96	average of 1 points	29.03.2010 10:12:	2,15	16,15	1,68	2	
3	☑	Point 1	250,00	10,83	23,08	250CO_5000CO2__3_27.11.2	27.11.2008 12:07:	10,77	0,55	1,67	1	User1
4	☑	Point 2	50,00	1,85	26,96	50co_10000co21 (2)	27.11.2008 12:41:	2,15	16,15	1,68	2	User1

CP4900_Cal
Component :H2
Date : 27.11.2008 12:07:09

Results
X : ppm Y : Area
Polynom : y = b x +a
Regression coefficient = 1,0000
a = 0
b = 0,05807

☐ Point to point
☑ Polynomial order : 1 ☑ force through (0,0)

Calibration Points

#	Used	Name	ppm	Area	RF	Chromatogram	Date	Area (recalc	Res %	time [Min]	Level	Username
1	☑	Ave. Level 1	1000,00	60,66	16,49	average of 1 points	29.03.2010 10:12:	58,07	4,26	0,33	1	
2	☑	Ave. Level 2	10000,00	580,47	17,23	average of 2 points	29.03.2010 10:12:	580,72	0,04	0,33	2	
3	☑	Point 1	1000,00	60,66	16,49	250CO_5000CO2__3_27.11.2	27.11.2008 12:07:	58,07	4,26	0,33	1	User1
4	☑	Point 2	10000,00	580,47	17,23	50co_10000co21 (1)	27.11.2008 12:31:	580,72	0,04	0,33	2	User1
5	☑	Point 3	10000,00	580,47	17,23	50co_10000co21 (1)	27.11.2008 12:34:	580,72	0,04	0,33	2	User1

Figure 3.9. Screen-shot of calibration graphs of CO and H_2 for a certain concentration range.

Table 3.2. Concentration ranges of H_2, CO, and CO_2 after calibrating micro GC.

Gas	**Calibrated concentration range**
H_2	1000-10000 ppm
CO	50-250 ppm
CO_2	5000-10000 ppm

3.3.4 Procedure for gas permeance measurement used in this work

The first step in permeance measurement is to evacuate the permeation cell and tubings. In order to remove residual air between pressure regulators and MFCs, the connections are also flushed with gases. While system is getting evacuated, heating of permeation cell is simultaneously done at a slow heating rate of about 2 °C min^{-1}. When system is reached to its ultimate vacuum level (< 1 mbar) and the temperature of the furnace is reached to a particular temperature of interest for measuring gas permeance, gas-mixture is fed to the feed-side of permeation cell.

To measure H_2 and CO permeance though a membrane, flow rates of H_2 and CO are entered in the LabVIEW program according to equation 3.2. Gases are mixed using gas mixing bench facility. The mixed gas is introduced into the cell. Pressure on the feed side is slowly increases and the gases start to permeate though membrane on the permeate side and are collected in the buffer tank. When the pressure on the feed side reaches to 1 bar (100 kPa), the stop-valve directly connected to retentate-side is opened to exhaust to maintain the pressure on the feed side at a constant value of 1 bar. The time taken (Δt) for the permeate side pressure to reach from 4 kPa to 6.5 kPa is recorded. When buffer tank pressure reaches in the range of 55–65 kPa, the valve between buffer tank and the permeate-end of permeation cell is closed. Nitrogen gas is introduced into the buffer tank to dilute the permeated gases so that the pressure in the buffer tank is well above (> 90 kPa) for gas chromatography analysis.

After analysing the concentration of permeated gases using micro-GC, permeance and selectivity of different gases are calculated based on formulae listed in Table 3.1.

To measure single gas permeance of pure gases, such as Ar, He, N_2, CO_2, etc., using our permeance set-up, where molar fractions of gas i on feed side and permeate side are same ($M_i^f = M_i^p = 1$). Hence, the permeance equation of pure gas i can be rewritten as $P_i = F/(p_1 - p_2)$ from Table 3.1. In this case there is no need to dilute permeated gas by N_2 for concentration measurement using micro GC. This principle was used for measuring permeance of pure H_2, CO_2 at IKTS, Germany which is presented in Chapter 6.

The permeance measurement experimental set-up that has been realized in this work could be used for measuring permeance of mixed-gas (H_2, CO, CO_2) within certain gas concentration ranges as well as for single gas permeance measurements for pure gases (Ar, He, N_2, CO_2, Kr etc.). Nevertheless, this experimental set-up has some limitations: (i) the gas concentration of H_2 and CO (few hundreds of ppm level) used, due to safety regulations, for measurements is much smaller than that is produced at the hydrogen production site (in syn gas), (ii) the realized permeation system is applicable only for dry-gas permeation test. Steam can destroy micro GC, (iii) the maximum temperature at which permeation could be measured accurately is limited to 450 °C. The operational temperature can be increased by applying suitable ceramic glue which gives a gas-tight connection between membrane and Swagelok parts, (iv) presently permeation measurements are done with a transmembrane pressure of 1 bar. Transmembrane pressure can be increased by applying back-pressure regulators to increase flux which will reduce permeance measurement time.

3.4. References

[1] http://www.astm.org/Standards/D1434.htm.

[2] R.R. Bhave, *Inorganic Membranes: Synthesis, Characteristics and Applications*, Van Nostransd Reinhold, New York, 1991.

Chapter 4. Engineering multilayered membranes with gradient porosity

4.1. Concept

Membranes for hydrogen separation possess multilayered structure consisting of layers with different porosity: (i) macroporous ceramic support, (ii) intermediate mesoporous layer and (ii) microporous separation layer (so-called top layer) (see Figure 1.3, Chapter 1). Macroporous support provides mechanical support. To minimize the defects of top microporous ceramic membrane and to control overall porosity mesoporous layer is developed on the tubular macroporous supports. The pore opening of the mesoporous membranes (few nm) avoids infiltration of the microporous ceramic into the pores of support, minimizing the effective thickness of the microporous membrane layer.

Important requirements for the development of supported membranes are: (i) thermal stability of macroporous support for the deposition of intermediate mesoporous layer and top microporous layer at higher temperature, (ii) hydrothermal stability of membranes, i.e., stability under humid air at temperature above 300 ºC — similar environment as that of hydrogen production site. In this work the main focus is given to thermal stability of macroporous support rather than hydrothermal stability of membrane layers in order to study the behaviour of polymer-derived ceramics (PDCs) for hydrogen separation to establish a proof-of-concept if PDCs can be applied for hydrogen separation application.

Accordingly, the structure, pore-size characteristics and stability of ceramic support and intermediate layers are described in the sections 4.2 and 4.3. Section 4.4 gives an overview about materials studied as microporous separation layers that are described in detail in the Chapters 5, 6 and 7 (see Table 4.7).

4.2. Macroporous support: structure and stability

Two different types of tubular porous supports were used: (i) as received from Noritake Company Ltd., Japan to deposit ceramic membranes on the outer wall of tubular supports, (ii) the second type used for depositing membranes on the inner wall of the supports provided by Fraunhofer Institute for Ceramic Technologies and Systems (IKTS), Hermsdorf, Germany. The α-Al_2O_3 tubes with a length of 40 mm and internal / outer diameter of 4 / 6 mm (Figure 4.1), provided by Noritake, are used as macroporous supports for the deposition of mesoporous γ-Al_2O_3 intermediate and top gas-separation layers. These supports are fabricated by ceramic extrusion method using α-Al_2O_3 powder with particle size of about 3.5 µm as described elsewhere [1]. The support consists of two layers, Layer A and Layer B, as shown in Figure 4.1(a1–a3). Layer B of thickness of about 50 µm is coated on the outer wall of the base α-Al_2O_3 support (Layer A). The intermediate support layer (Layer B) is made from α-Al_2O_3 particle of average size 300 nm.

The second type of tubular porous supports (provided by IKTS) used have a length of 105 mm and internal / outer diameter of 7 / 10 mm. The base macroporous support is made of α-Al_2O_3. These supports contain five intermediate Al_2O_3 based layers deposited on the inner wall of the supports, as shown in Figure 4.1(b1–b3). The pore size and thickness of the intermediate layers (in the as-received form) for both types of supports used in this work are listed in Table 4.4 and 4.5.

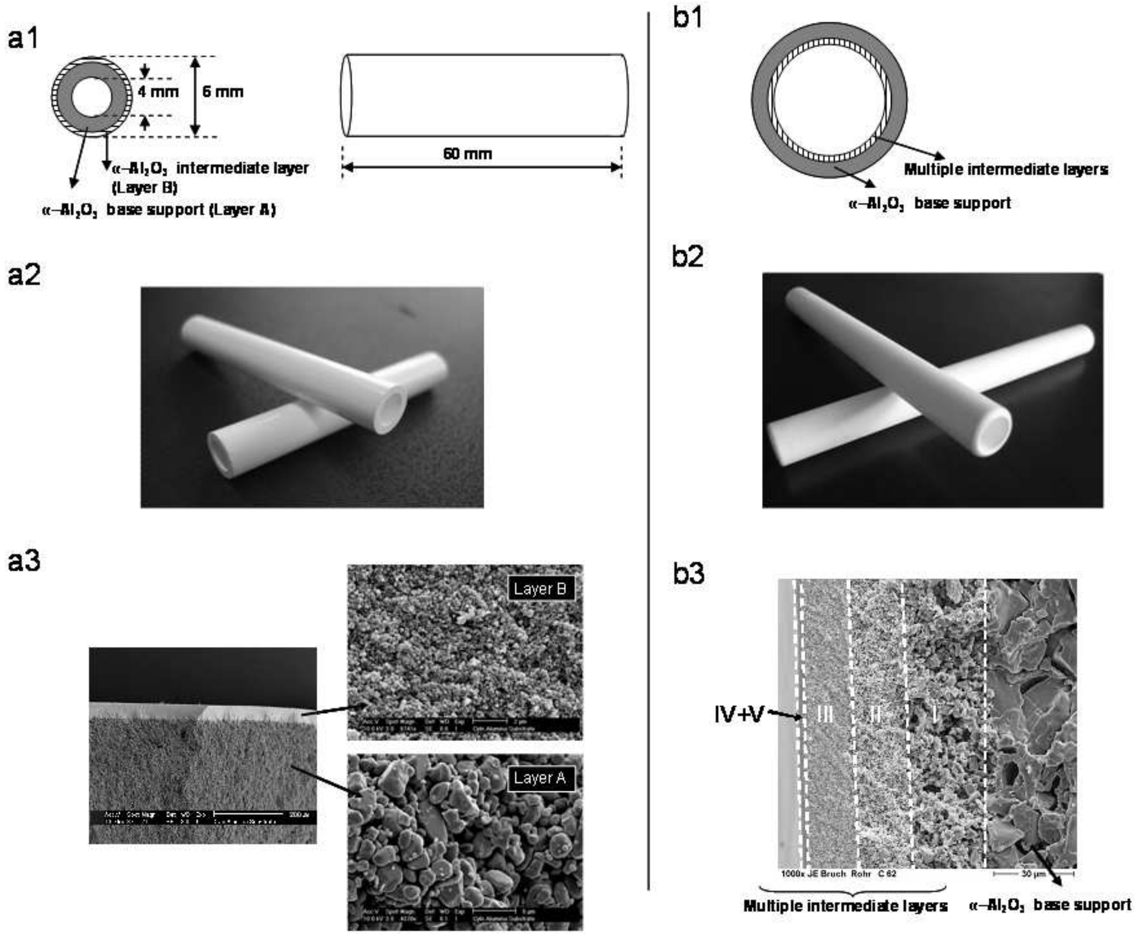

Figure 4.1. (a1, b1) Schematic, (a2, b2) digital, and (a3, b3) microscopic (SEM) images of as-received porous α-Al_2O_3 supports. (a1–a3): provided by Noritake, Japan and (b1–b3): provided by IKTS, Germany.

The thermal stability of tubular macroporous α-Al_2O_3 supports treated under different conditions is evaluated through (i) change in their phase composition (XRD pattern) (Figure 4.2, Table 4.1) and (ii) stability of their pore-size characteristics measured by mercury porosimetry method (Figure 4.3, Table 4.1). The annealing conditions (temperature, gas atmosphere) are selected as being similar to the procedures applied for the deposition of intermediate mesoporous and top microporous layers as well as those applied for the characterization of membrane performance. The above mentioned thermal stability characterizations have been done only for the porous supports provided by Noritake co. in the section 4.2. Deposition of intermediate mesoporous and top gas-separation membranes on the porous supports as received from IKTS has been done based on the thermal stability data range information provided by them.

Here it should be noted that the thermal stability of macroporous porous supports have been evaluated based on the temperature and atmosphere under which intermediate mesoporous layers and top gas-separating microporous ceramic membranes are formed by polymer-derived ceramic routes. Initially the plan was to develop top microporous ceramic membrane only in argon atmosphere. Hence, thermal stability of macroporous support is examined in air and argon atmosphere. The reason for choosing air as medium is related to the deposition of intermediate mesoporous γ-Al_2O_3 layer which is described in section 4.3. The effect on pore-size distribution and phase stability of macroporous support after treatment under ammonia has been described in this chapter but the influence of ammonia treatment on the development of top gas-separating membrane at the membrane/support interface could be recognized only in chapter 6 — related to development of membranes under ammonia. The reasons for selecting different conditions to evaluate thermal stability of macroporous support is listed in Table 4.1.

Table 4.1. Summary of applied treatment conditions to evaluate thermal stability of macroporous α-Al_2O_3 supports provided by Noritake co. Ltd., Japan.

Support	**Annealing temperature (ºC)**	**Gas atmosphere**	**Reason for choosing different treatment conditions**
macroporous α-Al_2O_3 support with intermediate α-Al_2O_3 layer	800	air	Economical to deposit intermediate layer material (γ-Al_2O_3), up to 800 ºC γ-Al_2O_3 retains its phase.
	800	argon	Most PDCs membranes are obtained under argon.
	800	ammonia	Another environment under which PDCs can be obtained (discussed in Chapter 6).
	1100	air	To check if macroporous support can retain thermal stability up to this temperature.

XRD patterns of the α-Al_2O_3 supports treated under various conditions are shown in Figure 4.2. It could be observed that the α-Al_2O_3 supports remain single phase irrespective of their treatments under air/argon/ammonia.

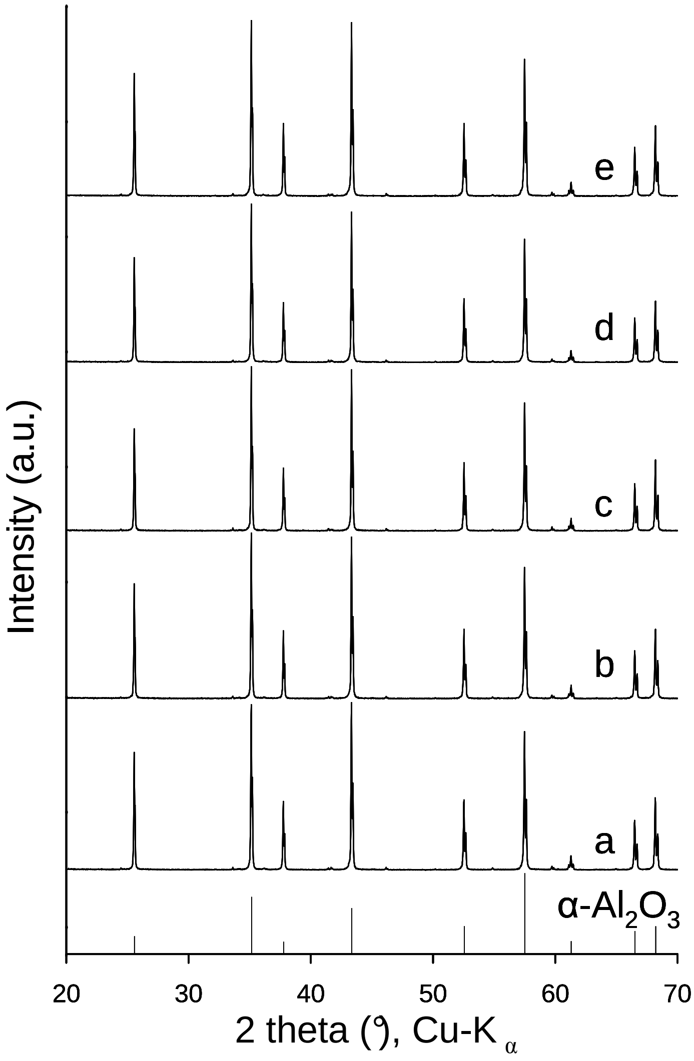

Figure 4.2. XRD patterns of α-Al_2O_3 support: (a) specimen A, as-received, (b) specimen A annealed in air at 800 ºC, (c) specimen A annealed in air at 1100 ºC, (d) specimen A annealed in argon at 800 ºC, and (e) specimen A annealed in ammonia at 800 ºC.

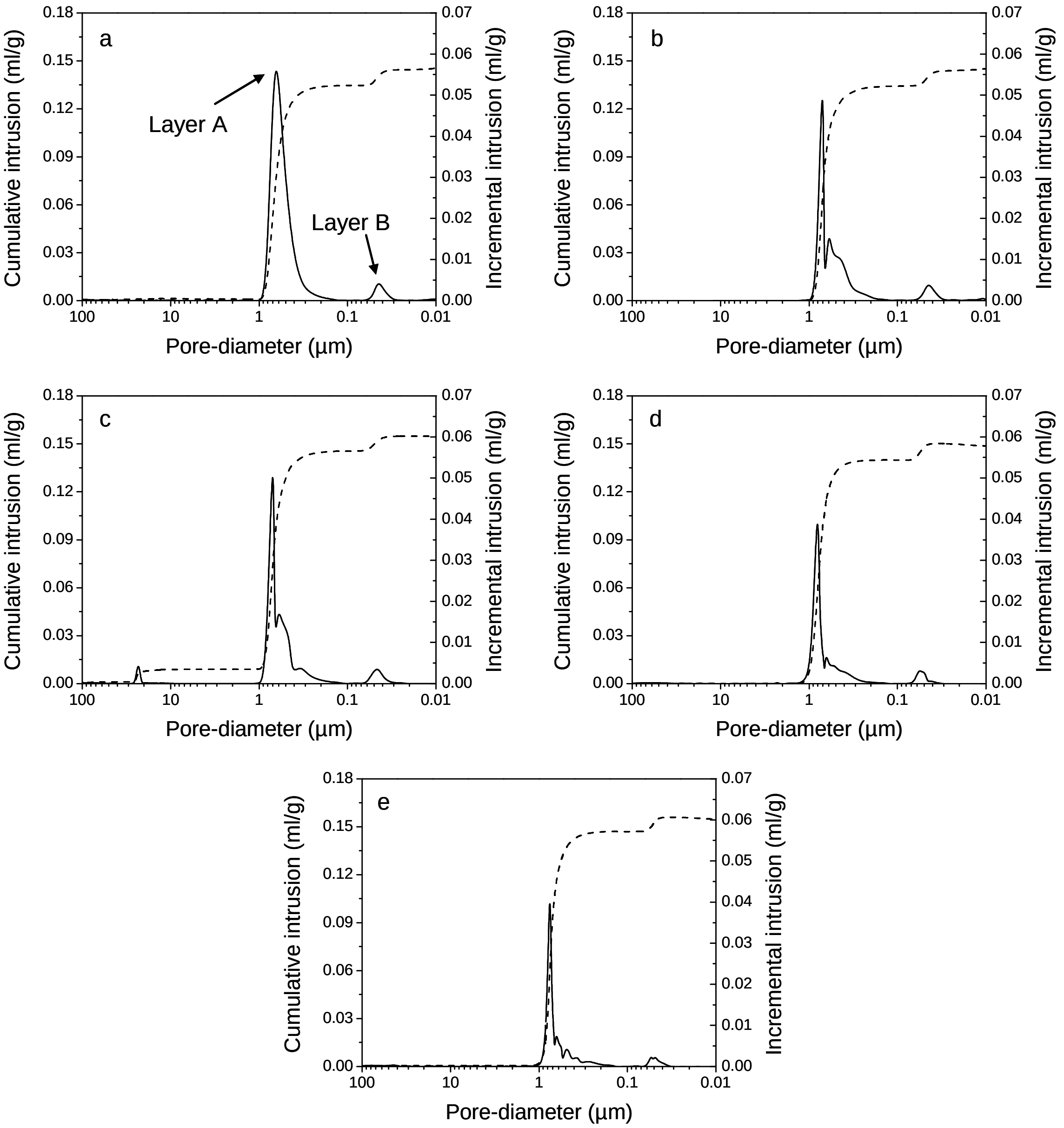

Figure 4.3. Pore-size distribution of α-Al_2O_3 support: (a) specimen A, as-received, (b) specimen A annealed in air at 800 ºC, (c) specimen A annealed in air at 1100 ºC, (d) specimen A annealed in argon at 800 ºC, and (e) specimen A annealed in ammonia at 800 ºC; measured by mercury porositmetry method.

Pore-size distribution shows the as-received α-Al_2O_3 base support (Layer A) has an average pore-size of 0.64 µm and the intermediate α-Al_2O_3 (Layer B) has a mean pore-size of 0.045 µm, as shown in Figure 4.3a. In the condition listed in Table 4.1, the support annealed in air at 800 ºC showed similar pore-size distribution (Figure 4.3b) as that of as-received support, but after annealing as-received support at 1100 ºC new pores of diameter around 23 µm have been developed (Figure 4.3c). Pore-size distribution of the supports which have been annealed under argon and under ammonia at 800 ºC is found to be similar to that of as-received support (Figure 4.3d, Figure 4.3e).

Table 4.2 summarizes the pore-size distribution of porous two-layered α-Al_2O_3 support annealed at different temperatures under air/argon/ammonia. No significant changes in the pore-size distribution are observed for as-received support and the supports treated under different atmospheres at 800 ºC. Hence, α-Al_2O_3 macroporous support could be treated up to 800 ºC for the deposition of intermediate mesoporous γ-Al_2O_3 layer and top microporous membrane layer in air, under argon and under ammonia.

Table 4.2. Phase composition and mean pore size of macroporous two-layered α-Al_2O_3 supports in the as-received form and after annealing at different temperatures under different atmospheres. These supports were provided by Noritake co. Ltd., Japan.

Support	**Annealing temperature (ºC)**	**Gas atmosphere**	**Phase composition**	**Pore size (nm)**
macroporous α-Al_2O_3 support with intermediate α-Al_2O_3 layer	as-received	air	α-Al_2O_3	640 + 45
	800	air	α-Al_2O_3	640 + 45
	800	argon	α-Al_2O_3	640 + 45
	800	ammonia	α-Al_2O_3	640 + 45
	1100	air	α-Al_2O_3	640 + 45 + 23000

4.3. Mesoporous intermediate layer: deposition, structure and stability

Two materials, gamma-alumina (γ-Al_2O_3) and magnesium aluminum spinel ($MgAl_2O_4$), are evaluated for their suitability as intermediate mesoporous layers considering the stability conditions of macroporous support given above in Table 4.1.

4.3.1 Gamma-alumina (γ-Al_2O_3)

Gamma-alumina (γ-Al_2O_3) is synthesized by a typical method of calcining the boehmite (γ-AlOOH) at temperatures between 500 and 800° C. As known, boehmite to γ-alumina transition starts at 450 ºC [2] in accordance with:

$$2\ \gamma\text{-}AlOOH \rightarrow \gamma\text{-}Al_2O_3 + H_2O\uparrow \qquad (4.1)$$

To find the temperature region for obtaining an appropriate mesoporous layer and to examine the phase stability of γ-Al_2O_3, boehmite colloidal dispersion (4 wt. % in H_2O) is dried at 100 ºC in air with subsequent thermal treatment at four different temperatures, i.e. 500, 800, 1000 and 1200 ºC in air. Air is chosen for evaluating pore size of γ-Al_2O_3 as a function of temperature because it is easy to handle boehmite in air rather than in argon as well as to save argon gas. As already mentioned that most polymer-derived ceramics are synthesized by the pyrolysis of polymer-precursor under argon, hence, thermal stability evaluation of mesoporous γ-Al_2O_3 obtained by calcination is carried out under argon. The treatment of calcined γ-Al_2O_3 under argon is done based on the phase stability range of α-Al_2O_3 (Table 4.1).

Figure 4.4 shows the XRD patterns of the five alumina samples which are derived from boehmite sol under different conditions. At 800 ºC broad diffraction peaks corresponding to γ-Al_2O_3 appear in the diffraction pattern (Figure 4.4b). As known, the γ-Al_2O_3 phase is not stable above 800 ºC undergoing phase transition into more stable theta-/delta-/alpha-alumina phases [2-3]. In our case boehmite calcined at 1000 ºC transforms to delta-alumina (Figure 4.4c) which transforms into alpha-alumina after treatment at 1200 ºC (Figure 4.4d). No phase change could be observed for γ-Al_2O_3 (which is obtained after calcination in air at 800 ºC) annealed under argon at 800 ºC (Figure 4.4e).

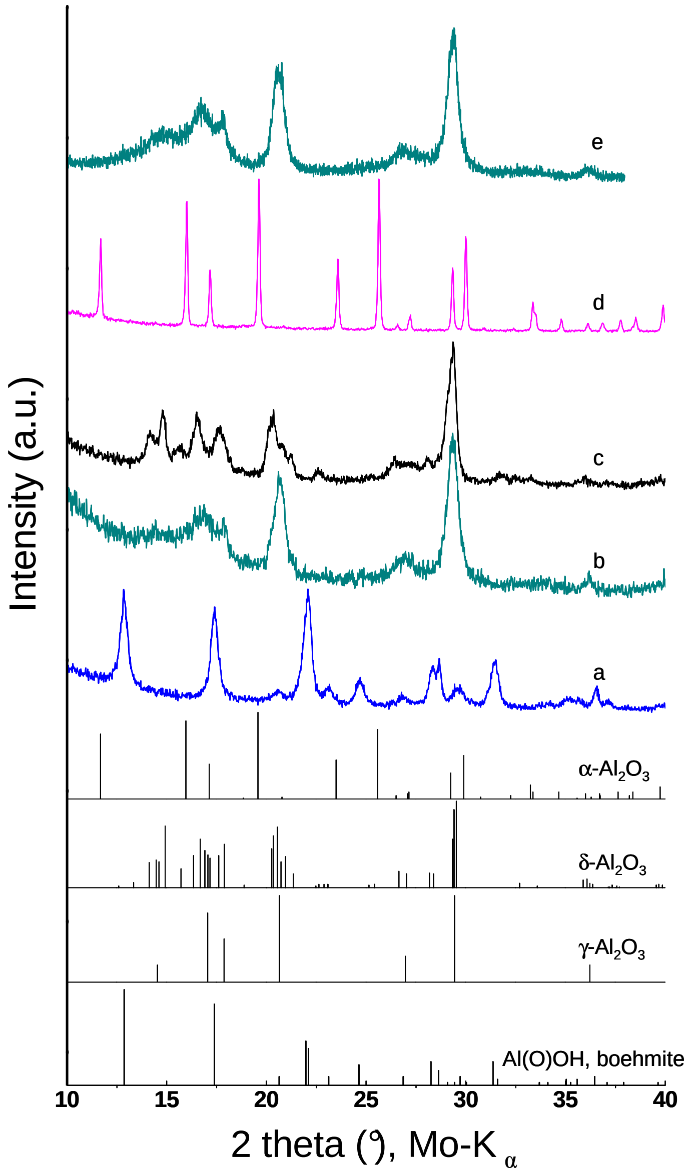

Figure 4.4. XRD of boehmite derived powders (a) specimen A, dried at 100 ºC, boehmite, (b) specimen B – specimen A calcined at 800 ºC, γ-Al_2O_3, (c) specimen A calcined at 1000 ºC, δ-Al_2O_3, (d) specimen A calcined at 1200 ºC, α-Al_2O_3, and (e) specimen B annealed under argon at 800 ºC.

Pore-size distribution and BET specific surface area of alumina samples obtained as described above are shown in Figure 4.5 and summarized in Table 4.3. As the calcination temperature is increased surface area of γ-Al_2O_3 decreased with an increase in mean pore-size. The sample which is calcined at 800 ºC has a surface area of 144 m^2 g^{-1} and mean pore diameter of about 8 nm. During exposure to high temperatures (> 800 ºC), a large loss of surface-area occurs with changes in pore structure to accommodate complete densification. The sample retains mesoporous structure at 1000 ºC but with a phase transformation from γ- to δ- Al_2O_3. The transition to α-alumina at 1200 ºC is accompanied by a large loss of specific surface area and with the complete loss of mesoporous structure. The obtained γ-Al_2O_3 at 800 ºC in air after annealing under argon maintain pore size of about 8 nm with a small decrease in surface area.

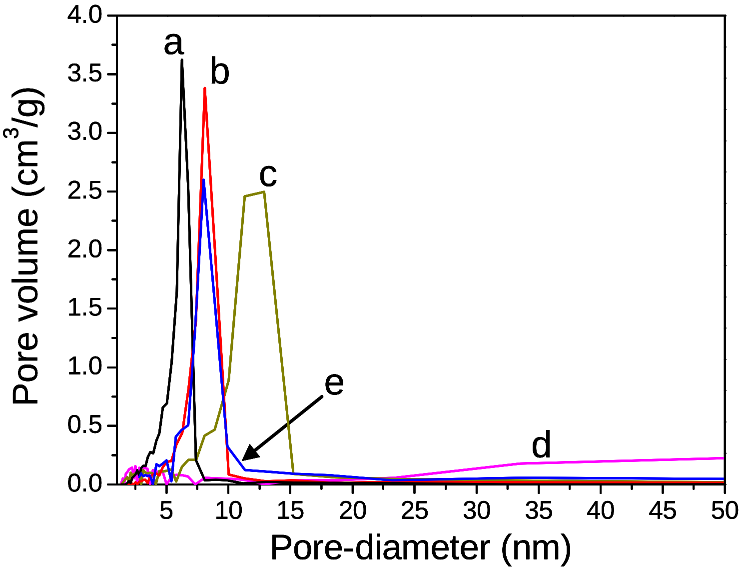

Figure 4.5. Pore-size distribution of γ-Al_2O_3 which are derived from boehmite sol after calcinations at (a) 500 ºC, (b) specimen A, 800 ºC, (c) 1000 ºC, (d) 1200 ºC, and (e) specimen A annealed under argon at 800 ºC.

Table 4.3. Microstructural characteristics of unsupported alumina membranes which are derived from boehmite sol as a function of calcination temperature and γ-Al_2O_3 (obtained at 800 ºC in air) annealed under argon at 800 ºC.

Temperature (ºC)	**Phase**	**Mean pore size (nm)**	**BET surface area (m^2 g^{-1})**
500, in air	γ-Al_2O_3	6	220
800, in air	γ -Al_2O_3	8	144
1000, in air	δ-Al_2O_3	11-13	109
1200, in air	α-Al_2O_3	-	30
800, in argon	γ-Al_2O_3	8	135

Accordingly, conditions were chosen for the deposition of intermediate mesoporous γ-Al_2O_3 layer on macroporous tubular α-Al_2O_3 supports (section 4.2) by dipping them in the boehmite colloidal dispersion with subsequent calcination at 800 °C for 2 h. The reasons for performing calcination (instead of thermolysis under argon) to deposit mesoporous γ-Al_2O_3 layer on macroporous α-Al_2O_3 support at 800 °C are: (i) γ-Al_2O_3 obtained after calcination at 800 °C retains its mesoporous nature even after annealing under argon 800 °C (from Table 4.3), (ii) the thermal stability range of macroporous support (Table 4.2) allows the support to be used in air as well as under argon at 800 °C, and (iii) it is more economical to develop mesoporous membrane on macroporous support in air rather than under argon. The support functionalized in this way shows formation of mesoporous γ-Al_2O_3 layer with thickness of about 1 µm (Figure 4.6) after single-fold coating and calcination step at 800 °C.

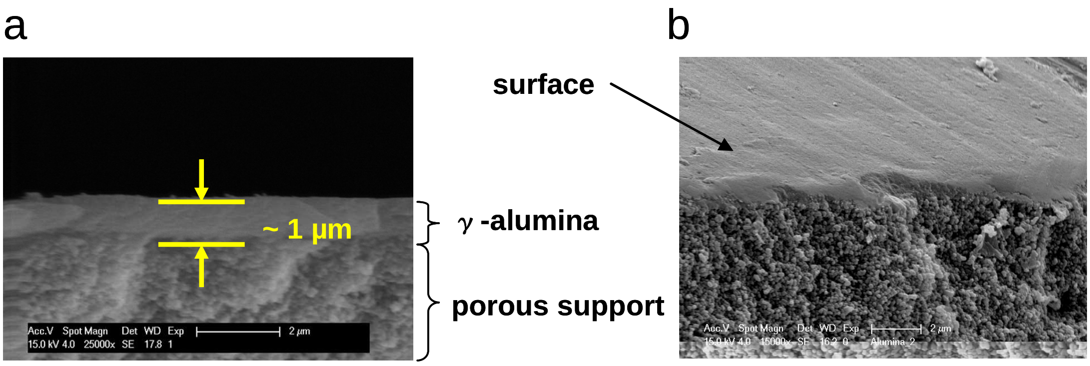

Figure 4.6. SEM images of γ-Al_2O_3 coated α-Al_2O_3 support (a) cross-sectional view, (b) surface of coated support after single-fold coating and calcination at 800 °C.

Porous layers characteristics (layer thickness, pore type and pore volume) of single-fold coated γ-Al_2O_3 layer on α-Al_2O_3 macroporous support are summarized in Table 4.4. The data for α-Al_2O_3 is taken from the section 4.2. These γ-Al_2O_3/α-Al_2O_3 composite multilayered membrane supports were selected for the deposition of top gas-separation membranes. The porous layer data of the supports received from IKTS, Germany is listed in Table 4.5.

Table 4.4. Thickness, pore type, pore diameter and pore volume data of different layers in γ-Al_2O_3/α-Al_2O_3 multilayer membranes (support provided by Noritake co. Ltd., Japan).

Porous layer	**Layer thickness**	**Pore diameter (nm)**	**Pore type**	**Pore volume (ml/g)**
α-Al_2O_3 (support)	1 mm [a] ; 50 µm [b]	640 [a]; 45[b]	macro-	16.31[c]
Intermediate γ-Al_2O_3 layer	1 µm	8	meso-	0.44

[a] support; [b] outer α-Al_2O_3 layer [c] measured by mercury-porosimetry, section 4.2

Table 4.5. Thickness, pore type, and pore diameter data of different layers in γ-Al_2O_3/α-Al_2O_3 multilayer membranes (support provided from IKTS, Germany), based on the data received from the IKTS.

Porous layer[a]	**Layer thickness**	**Pore diameter (nm)**	**Pore type**
α-Al_2O_3	2 mm	30000	macro-
Intermediate α-Al_2O_3 layer: I	12-15 µm	800	macro-
Intermediate α-Al_2O_3 layer: II	12-15 µm	200	macro-
Intermediate α-Al_2O_3 layer: III	12-15 µm	70	macro-
Intermediate γ-Al_2O_3 layer: IV/V	1.8-2 µm	5	meso-

[a] Figure 4.1b3

Although γ-Al_2O_3 membranes exhibit well defined pore sizes, its chemical and thermal stabilities are limited. Long time use at elevated temperature can cause phase transformation of γ-Al_2O_3 to δ-/α-Al_2O_3, which degrades the membrane performance. Therefore, applications of γ-Al_2O_3 membranes as an intermediate mesoporous layer at high temperatures are limited. The obtained γ-Al_2O_3 membranes could be used in both atmospheres in air and argon up to 800 °C.

4.3.2 Magnesium aluminum spinel ($MgAl_2O_4$)

Spinel, $MgAl_2O_4$, shows no phase transformation up to its melting point of 2135 °C and hence slow rate of particle growth is expected in this material. $MgAl_2O_4$ spinel also exhibits high thermochemical stability.

Therefore, we have synthesized the magnesium aluminium spinel via the sol-gel route using magnesium aluminium isopropoxide ($MgAl_2(^iPrO)_8$) according to the procedure reported in reference [4].The stable $MgAl_2O_4$ sol is obtained by hydrolysis of Mg/Al alkoxide, followed by peptization, is dried and calcination is done at different temperatures (equation 4.2):

$$MgAl_2(^iPrO)_8 \xrightarrow{H_2O} MgAl_2(OH)_8 \xrightarrow{H^+,\text{peptization}} \begin{array}{c}\text{Colloidal}\\ \text{suspension}\end{array} \xrightarrow{\text{Calcination}} MgAl_2O_4 \qquad (4.2)$$

The XRD patterns of the powders calcined at 800 and 1000 °C confirm the formation of $MgAl_2O_4$ spinel (Figure 4.7).

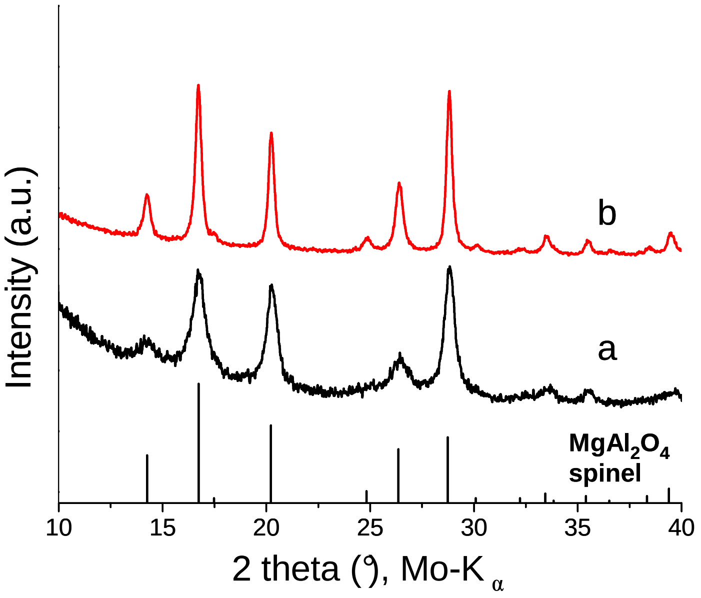

Figure 4.7. XRD patterns of powders obtained by hydrolysis of $MgAl_2(^iPrO)_8$ followed by calcination (1) at 800 °C, $MgAl_2O_4$ spinel, (2) at 1000 °C, $MgAl_2O_4$ spinel.

Pore-size distribution and BET specific surface area of the alkoxide derived $MgAl_2O_4$ spinel are shown in Figure 4.8 and summarized in Table 4.6. These results show that the spinel which is obtained at 800 ºC is mesoporous with a pore size of about 7.3 nm. The pore-size of the spinel obtained at 1000 ºC is found to be of 13.6 nm, where as the spinel powder after calcination at 1200 ºC shows very broad range of mesopores. In contrast to the mesoporous γ-Al_2O_3, which is synthesized by calcination at 1000 ºC, the $MgAl_2O_4$ spinel shows relatively more uniform distribution of mesopores (see Figure 4.5 and Figure 4.8). An interesting result is found for the spinel obtained at 1200 ºC. At this temperature $MgAl_2O_4$ spinel remains mesoporous with a broad distribution of pores, where as boehmite derived alumina completely loses its mesoporous nature.

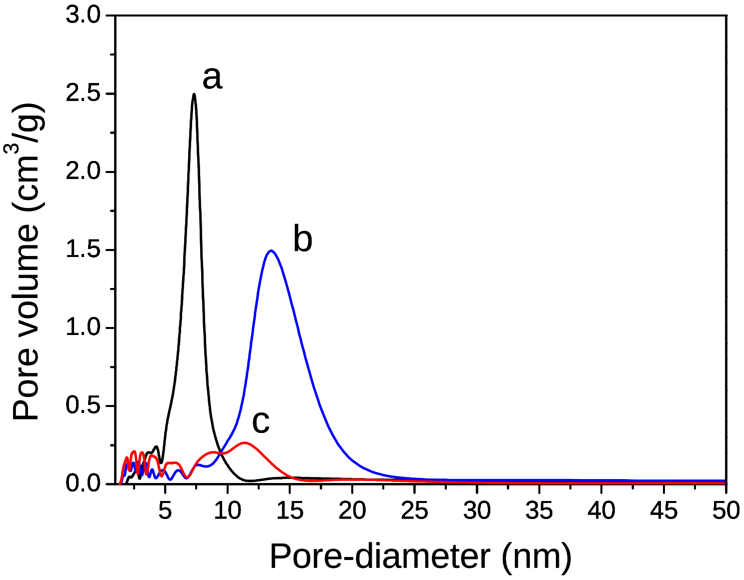

Figure 4.8. Pore-size distribution of $MgAl_2O_4$ spinel which is obtained by hydrolysis of $MgAl_2(^iPrO)_8$ followed by calcination at (a) 800 ºC, (b) 1000 ºC, and (c) 1200 ºC.

Table 4.6. Pore-size distribution and BET surface are of unsupported $MgAl_2O_4$ spinel membrane as a function of calcination temperature.

Temperature (ºC)	**Mean pore size (nm)**	**BET surface area ($m^2\ g^{-1}$)**
800	7.3	155
1000	13.6	118
1200	broad distribution of mesopores	35

Based on the results obtained for mesoporous $MgAl_2O_4$ spinel we can conclude that $MgAl_2O_4$ appears to be a promising candidate which can be applied as an intermediate mesoporous layer. The possibility to use mesoporous $MgAl_2O_4$ spinel as an intermediate mesoporous membrane layer needs to be further explored which has not been carried out in this work.

4.4. Polymer-derived microporous top coating

Microporous membranes have been synthesised using different polymers with different pyrolysis conditions under different atmospheres which are listed in Table 4.7. Various types of commercially available polysilazane have been used in as-received form and with some modification to get top-layer microporous membranes. Structural characteristics of pre-ceramic precursors and pore-size characteristics of different microporous ceramics which are obtained after pyrolysis of the polymers and their performances with respect to H_2/CO or H_2/CO_2 selectivity and their integration with gas sensors are described in Chapter 5 and Chapter 6.

Table 4.7. List of precursors and the corresponding ceramics obtained under different pyrolysis/annealing atmospheres in this thesis work.

Precursor	**Pyrolysis/annealing atmosphere**	**ceramic**
Polyborosilazanes	argon	SiBCN[a]
Polysilazane (KiON HTT 1800)	argon	SiCN[b]
Polysilazane (KiON HTT 1800)	ammonia	Si_3N_4[b]
Polysilylcarbodiimide	argon	SiCN[c]

[a] Chapter 5, [b] Chapter 6, [c] Chapter 7.

γ-Al_2O_3/α-Al_2O_3 composite membrane support was obtained by dip-coating of α-Al_2O_3 tubular support in boehmite colloidal dispersion followed by calcination at 800 °C. The thickness of the single time coated γ-Al_2O_3 intermediate layer was about 1 µm with pore-size distribution at around 8 nm. This type of multilayered composite supports was found to be thermally stable under air and argon up to 800 °C. Above 800 °C γ-Al_2O_3 phase changed to δ-Al_2O_3. Hence, the application of γ-Al_2O_3/α-Al_2O_3 was limited up to 800 °C for coating with microporous membrane layers.

4.5. References

[1] Y. Yoshino, T. Suzuki, B.N. Nair, H. Taguchi, N. Itoh, "Development of tubular substrates, silica based membranes and membrane modules for hydrogen separation at high temperature," *Journal of Membrane Science*, 267 (2005) 8-17.

[2] R.K. Iler, "Fibrillar colloidal boehmite - Progressive conversion to gamma, theta, and alpha aluminas," *Journal of the American Ceramic Society*, 44 (1961) 618-624.

[3] C.E. Warble, "Surface-structure of spherical gamma-alumina," *Journal of Materials Science*, 20 (1985) 2512-2516.

[4] K.B. Pflanz, R. Riedel, H. Chmiel, "Preparation of spinel ultrafiltration membranes," *Advanced Materials*, 4 (1992) 662-665.

Chapter 5. Hydrogen separation in microporous SiBCN membranes

The SiBCN ceramics, which are thermally stable up to 1700 °C and also exhibit excellent oxidation resistance [1], are obtained by the pyrolysis of polyborosilazanes. The structure of resulting polymers (polyborosilazanes) after hydroboration reaction of cyclosilazanes are studied by solid-state magic-angle spinning (MAS) NMR spectroscopy and Attenuated total reflection infrared (ATR-IR) spectroscopy which are described in section 5.1. Polymer-to-ceramic transformation, structural characterizations and porosity analysis of the SiBCN ceramics are illustrated in sections 5.2-5.5. The performances of SiBCN ceramic membranes — obtained by dip-coating of preceramic polyborosilazane solution on porous alumina support and on SnO_2 based gas sensor support followed by pyrolysis under inert atmosphere — have been studied with respect to H_2/CO selectivity and as a protection coating for SnO_2 based gas sensors against reduction in harsh reducing atmosphere are described in sections 5.6-5.7.

5.1. Synthesis of cyclic polyborosilazanes

The synthesis of the pre-ceramic polymers, i.e. polyborosilazanes, is performed through hydroboration of 1,3,5-trivinyl-1,3,5-trimethyl-cyclosilazane (**tricyclosilazane** hereafter) and 1,3,5,7-tetravinyl-1,3,5,7-tetramethyl-cyclosilazane (**tetracyclosilazane** hereafter) using borane dimethylsulphide (Figure 5.1) according to the procedure applied by Hauser et al [2]. From here onwards the synthesized polymers which are obtained by hydroboration of tricyclosilazane and tetracyclosilazane are denoted as **polyborotrisilazane** and **polyborotetrasilazane**, respectively.

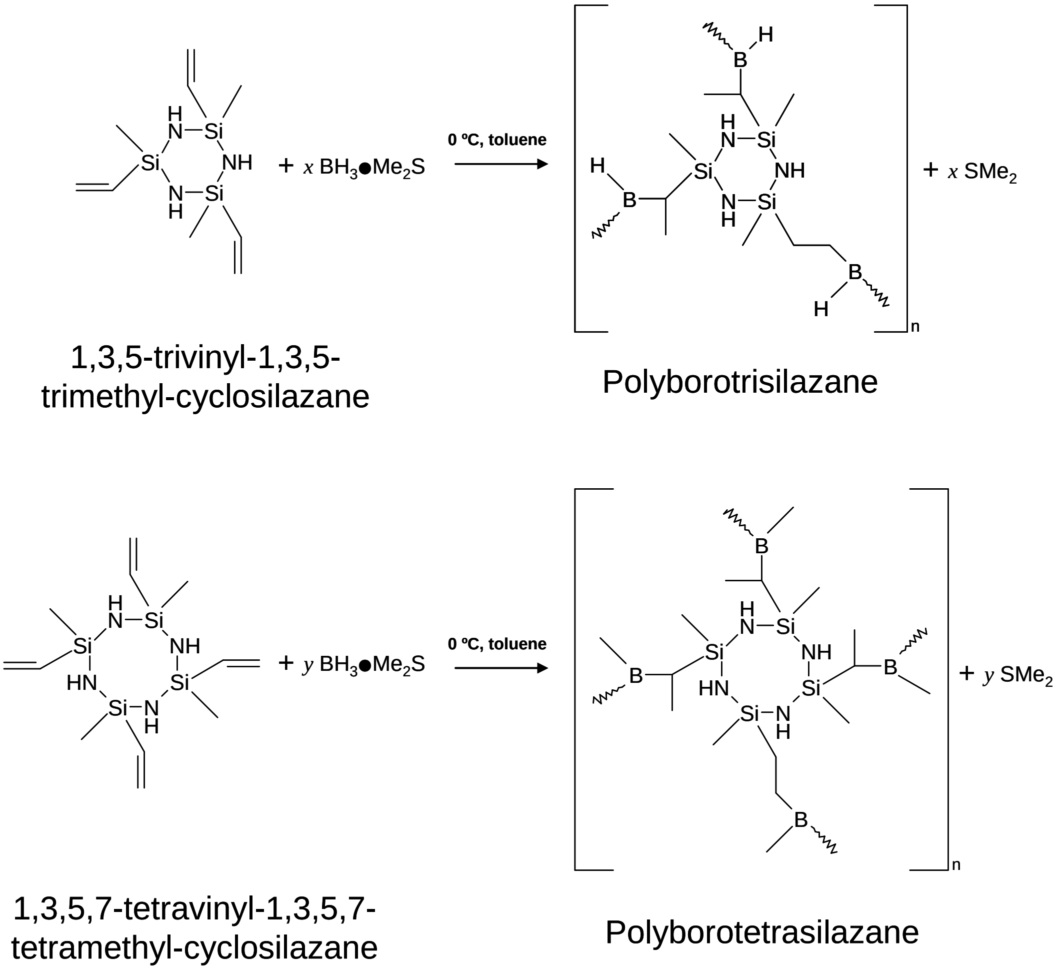

(5.1)

(5.2)

Figure 5.1. Idealized structure of as-synthesized polymers: (a) polyborotrisilazane and (b) polyborotetrasilazane, obtained by hydroboration of 1,3,5-trivinyl-1,3,5-trimethyl-cyclosilazane and 1,3,5,7-tetravinyl-1,3,5,7-tetramethyl-cyclosilazane, respectively. Structure of starting monomers 1,3,5-trivinyl-1,3,5-trimethyl-cyclosilazane and 1,3,5,7-tetravinyl-1,3,5,7-tetramethyl-cyclosilazane are drawn from information as provided by the supplier (ABCR chemicals).

The above Scheme (5.1 and 5.2) shows the expected molecular structures of polymers after hydroboration. The structures of the as-synthesized polyborosilazanes are studied by solid-state MAS NMR and ATR-IR measurements which are described in section 5.2.

One of the main limitations of synthesized polyborosilazanes is their rheological stability at room temperature. The borane adduct (borane dimethylsulphide) provides a source of B and also induces polymerization. Vinyl functional groups of tricyclosilazane and tetracyclosilazane react with borane dimethylsulphide resulting in the cross-linking which leads to gelation. Gel formation is not observed by mixing borane dimethylsulphide and respective monomers at 0 °C. Only after keeping the synthesized polymers at room temperature for more than 30 minutes causes gelation in the polymeric solution (Figure 5.2). This gelation creates problems while coating the polymer on porous supports or on sensors to obtain microporous layers. In order to perform successful dip-coating to deposit microporous membranes, polymeric solutions after hydroboration reactions are preserved as in solution form in a deep freezer maintaining temperature of about -50°C.

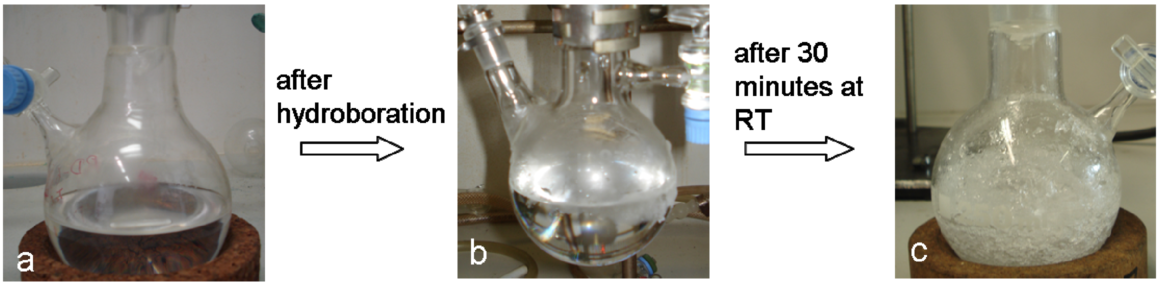

Figure 5.2. View of the reaction systems at different processing stages: (a) 1,3,5-trivinyl-1,3,5-trimethyl-cyclosilazane, (b) polyborotrisilazane after hydroboration reaction, and (c) after gelation.

5.2. Structure of cyclic polyborosilazanes

As discussed above, as-synthesized polyborosilazanes are not stable as solution at room temperature forming gels. These gels are not soluble in C_6D_6, a typical solvent applied for performing liquid state NMR measurements. Therefore, the structures of polymers are studied by solid-state NMR and ATR-IR spectroscopy.

5.2.1 Solid-state MAS NMR characterization

The synthesized polymers, polyborotrisilazane and polyborotetrasilazane, are analyzed by ^{29}Si CP-, ^{13}C CP- and ^{11}B solid-state MAS NMR measurements.

Cross-polarization (CP) ^{29}Si {^{1}H} NMR

The ^{29}Si spectra of boron-modified cyclosilazanes are shown in Figure 5.3 and listed in Table 5.1. In agreement with the references number [3-4], the spectra are dominated by peaks at -3 ppm related to [*Si*(CH$_3$)(CHBCH$_3$)NH] sites produced by the hydroboration and to [*Si*(CH$_3$)(CH=CH$_2$)NH] silicon sites in intact silazane ring (-18 to -20 ppm) mainly in polyborotetrasilazane. In polyborotetrasilazane, the [*Si*(CH$_3$)(CHBCH$_3$)NH] site is shifted to slightly lower ppm (about -7 ppm) values as compared to the polyborotrisilazane [4], most likely because of the less constrained ring structure.

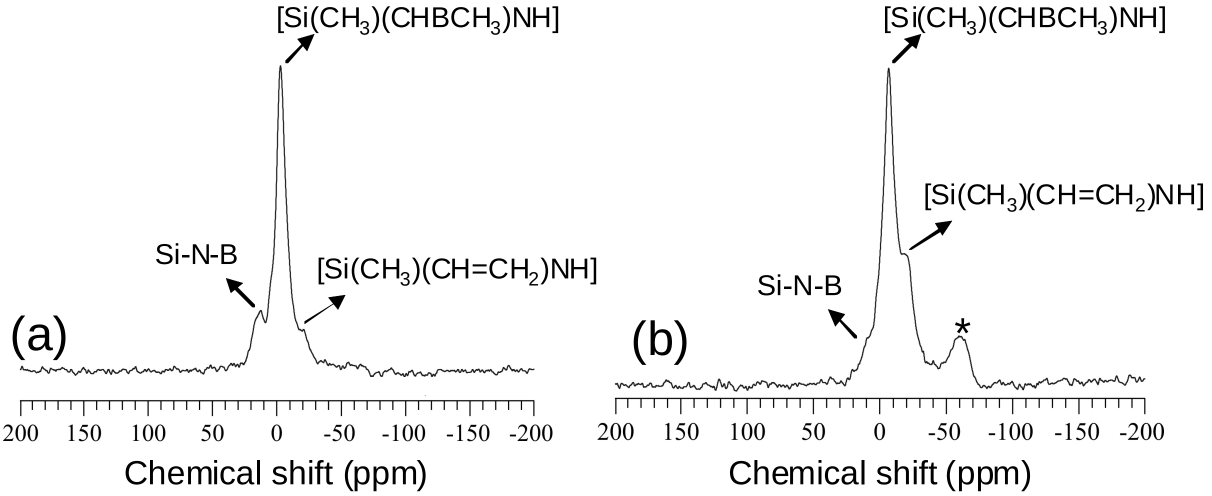

Figure 5.3. ^{29}Si{^{1}H} cp spectra of as-synthesized polymers: (a) polyborotrisilazane and (b) polyborotetrasilazane. * - unidentified peak(s).

As the spectra have been acquired using the cross polarization technique, it is not possible to quantify the relative amounts of [*Si*(CH$_3$)(CHBCH$_3$)NH]/[*Si*(CH$_3$)(CH=CH$_2$)NH] sites. The formation of higher percentage of boron-substituted groups is particularly pronounced in the case of polyborotrisilazane (see Figure 5.3a) where the intensity of unreacted [*Si*(CH$_3$)(CH=CH$_2$)NH] sites is very low.

Besides the expected main peaks, other extra signals are identified. In polyborotrisilazane, the presence of a third peak at about 12 ppm suggests the formation of B-N bonds with the silazane ring [4]. Probably, the same peak can be identified also in the polyborotetrasilazane but in this case as a weak shoulder. The ^{29}Si NMR spectrum of the polyborotetrasilazane polymer possesses an extra signal at -60 ppm, which could not be assigned yet.

Table 5.1. Experimental ^{29}Si chemical shifts of polyborotrisilazane and polyborotetrasilazane polymers.

Polymer	**^{29}Si chemical shifts (ppm)**			
	Si-N-B	[Si(CH$_3$)(CHBCH$_3$)NH]	[Si(CH$_3$)(CH=CH$_2$)NH]	?*
polyborotrisilazane	12.4	-2.8	-20.8	-
polyborotetrasilazane	shoulder	-6.7	-18.3	-61.0

* - unidentified peak(s)

CP ^{13}C {^{1}H} NMR

In agreement with reference number [4], in the respective ^{13}C spectra (Figure 5.4) we can identify the signals corresponding to methyl and methylene groups attached to silicon (Si-CH_3/CH_2, 1.9 ppm), unreacted vinyl groups (CH_2=CH_2, 128–129 ppm) with very low intensity peak and methylene groups bonded to B (CH_2-B, 10–12 ppm) formed by hydroboration reaction.

Besides the aforementioned expected signals (Table 5.2), five more ^{13}C signals are present in case of both polymers — polyborotrisilazane and polyborotetrasilazane. To exclude completely the possibility of spinning side bands, the spectra have been acquired at a different spinning speed (8 kHz) confirming the presence of extra signals. The signals at 7, 18 and 22 ppm could be related to ~CH_2-CH_2~ segments, formed for example by the polymerization of vinyl groups [3]. Chemical shifts at 40–60 ppm are generally indicative of sp^3-C bonded to heteroatoms, like for example N or O; while the chemical shifts in the range of 150–170 ppm are attributed to resonate sp^2-C double bonded to heteroatoms.

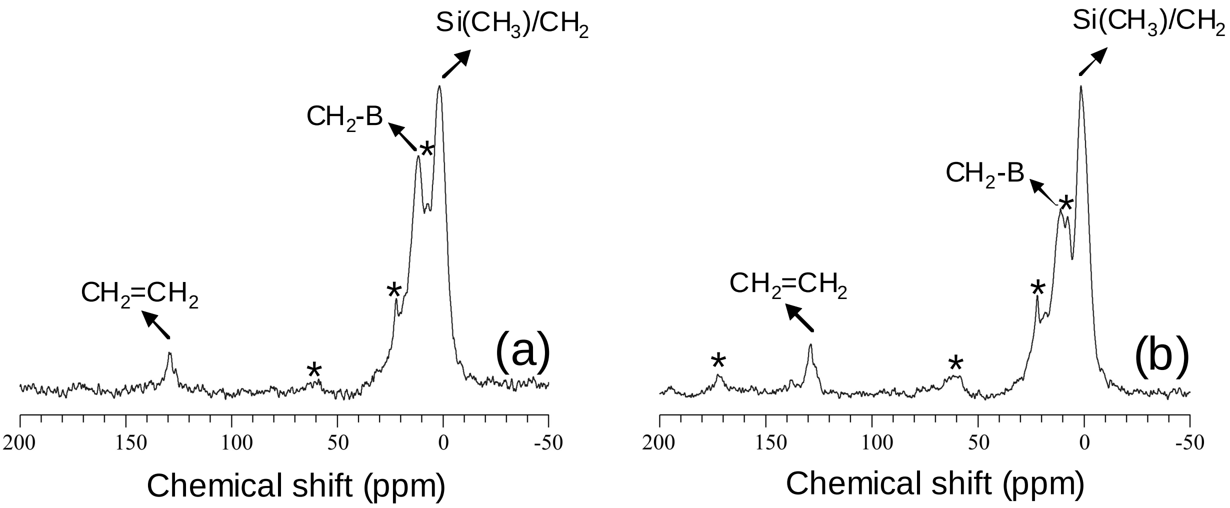

Figure 5.4. $^{13}C\{^1H\}$ cp spectra of as-synthesized polymers: (a) polyborotrisilazane and (b) polyborotetrasilazane.

Table 5.2. Experimental ^{13}C chemical shifts of polyborotrisilazane and polybrotetrasilazane polymers.

Polymer	**^{13}C chemical shifts (ppm)**							
	Si-CH_3/CH_2	?*	CH_2-B	?*	?*	?*	CH_2=CH_2	?*
polyborotrisilazane	1.7	7.0	11.7	weak	22.1	60.8	129.5	
polyborotetrasilazane	1.4	7.7	11.1	18.3	22.0	60.0	128.6	172.6

* - unidentified peak(s)

Single pulse ^{11}B NMR

The ^{11}B single pulse spectra of polyborotrisilazane and polyborotetrasilazane (Figure 5.5) have very similar features. Because of the residual quadrupolar coupling constant of ^{11}B, the spectra are appeared broad. A complete resolution of the spectra could be achieved only by operating at higher magnetic field, i.e. 14T. The broad resonance results most likely from the overlapping of at least three resonance signals: one sharp single line centred at -0.5 ppm and other two broader lines ranging from about -30 to +30 ppm and -10 to + 10 ppm, respectively. The sharp signal is indicative of ^{11}B sites in a tetragonal BX_4 configuration.

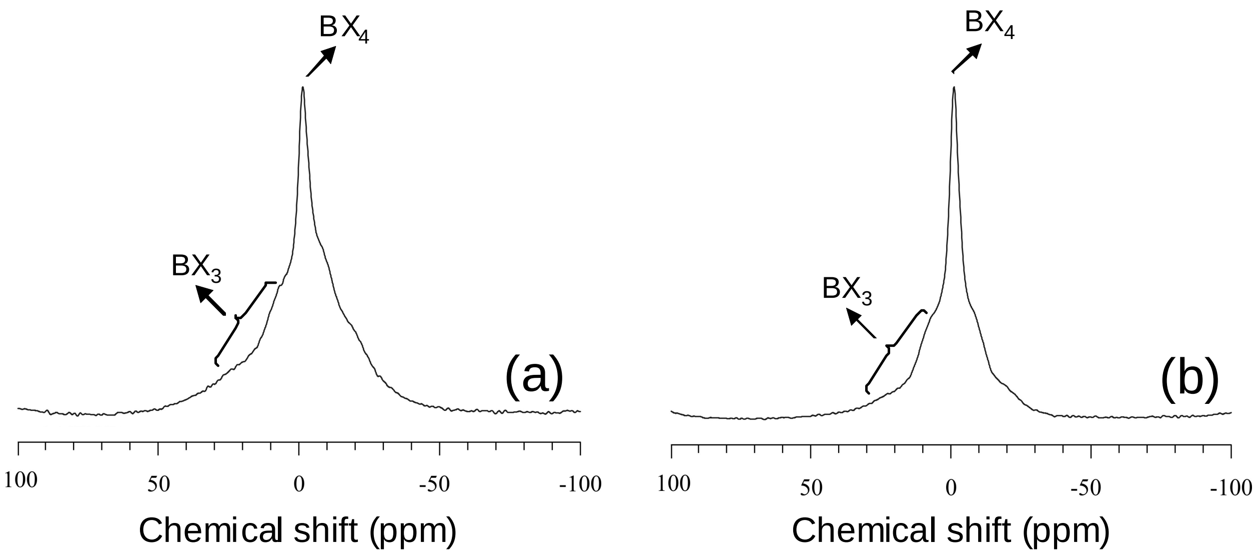

Figure 5.5. $^{11}B\{^{1}H\}$ spectra of polymers: (a) polyborotrisilazane and (b) polyborotetrasilazane.

Though the two broad lines are overlapped, the typical line shape due to the second order quadrupolar coupling can be seen through. The high field shifted shoulder of the main peak indicates the presence of trigonal BX_3 sites. Moreover, the components are characterized by different widths suggesting the presence of trigonal sites in different BC_xN_y environments. The experimental ^{11}B NMR spectra of polymers reflect a large heterogeneity in the local environment of the boron nuclei. In general, this holds for both — trigonal and tetragonal — coordination number [1].

5.2.2 ATR-IR characterization

Figure 5.6 shows ATR-IR spectra of as-synthesized polyborotrisilazane and polyborotetrasilazane polymers. Vibration bands of N-H are observed at 3398/1146 and 3387/1158 cm^{-1} [6] for polyborotrisilazane and polyborotetrasilazane, respectively. Bands at about 2900 cm^{-1} are assigned to aliphatic C-H stretching and those at about 1590 cm^{-1} is associated to C=C stretching [7], which indicates vinyl polymerization is not completed after hydroboration. However, intensity of the bands at 1590 cm^{-1} are very low indicating very low amount of C=C groups after hydroboration polymerization. Nevertheless, no absorption band at 3020–3100 cm^{-1}, which could be assigned to residual vinyl groups, is detected. The absorption band at 2360 cm^{-1} confirms the presence of B-H bonds in the synthesized polymers [2]. In Table 5.3, the vibration bands and respective bonds are listed.

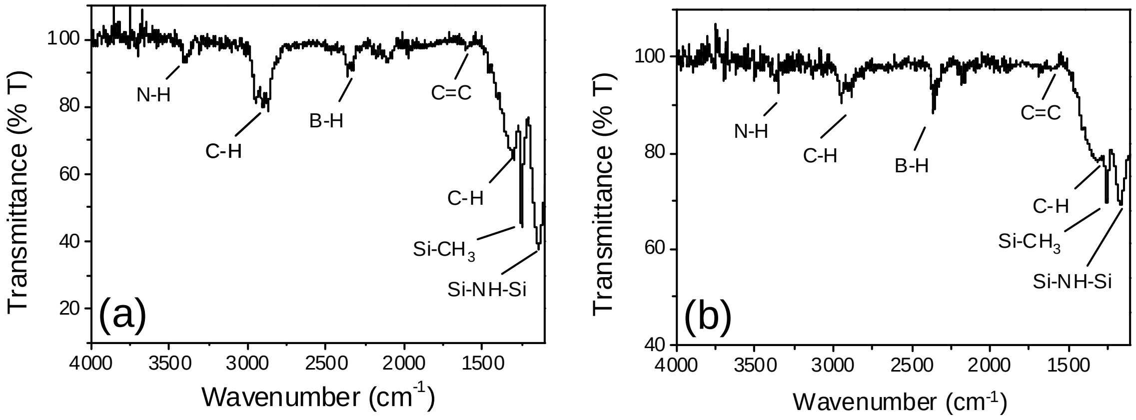

Figure 5.6. ATR-IR spectra of as-synthesized polymers: (a) polyborotrisilazane and (b) polyborotetrasilazane.

Table 5.3. Vibration bands and respective bonds of polyborotrisilazane and polyborotetrasilazane polymers measured by ATR-IR measurement.

Vibration band (cm^{-1}) of polymers		**Bond assignments[a]**
polyborotrisilazane	**polyborotetrasilazane**	
3398	3387	ν(N-H)
2948–2865	2948–2884	ν(C-H)
2360	2357	ν(B-H)
1590	1593	ν(C=C)
1308	1308	δ(C-H)
1250	1254	δ(Si-CH$_3$)
1146	1158	δ(N-H)

[a] ν – stretching, δ – deformation.

Based on the results of solid-state NMR and ATR-IR characterizations, the structure of the resulting polymeric networks of polyborotrisilazane and polyborotetrasilazane could be represented as shown in the Figure 5.7a and Figure 5.7b, respectively.

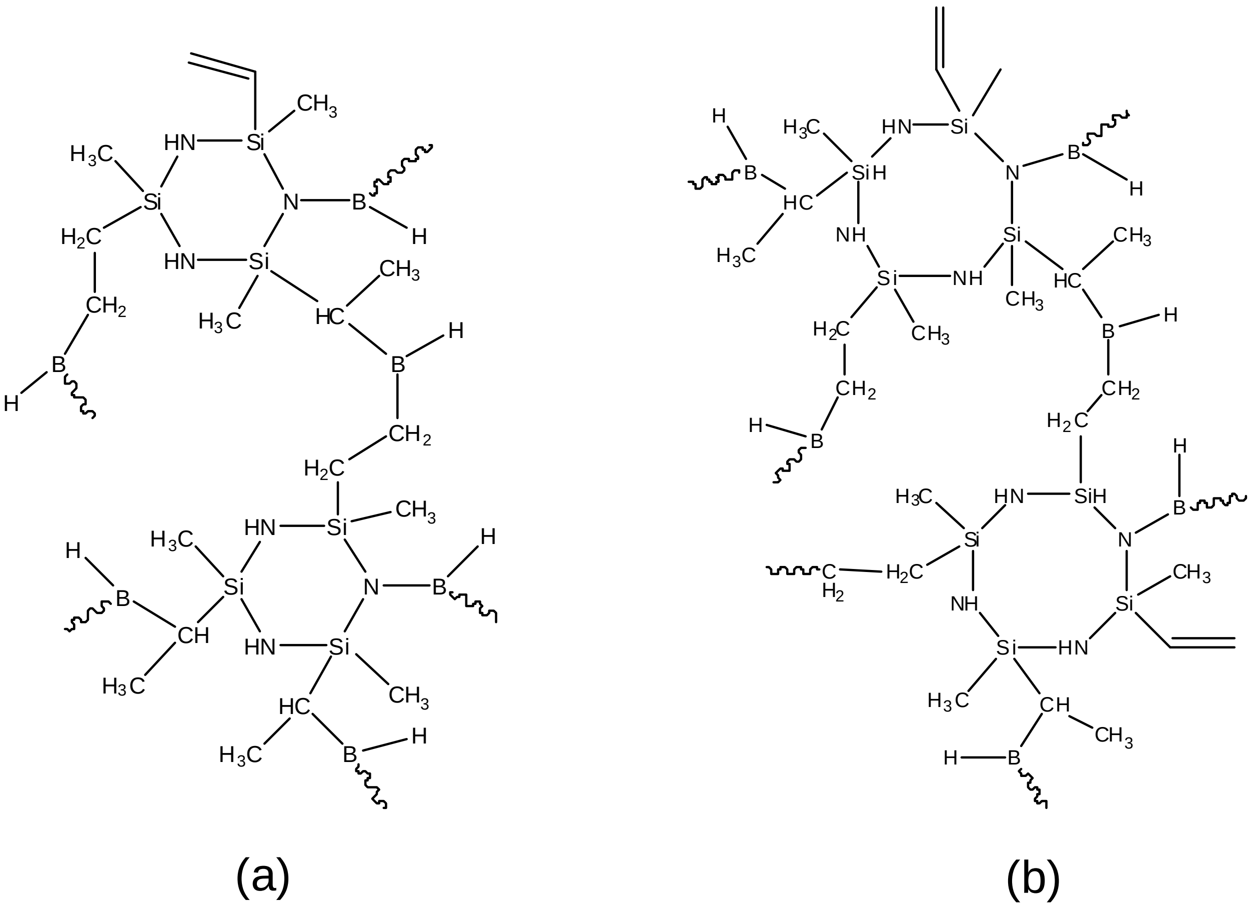

Figure 5.7. Polymeric network of polyborotrisilazane (a) and polyborotetrasilazane (b), which are obtained by hydroboration of tricyclosilazane and tetracyclosilazane, respectively. Structures are drawn based on the results of solid-state NMR and ATR-IR measurements of the synthesized polymers. The presence of both structural units, namely >CH-CH_3 and –CH_2-CH_2- bridges interconnecting Si and B in the synthesized polymers can be explained by the addition of boron to the α- and β-vinyl carbon atoms which are formed by hydroboration of vinyl groups [9-10].

5.3. Polymer to ceramic transformation

5.3.1 STA characterization

The results of the simultaneous thermal analysis (STA) measurements are used to define the temperature profiles for the pyrolytic conversion of the polymers into the SiBCN ceramics and to optimize the pyrolysis temperature to obtain unsupported ceramic powder for microstructural characterizations and for the development of membrane layers on porous alumina supports and on sensors.

The transformation of pre-ceramic polymers into ceramics are monitored by STA coupled with mass and IR spectrometry. The thermogravimetry (TG) and corresponding differential thermogravimetric (DTG) curves of polyborotrisilazane and polyborotetrasilazane are illustrated in Figure 5.8a and Figure 5.8b, respectively.

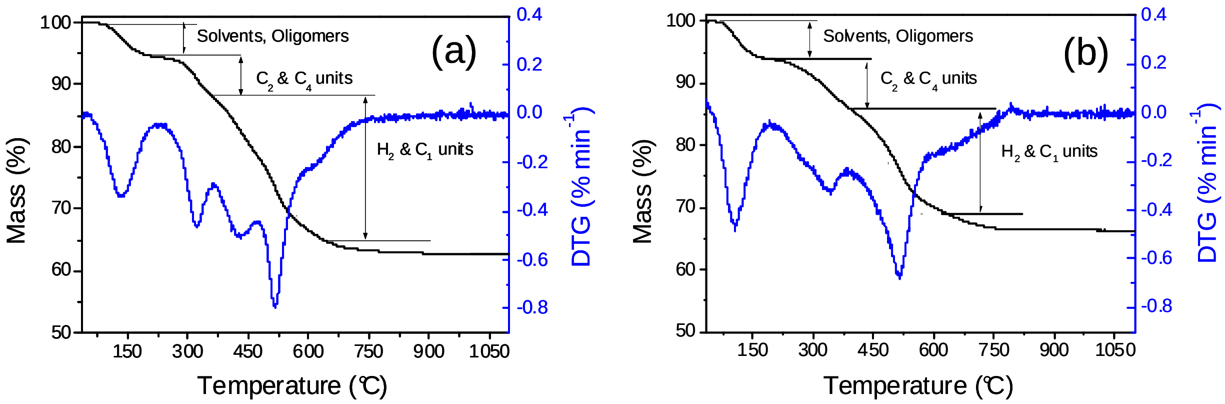

Figure 5.8. Thermal gravimetric analysis (TGA) of pre-ceramic polymers: (a) polyborotrisilazane and (b) polyborotetrasilazane (heating rate 5 °C min^{-1} in flowing argon).

Similar TGA profiles are observed for polyborotrisilazane and polyborotetrasilazane. According to MS analysis mass loss could be observed in several steps (Figure 5.8). Solvents (toluene, m/z: 92, 91) and oligomers (m/z: 170, 156) are detected in the first step of mass loss from 90 to 240 °C, which accounts for about 6 % mass loss. In the second step, C_2 (m/z: 28, 27) and C_4 (m/z: 56, 55) units are observed up to 380 °C. Major mass loss are observed in the temperature range from 390 to 660 °C in the form of methane (m/z: 16, 15) and hydrogen (m/z: 2). Very little mass loss can be observed above 800 °C – due to the release of residual hydrogen – with ceramic yields of about 63 % and 65 % by mass for polyborotrisilazane and polyborotetrasilazane, respectively.

The gases such as CH_4, H_2, etc., which are released during polymer-to-ceramic transformation generate micropores – in the range of the molecular diameter of released gases – in the obtained SiBCN ceramics. This process by which pore-generation occurs in polymer-derived ceramics is the crucial step for obtaining microporous polymer-derived *ceramics*. This microporosity is however transient, because it is eliminated when the pyrolysis temperature leading to the completion of the ceramization process is increased, according to a densification mechanism based on surface reaction accommodated by viscous flow [11]. Therefore, selection of pyrolysis temperature is an important factor to obtain suitable microporous membrane for gas purification application.

TGA curves of both polymers show almost constant mass at temperature ≥ 800 °C which is an indication of completion of ceramization process. Further structural characterizations (XRD, elemental analysis, porosity measurement) are performed on the SiBCN ceramics obtained by the pyrolysis of polymers at and above 800 °C.

5.4. Microstructural characterization of unsupported ceramic powders

5.4.1 XRD characterization

Figure 5.9 shows X-ray powder diffraction patterns of pyrolyzed ceramics obtained by pyrolyzing polyborotrisilazane and polyborotetrasilazane, at 800 °C and 1000 °C under flowing argon. The reasons for choosing two temperatures (800 and 1000 °C) for the XRD measurements for the ceramics obtained at these temperatures are: (i) γ-Al_2O_3/α-Al_2O_3 porous supports are thermally unstable above 800 °C which limits pyrolysis temperature of polyborosilazane coated porous supports to develop ceramic membrane on it. STA curve shows ceramization formation at T ≥ 800 °C, in accordance with the condition discussed in Chapter 4 (section 4.3), and (ii) to examine the crystallinity of ceramic obtained above 800 °C. The ceramics derived from polyborotrisilazane and polyborotetrasilazane at 800 and 1000 °C under flowing argon are amorphous — confirmed by broad, featureless powder diffraction patterns (Figure 5.9). Presence of amorphous phase in the ceramic, in the studied temperature range 800-1000 °C, is a good indication of obtaining crack-free ceramic membranes. Intercrystalline spaces in microporous crystalline materials, such as, in zeolite, are considered as microdefects that can cause significant decrease in permselectivity of gases.

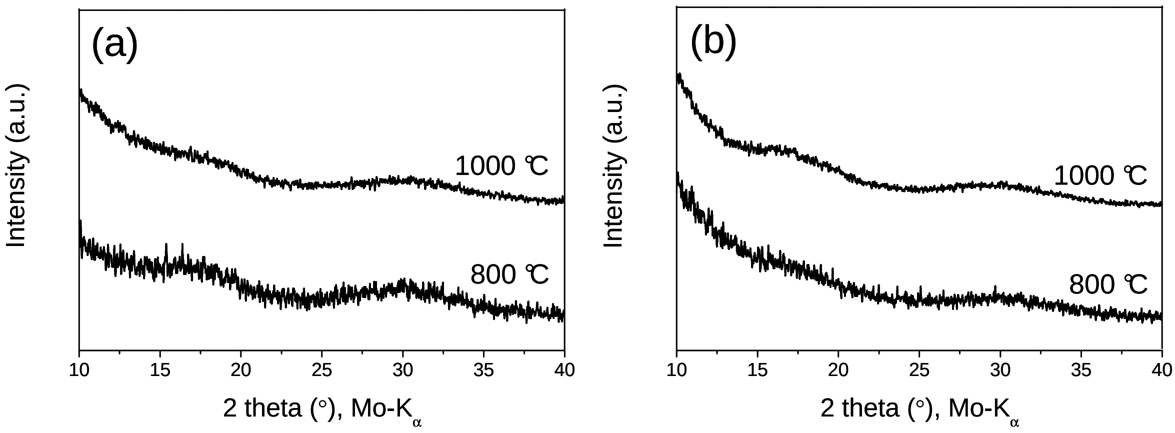

Figure 5.9. XRD patterns of SiBCN ceramics powders obtained at 800 ºC and 1000 ºC by the pyrolysis of: (a) polyborotrisilazane and (b) polyborotetrasilazane, under flowing argon.

5.4.2 TEM characterization

High-Resolution TEM (HRTEM) studies of SiBCN ceramic powder obtained by the pyrolysis of polyborotrisilazane at 800 °C (Figure 5.10) reveals worm-like microstructural features that are characteristic of amorphous polymer-derived ceramics. The SiBCN ceramic matrix is predominantly amorphous as indicated in SAD diffraction pattern (inset on the right upper corner in Figure 5.10) which is in agreement with the results of XRD (Figure 5.9).

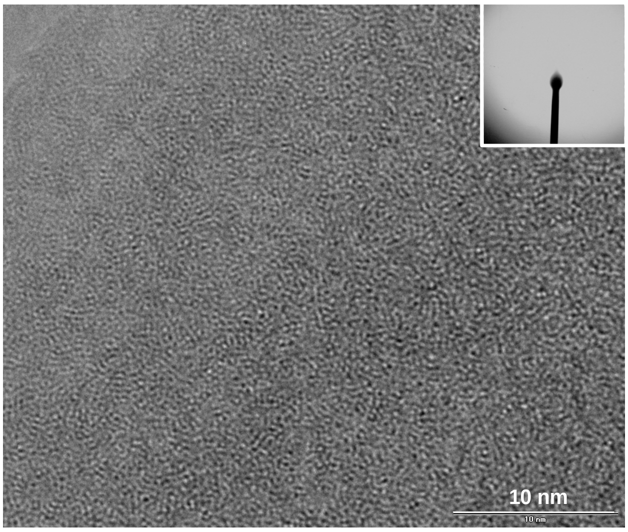

Figure 5.10. HRTEM micrograph of SiBCN powder derived from polyborotrisilazane by pyrolysis at 800 °C under argon. Amorphous SiBCN as indicated by SAD diffraction pattern, inserted on right upper corner.

5.4.3 Elemental analysis

According to the conditions mentioned in Chapter 4 (section 4.3), γ-Al_2O_3/α-Al_2O_3 porous supports are not thermally stable above 800 °C; therefore development of ceramic membrane on these supports by the coating of polyborosilazanes followed by pyrolysis above 800 °C could lead to defects in the final membrane. Hence, elemental analysis is done for the ceramics obtained after pyrolysis at 800 °C. The as-synthesized ceramics obtained after pyrolyzing polyborotrisilazane and polyborotetrasilazane at 800 °C in argon atmosphere are found to be black in colour with the chemical compositions of $Si_2B_1C_{3.7}N_{1.6}O_{0.2}$ and $Si_2B_1C_{2.8}N_{1.2}O_{0.2}$, respectively. The result of elemental analysis is presented in Table 5.4.

Table 5.4. Elemental composition of the ceramics obtained after pyrolysis of polyborotrisilazane and polyborotetrasilazane polymers at 800 °C under argon.

Ceramic from polymer	**Si (wt %)**	**B (wt %)**	**C (wt %)**	**N (wt %)**	**O[a] (wt %)**	**Empirical Formula**
polyborotrisilazane	41.2	7.9	31.8	16.8	2.3	$Si_2B_1C_{3.7}N_{1.6}O_{0.2}$
polyborotetrasilazane	47.1	9.4	29.1	11.1	3.1	$Si_2B_1C_{2.8}N_{1.2}O_{0.2}$

[a] small oxygen contamination may have occurred during manipulation of samples in air. Very low amount of hydrogen is generally found in pyrolyzed ceramics; therefore, hydrogen wt% was neglected in the present calculation.

5.5. Morphology and structure of the membrane coating

It has been shown in section 5.3.1 that polymer-to-ceramic transformation in polyborosilazanes is achieved at T ≥ 800 °C (see TGA curves in Figure 5.8). Moreover, as already discussed in Chapter 4 (sections 4.2 and 4.3) that α-Al_2O_3 macroporous supports and intermediate γ-Al_2O_3 mesoporous layers remain thermally stable up to 800 °C. According to the conditions for the deposition of polymers on porous supports (Chapter 4, Table 4.1), polymer is coated on porous supports by dip-coating method followed by pyrolysis at 800 °C under argon to get an appropriate top-layer SiBCN ceramic coating. Polyborotetrasilazane is not used for membrane deposition on porous supports because the pore-size distribution of ceramic powder (discussed in section 5.5) obtained by the pyrolysis of this polymer at 800 °C does not show a characteristic of a microporous ceramics. The morphology and structure of the membrane coatings are studied by SEM and TEM, which are described in sections 5.5.1 and 5.5.2.

5.5.1 SEM characterization

To estimate the thickness of SiBCN membrane SEM images of the cross-section of broken membrane coated supports are taken. SiBCN top layer is prepared by dipping porous γ-Al_2O_3/α-Al_2O_3 and α-Al_2O_3 support in polyborotrisilazane polymeric solution followed by pyrolysis at 800 °C under argon.

Figure 5.11 shows the SEM images of SiBCN coated on a γ-Al_2O_3/α-Al_2O_3 and α-Al_2O_3 supports. It shows a crack-free SiBCN layer with a thickness of about 2.8 µm after 3-fold coatings/pyrolysis steps at 800 °C (Figure 5.11a). A 5-fold SiBCN membrane developed on α-Al_2O_3 support (without intermediate γ-Al_2O_3 layer) shows crack-free membrane with a thickness of about 4 µm (Figure 5.11c). In both cases, for α-Al_2O_3 support coated with and without intermediate mesoporous γ-Al_2O_3 layer, crack-free SiBCN membrane formation is observed. These results show that one of most important objectives of the present work — to deposit a crack-free and thin ceramic membrane layer — is achieved using dip-coating of a silicon based polymer on porous supports followed by pyrolysis at 800 °C.

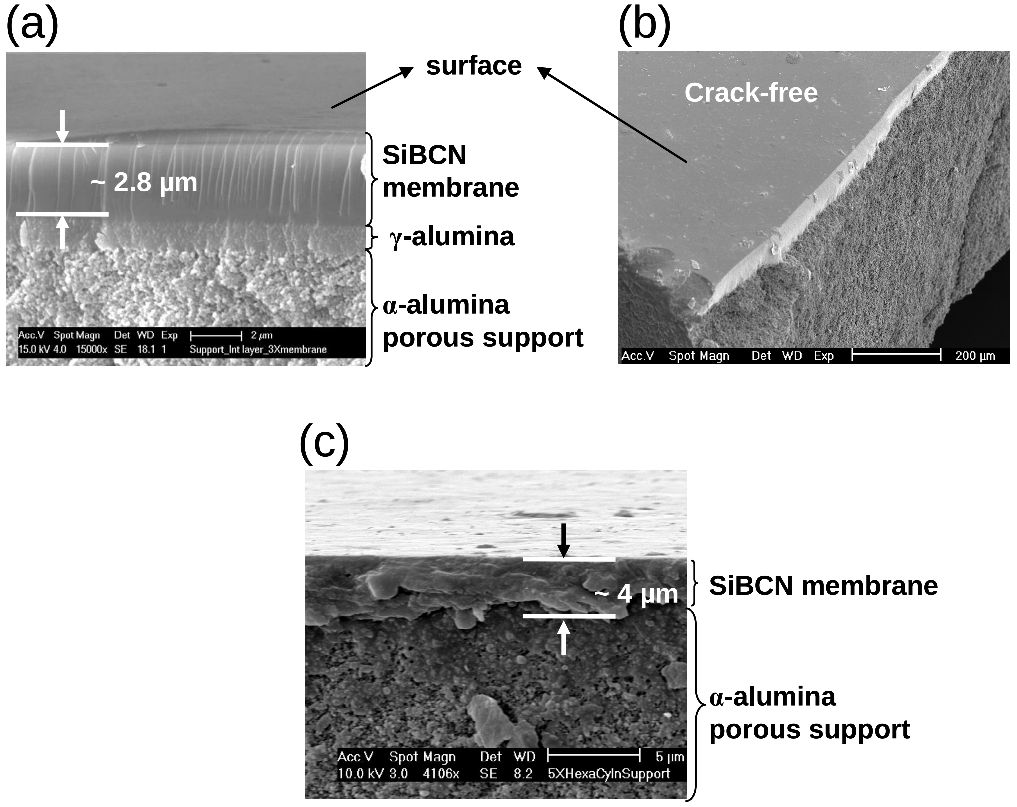

Figure 5.11. Scanning electron microscopy (SEM) images: (a,b) cross-sectional view and top-surface of a 3-fold coated SiBCN membrane on γ-Al_2O_3/α-Al_2O_3 support and (c) cross-sectional view of 5-fold coated SiBCN membrane on α-Al_2O_3 support. Polyborotrisilazane was used as preceramic polymer for coating on porous supports.

5.5.2 TEM characterization

To achieve high permeance through SiBCN membrane layer, thickness of membrane layer should be as small as possible. Therefore, dilution of preceramic polymer with dry toluene is done to obtain a thin SiBCN membrane layer. As already shown in Chapter 4 that pore-size of γ-Al_2O_3 intermediate layer deposited on α-Al_2O_3 support is of about 8 nm (section 4.3.1). Therefore, there is a probability of impregnation of polymer in the pores of γ-Al_2O_3/α-Al_2O_3 porous support during the coating of polymeric solution on porous support. To investigate the impregnation of polymeric material into γ-Al_2O_3/α-Al_2O_3 support and to examine uniform distribution of constituents' elements in SiBCN ceramic layer, EDX line scanning is performed along the cross-section of multilayered SiBCN/γ-Al_2O_3/α-Al_2O_3.

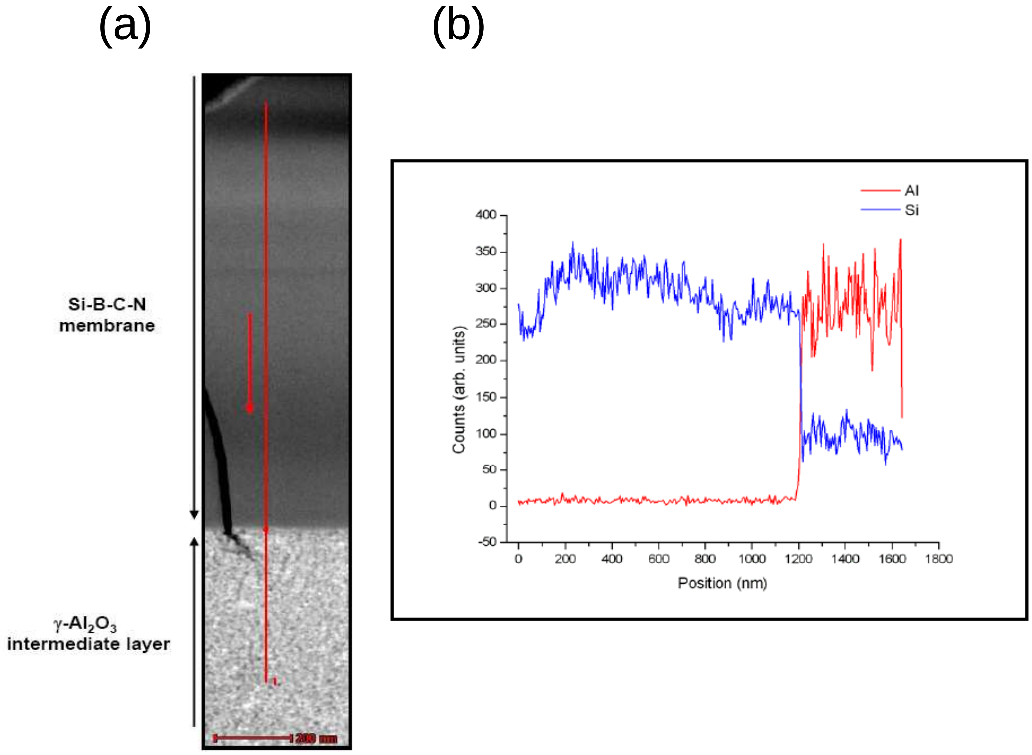

Figure 5.12. (a) STEM dark field image, and (b) EDX line scan through 3-fold SiBCN/γ-Al_2O_3/α- Al_2O_3 membrane synthesized at 800 °C. Polyborotrisilazane was used as preceramic polymer for coating on porous supports.

Figure 5.12 shows Scanning Transmission Electron Microscopy (STEM) dark field image and EDX scanning of 3-fold SiBCN coated γ-Al_2O_3/α-Al_2O_3 membrane done at interface of SiBCN and γ-Al_2O_3. EDX line scanning confirms incorporation of Si in the γ-Al_2O_3 intermediate layer (Figure 5.12b). The incorporation of Si (basically SiBCN ceramic) into the pores of γ-Al_2O_3 intermediate layer could increase the resistance against transportation of gases through membrane; however, the SiBCN/γ-Al_2O_3 interface looks perfectly bonded to each other. Therefore, a good physical bonding between different layers in the membrane system could be expected in this configuration.

In order to examine uniform distribution of boron in the synthesized SiBCN ceramic, boron elemental mapping of SiBCN membrane layer is done, as shown in Figure 5.13. A homogenous distribution of boron is observed in the SiBCN membrane layer.

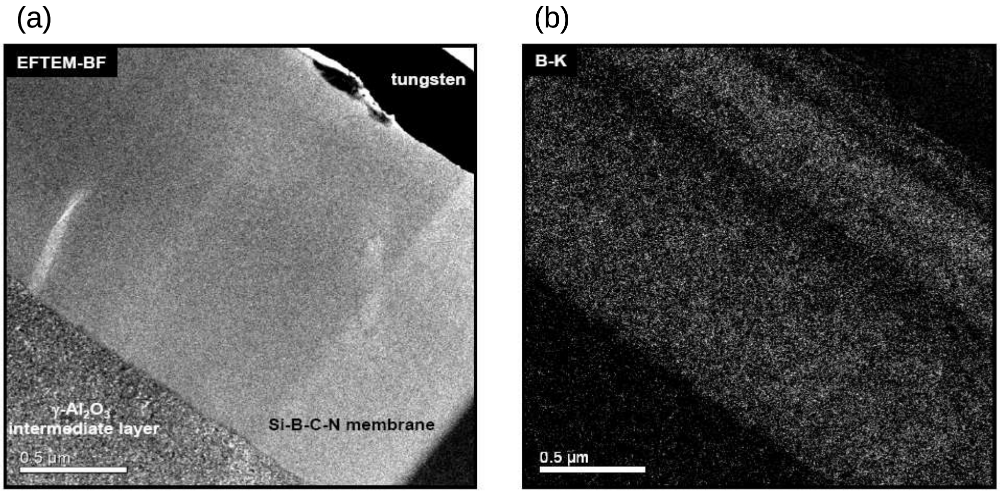

Figure 5.13. EFTEM bright field image (a) and boron elemental mapping (b) of SiBCN membrane layer of a 3-fold coated SiBCN/γ-Al_2O_3/α-Al_2O_3 membrane. Polyborotrisilazane was used as preceramic polymer for coating on porous supports.

A typical transmission electron micrograph of a focused ion beam (FIB) cross section of 3-fold coated SiBCN membrane on γ-Al_2O_3/α-Al_2O_3 is shown in Figure 5.14. The thickness of this SiBCN membrane is found to be about 1.8 µm which is lower than that is observed in the case of another 3-fold coated SiBCN membrane sample examined by SEM measurement (Figure 5.11) which shows a thickness of 2.8 µm. This difference in the thickness of SiBCN layers for the same number of coating/pyrolysis steps at the same pyrolysis temperature using the same polymer could be due to the change in viscosity of the preceramic polymeric solution, i.e. due to instability of polymeric solution at different atmospheric temperatures when used for coating on porous supports. The coating thicknesses of SiBCN membranes on γ-Al_2O_3/α-Al_2O_3 supports which are measured by SEM and TEM micrographs are done in summer and winter season, respectively. The polyborotrisilazane based polymeric solution which is used for coating during summer could have become more viscous due to faster gelation in summer and hence thicker ceramic membrane layer is found after pyrolysis compared to the same polymer solution of same chemical composition used in winter.

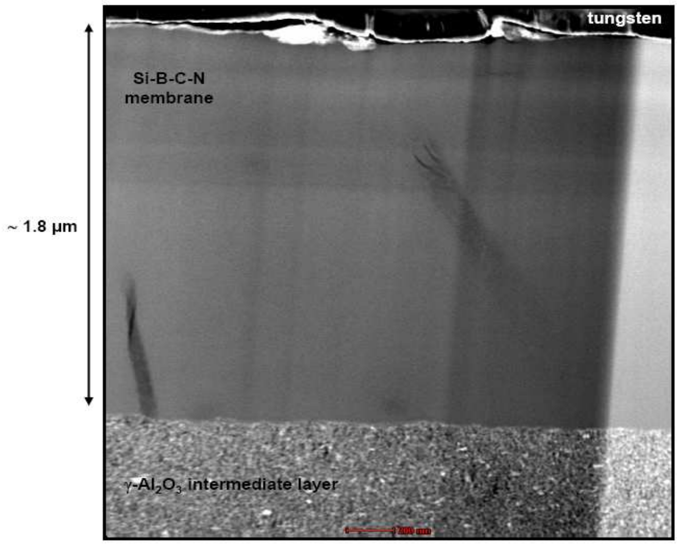

Figure 5.14. TEM image (cross-sectional view) of a 3-fold coated SiBCN membrane on γ-Al_2O_3/α-Al_2O_3 support. Polyborotrisilazane was used as preceramic polymer for coating on porous supports.

Above results show that polymeric solution is impregnated into the pores of γ-Al_2O_3/α-Al_2O_3 support and hence SiBCN ceramic occupies space in the porous support as well. However, uniform distribution of B is analyzed in the SiBCN ceramic layer confirming homogeneous distribution of B in the preceramic polymeric solution of polyborotrisilazane after hydroboration. It is also found that different laboratory temperature (during summer and winter) while coating the polymer on porous supports affects the thickness of the top membrane layer. These observations imply that the polymeric solution (polyborotrisilazane) should be preserved at low temperature (~0 °C) to avoid gelation of the polymer to develop uniform ceramic coatings on porous supports.

5.6. Porosity characteristics

5.6.1 Nitrogen-sorption measurement

One of the key properties of a porous ceramic is its pore-size distribution (PSD). The PSD value of an unsupported ceramic is used as an indicator to select ceramics for gas separation application when it shows microporosity (PSD < 2 nm). It can be measured by BET analysis directly on unsupported ceramic powder. However, the PSD which is obtained by BET analysis on powder can be different from the measurement done on corresponding membrane coated on porous support. Therefore, pore-size characteristics of both unsupported SiBCN ceramic powder (Figure 5.15) and supported SiBCN ceramic layers coated on γ-Al_2O_3/α-Al_2O_3 (Figure 5.16) are evaluated using gas adsorption method.

Figure 5.15 shows nitrogen-sorption isotherms of SiBCN ceramic powders which are obtained by the pyrolysis of as-synthesized polymers — polyborotrisilazanae and polyborotetrasilazane — at 800 °C. The isotherm of the ceramic powder derived from polyborotrisilazane is found to be of Type I in nature [12], confirming formation of microporous SiBCN ceramic (Figure 5.15a), whereas the pore-size distribution of the ceramic derived from polyborotetrasilazane (Figure 5.15b) shows the presence of both micro- and mesopores. Hence, polyborotrisilazane is selected and used for the deposition on porous supports for gas permeance measurements. Unsupported SiBCN ceramic powder derived from polyborotrisilazane shows a BET specific surface area and micropore volume of about 67 m^2 g^{-1} and 0.063 cm^3 g^{-1}, respectively.

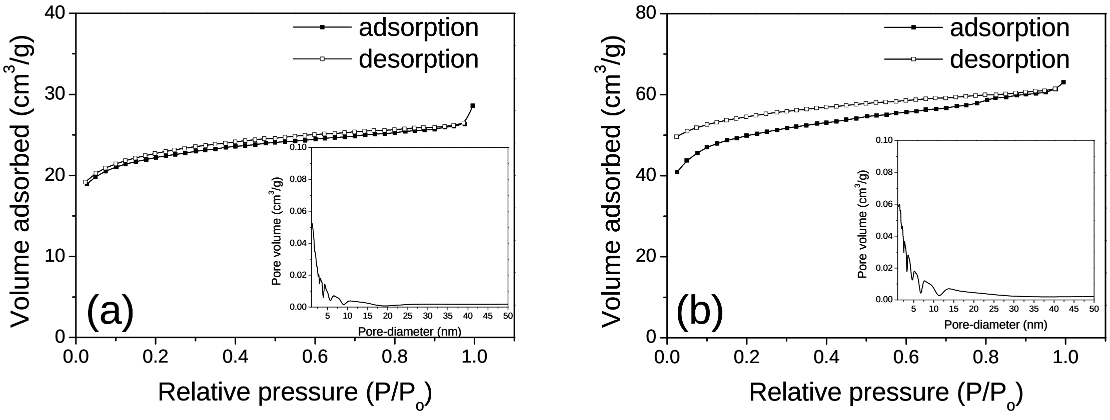

Figure 5.15. Nitrogen physisorption isotherms at 77 K of unsupported SiBCN ceramic powders obtained by the pyrolysis of (a) polyborotrisilazane and (b) polyborotetrasilazane at 800 °C.

Figure 5.16 shows pore-size distribution of 3-fold SiBCN membranes coated on α-Al_2O_3 support and on γ-Al_2O_3/α-Al_2O_3 support (cross-sectional SEM image of this membrane coated support is shown in Figure 5.11a) measured by nitrogen gas adsorption method. SiBCN membrane layers are obtained by dip-coating/pyrolysis steps of polyborotrisilazane polymeric solution on both of the porous supports. The result obtained by the N_2-adsorption method indicates the presence of microporosity in the SiBCN membranes and shows also a smaller mean pore-size — 6.8 vs. 7.4 Å — with the intermediate mesoporous γ-Al_2O_3 layer when compared to those without. The thickness, pore diameter, and pore volume data of different layers in a 3-fold SiBCN coated on γ-Al_2O_3/α-Al_2O_3 support is presented in Table 5.5.

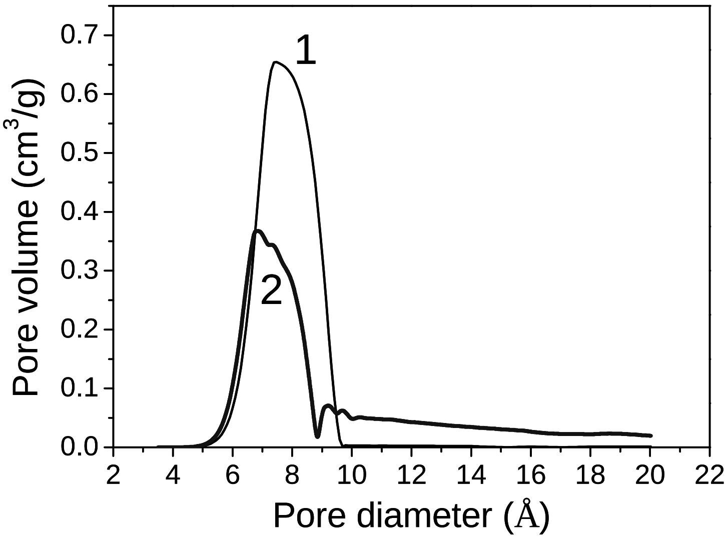

Figure 5.16. Pore-size distribution (only micropores are shown) of multilayer 3-fold coated SiBCN/α-Al_2O_3 (1) and 3-fold coated SiBCN/γ-Al_2O_3/α-Al_2O_3 (2) membranes evaluated by N_2-adsorption isotherm analysis using the Saito-Foley (SF) method. Polyborotrisilazane was used as preceramic polymer for coating on porous supports.

Table 5.5. Thickness, pore diameter, and pore volume data of different layers in SiBCN/γ-Al_2O_3/α-Al_2O_3 multilayer membrane (Figure 5.11). Data for the α-Al_2O_3 porous support and intermediate γ-Al_2O_3 is taken from Chapter 4.

Layer	**Thickness**	**Mean pore diameter (nm)**	**Pore type**	**Pore volume (ml g^{-1})**
α-Al_2O_3 (support)	1 mm[a]; 50 μm[b]	640[a] ; 45[b]	Macro-	16.31
γ-Al_2O_3 (intermediate layer)	1 μm	8	Meso-	0.44
SiBCN (top layer)	2.8 μm	0.68; 0.73	Micro-	0.17

[a] support, [b] outer α-Al_2O_3 layer

5.6.2 SAXS characterization

SAXS measurement is performed on unsupported SiBCN powder obtained by the pyrolysis of polyborotrisilazane at 800 °C under argon. The evaluation of SAXS data is mainly concentrated on the modelling of the surface area and pore size using the Guinier and Porod analysis [13-14].

The usual method to evaluate the microporosity of materials is based on the gas adsorption measurements (N_2 at 77 K). However, nitrogen molecules cannot migrate into pores smaller than their own cross-sectional diameter. Therefore, it is not possible to investigate the pores having diameters less than 4 Å using N_2-adsorption measurement at -196 °C (77K) or even by CO_2 at 0 °C [15]. Also micropores are so narrow that they cannot accommodate two layers of adsorptive molecules [16]. The small-angle x-ray scattering (SAXS) method is known to be widely employed in studies of nm-scale structural nonuniformities in disperse systems, including porous materials [17]. The SAXS can be applied to estimate the average size of the scattering fragments (clusters or pores), the geometry of pore space and surface area in microporous materials by the interpretation of SAXS data within reasonable models, as it has been shown in previous works [16, 18-23].

Guinier's law should be valid for small q values. Determination of R_g has long been the most important tool in the analysis of scattering from isotropic systems and continues to be very useful at the first stage of data analysis. However, in solid state solutions or particulate aggregates, Guinier's approach should be taken with caution because of interparticle interferences, that may influence the initial part of the scattering curve, and particle aggregates, which could cause a distortion of the curve. Figure 5.17 shows small angle X-ray scattering curve of the SiBCN sample after intensity normalization. The shoulder appearing above q value of about 2 nm^{-1} is characteristic of microporosity. This confirms presence of microporosity in the unsupported SiBCN ceramic powder as also observed by N_2-sorption measurement. For the SiBCN sample the Guinier region is found for the q values between 0.19 and 0.29 nm^{-1}. The R_g value is calculated of about 15.17 nm from the slope ~$R_g^2/3$ of log-log plot of equation 2.2 (see chapter 2, section 2.3.11).

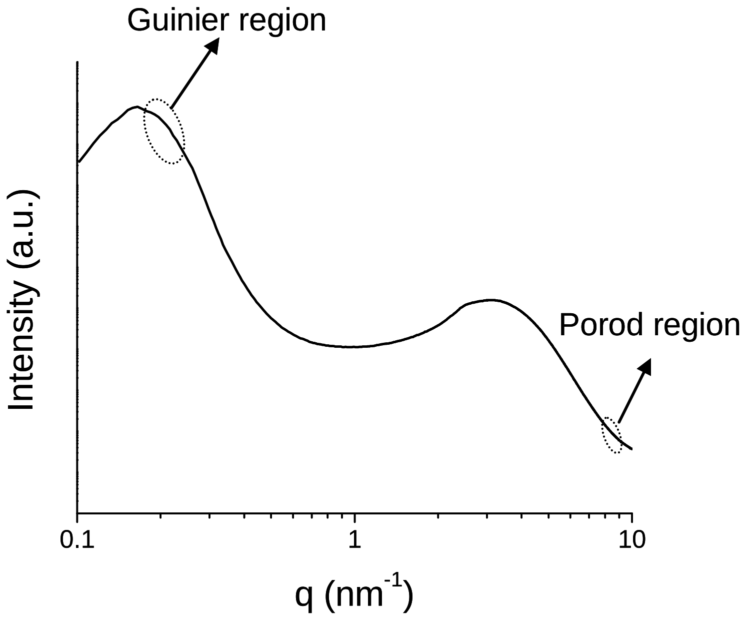

Figure 5.17. Intensity I(q) versus q for SiBCN ceramic powder obtained by pyrolysis of polyborotrisilazane at 800 °C.

In the large q-range, the SAXS intensity depends upon the surface area and it can be approximated by Porod's Law

$$I(q) = 2\pi(\Delta\rho)^2 Sq^{-4} \tag{5.3}$$

In the limit $q \rightarrow \infty$, $I(q)q^4$ is a constant that allows the determination of the interface area of the particles since $(\Delta\rho)^2$ is known. The Porod region for the SiBCN ceramic powder is found for q values between 8.1 and 9.6 nm^{-1} calculated from the linear portion of the plot between $I(q)q^4$ and q^4.

Whenever the particle contrast, $\Delta\rho$, is an unknown value, it is possible to use the so-called *Porod invariant (Q)*. *Q* represents the integral over the scattering intensity in the reciprocal space and is directly related to the mean square fluctuation of electron density. The plot $\ln[I(q)q^3]$ vs q^2 combined with the *Q* has been employed to calculate the S/V value. The intercept with the y-axis is proportional to the surface area of the particle. $\ln[I(q)q^3] = a + bq^2$; $\frac{S}{V} = \frac{K}{Q}$, where a = lnK and $Q = \int_0^\infty q^2 I(q)dq$.

For a two phase system, particle solution or a system of identical particles embedded in a matrix, the contrast, *Δρ*, describe the difference between the mean electron density of the particles and solvent or matrix and is one of the most important parameters in small angle scattering studies. Thus, the integral *Q* of the SAXS intensity can be rewritten as a function of contrast and volume fraction of the phases:

$$Q = \int_0^\infty q^2 I(q)dq = 2\pi(\Delta\rho)^2 \varphi(1-\varphi)V \qquad (5.4)$$

where φ and $(1-\varphi)$ are the volume fraction of both phases and *V* is the irradiated volume of the sample. The specific surface (S/V) of SiBCN ceramic powder is calculated to be about 1.63 cm^{-1}.

Table 5.6. Calculated co-efficients for Guinier and Porod laws, Porod invariant (Q), Radius of gyration (R_g) and specific surface value (S/V) of SiBCN ceramic powder obtained by the pyrolysis of polyborotrisilazane at 800 °C.

Sample	**Guinier**		**Porod**		**Q**	**R_g**	**S/V**
	m	**n**	**a**	**b**		**(nm)**	**(cm^2/cm^3)**
SiBCN, 800 °C	3.30	-5.06	5.39	-1.89E-4	7.84E+23	15.17	1.63

SAXS data which is obtained after subtracting background and normalization process are modelled and analyzed using Igor Pro/Irena package to estimate the pore-channel length that is formed by the interconnection of micropores. The cross-sectional diameter of pore-channels, for feeding data to simulation, is taken from the pore-size distribution obtained by gas-adsorption method (Figure 5.16). Following parameters are used for calculating size distribution:

- Distribution parameter- maximum and minimum diameter of 4 and 100 Å, respectively
- Particle shape model- cylindrical AR (aspect ratio).

- IPG/TNNLS (Total Non-Negative Least Square) method, NNLS approach parameter of 0.56 (approach parameter is the step-size which is made in each step towards calculated ideal solution), a maximum of 1000 iteration is done for the convergence of results.

Using the above parameters, the simulation is performed with different aspect ratios (length-to-diameter ratios). The best match between the measured and simulated SAXS data is observed by using an aspect ratio of 900 (Figure 5.18) for the size distribution 6.8–7.3 Å which is obtained by N_2-adsorption measurement. Assuming an average cross-sectional diameter of pore-channels of about 7 Å gives the corresponding average pore-channel length of about 0.63 μm (aspect ratio ~900).

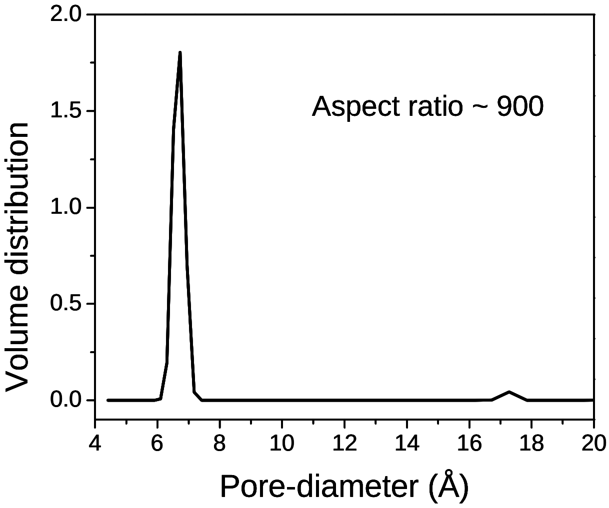

Figure 5.18. Pore-size distribution of SiBCN ceramic powder obtained by the simulation of SAXS data using Igor Pro/Irena package and fitted best with the N_2-adsorption result for an aspect ratio of 900 (considering cylindrical shape model). SiBCN ceramic is derived by the pyrolysis of polyborotrisilazane at 800 °C under flowing argon.

5.7. Performance of SiBCN membrane in hydrogen separation and mechanism of gas permeance

As mentioned above (see section 5.5.1), the SiBCN ceramic which is obtained by the pyrolysis of polyborotrisilaznae shows microporous nature but not the one derived from polyborotetrasilazane (Figure 5.15). Therefore, polyborotrisilaznae is selected and coated on γ-Al_2O_3/α-Al_2O_3 support followed by pyrolysis to get multilayed SiBCN/γ-Al_2O_3/α-Al_2O_3

membrane. To measure H_2/CO selectivity, permeance through SiBCN/γ-Al_2O_3/α-Al_2O_3 membranes for different numbers of top-coating layers are measured using a mixture of H_2, CO, and N_2 mixed in different concentrations based on constant volume manometric method as described in Chapter 3 (section 3.2). Permeance of H_2 and CO through the membranes measured at 440 °C is presented in Table 5.7 and Figure 5.19.

Table 5.7. H_2 and CO permeance and H_2/CO selectivity of SiBCN/γ-Al_2O_3/α-Al_2O_3 multilayer membranes at 440 °C determined in mixed-gas measurements.

Number of SiBCN layers	**H_2 permeance ($mol\ m^{-2}\ s^{-1}\ Pa^{-1}$)**	**CO permeance ($mol\ m^{-2}\ s^{-1}\ Pa^{-1}$)**	**H_2/CO selectivity**
1	3.91×10^{-7}	1.74×10^{-7}	2.24
2	2.42×10^{-7}	5.04×10^{-8}	4.81
3	1.29×10^{-7}	2.27×10^{-8}	5.68
4	1.14×10^{-7}	1.46×10^{-8}	7.81
3 [a]	1.05×10^{-8}	1.00×10^{-9}	10.5

[a] precursor polymer is stirred for a longer time after taking out from deep freezer (1 h extra compared to stirring during synthesis) until the solution appears more viscous

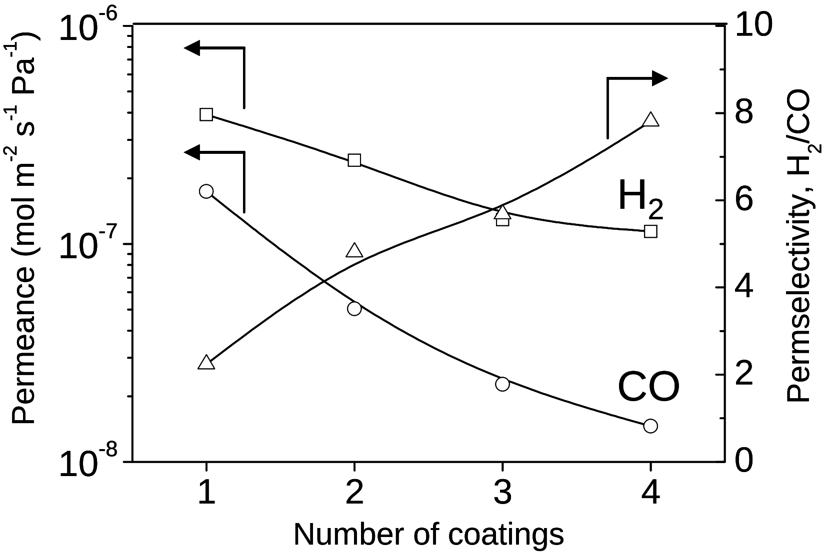

Figure 5.19. H_2 and CO permeance and H_2/CO selectivity of amorphous SiBCN/γ-Al_2O_3/α-Al_2O_3 multilayer membranes for different number of SiBCN coatings measured at 440 °C.

The permeance measurement implies that by increasing the number of coatings result in lower permeances, which, however, differ significantly for H_2 and CO. For 1-fold SiBCN-coated multilayer membrane the H_2 permeance found to be 3.91 x 10^{-7} mol m^{-2} s^{-1} Pa^{-1} and H_2/CO selectivity is 2.24 (which less than theoretical Knudsen diffusion selectivity for H_2/CO of 3.74) at 440 °C. The low H_2 selectivity could be attributed to the presence of nonselective membrane defects, such as, macro pinholes in 1-fold SiBCN layer. Whereas for 4-fold SiBCN-coated multilayer membranes the H_2 permeance is 1.14×10^{-7} mol m^{-2} s^{-1} Pa^{-1} and the H_2/CO selectivity reaches 7.8 (Table 5.7). This finding — increase in H_2/CO selectivity values of SiBCN/γ-Al_2O_3/α-Al_2O_3 membranes with increasing number of SiBCN coatings — indicates that a substantial amount of preceramic polymer (polyborotrisilazane) needs to be deposited inside the pores of γ-Al_2O_3 to repair imperfections before the top SiBCN could be formed.

It is also found that the membranes functionality can be influenced through controllable gelation of the pre-ceramic polymer. When the precursor solution is stirred for longer time and dip-coating is performed from the resultant more viscous solution, the three times coated multilayer membranes show higher H_2/CO selectivities of about 10.5, but the H_2 permeance is decreased to 1.05×10^{-8} mol m^{-2} s^{-1} Pa^{-1} at 440 °C (Table 5.7).

Very limited information about H_2/CO selectivity is available for porous ceramic membranes. If compared to the state of the art microporous membranes (Figure 5.20), polymer-derived SiBCN membranes appear to be interesting candidates for hydrogen production via natural gas reformation because of their tunable nature and high-temperature and high-pressure stability. Moreover, they show high H_2/CO selectivity at high temperatures.

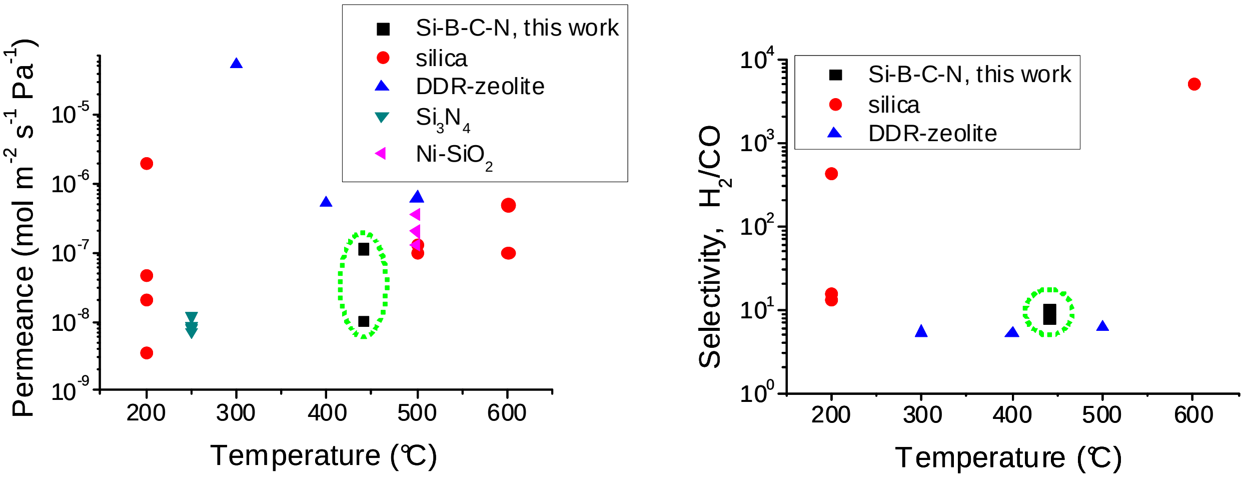

Figure 5.20. Performance (H_2 permeance and H_2/CO selectivity) for SiBCN/γ-Al_2O_3/α-Al_2O_3 multilayer membranes in comparison to that of other microporous ceramic membranes, i.e. silica, DDR-zeolite, Si_3N_4, Ni-doped SiO_2 (data are taken from the references [24-34]).

Different gas transport mechanisms are already described in Chapter 1 (section 1.2.2) and are also summarized here with key parameters in Table 5.8. Generally the flow of a gas permeating through a macroporous support (pore-diameter > 50 nm) can be described in terms of viscous flow, which is completely nonselective for molecules [35]; whereas Knudsen diffusion is dominating gas diffusion mechanism in mesoporous materials (pore-diameter between 2–50 nm). Activated diffusion becomes operative in microporous membranes (pore-diameter < 2 nm).

Table 5.8. Important gas-transport mechanisms through membranes with keys parameters.

Mechanism	**Permeance proportional to**
Viscous flow	$d_p P T^{-1}$
Knudsen diffusion	$M^{-1/2} d_p T^{-1/2}$
Surface diffusion	$M^{-1/2} d_p P \exp(-E_s/RT)$
Activated diffusion	$\exp(-E_a/RT)$

T – temperature, P – pressure, M – molecular mass, d_m – kinetic molecular diameter, d_p – pore diameter, λ – molecular collision free path, P – pressure, E_s and E_a are activation energy for surface and activated diffusion, respectively.

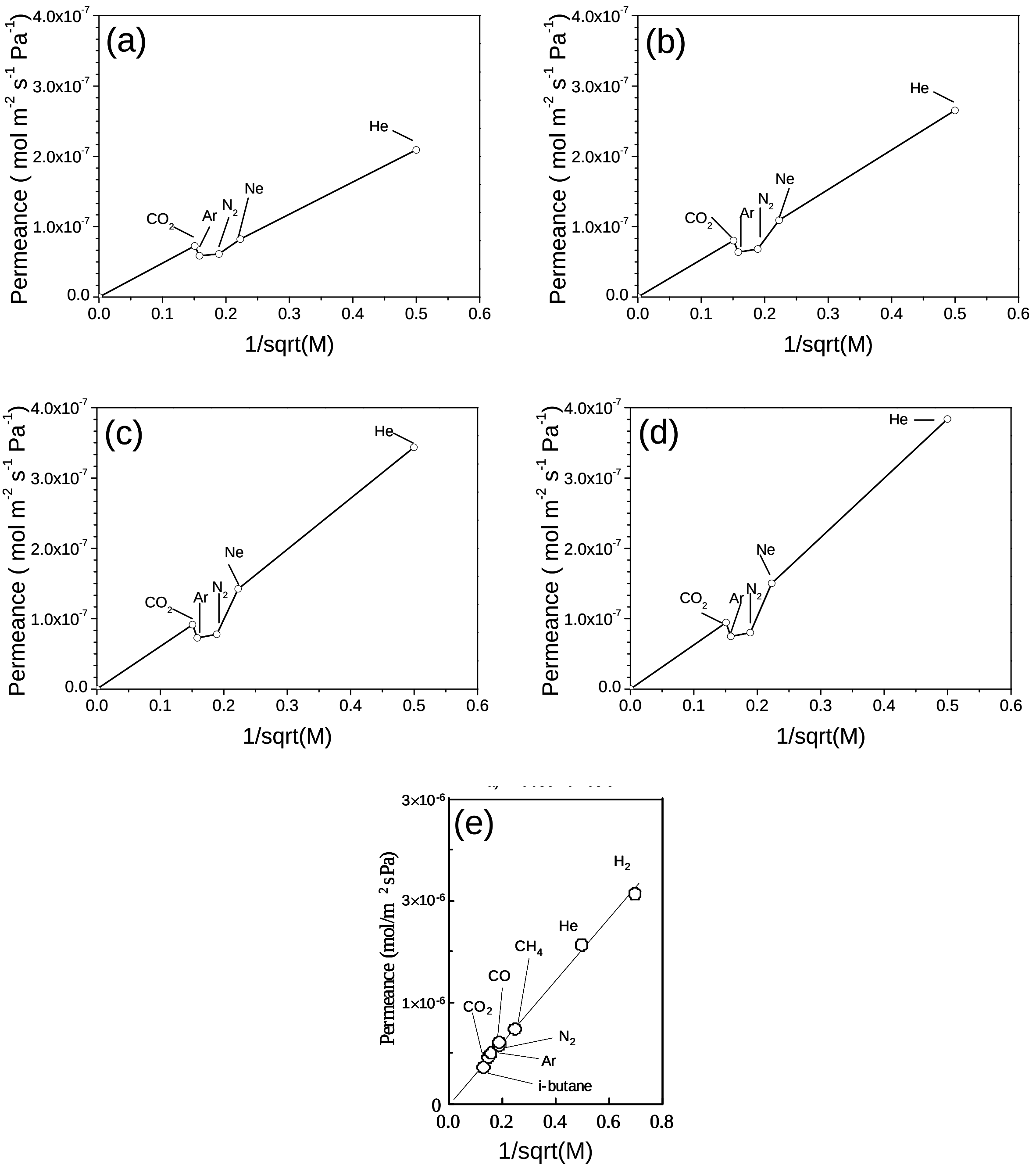

Figure 5.21. Gas permeation behaviour of 3-fold SiBCN membrane coated γ-Al_2O_3/α-Al_2O_3 support at different temperatures (a) 100 °C, (b) 200 °C, (c) 300 °C, (d) 400°C, and (e) Knudsen diffusion behaviour through an alumina membrane (pore diameter ≈ 3 nm) [36].

To study the gas transport properties of SiBCN membrane, single gas permeance through the 3-fold coated SiBCN/γ-Al_2O_3/α-Al_2O_3 membrane were measured for pure He, Ne, N_2, Ar and CO_2 at four different temperatures (100, 200, 300 and 400 °C). It can be seen from Figure 5.21a–d that the permeance through SiBCN membranes of the pure gases is not proportional to the inverse of square root of molecular mass of gases, whereas permeance through a mesoporous alumina membrane (Figure 5.21e [36]) shows linear dependence between the permeance and inverse of square root of molecular mass of pure gases. The linear dependence is measured when the gases follow pure Knudsen diffusion mechanism through a membrane.

Another way of representing permeance of pure gases through a membrane is to plot the permeance of gases vs. temperatures, as shown in Figure 5.22. The permeance of He and Ne increases with temperature, but a slow increase in the permeance is analyzed for gases with higher molecular diameter (N_2, Ar and CO_2) between 300 and 400 °C. The increase in permeance for He and Ne gases with increase in temperature could be attributed to thermal activated diffusion. In case of pure Knudsen diffusion, the permeance decreases with increase in temperature [3]. These results indicate that the gases do not follow a pure Knudsen diffusion mechanism through the SiBCN/γ-Al_2O_3/α-Al_2O_3 membrane.

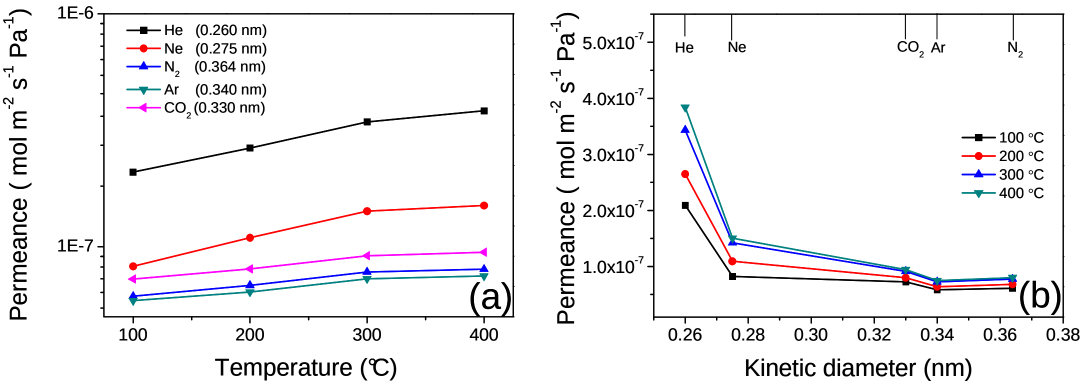

Figure 5.22. Permeances as a function of temperature (a) and kinetic diameter (b) of He, Ne, CO_2, Ar and N_2 through through 3-fold SiBCN/γ-Al_2O_3/α-Al_2O_3 membrane.

Generally, the permeance of a gas molecule through a microporous membrane decreases as the diameter of a gas molecule increases. However, polymer-derived membranes often show a selective increase in permeance of larger gas molecules, such as CH_4 through polysilazane-derived amorphous silica membrane [32], and CO_2 through polycarbosilane-derived amorphous Si-C-O membranes [38-39]. This could be due to the formation of selective diffusion channel sites for CH_4 [32] or CO_2 [38-39] during the polymer-ceramic thermal conversion process. Also, amorphous-SiBCN/γ-Al_2O_3/α-Al_2O_3 possesses micropore channels with diameters of about 6.8–7.3 Å (see Figure 5.16, measured by gas-adsorption method) that could have formed by interconnection of several micropores acting as “defects”, herein the gas transportation pathway is governed by the Knudsen diffusion mechanism. However, 3- and 4-fold SiBCN-coated membrane show H_2/CO selectivity of about 5.7 and 7.8 (see Table 5.7) which is higher than that of the corresponding theoretical Knudsen diffusion selectivity of 3.7. This higher value of selectivity indicates the existence of pores of diameter of about 3 Å — which cannot not be detected by N_2-adsorption method — in microporous amorphous SiBCN network, which acts as a molecular sieve in H_2/CO separation wherein the H_2 permeation is activated at high temperatures. Accordingly, the H_2 and CO separation in multilayer SiBCN/γ-Al_2O_3/α-Al_2O_3 membranes could be explained taking into account the contribution of both mechanisms.

For the molecular sieving, no difference in permeance would be expected for CO and H_2 which have kinetic diameters of 3.86 and 2.89 Å, respectively, and which are smaller than the diameter of micropore channel “defects” in SiBCN membrane layer. As mentioned earlier, for the Knudsen diffusion, the experimentally observed H_2/CO selectivities (Table 5.7) differ from the theoretical Knudsen prediction (inverse square root of the masses) for H_2/CO of 3.7. Therefore, the influence of the deposited number of SiBCN layers on permeance properties could be understood in the following way: (i) the H_2 permeance is decreased with increasing number of coatings (membrane thickness) due to an increase in the diffusion path length through the microporous SiBCN amorphous network and (ii) the H_2/CO permselectivity is increased by the decreasing number of micropore channel defects. Accordingly, an ideal SiBCN/γ-Al_2O_3/α-Al_2O_3 composite membrane with enhanced H_2 permeance and H_2/CO permselectivity could be realized by (a) minimizing the membrane thickness, and (b) minimizing the formation of defects (see Figure 5.23).

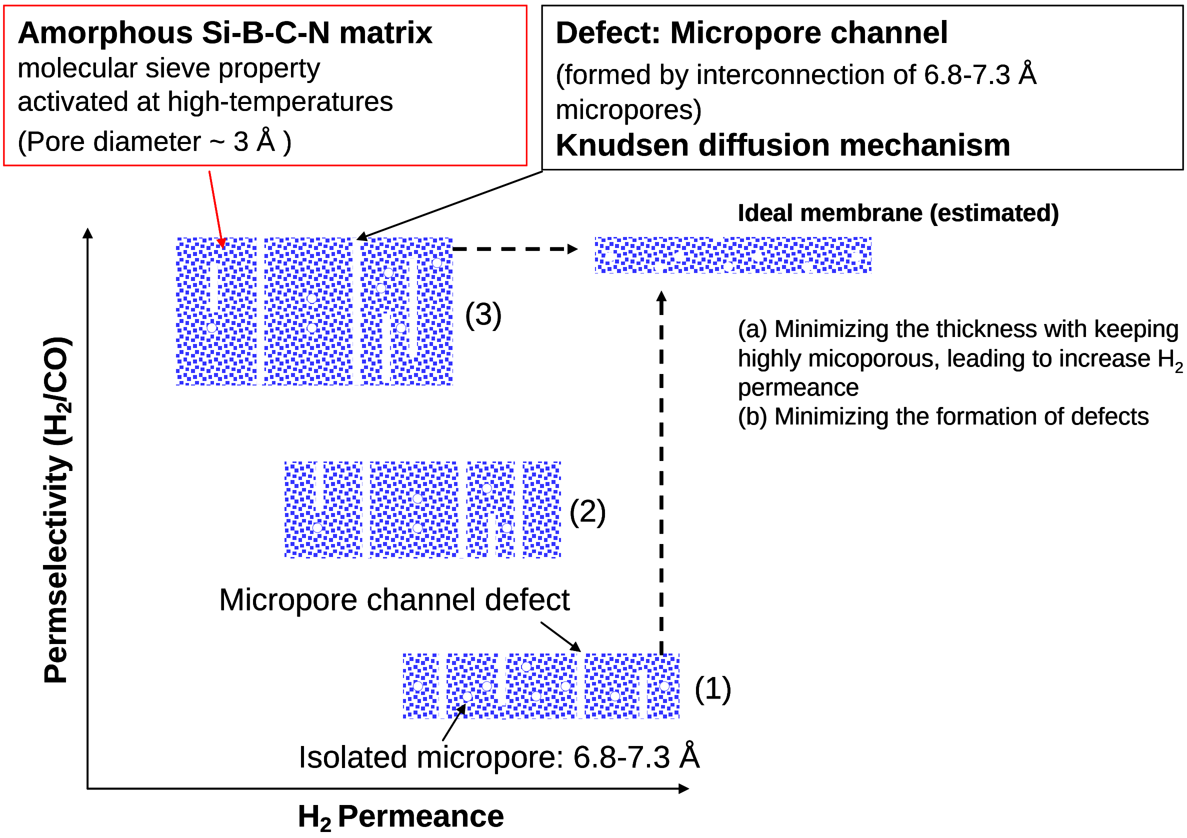

Figure 5.23. Relationship between microstructure and porosity in multilayer amorphous-SiBCN/γ-Al_2O_3/α-Al_2O_3 membranes. Amorphous SiBCN matrix with pore diameter ~3 Å possesses molecular sieve property: H_2 permeation could be activated at high-temperatures. Micropore channel defect is formed by interconnection of 6.8-7.3 Å micropores: both H_2 and CO permeations were governed by the Knudsen diffusion mechanism. Length of micropore channel defects has been drawn based on calculated aspect ratio ~900 obtained by the simulation of SAXS data (section 5.5.2). **(1)**, **(2)**, and **(3)** correspond to membrane thickness after 1-fold, 2-fold, and 3-fold coatings, respectively.

The determined gas permeation properties of mixed gas (Figure 5.19) and single gas permeation measurements (Figure 5.22) point out that the transportation of the gas molecules through the SiBCN membrane is governed by both activated and Knudsen diffusion.

5.8. Membrane/sensor integration: protection coating on SnO_2 sensor

Detection of low amount of CO in fuel cell conditions — high hydrogen background in the absence of oxygen — is a challenging problem for SnO_2-based gas sensors. SnO_2 is not stable in hydrogen-rich background at high temperature being reduced to metallic tin [40-41]. In this section, the membrane/sensor integration possibilities as well as the effect of the membrane on the selectivity of “classical” SnO_2 sensors are investigated. The stability and sensing characteristics of amorphous microporous SiBCN layers coated on SnO_2 sensors is studied in oxygen free atmospheres. For sensor tests, both polymeric-precursors — polyborotrisilazane and polyborotetrasilazane — are used for the deposition of SiBCN layers on SnO_2 sensors.

5.8.1 SiBCN layer (polyborotrisilazane-dervied)/SnO_2 integration

A SnO_2 sensor, previously deposited by screen-printing onto an alumina substrate, is coated with a SiBCN layer by dip-coating of a preceramic polymer followed by pyrolysis at 800 °C for 2 h under flowing argon as described in the experimental procedure (Chapter 2). The latter appeared to be crack-free with a thickness of about 1 µm after single coating and pyrolysis step (Figure 5.24c).

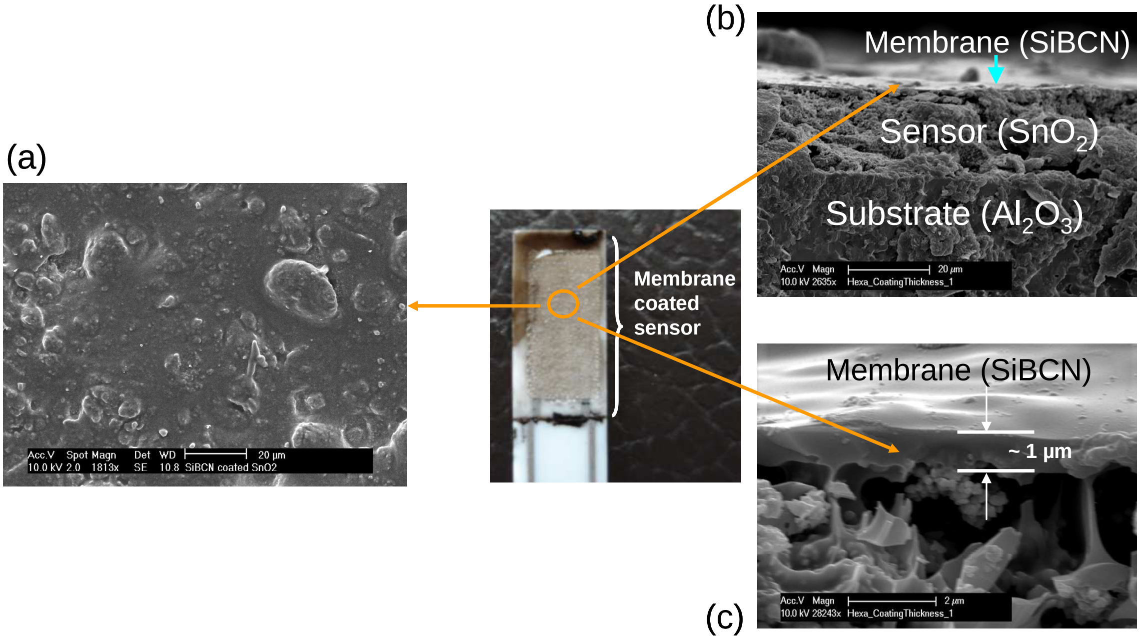

Figure 5.24. Scanning electron microscopy (SEM) image of the surface (a) and the cross-section (b, c) of a 1-fold SiBCN layer coated SnO_2 sensor.

To achieve a sufficient thickness of the ceramic membrane for decreasing/repairing defects in ceramic layers, dip-coating/pyrolysis procedures are repeated several times (i.e. 3 times and 5 times; denoted in the following as 3*SiBCN and 5*SiBCN). Three samples are tested, namely uncoated-, 3 times coated- and 5 times coated-SnO_2 sensors. The background gas is almost oxygen free nitrogen, the test gases used are CO (10, 20 and 150 ppm) and H_2 (40, 400 and 900 ppm) and the total gas flow rate of 500 ml min^{-1} is maintained during the measurement.

As already mentioned, the results obtained by the N_2-adsorption method indicate that the SiBCN layers are microporous with mean pore diameters of about ~7 Å (Figure 5.16) which is larger than that of the the kinetic diameter of H_2 (2.89 Å) and CO (3.86 Å) molecules, allowing in this way their diffusion towards the bottom SnO_2 sensing layer. As demonstrated in Figure 5.25, which shows the transient response to CO and H_2 of uncoated blank SnO_2 and 3-/ 5-fold SiBCN coated SnO_2 sensors at 350 and 530 ºC. A significant difference is found between uncoated and SiBCN coated SnO_2 sensors as well as between sensor response to CO and H_2. For all sensors, reversible resistance changes towards CO exposure are analyzed (Figure 5.25a,c). The SiBCN-coated sensors show larger response/recovery times if compared with those of uncoated SnO_2. Contrary to CO exposure, the hydrogen exposure results in irreversible resistance change of uncoated SnO_2 sensors at 530 ºC. In contrast to the uncoated SnO_2-sensors, the 3-fold and 5-fold SiBCN-coated SnO_2 sensors remained stable and showed a reversible change in the resistance while exposed to H_2.

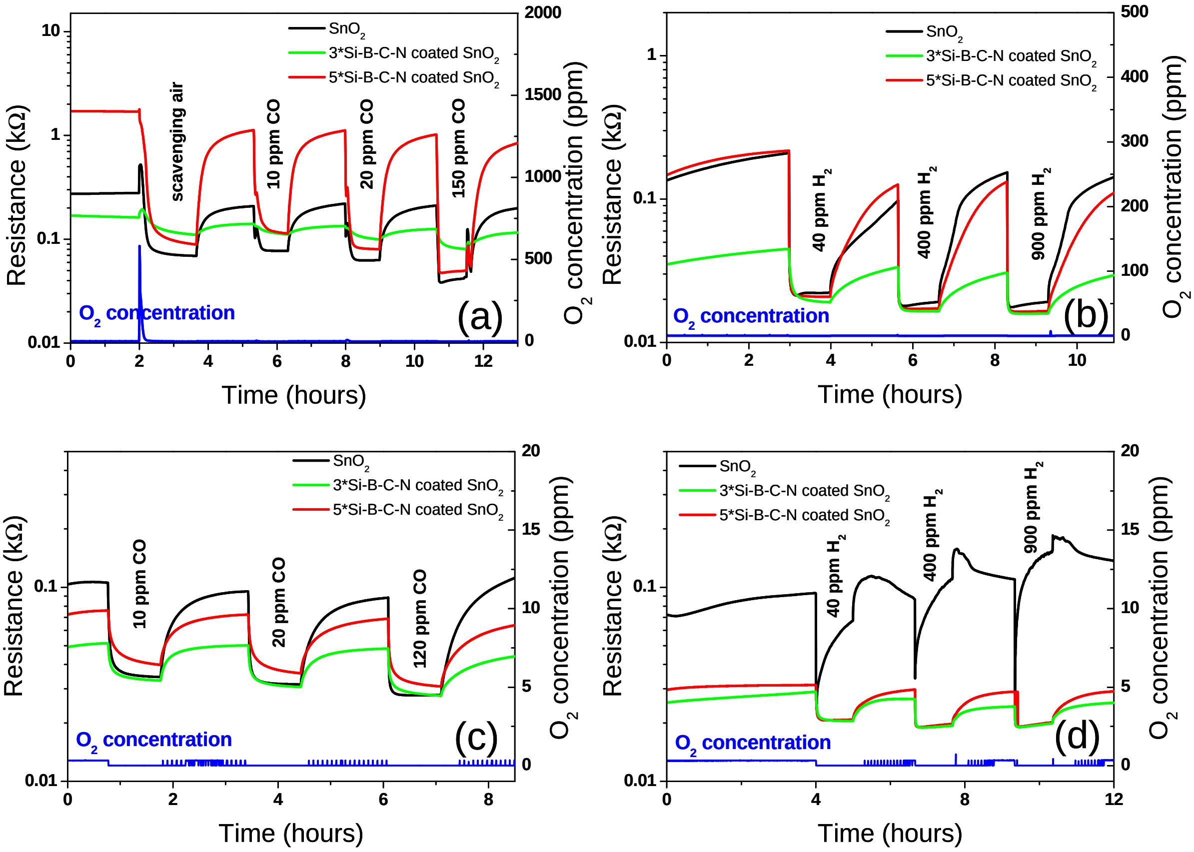

Figure 5.25. Transient response of uncoated and SiBCN (polyborotrisilazane-derived) coated sensors during exposure to CO and H_2 in nitrogen at 350 °C (a, b) and 530 °C (c, d).

Figure 5.26 shows sensor signals of uncoated-, 3- and 5-fold SiBCN coated sensors measured at 350 and 530 °C (except for uncoated SnO_2 sensor at 530 °C). For all gases (CO and H_2 in N_2)/temperatures combinations with exception of H_2 detection on 5-fold SiBCN coated SnO_2 at 350 °C, the 3- and 5-fold SiBCN coated SnO_2 sensors possess smaller sensors signals to H_2 and CO if compared to those of uncoated SnO_2 sensors. This finding indicates that for the 5-fold SiBCN coated SnO_2 sensor, the sensor signals at 350 °C to H_2 are higher and that the ones to CO are almost unaffected if compared to those of the uncoated SnO_2 sensors. This could be due to the formation of cracks in the SiBCN layer or a possible additional contribution of SiBCN to the overall sensing performance.

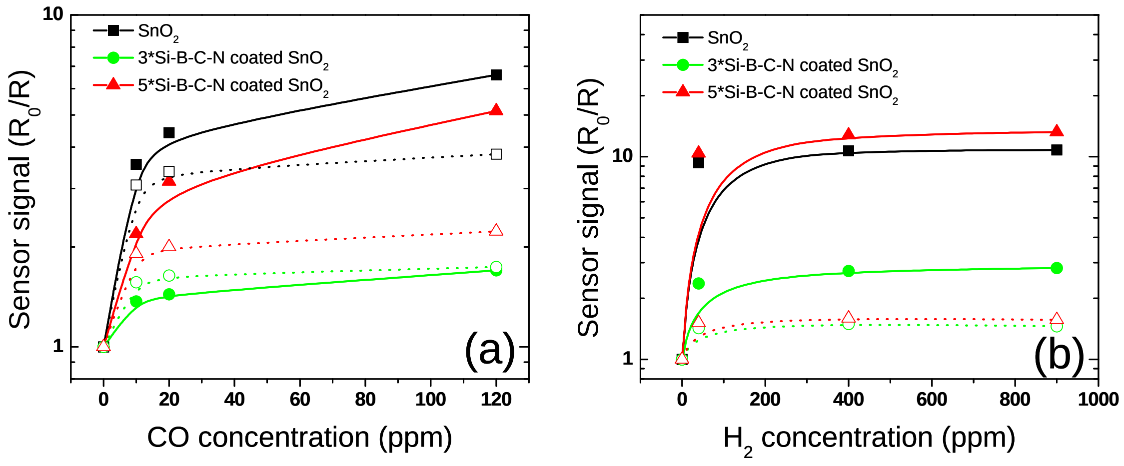

Figure 5.26. Sensor signals (R_0/R) to CO and H_2 in nitrogen at 350 °C (solid lines) and 530 °C (doted lines) for uncoated and SiBCN (polyborotrisilazane-derived) coated SnO_2 sensors.

XRD measurements of the all sensors were done after gas sensing measurement at 530 ºC. The results confirm that the irreversible resistance change of SnO_2 sensors is due to the reduction of SnO_2 to metallic tin (Figure 5.27). Unprotected SnO_2 sensor shows the pattern of metallic tin after sensor test at 530 ºC in 1 vol.% H_2/N_2, while SiBCN coated SnO_2 sensors show no reduction of SnO_2. Accordingly, the top SiBCN layer offers protection to the SnO_2 sensing layers against reduction providing therefore an opportunity for CO/H_2 sensing with SnO_2 under extremely harsh conditions.

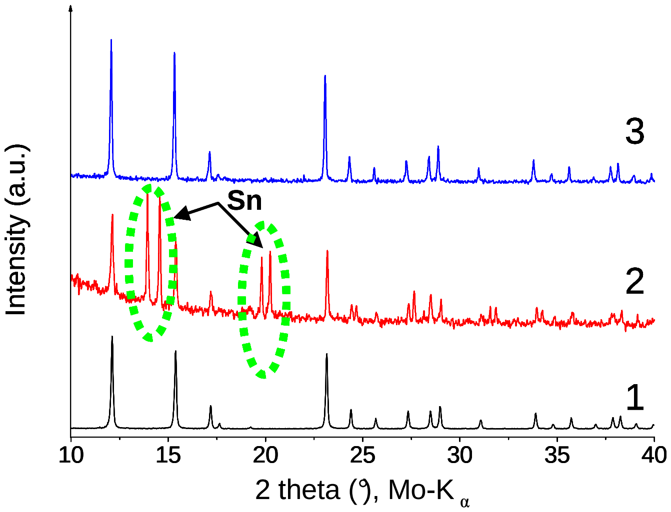

Figure 5.27. X-ray powder diffraction (XRPD) patterns of (1) uncoated SnO_2, (2) SnO_2 after sensor tests at 530 °C in 1 vol.% H_2 /N_2 and (3) SiBCN-coated SnO_2 after sensor tests at 530 °C in 1 vol.% H_2 /N_2. Arrows indicate appearance of Sn pattern.

Therefore, a paradoxical situation appears: H_2 reaches the SnO_2 layer, after passing through SiBCN pore channels, changing their conductivity and simultaneously SnO_2 is not getting reduced at 530 °C. A possible reason is described below.

As discussed recently [40-41], the thermodynamic calculations predict a total reduction of SnO_2 to metallic tin (Sn) according to the reaction (5.5) in 4.5 vol. % H_2 in N_2 at T > 380 K (~107 °C) if the oxygen concentration in the ambient gas is below 5 ppm and at T > 720 K (~447 °C) at oxygen concentrations of about ~1000 ppm.

$$\tfrac{1}{2}\,SnO_2\,(s) + H_2\,(g) \leftrightarrow \tfrac{1}{2}\,Sn\,(s) + H_2O\,(g) \qquad (5.5)$$

The increased stability of SnO_2 in the SiBCN-coated SnO_2 sensors could result from the interplay of at least two factors: (i) the equilibrium of the reaction (5.5) is shifted to the left because the product — gaseous water — cannot diffuse outside through the SiBCN layer freezing in this way the SnO_2 reduction and (ii) the actual H_2 concentration in contact with the SnO_2 layer is much less compared to that required for the reduction of SnO_2. The latter is indirectly confirmed by much lower sensor signal to H_2 at 530 °C in case of the SiBCN-coated SnO_2 if compared to those of the uncoated SnO_2 (Figure 5.26). For the former we have to take into consideration the transport of H_2 and H_2O gas molecules within the SiBCN ceramic layers. As we have already discussed (see section 5.6), the gas transport in amorphous SiBCN layers is due to the interplay of Knudsen diffusion and activated diffusion. Considering the transport of H_2/H_2O occurs through the micropore channels (i.e. “defects” ~7 Å) in the SiBCN-structure, no difference in permeance is expected for H_2 and H_2O which have comparable kinetic diameter (2.89 and 2.65 Å, respectively) and in principle H_2/H_2O could diffuse through the micropore channels in the SiBCN layer. For the Knudsen diffusion, the theoretical Knudsen prediction (inverse square root of the molecular masses) for H_2/H_2O gives a ratio of about of 3.0 which indicates much lower H_2O diffusivity through the SiBCN layer.

An increased stability of microporous SiBCN-coated SnO_2 layer in harsh reducing conditions has been analyzed. The 3-/5-fold SiBCN coated SnO_2 sensors show stable sensor signals towards hydrogen and carbon monoxide in the absence of oxygen whereas the unprotected SnO_2 sample is reduced with time.

5.8.2 SiBCN layer (polyborotetrasilazane-dervied)/SnO_2 integration

Polyborotertasilazane-derived SiBCN ceramics are also used in this work to integrate them with SnO_2 sensors and gas sensing characteristics of membrane/sensors are studied. Four different samples are tested; an uncoated SnO_2 sensor and three other sensors prepared by depositing 1-, 3- and 5-times SiBCN layers on SnO_2 sensors. For sensing measurements, concentration of CO is kept on the same level as used in the previous section 5.7.1 for the sensing measurements of SiBCN (polyborotrisilazane-derived)/SnO_2 while 10, 15, 20 and 150 ppm of H_2 are used. A maximum of 150 ppm H_2 concentration is chosen to avoid reduction of uncoated SnO_2 and to compare its sensing characteristics with SiBCN layer coated SnO_2 sensors. Measurements are performed at 350 and 530 °C.

Typical sensor responses are recorded during CO and H_2 exposures and are shown in Figure 5.28. The resistance changes are found to be reversible for all sensors for all combinations of gases/temperatures. In contrast to the results found in the previous section (section 5.7.1), here we can see reversible resistance for SiBCN ceramic coated SnO_2 sensors when exposed to 150 ppm of H_2 at 530 °C, which indicates that ceramic coated sensors are not reduced at 530 °C. We can also observe that SiBCN coatings on SnO_2 have increased response/recovery time and the effect is more prominent for CO. This increase in response/recovery time could be due to the resistance offered to the gases (H_2, CO) while passing through the SiBCN layers. Although we have not measured pore-size distribution of polyborotetrasilazane-derived SiBCN layer coated on porous supports, but the pore-size distribution of unsupported ceramic (Figure 5.15b) shows presence of significant amount of mesopores along with micropores. Indeed, H_2 and CO passes through these mesoporous channels to reach SnO_2 sensing surface. Based on Knudsen diffusion mechanism (generally observed for mesoporous membranes) H_2/CO selectivity is about 3.74 which indicates faster diffusivity of H_2 compared to CO and hence faster response/recovery when sensors are exposed to H_2.

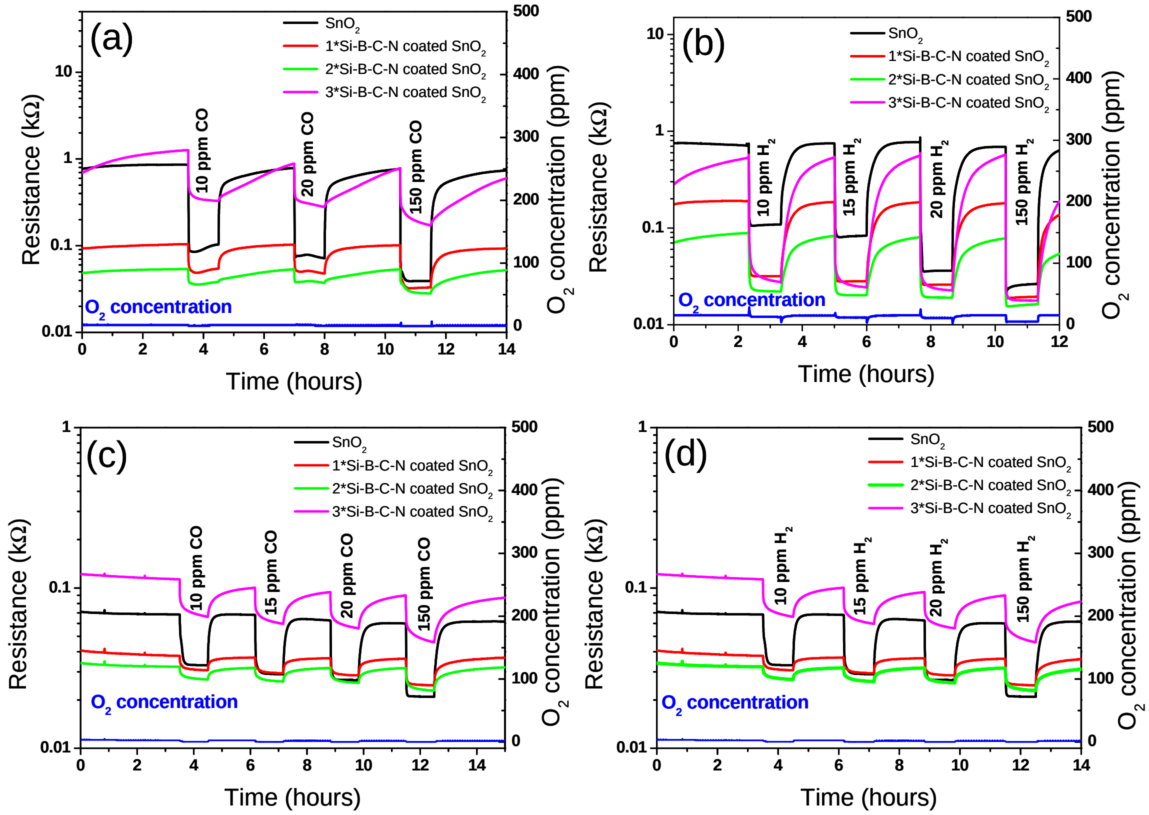

Figure 5.28. Transient response of uncoated and SiBCN (polyborotetrasilazane-derived) coated sensors during exposure to CO and H_2 in nitrogen at 350 °C (a,b) and 530 °C (c,d).

In Figure 5.29, the effect of SiBCN coating layers on the sensor signals are illustrated. At 350 °C one can observe a remarkable increase of the selectivity for H_2 detection brought about by the 3-fold SiBCN layer obtained by pyrolysis of polyborotetrasilazane polymer for all gases/temperature combination. These results indicate that the SiBCN layer acts as a filter for CO molecules and fulfills the expected role of allowing more number of smaller H_2 molecules compared to CO molecules to reach the sensing layer.

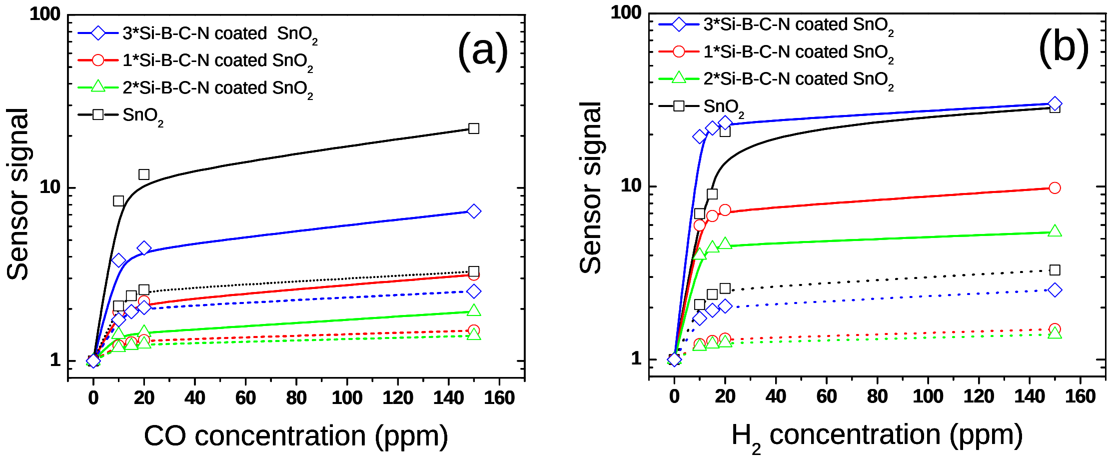

Figure 5.29. Sensor signals (R_0/R) to CO and H_2 in nitrogen at 350 °C (solid lines) and 530 °C (doted lines) for uncoated and SiBCN (polyborotetrasilazane-derived) coated SnO_2 sensors.

5.9. Perspectives for hydrogen separation and sensing

In summary, polymeric precursors — polyborotrisilazane and polyborotetrasilazane — for SiBCN ceramics are synthesized by the hydroboration of cyclotrisilazane and cyclotetrasilazane monomers, respectively. The SiBCN ceramic obtained from polyborotrisilazane precursor is found to be microporous and used for gas permeance measurement and sensing tests by dip-coating of precursor on porous supports and sensors. Polyborotetrasilazane based SiBCN ceramics are also coated on SnO_2 sensors and gas sensing characteristics of membrane/sensor is evaluated. Based on permeance measurements and sensing tests, we can come to many important conclusions.

The observed gas permeation properties point out that the transportation of gas molecules through the membrane is governed by both activated and Knudsen diffusion. H_2 permeation is activated at high-temperatures in amorphous SiBCN matrix which possesses molecular sieve property. In the micropore channel defects of 0.68–0.73 nm, formed by interconnection micropores, both H_2 and CO permeations are governed by the Knudsen diffusion mechanism. The SiBCN membranes exhibit H_2/CO permselectivity of about 10.5 at 440 °C which — in combination with their thermal stability up to 1700 °C [1] — is especially promising for high temperature H_2 purification.

The gas sensing measurements of SiBCN membrane (polyborotrisilazane-dervied) /SnO_2 sensor integration show some remarkable results. At 350 °C the signals to H_2 are considerable higher than the ones for CO. Uncoated SnO_2 sensor at 530 ºC is irreversibly reduced to tin in H_2 while SiBCN coated SnO_2 sensors show reversible resistance changes while exposed to CO and H_2. Presence of the SiBCN filter on SnO_2 sensor results in increase in sensor response and recovery times. However, polyborotetrasilazane-derived 3-fold SiBCN ceramic coated SnO_2 sensor show relatively high H_2 selectivity. In conclusion, the objective of protecting the sensing layer in harsh conditions is achieved by membrane/sensor integration.

5.10. References

[1] R. Riedel, A. Kienzle, W. Dressler, L. Ruwisch, J. Bill, F. Aldinger, "A silicoboron carbonitride ceramic stable to 2000°C," *Nature*, 382 (1996) 796-798.

[2] R. Hauser, S. Nahar-Borchard, R. Riedel, Y.H. Ikuhara, Y. Iwamoto, "Polymer-derived SiBCN ceramic and their potential application for high temperature membranes," *Journal of the Ceramic Society of Japan*, 114 (2006) 524-528.

[3] M.A. Schiavon, G.D. Soraru, I.V.P. Yoshida, "Synthesis of a polycyclic silazane network and its evolution to silicon carbonitride glass," *Journal of Non-Crystalline Solids*, 304 (2002) 76-83.

[4] W.R. Schmidt, D.M. Narsavage-Heald, D.M. Jones, P.S. Marchetti, D. Raker, G.E. Maciel, "Poly(borosilazane) precursors to ceramic nanocomposites," *Chemistry of Materials*, 11 (1999) 1455-1464.

[5] F. Berger, A. Muller, F. Aldinger, K. Muller, "Solid-state NMR investigations on Si-B-C-N ceramics derived from boron-modified poly(allylmethylsilazane)," *Zeitschrift Fur Anorganische Und Allgemeine Chemie*, 631 (2005) 355-363.

[6] H.N. Han, D.A. Lindquist, J.S. Haggerty, D. Seyferth, "Pyrolysis chemistry of poly(organosilazanes) to silicon ceramics," *Chemistry of Materials*, 4 (1992) 705-711.

[7] M.A. Schiavon, S.U.A. Redondo, S.R.O. Pina, I.V.P. Yoshida, "Investigation on kinetics of thermal decomposition in polysiloxane networks used as precursors of silicon oxycarbide glasses," *Journal of Non-Crystalline Solids*, 304 (2002) 92-100.

[8] K. Nakamoto, *Infrared spectra of inorganic and coordination compounds*, Wiley, New York, 1978.

[9] M. Weinmann, T.W. Kamphowe, P. Fischer, F. Aldinger, "Tris(hydridosilylethyl)boranes: highly reactive synthons for polymeric silicon compounds," *Journal of Organometallic Chemistry*, 592 (1999) 115-127.

[10] C. Gervais, F. Babonneau, L. Ruwisch, R. Hauser, R. Riedel, "Solid-state NMR investigations of the polymer route to SiBCN ceramics," *Canadian Journal of Chemistry-Revue Canadienne De Chimie*, 81 (2003) 1359-1369.

[11] J.L. Wan, M.J. Gasch, A.K. Mukherjee, "In situ densification behavior in the pyrolysis consolidation of amorphous Si-N-C bulk ceramics from polymer precursors," *Journal of the American Ceramic Society*, 84 (2001) 2165-2169.

[12] K.S.W. Sing, D.H. Everett, R.A.W. Haul, L. Moscou, R.A. Pierotti, J. Rouquerol, T. Siemieniewska, "Reporting physisorption data for gas solid systems with special reference to the determination of surface-area and porosity (Recommendations 1984)," *Pure and Applied Chemistry*, 57 (1985) 603-619.

[13] A. Guinier, G. Fournet, *Small-Angle Scattering of X-rays*, John Wiley & Sons, New York, 1955.

[14] O. Glatter, O. Kratky, *Small Angle X-ray Scattering*, Academic Press, London, 1982.

[15] T. Takei, M. Chikazawa, "Measurement of pore size distribution of low-surface-area materials by krypton gas adsorption method," *Journal of the Ceramic Society of Japan*, 106 (1998) 353-357.

[16] A.P. Radlinski, M. Mastalerz, A.L. Hinde, A. Hainbuchner, H. Rauch, M. Baron, J.S. Lin, L. Fan, P. Thiyagarajan, "Application of SAXS and SANS in evaluation of porosity, pore size distribution and surface area of coal," *International Journal of Coal Geology*, 59 (2004) 245-271.

[17] R.N. Kyutt, E.A. Smorgonskaya, A.M. Danishevskii, S.K. Gordeev, A.V. Grechinskaya, "Structural study of nanoporous carbon produced from polycrystalline carbide materials: small-angle x-ray scattering," *Physics of the Solid State*, 41 (1999) 1359-1363.

[18] B.J. Olivier, R.R. Lagasse, D.W. Schaefer, J.D. Barnes, G.G. Long, "A small-angle-scattering study of the pore-orientation periodicity in porous polymer and carbon materials," *Macromolecules*, 29 (1996) 8615-8621.

[19] D. Lozano-Castello, J.A. Macia-Agullo, D. Cazorla-Amoros, A. Linares-Solano, M. Muller, M. Burghammer, C. Riekel, "Isotropic and anisotropic microporosity development

upon chemical activation of carbon fibers, revealed by microbeam small-angle X-ray scattering," *Carbon*, 44 (2006) 1121-1129.

[20] D. Fairen-Jimenez, F. Carrasco-Marin, D. Djurado, F. Bley, F. Ehrburger-Dolle, C. Moreno-Castilla, "Surface area and microporosity of carbon aerogels from gas adsorption and small- and wide-angle x-ray scattering measurements," *Journal of Physical Chemistry B*, 110 (2006) 8681-8688.

[21] S. Berthon-Fabry, D. Langohr, P. Achard, D. Charrier, D. Djurado, F. Ehrburger-Dolle, "Anisotropic high-surface-area carbon aerogels," *Journal of Non-Crystalline Solids*, 350 (2004) 136-144.

[22] G. Laudisio, R.K. Dash, J.P. Singer, G. Yushin, Y. Gogotsi, J.E. Fischer, "Carbide-derived carbons: A comparative study of porosity based on small-angle scattering and adsorption isotherms," *Langmuir*, 22 (2006) 8945-8950.

[23] Y. Gogotsi, A. Nikitin, H.H. Ye, W. Zhou, J.E. Fischer, Y. Bo, H.C. Foley, M.W. Barsoum, "Nanoporous carbide-derived carbon with tunable pore size," *Nature Materials*, 2 (2003) 591-594.

[24] T.M. Nenoff, R.J. Spontak, C.M. Aberg, "Membranes for hydrogen purification: An important step toward a hydrogen-based economy," *MRS Bulletin*, 31 (2006) 735-741.

[25] G.Q. Lu, J.C.D. da Costa, M. Duke, S. Giessler, R. Socolow, R.H. Williams, T. Kreutz, "Inorganic membranes for hydrogen production and purification: A critical review and perspective," *Journal of Colloid and Interface Science*, 314 (2007) 589-603.

[26] J. Dong, Y.S. Lin, M. Kanezashi, Z. Tang, "Microporous inorganic membranes for high temperature hydrogen purification," *Journal of Applied Physics*, 104 (2008) -.

[27] P. Bernardo, E. Drioli, G. Golemme, "Membrane gas separation: A review/state of the art," *Industrial & Engineering Chemistry Research*, 48 (2009) 4638-4663.

[28] Y. Iwamoto, "Precursors-derived ceramic membranes for high-temperature separation of hydrogen," *Journal of the Ceramic Society of Japan*, 115 (2007) 947-954.

[29] M.C. Duke, J.C.D. da Costa, D.D. Do, P.G. Gray, G.Q. Lu, "Hydrothermally robust molecular sieve silica for wet gas separation," *Advanced Functional Materials*, 16 (2006) 1215-1220.

[30] W. Feng, T.W. Tan, P.J. Ji, D.X. Zheng, "Exploration of hydrogen production in a membrane reformer," *Aiche Journal*, 52 (2006) 2260-2270.

[31] B. Elyassi, M. Sahimi, T.T. Tsotsis, "Silicon carbide membranes for gas separation applications," *Journal of Membrane Science*, 288 (2007) 290-297.

[32] Y. Iwamoto, K. Sato, T. Kato, T. Inada, Y. Kubo, "A hydrogen-permselective amorphous silica membrane derived from polysilazane," *Journal of the European Ceramic Society*, 25 (2005) 257-264.

[33] N.W. Ockwig, T.M. Nenoff, "Membranes for hydrogen separation," *Chemical Reviews*, 107 (2007) 4078-4110.

[34] Y.F. Gu, S.T. Oyama, "High molecular permeance in a poreless ceramic membrane," *Advanced Materials*, 19 (2007) 1636-1640.

[35] J. Hedlund, F. Jareman, "Single gas permeance ratios in MFI membranes: Effects of material properties and experimental conditions," *Microporous and Mesoporous Materials*, 82 (2005) 201-207.

[36] Y. Iwamoto, "Precursors Derived Ceramic Membranes," E-MRS Spring Meeting, Strasbourg, 2004.

[37] R.R. Bhave, *Inorganic Membranes: Synthesis, Characteristics and Applications*, Van Nostransd Reinhold, New York, 1991.

[38] K. Kusakabe, Z.Y. Li, H. Maeda, S. Morooka, "Preparation of supported composite membrane by pyrolysis of polycarbosilane for gas separation at high-temperature," *Journal of Membrane Science*, 103 (1995) 175-180.

[39] Z.Y. Li, K. Kusakabe, S. Morooka, "Preparation of thermostable amorphous Si-C-O membrane and its application to gas separation at elevated temperature," *Journal of Membrane Science*, 118 (1996) 159-168.

[40] O. Wurzinger, G. Reinhardt, "CO-sensing properties of doped SnO_2 sensors in H_2-rich gases," *Sensors and Actuators B: Chemical*, 103 (2004) 104-110.

[41] S. Albert, J.P. Viricelle, G. Tournier, P. Breuil, C. Pijolat, "Detection of oxygen traces in nitrogen- and hydrogen-rich atmosphere," *Sensors and Actuators B: Chemical*, 139 (2009) 298-303.

Chapter 6. Microporous Si_3N_4 membranes through ammonia-assisted pyrolysis of polysilazane

In this chapter, polysilazane HTT 1800 derived Si_3N_4 ceramics are characterized with respect to hydrogen purification and as a filter to improve selectivity of gas sensors. KiON HTT 1800 is a patented liquid polysilazane-based resin. It is a pale yellow, low viscosity liquid. As-received commercially available polysilazane HTT 1800 is treated without further purification under argon and ammonia to get ceramic membranes. Two different GaN powders are used in this work as sensing materials: (i) as-synthesized and (b) commercial GaN.

Section 6.1 describes the structure of as-received polymer which is studied by liquid-state NMR spectroscopy and ATR-IR spectroscopy. Polymer-to-ceramic transformation, microstructure characterizations and morphology of the Si_3N_4 membrane coating are illustrated in sections 6.2–6.4. The performances of Si_3N_4 ceramic membranes — obtained by dip-coating of preceramic polymeric solution on porous alumina supports and on GaN based gas sensors followed by pyrolysis under dry ammonia — have been studied with respect to H_2/CO_2 selectivity and as a H_2 selective gas sensors, which are described in sections 6.5–6.6.

6.1. Structure of the pre-ceramic polymer

Molecular structure of as-received polymer HTT 1800 polysilazane is analyzed using ^{1}H, ^{29}Si and ^{13}C liquid-state NMR and ATR-IR spectroscopic characterization.

6.1.1 Liquid-state NMR characterization

^{1}H NMR

The ^{1}H spectrum of HTT 1800 is shown in Figure 6.1 and the respective chemical shifts (Si-CH_3, Si-H, C-H, N-H) are listed in Table 6.1.

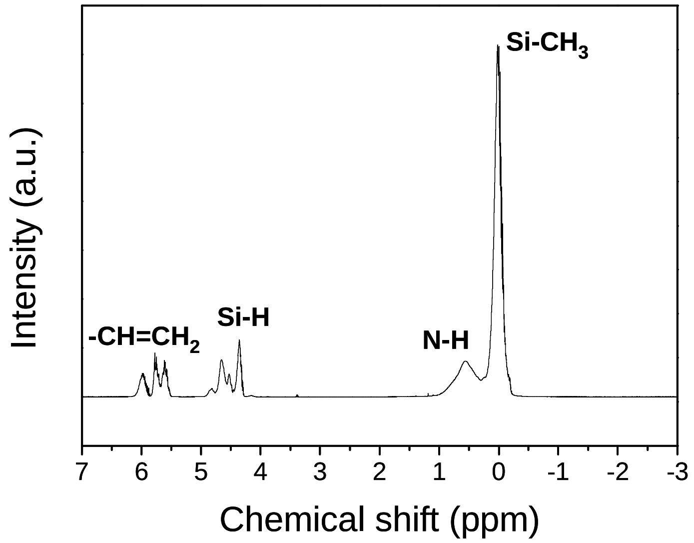

Figure 6.1. ^1H liquid-state NMR spectrum of HTT 1800 polysilazane, C_6D_6 as solvent.

Si*H* protons appear as multiplets between 4.28 and 4.92 ppm [1]. N*H* resonace can be observed as broad signals at around 0.6 ppm [1]. SiCH_3 protons are found as a broad resonance around 0 ppm [1]. The different chemical environments of the methyl groups can be seen as broad resonance centred at 0 ppm. Multiplets between 5.50 and 6.12 ppm can be attributed to the presence of Si-CH=CH_2 [2].

Table 6.1. Experimental ^1H chemical shifts of KiON HTT 1800 polysilazane.

Polymer	**^1H chemical shifts (ppm)**			
	Si-CH_3	**N-H**	**Si-H**	**Si-CH=CH_2**
HTT 1800 polysilazane	0.18 – -0.14	0.95 – 0.35	4.92 – 4.28	6.12 – 5.50

^{29}Si NMR

In agreement with literature [3] the observed broad resonance peaks ranging from -18 to -24 ppm confirms dominant peaks are related to [-Si(CH_3)(CH=CH_2)-NH], Figure 6.2. The minor ^{29}Si peak at -32 ppm could be assigned to presence of trace amount of -SiH_2- functionality [4].

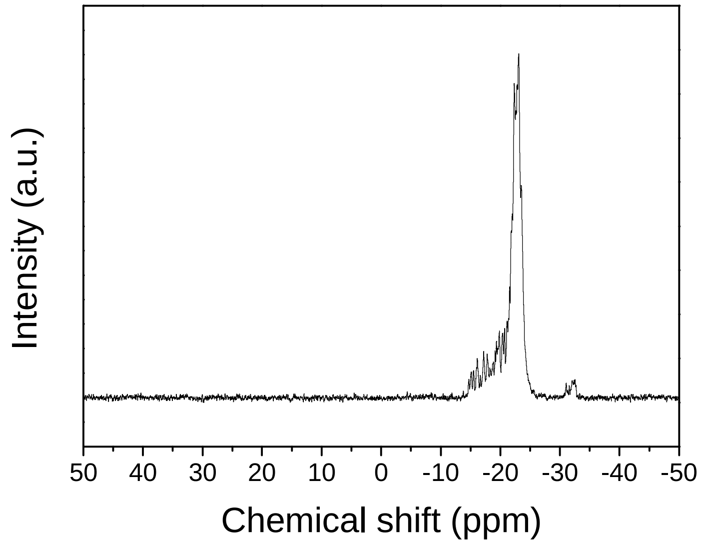

Figure 6.2. ^{29}Si DEPT liquid-state NMR spectrum of HTT 1800 polysilazane, C_6D_6 as solvent.

^{13}C NMR

In the ^{13}C spectrum (from Figure 6.3 and Table 6.2), the signals corresponding to methyl and vinyl groups attached to silicon are observed. The broad resonance signals in the range -0.57 to 7.0 ppm is related to $Si-CH_3$. Chemical shifts of 132–141 ppm are assigned to $Si-CH=CH_2$ [2].

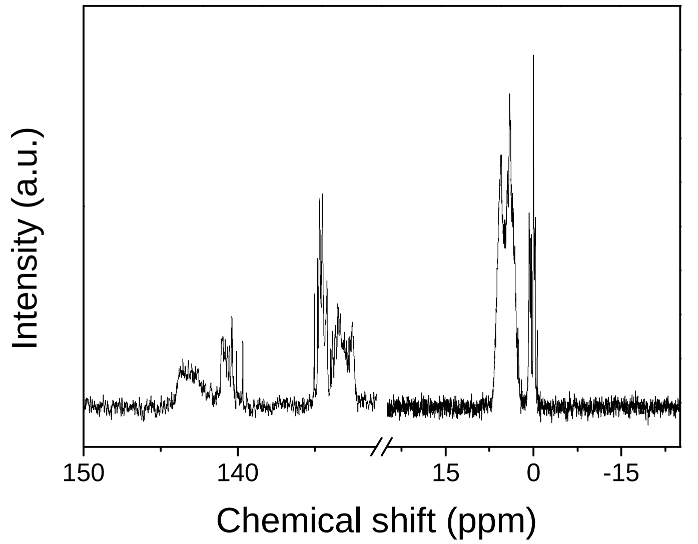

Figure 6.3. ^{13}C liquid-state NMR spectrum of HTT 1800 polysilazane, C_6D_6 as solvent.

Table 6.2. Experimental ^{13}C chemical shifts of KiON HTT 1800 polysilazane

Polymer	**^{13}C chemical shifts (ppm)**	
	Si-CH_3	**Si-CH=CH_2**
HTT 1800 polysilazane	7.06 – -0.57	141.41 – 132.21

6.1.2 ATR-IR characterization

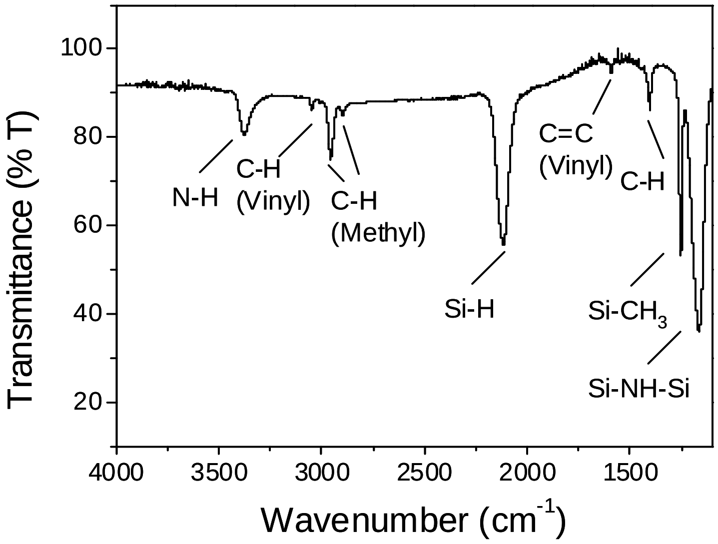

Figure 6.4. ATR-IR spectrum of HTT 1800 polysilazane.

The ATR-IR spectrum (Figure 6.4) of the polymer shows a strong and broad band of Si-H at 2217 cm^{-1}. A strong band at 1254 cm^{-1} is ascribed to Si-CH_3. Other absorptions are present at 3047, 2957, 2898 and 1404 cm^{-1} (C-H); two broad bands at 3379 and 1165 cm^{-1} could be assigned to N-H and Si-NH-Si bonds respectively [1]. The vibration bands and respective bonds of the polymer are listed in Table 6.3.

Table 6.3. Vibration bands and respective bonds of as-received HTT 1800 polysilazane polymer measured by ATR-IR.

Vibration band (cm^{-1}) of HTT 1800 polysilazane	**Bond assignment**[a]
3423–3308	*ν*(N-H)
3061–3032	*ν*(C-H) Vinyl
2987–2879	*ν*(C-H) Methyl
2190–2046	*ν*(Si-H)
1590	*ν*(C=C) Vinyl
1404	*δ*(C-H)
1254	*δ*(Si-CH_3)
1165	*δ*(N-H)

[a] *ν* – stretching, *δ* – deformation.

Based on the results obtained by liquid-state NMR and ATR-IR measurements, the molecular structure of the as-received commercial KiON HTT 1800 polysilazane could be inferred as shown in Figure 6.5.

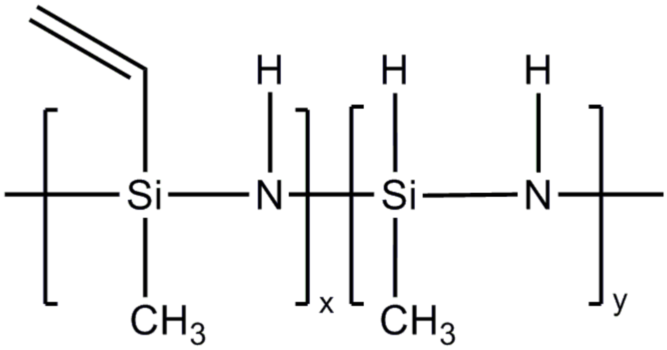

Figure 6.5. Molecular structure of as-received HTT 1800 polysilazane based on liquid-state NMR and ATR-IR measurements.

6.2. Pyrolysis of HTT 1800 polysilazane under argon

6.2.1 Polymer to ceramic transformation

In order to determine polymer-to-ceramic transformation temperature and to select an appropriate pyrolysis temperature for depositing ceramic membrane on porous supports and on gas sensors, Simultaneous Thermal Analysis (STA) is performed.

6.2.1.1 STA characterization

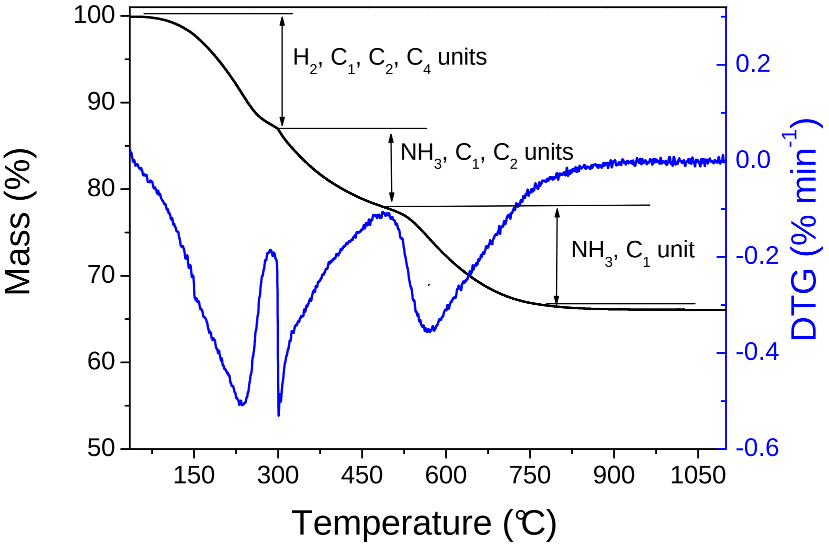

Figure 6.6. Thermal gravimetric analysis (TGA) curve of HTT 1800 polysilazane (heating rate 5 °C min^{-1} in flowing argon). Ceramic yield: 67% by mass.

TGA/DTG curves of HTT 1800 polysilazane under argon environment are shown in Figure 6.6. Mass loss is observed mainly in three different temperature regions. In the first region (100–300 °C) during cross-linking of polymer hydrogen (m/z: 2, 1), methane (m/z: 16, 15), C_2 (m/z: 28, 27), C_3 (m/z: 41) and C_4 (m/z: 102, 101) are detected. In the second region, ammonia (m/z: 17), methane (m/z: 28, 27) and C_2 (m/z: 28, 27) units are observed up to 500 ºC. In the temperature range from 500 to 800 ºC, masses are lost in the form of methane (m/z: 16, 15) and ammonia (m/z: 17). Almost no mass loss is observed above 750 °C indicating completion of ceramization process with a ceramic yield of about 67 % by mass under argon.

Based on the thermogravimetric analysis (TGA) of HTT 1800 polysilazane, unsupported ceramic powders are synthesized by pyrolysing polysilazane under argon atmosphere at T ≥ 800 ºC, i.e. the lowest temperature above which minimal mass loss is observed. Structural characterizations of synthesized ceramic powders are discussed below.

6.2.2 Microstructural characterization of unsupported ceramic powders

The information that is obtained by microstructure investigation of ceramic powder is the first and an important aspect to determine if the ceramic can be used for a specific application. Therefore, microstructural characterizations of the ceramic powder are performed using XRD, Pore-size analysis, solid-state MAS NMR measurement and elemental analysis.

6.2.2.1 XRD characterization

X-ray powder diffraction patterns of HTT 1800 polysilazane derived ceramics obtained by pyrolysis of HTT 1800 polysilazane at two different temperatures 800 °C and 1000 °C under flowing argon is shown in Figure 6.7. The obtained ceramics are found to be X-ray amorphous.

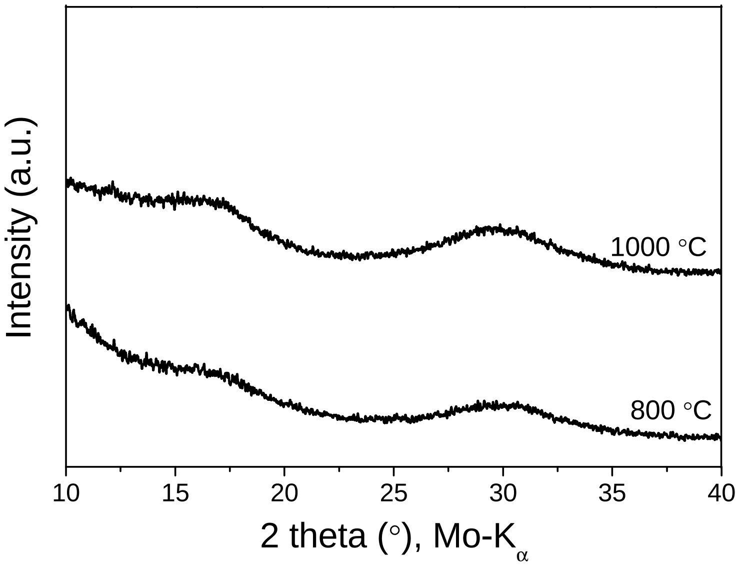

Figure 6.7. XRD patterns of HTT 1800 polysilazane derived ceramics obtained at 800 ºC and 1000 ºC by pyrolysing under argon.

6.2.2.2 Porosity characteristics

A nitrogen physisorption isotherm, as shown in Figure 6.8a, of the obtained powdered Si_3N_4 sample is found to be type II in nature according to IUPAC classification [6]. Very low uptake of nitrogen at low pressure indicates absence of microporosity. The increasing uptake at relative high pressure could be attributed to the presence of macropores or interparticular space. Therefore, membrane obtained at this temperature could not be used for permeance measurements.

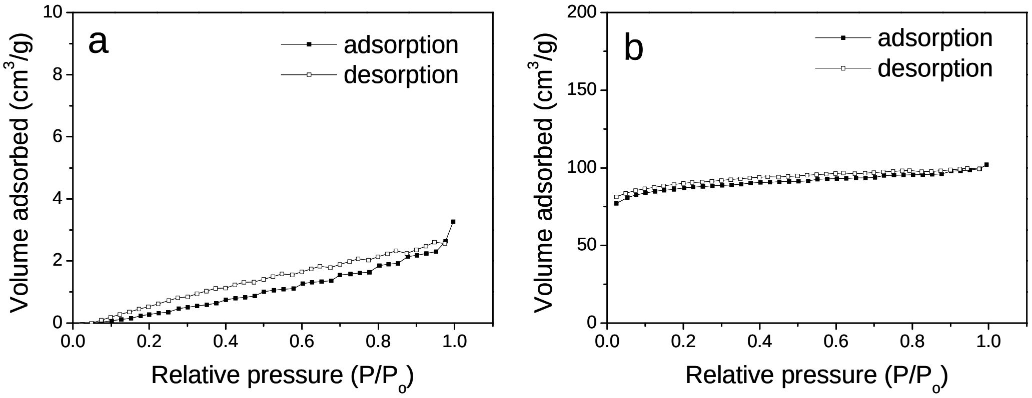

Figure 6.8. Nitrogen physisorption isotherms at 77 K for the unsupported ceramic powders obtained by pyrolysis of HTT 1800 polysilazane in flowing argon (a) at 800 °C and (b) at 600 °C.

In order to verify if gases coming out during pyrolysis of polysilazane at lower temperatues under argon leads to microporous ceramic formation, two other samples were prepared under argon at 700 ºC and 600 ºC. The sample pyrolyzed at 700 ºC is also found to be non-porous like the one obtained at 800 ºC, based on nitrogen physisorption isotherm. Nitrogen physisorption isotherm (see Figure 6.8b) of the sample pyrolyzed at 600 ºC is found to be of the type I in nature [6], which confirms that samples pyrolyzed at T (< 700 °C) are microporous. But these samples are not suitable to be used for membrane synthesis because of their instability due to the incomplete polymer-to-ceramic transformation (see Figure 6.6). The pore-size characterisctics of the samples obtained by pyrolysis at and above 600 ºC under argon environment imply that the micropores that are generated at temperatures below 700 ºC during gas evolution from the polymer gets collapses at higher temperatures due to viscous flow [7] in the material.

Table 6.4. Results of nitrogen physisorption measurements (specific surface area, micropore volume, pore-type) of polymer derived ceramic from HTT 1800 polysilazane by pyrolysis under argon at different temperatures (600–800 °C).

Pre-ceramic polymer	**Pyrolysis temperature & environment**	**BET specific surface area (m^2 g^{-1})**	**Micropore volume[a] (cm^3 g^{-1})**	**Porous structure**
KiON HTT 1800 polysilazane	600 °C, argon	295	0.13	microporous
	700 °C, argon	< 10	-	non-porous
	800 °C, argon	< 10	-	non-porous

[a] using ‘t-method’

6.2.2.3 Elemental analysis

The result of elemental analysis of the sample pyrolyzed at 800 °C under argon is presented in Table 6.5. Ceramic powder obtained after pyrolysis under argon was black in color and contain 20.65 wt.% of carbon.

Table 6.5. Elemental composition of the ceramics obtained after pyrloysis of HTT 1800 polysilazane under flowing argon at 800 °C.

Ceramic from HTT 1800 polysilazane	**Si (wt. %)**	**C (wt. %)**	**N (wt. %)**	**H (wt. %)**	**O[a] (wt. %)**	**Empirical Formula**
800 °C (argon)	54.23	20.65	22.40	0.58	2.14	$Si_1C_{0.89}N_{0.82}O_{0.06}H_{0.3}$

[a] small oxygen contamination may have occurred during manipulation of samples in air.

The above results indicate that ceramics obtained by the pyrolysis of HTT 1800 polysilazane under argon are not suitable for membrane synthesis.

6.3. Pyrolysis of HTT 1800 polysilazane under ammonia

There have been several works [8-10] done by different research groups to obtain unsupported microporous ceramic powders by the pyrolysis of different types of polysilazanes under ammonia atmosphere. However, not much work has been attempted to develop membranes on porous supports through ammonia-assisted pyrolysis of polysilazane. In our case, pyrolysis of HTT 1800 polysilazane under dry ammonia has been done to obtain suitable ceramic membranes — to study their gas separation performances — which are discussed in the following sections.

6.3.1 Polymer to ceramic transformation

6.3.1.1 Thermal gravimetric analysis (TGA) characterization

TGA characterization of HTT 1800 polysilazane pyrolyzed under ammonia is performed using the experimental procedure described in Chapter 4 to know its yield under ammonia. Very little mass loss is observed above 700 °C indicating completion of ceramization process with a ceramic yield of about 51% by mass under argon (see Figure 6.9). Comparing the yield of polysilazane under argon (Figure 6.6) and under ammonia illustrates that pyrolysis under ammonia suffers more mass loss compared to when done under argon.

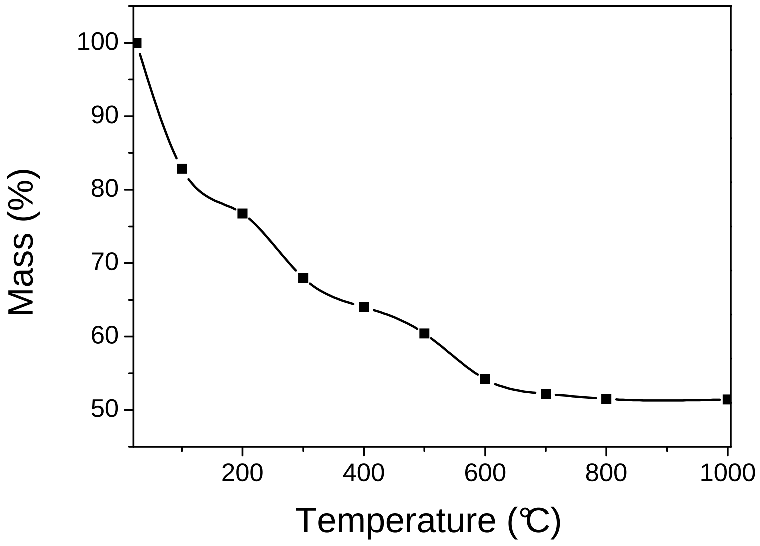

Figure 6.9. Thermal gravimetric analysis (TGA) curve of HTT 1800 polysilazane (heating rate 1 °C min^{-1} in flowing ammonia).

The above TG curve shows completion of ceramization process above 700 °C; therefore, HTT 1800 polysilazane was pyrolyzed under ammonia at 800 °C and 1000 °C to obtain useful microporous ceramics and to examine their thermal stability. The microstructural characteristics of the as-synthesized samples were studied and are discussed below.

6.3.2 Microstructural characterization of unsupported ceramic powders

6.3.2.1 XRD characterization

X-ray powder diffraction patterns of HTT 1800 polysilazane derived ceramics obtained by pyrolysis of HTT 1800 polysilazane at 800 °C and 1000 °C under flowing ammonia are shown in Figure 6.10. The ceramics obtained at both temperatures are found to be amorphous. Amorphous ceramics are more favorable because grain boundary in crystalline materials can act as a defect for gas separation applications.

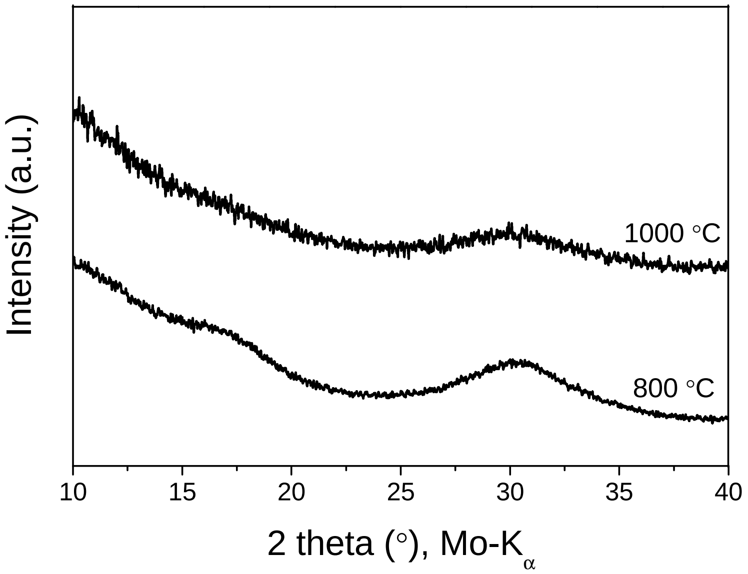

Figure 6.10. XRD patterns of HTT 1800 polysilazane derived ceramics obtained at 800 ºC and 1000 ºC by pyrolysing under ammonia.

6.3.2.2 Porosity characteristics

Nitrogen-adsorption isotherms and pore-size distribution of synthesized powdered samples are shown in Figure 6.11a, b and BET surface area and microporous volume data are listed in Table 6.6. Nitrogen physisorption isotherm of the obtained ceramic by ammonolysis at 800 °C is found to be of type I, while the presence of small amount of hysteresis in the sample ammonolyzed at 1000 °C could be attributed to development of mesoporosity at higher temperature. Micropore volume of the powder obtained by dry ammonia pyrolysis at 800 °C is found to be 0.11 cm^3 g^{-1} using ‘t-method’ [6] (see Table 6.6).

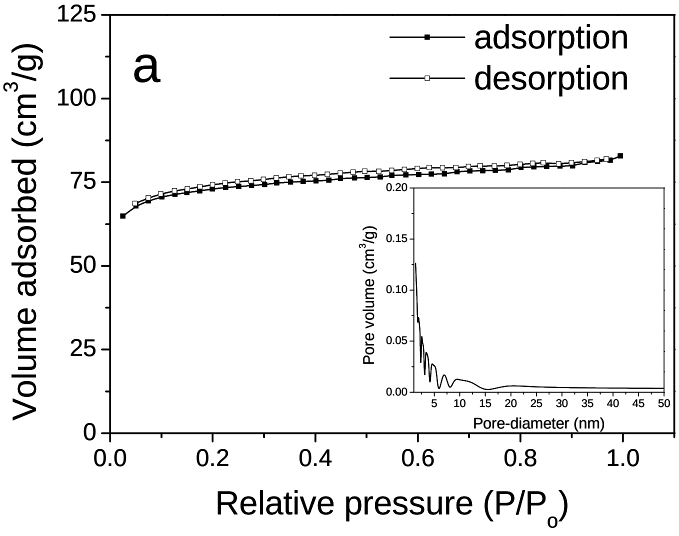

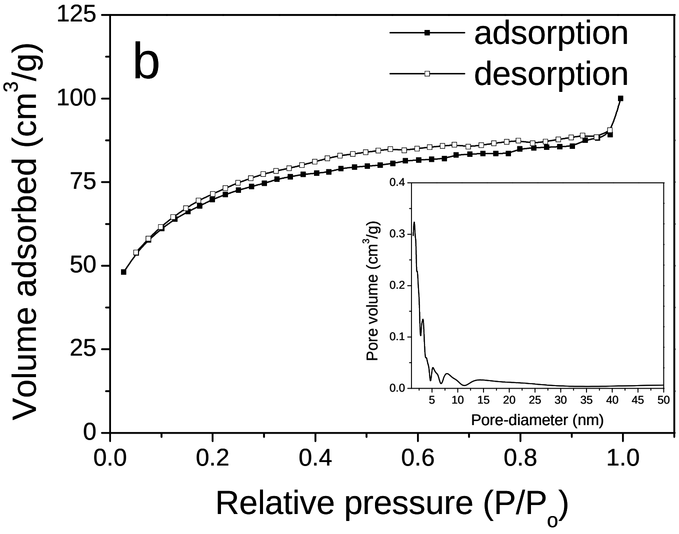

Figure 6.11. Nitrogen physisorption isotherms at 77 K and pore-size distribution (Inset) of pyrolysed HTT 1800 polysilazane in flowing dry ammonia (a) at 800 °C and (b) at 1000 °C.

Table 6.6. Results of nitrogen physisorption measurements (specific surface area, micropore volume, pore-type) of polymer derived ceramic from HTT 1800 polysilazane by pyrolysis under argon and ammonia at different temperatures.

Pre-ceramic polymer	**Pyrolysis temperature & environment**	**BET specific surface area (m^2 g^{-1})**	**Micropore volume[a] (cm^3 g^{-1})**	**Porous structure**
KiON HTT 1800 polysilazane	800 °C, NH_3	255	0.11	microporous
	1000 °C, NH_3	237	0.09	microporous, small amount of mesoporous

[a] using ‘t-method’

6.3.2.3 Elemental analysis

Elemental analysis of the sample pyrolyzed at 800 °C under in dry ammonia is presented in Table 6.7. It indicates a very high amount of carbon is lost by the ammonolysis of polysilazane. Ceramic powder obtained after pyrolysis under argon and under ammonia contain 20.65 (Table 6.5) and 2.19 wt.%, respectively, of carbon. Ceramic obtained by pyrolysis under argon is found to be black in color whereas the amorphous ceramic powder obtained by ammonolysis is appeared to be grey-white. Change in colour from black to grey-white by pyrolysis under ammonia could be due to loss of almost all carbon present in the polymer.

Table 6.7. Elemental composition of the ceramics obtained after pyrloysis of HTT 1800 polysilazane under flowing argon and in dry ammonia at 800 °C.

Ceramic from HTT 1800 polysilazane	**Si (wt. %)**	**C (wt. %)**	**N (wt. %)**	**H (wt. %)**	**O[a] (wt. %)**	**Empirical Formula**
800 °C (ammonia)	56.90	2.19	38.89	1.30	0.72	$Si_1C_{0.09}N_{1.37}O_{0.04}H_{0.34}$

[a] small oxygen contamination may have occurred during manipulation of samples in air.

6.3.2.4 Solid-state MAS NMR (^{29}Si) characterization

Based on nitrogen-isotherms and pore-size distribution of the ceramics obtained by the ammonolysis of HTT 1800 polysilazane, it is clear that the ceramics which are obtained at and above 800 °C are microporous and could be used for hydrogen purification. To understand the structure of the amorphous ceramic powders obtained, solid-state ^{29}Si MAS NMR measurements are performed. ^{13}C MAS NMR measurement is not performed due to the presence of very small amount of carbon left in the ceramic powder after ammonolysis — based on elemental analysis result (from Table 6.7). Figure 6.12 illustrates the ^{29}Si MAS NMR spectra of the grey-white amorphous ceramic obtained at 800 °C and 1000 °C.

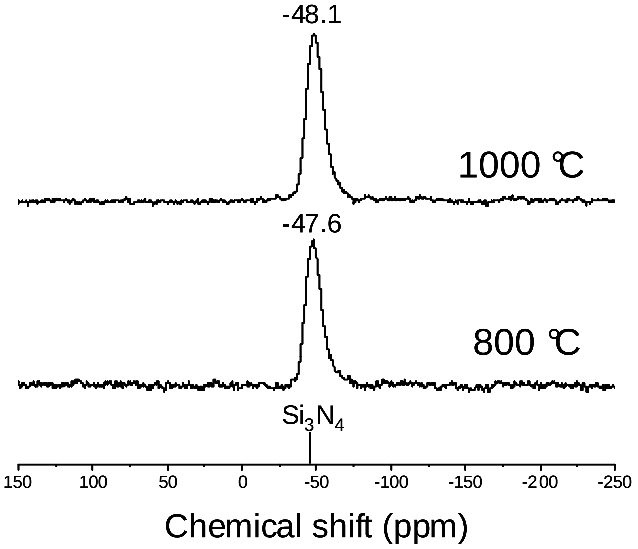

Figure 6.12. ^{29}Si MAS NMR spectrum of the grey-white amorphous ceramic powders obtained by dry ammonia pyrolysis of HTT 1800 polysilazane at 800 and 1000 °C.

The spectra exhibit single peak for the samples ammonolyzed at 800 and 1000 °C. A broad peak at -47.6 ppm is present for powder obtained at 800 °C. The ^{29}Si spectrum of the sample obtained at 1000 °C displays a signal at -48.1 ppm. Peaks in these positions are typical of Si_3N_4-type species and have been observed in previous studies of other polysilazane, polycarbosilazane polymers after pyrolysis in dry ammonia [9]. No silicon oxide impurities (-100 $\pm$ 10 ppm) are detected in the ^{29}Si spectra. As no sharp signal is found at -41 ppm which could be attributed to silicon imidonitride [2] , we can confirm the absence of amide/imide group in the samples synthesised at 800 and 1000 °C in dry ammonia. Presence of amide/imide groups in the ceramics is prone to reaction with moisture.

XRD analysis, pore-size distribution measurement, elemental analysis and ^{29}Si MAS NMR measurement of the ceramic powder obtained by the ammonolysis of HTT 1800 polysilazane at 800 °C confirm formation of amorphous-microporous-Si_3N_4 ceramic powder.

6.4. Morphology and structure of the membrane coating

As shown in Chapter 4 (section 4.2 and 4.3), γ-Al_2O_3/α-Al_2O_3 support is thermally unstable above 800 °C, therefore pyrolysis temperature of 800 °C is selected for the deposition of Si_3N_4 membrane on porous alumina support under dry ammonia. The deposition of diluted-polysilazane polymeric solutions (60 by vol. % in dry toluene) is done by dip-coating method as described in the experimental procedure (see Chapter 2). The thickness of the ceramic membrane after ammonloysis is measured by scanning electron microscope.

6.4.1 SEM characterization

Figure 6.13 and Figure 6.14 show SEM image of Si_3N_4 membrane developed on a γ-Al_2O_3/α-Al_2O_3 porous membrane support and on a GaN sensor, respectively. The thickness of Si_3N_4 membrane after single coating/pyrolysis step on porous support and after three-fold coating/pyrolysis on GaN sensor at 800 °C in dry ammonia is found to be about 0.7 µm and 1 µm, respectively.

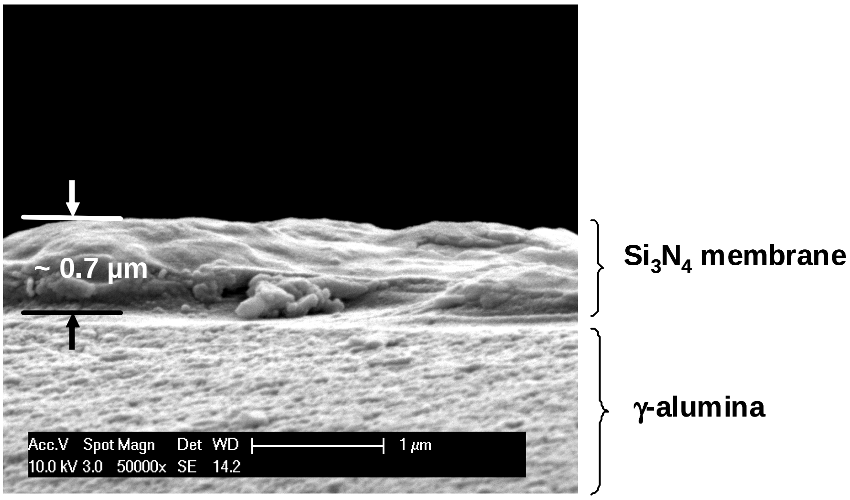

Figure 6.13. Scanning electron microscopy (SEM) image of the cross-section of amorphous Si_3N_4 membrane developed on γ-alumina/α-alumina membrane by ammonolysis of HTT 1800 polysilazane under dry ammonia at 800 °C.

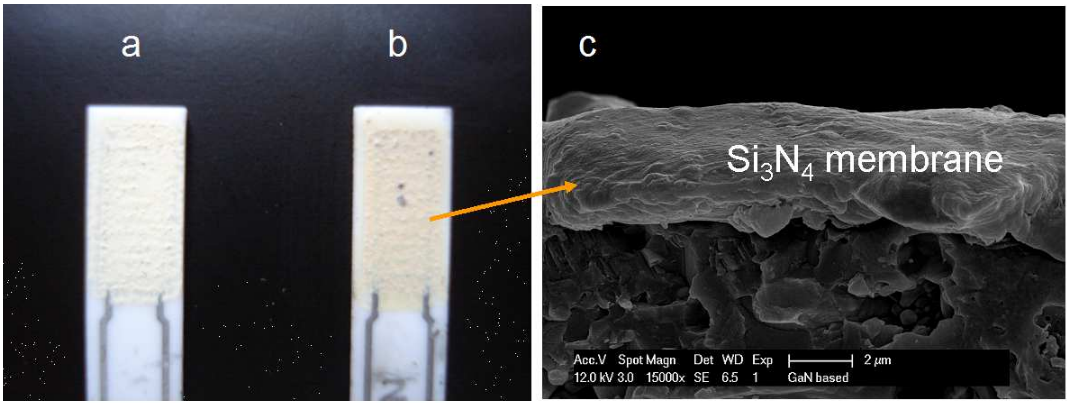

Figure 6.14. Digital images of the surface of (a) uncoated GaN sensor, (b) three fold-Si_3N_4 coated GaN sensor, and (c) Scanning electron microscopy (SEM) image of the cross-section of Si_3N_4 coated GaN sensor. As-synthesized GaN powder is used for sensing material.

6.5. Performance in hydrogen separation and mechanism of gas permeance

The high specific surface area ~255 m^2 g^{-1} of microporous Si_3N_4 synthesized at 800 °C (Table 6.6) indicates Si_3N_4 could be a promising candidate to achieve high flux of permeates. To evaluate its gas permeance performance microporous Si_3N_4 is coated on γ-Al_2O_3/α-Al_2O_3 hollow tubular supports (provided by IKTS Hermsdorf, Germany, see Chapter 4). The polymer is coated on the inner wall of supports followed by thermolysis under dry ammonia at 800 °C using the thermolysis condition described in the experimental procedure in Chapter

2. It is preferable that the separative layer to be coated inside of tubular support: (i) for the protection of polymeric layer during coating procedure/handling and (ii) while fixing membrane coated support in the permeance set-up before performing gas permeance measurements.

The gas transport properties of multilayer microporous $Si_3N_4/\gamma\text{-}Al_2O_3/\alpha\text{-}Al_2O_3$ membrane is measured using single gas permeance method for H_2 (0.289 nm), He (0.26 nm), N_2 (0.364 nm), O_2 (0.347 nm) and CO_2 (0.33 nm). In order to determine the fundamental operating mechanisms of gas separation, permeance measurements are performed over a range of different temperatures (20–300 °C). The results of permeance of pure gases through $Si_3N_4/\gamma\text{-}Al_2O_3/\alpha\text{-}Al_2O_3$ membrane are presented in Figure 6.16, Figure 6.15 and Table 6.8.

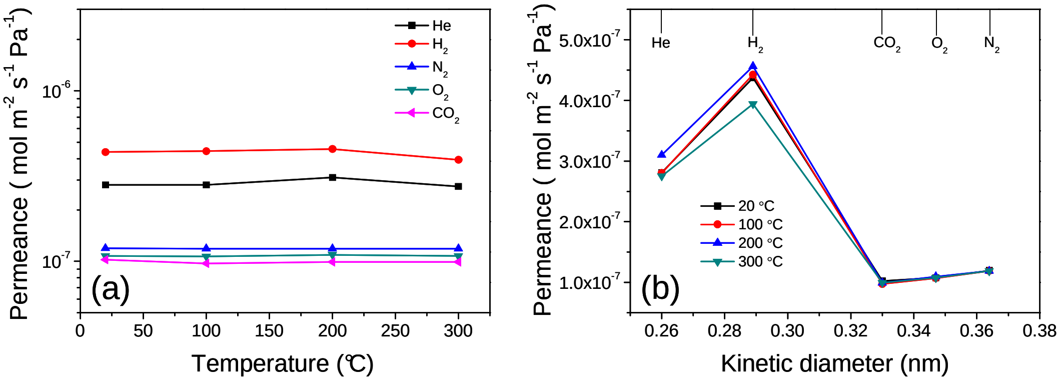

Figure 6.15. Permeances as a function of (a) temperature and (b) kinetic diameter of He, H_2, N_2, O_2, and CO_2 through amorphous 3-fold $Si_3N_4/\gamma\text{-}Al_2O_3/\alpha\text{-}Al_2O_3$.

Table 6.8. Permeances as a function of the measurement temperature of He, H_2, N_2, O_2, and CO_2 through amorphous 3-fold Si_3N_4 / $\gamma\text{-}Al_2O_3$ / $\alpha\text{-}Al_2O_3$.

Permeances of pure gases in mol m^{-2} s^{-1} Pa^{-1}					
Temp. [°C]	**He**	**H_2**	**CO_2**	**O_2**	**N_2**
20	2.8098×10^{-7}	4.3735×10^{-7}	1.0232×10^{-7}	1.0744×10^{-7}	1.1927×10^{-7}
100	2.8054×10^{-7}	4.4258×10^{-7}	9.7235×10^{-8}	1.0694×10^{-7}	1.1887×10^{-7}
200	3.1011×10^{-7}	4.5613×10^{-7}	9.9244×10^{-8}	1.0936×10^{-7}	1.1874×10^{-7}
300	2.7506×10^{-7}	3.9425×10^{-7}	9.9194×10^{-8}	1.0735×10^{-7}	1.1865×10^{-7}

It can be seen from Figure 6.15b that the gas permeance order is in the sequence H_2 (0.289) > He (0.260) > N_2 (0.364) > O_2 (0.347) > CO_2 (0.330). The permeances of gas molecules H_2 and He (molecular diameter < 0.3 nm) are found to be higher than other bigger gas molecules. The ideal permselectivity of H_2 towards CO_2, O_2 and N_2 is found be in the range of 3.5–5. For example, from Table 6.8 permselectivity of H_2/CO_2 at 20 °C, 100 °C, 200 °C and 300 °C is found to be 4.27, 4.55, 4.60 and 3.97, respectively.

The permeances of gases are plotted against square root of mass and are shown in Figure 6.16. It could be seen in Figure 6.16 that the gas permeance is nearly proportional to the reciprocal of the square root of the molecular weight. This linear dependence gives an impression that the mechanism of gas permeation behaviors through the $Si_3N_4/\gamma\text{-}Al_2O_3/\alpha\text{-}Al_2O_3$ membrane could be Knudsen diffusion. The maximum H_2/CO_2 selectivity obtained for Si_3N_4 based membrane is about 4.60 at 200 °C which is close to the ideal permselectivity value ~4.69 for H_2/CO_2 based on Knudsen diffusion. The H_2 permselectivities over other gases at 200 °C (He: 1.47, O_2: 4.17, N_2: 3.84) show a good agreement with theoretical Knudsen permselectivities values (He: 1.41, O_2: 4.0, N_2: 3.73).

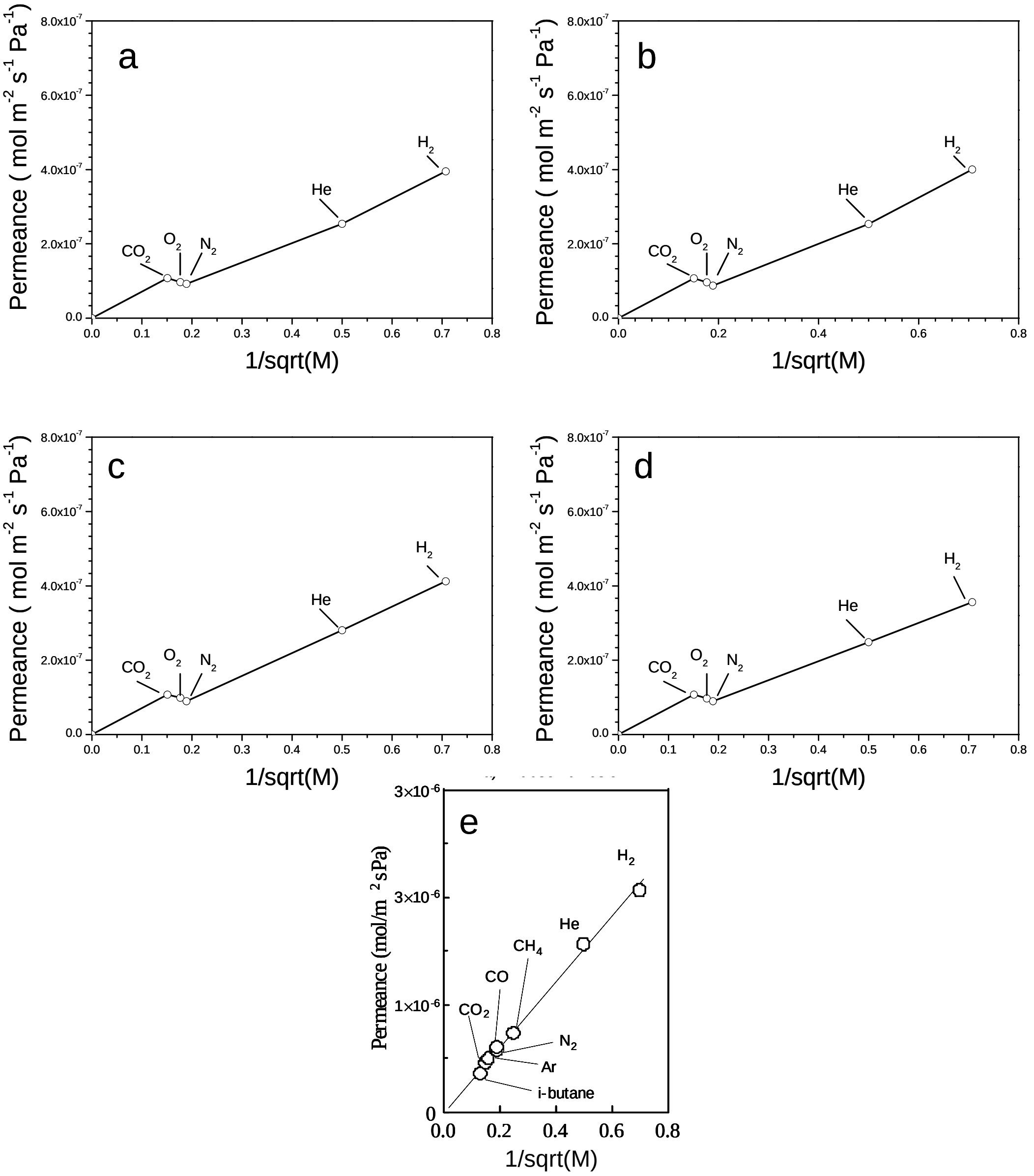

Figure 6.16. Gas permeation behaviors of 3-fold Si_3N_4 membrane coated γ-Al_2O_3 / α-Al_2O_3 support at different temperatures (a) 20 °C, (b) 100 °C, (c) 200 °C, (d) 300°C, and (e) Knudsen diffusion behaviour through an alumina membrane (pore diameter ≈ 3 nm) [11].

If Knudsen diffusion (which is the main gas diffusion mechanism through a crack-free mesoporous membrane) is the dominant gas diffusion mechanism through the Si_3N_4/γ-Al_2O_3/α-Al_2O_3 membrane the permeance would have decreased with the increase of temperature to a large extent. But here we see completely different results. Figure 6.15 and Table 6.8 indicate that no significant change in permeance is observed with increasing temperature between 20 and 100 °C. Between 100 and 200 °C a little increase can be observed for He and H_2. However, a slight decrease in permeance is found between 200 and 300 °C. There could be a one possible reason to explain this dilemma — 'cracks formation' within Si_3N_4 membrane. To examine this SEM image of the surface of $Si_3N_4/\gamma\text{-}Al_2O_3/\alpha\text{-}Al_2O_3$ membrane is taken which is shown in Figure 6.17. Many cracks can be seen along with few holes on the surface of $Si_3N_4/\gamma\text{-}Al_2O_3/\alpha\text{-}Al_2O_3$ membrane.

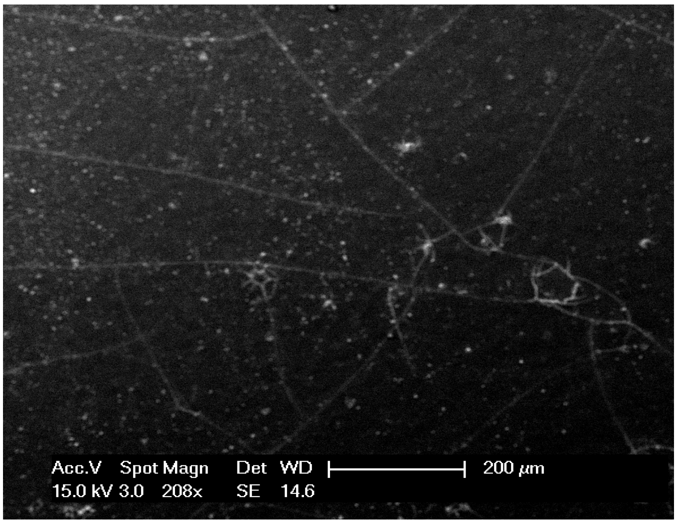

Figure 6.17. SEM image of the surface of $Si_3N_4/\gamma\text{-}Al_2O_3/\alpha\text{-}Al_2O_3$ membrane, showing crack formation in Si_3N_4 membrane.

In order to investigate the phenomena that would have caused crack formation in Si_3N_4 membrane deposited on $\gamma\text{-}Al_2O_3/\alpha\text{-}Al_2O_3$ support, $\gamma\text{-}Al_2O_3$ powder obtained by calcination at 800 °C is treated in dry ammonia at 800 °C for 5h. Calcined $\gamma\text{-}Al_2O_3$ is also heat-treated in air for 5 hours to compare its thermally stability with ammonolysed $\gamma\text{-}Al_2O_3$. Pore-size distributions of $\gamma\text{-}Al_2O_3$ treated in air and in dry ammonia are presented in Figure 6.18.

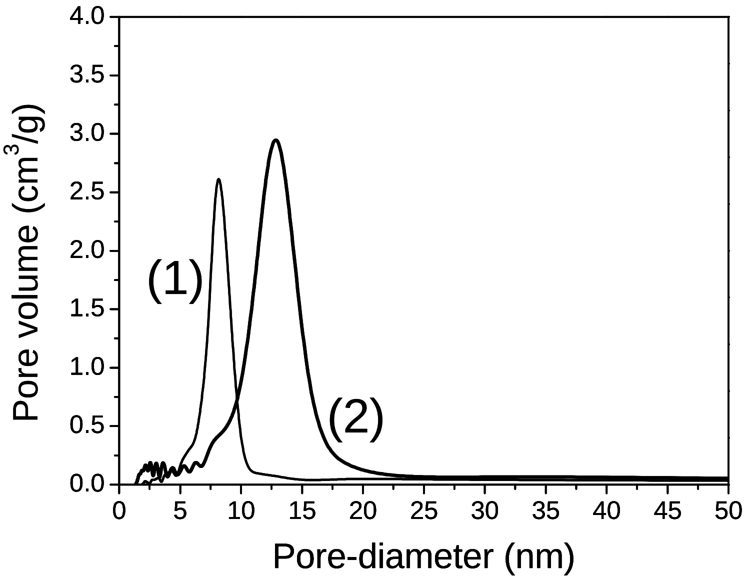

Figure 6.18. Pore-size distribution of γ-Al_2O_3 powder after treatment in (1) air at 800 ºC for 5 hours, and (2) in ammonia at 800 ºC for 5 hours.

As shown in Chapter 4, γ-Al_2O_3 (obtained by calcinations of boehmite at 800 °C) used for these treatments have pore-size of about 8Å. Figure 6.18 indicates that pore-size of γ-Al_2O_3 is increased from 8Å to about 13 Å after treatment in dry ammonia at 800 °C. No significant change can be observed in the XRD patterns of heat-treated γ-Al_2O_3 in air and ammonia, as shown in Figure 6.19. However, elemental analysis of ammonia treated γ-Al_2O_3 shows around 1 wt. % of nitrogen is doped in γ-Al_2O_3.

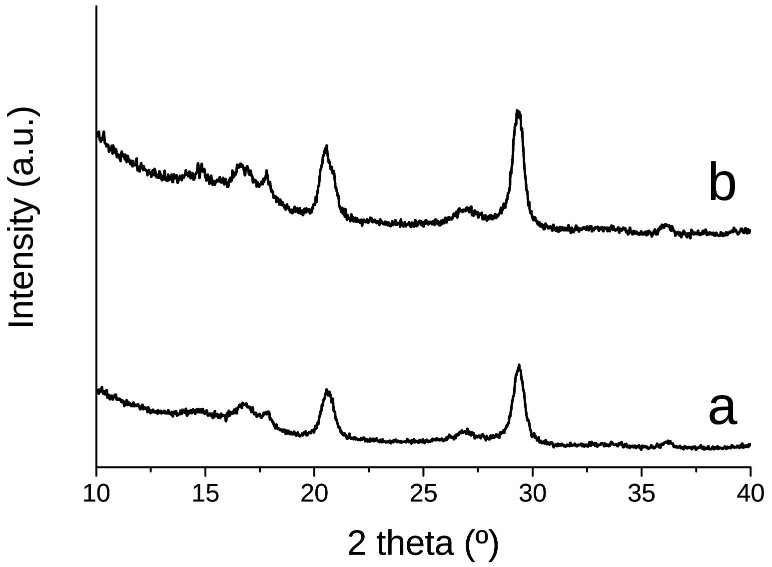

Figure 6.19. X-ray powder diffraction (XRPD) patterns of γ-Al_2O_3 after treatment in (a) air at 800 °C for 5 hours, and (b) ammonia at 800 °C for 5 hours.

Above results indicate that γ-Al_2O_3 does not remain stable with respect to pore-size and chemical composition when treated in dry ammonia at 800 °C. Therefore, the interface between pre-ceramic polymer and γ-Al_2O_3 does not remain stable while doing ammonolysis of polymer coated γ-Al_2O_3/α-Al_2O_3 support. This unstable behaviour of γ-Al_2O_3 during the pyrolysis of polymer coated γ-Al_2O_3/α-Al_2O_3 could lead to the formation of cracks within Si_3N_4 membrane leading to degrade the selectivity of H_2 with respect to larger size gas molecules like N_2, CO_2, etc.

6.6. Membrane/sensor integration: selective H_2 detection

In the previous chapter (Chapter 5, related to Si-B-C-N) we have shown successful deposition of Si-B-C-N membrane on SnO_2 based gas sensors. We have tried to coat Si_3N_4 membranes on SnO_2 sensors by dip-coating of diluted-HTT 1800 polysilazane followed by pyrolysis in dry ammonia. But this has not worked. The resistance of the membrane coated sensor is found to be very high to be measured due to the reduction of SnO_2 layer underneath of polymer layer by ammonia during membrane formation. After ammonolysis it is found that the SnO_2

layer from the sensor support is completely removed. Hence, GaN based sensors is used to integrate Si_3N_4 membrane/GaN sensor system for such reducing environment. GaN based sensors are known to be capable of operation in harsh environmental conditions [12-13]. The large bandgap of GaN allow high temperature operation with chemical stability and mechanical robustness [13]. Two different types of GaN powder is used for this work as sensing material: (i) as synthesized GaN by the nitridation of commercial Ga_2O_3 powder [14], (ii) commercial GaN powder. In the following, **GaN-s** and **GaN-c** has been used for **as-synthesized GaN** and **commercial GaN**, respectively. It should be noted that initially we did not plan to measure the sensing behaviour of the ammonia-treated GaN based gas sensors. After finding that Si_3N_4-coated GaN sensors showed very high selectivity for H_2 and almost no sensing effect towards CO, ammonia treatment of uncoated GaN sensor was additionally done to investigate its effect on the sensing performance.

To assess the performance of uncoated GaN, Si_3N_4 coated- and ammonia treated-GaN sensors in oxygen free-conditions, gas sensing properties of these sensors are studied at 350 and 530 °C towards different H_2 (40–900 ppm) and CO (10–120 ppm) concentrations. Sensor response towards CO and H_2 of uncoated GaN, Si_3N_4 coated and ammonia treated-GaN gas sensors at 350 and 530 ºC are shown in Figure 6.20 and Figure 6.21, respectively.

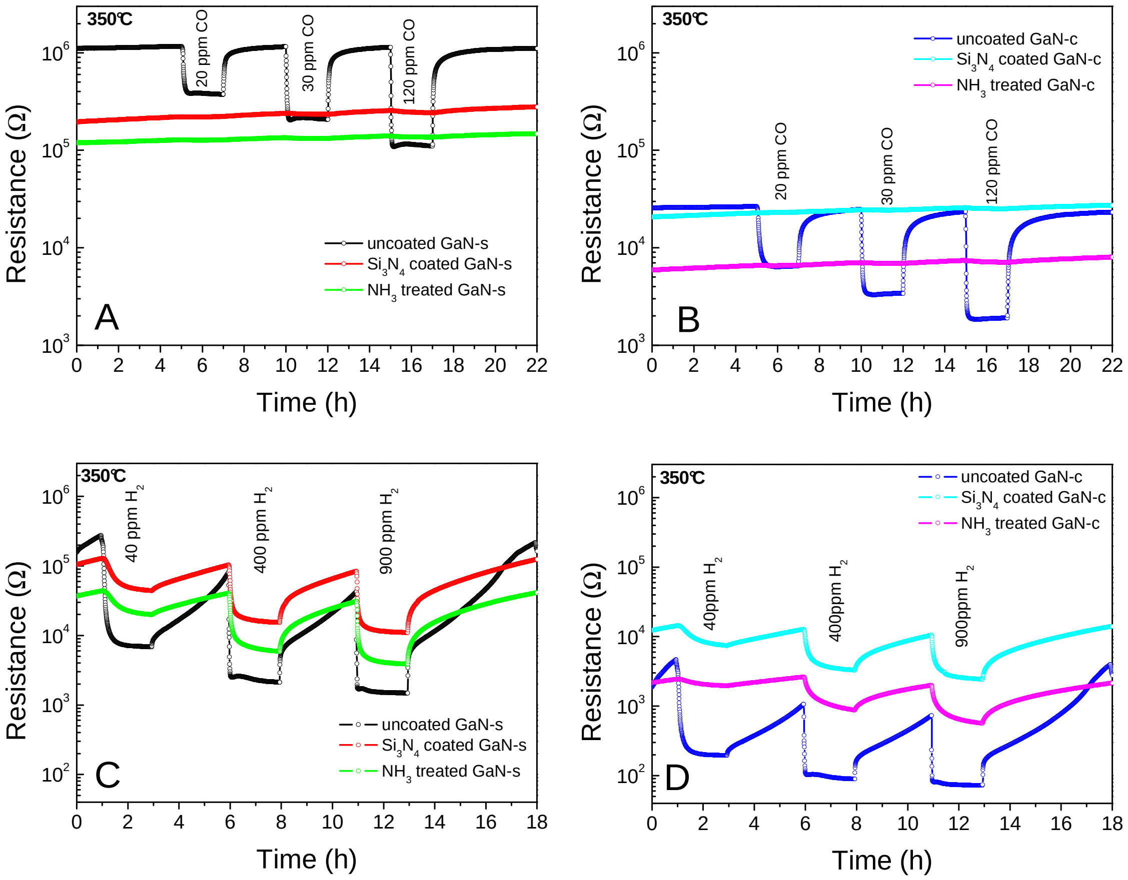

Figure 6.20. Transient response of uncoated, Si_3N_4 membrane coated- and ammonia treated-GaN sensors:(A,C) as-synthesized GaN is used as sensor material and (B,D) commercial GaN powder is used as sensor material, during exposure to CO and H_2 in nitrogen at 350 °C.

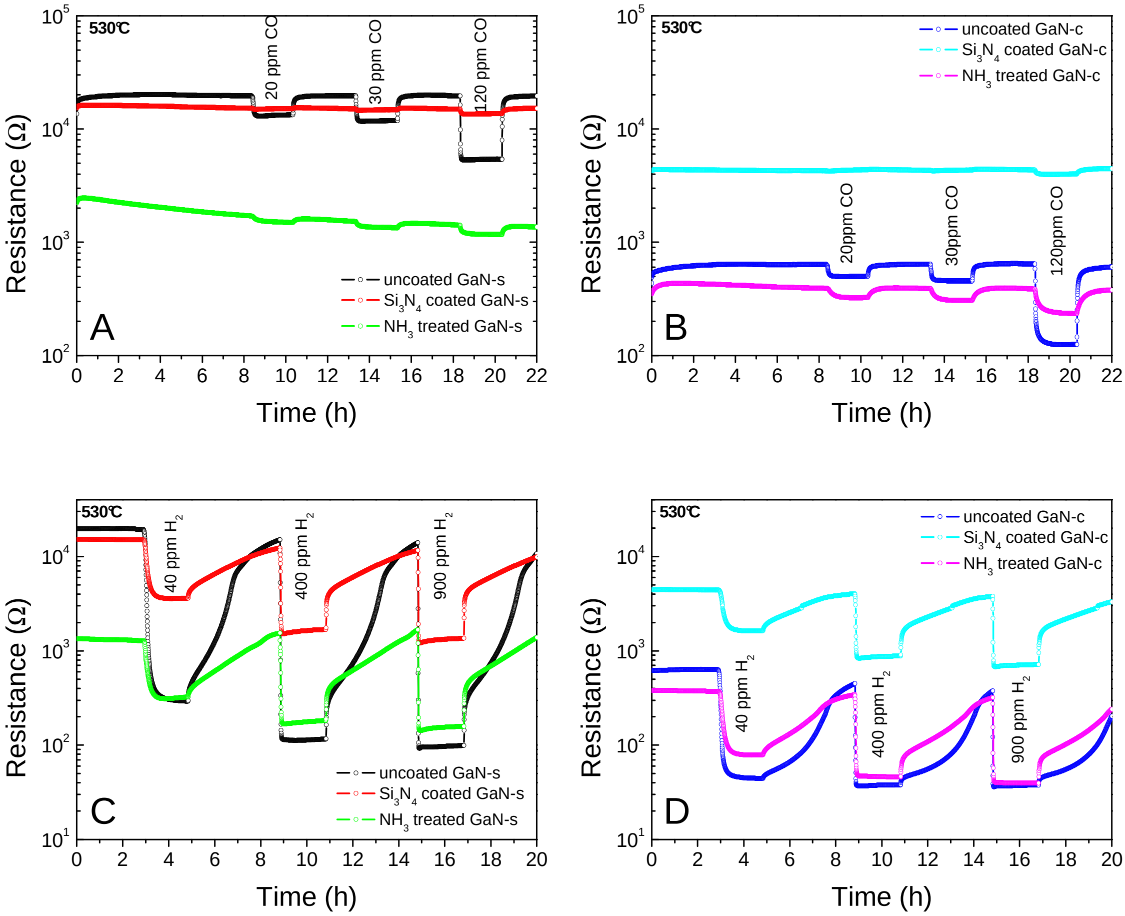

Figure 6.21. Transient response of uncoated, Si_3N_4 membrane coated- and ammonia treated-GaN sensors: (A, C) as-synthesized GaN is used as sensor material and (B, D) commercial GaN powder is used as sensor material, during exposure to CO and H_2 in nitrogen at 530 °C.

A number of significant differences could be observed among uncoated GaN, Si_3N_4-coated and ammonia-treated GaN sensors with respect to the response towards CO and H_2. Complete reversible resistance changes towards CO exposure are observed for all sensors at both temperatures. Upon CO exposure, reasonable resistance changes are measured for the uncoated GaN sensors with rather fast response and recovery times at both temperatures (350 °C and 530 °C). A large resistance change upon H_2 exposure is also recorded with quite fast response times. However, the recovery upon H_2 exposure compared to CO is found be very slow and the resistance change showed a strange development during the recovery period (Figure 6.20C, D and Figure 6.21C, D). It could also be observed that the allotted three hours under N_2 after the H_2 pulses is not enough to get fully back to the baseline resistance.

It can be concluded from Figure 6.21A, B that uncoated GaN based sensors remain stable at 530 ºC when exposed to the highest concentration of H_2 in N_2 (900 ppm), whereas uncoated SnO_2 sensors are found to be reduced in these conditions as already demonstrated in Chapter 5. This indicates that GaN sensors are highly stable under such harsh reducing atmospheres unlike SnO_2 based sensors.

By the additional coating of the sensors with the Si_3N_4 layer the performance is found to change dramatically. Si_3N_4-coated GaN sensors appeared to possess almost no response to CO at 350 ºC and very little response at 530 ºC is observed (see Figure 6.20A, B and Figure 6.21A, B).

Interestingly, the treatment of the uncoated GaN samples with ammonia shows a dramatic reduction of the response towards CO at both temperatures. Figure 6.20A, B shows almost no response to CO for ammonia treated GaN sensors at 350 ºC. At 530 ºC, very small response for all used CO concentration (20, 30 and 120 ppm) is found for ammonia-treated GaN sensors (Figure 6.21A, B). Nevertheless, the response for the Si_3N_4-coated GaN sensors is more reduced than that of ammonia-treated GaN sensors at 530 ºC. A very small response to 120 ppm of CO can be observed for Si_3N_4-coated GaN sensors at 530 ºC but no response to 20 and 30 ppm CO.

Although the response towards H_2 is also reduced (Figure 6.20C, D and Figure 6.21C, D) for both Si_3N_4-coated and ammonia-treated GaN sensors, still remarkable resistance changes could be observed. At 350°C a small decrease of the response time is observed for both Si_3N_4-coated and ammonia-treated GaN sensors. But the response time towards H_2 at 530°C is not influenced at all due to the ammonia treatment or the presence of the Si_3N_4 filter.

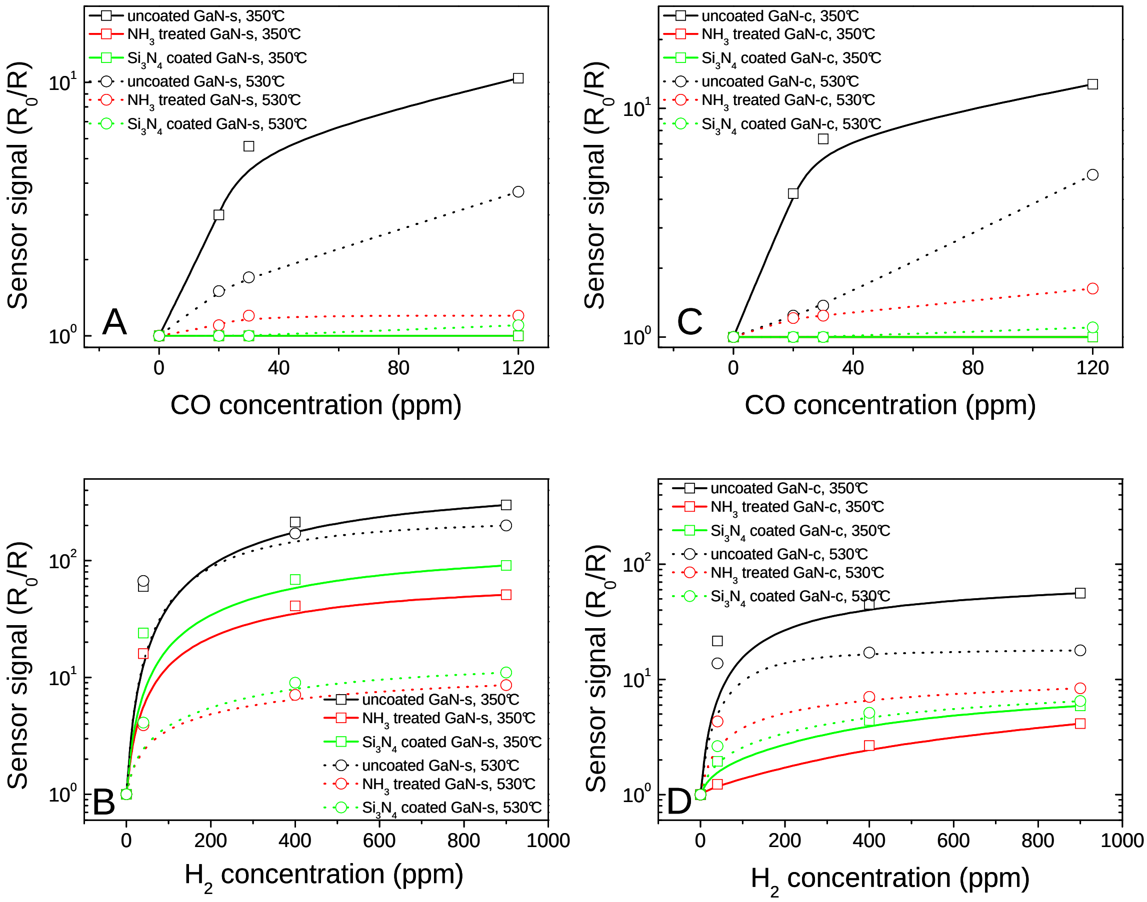

Figure 6.22. Sensor signals (R_0/R) to CO and H_2 in nitrogen at 350 and 530 °C of uncoated, Si_3N_4 membrane coated- and ammonia treated- GaN sensors: (A, B) as-synthesized GaN is used as sensor material and (C, D) commercial GaN powder is used as sensor material.

Figure 6.22 represents sensor signal (defined as the ration between the baseline resistance R_0 and the resistance during target gas exposure R_{gas}) plots of uncoated GaN, Si_3N_4-coated and ammonia treated-GaN sensors towards H_2 and CO exposure at 350 and 530 °C, respectively, for both as-synthesized and commercial GaN based sensors. Si_3N_4 membrane coated GaN sensors show either very little sensor signal (at 530 °C) or almost no signal (at 350 °C) to CO, as shown in Figure 6.22A and Figure 6.22C. The H_2 sensor signals are found to be reduced for membrane-coated — especially at 530°C — but are still quite remarkable whereas the signals towards CO almost disappeard. This could be attributed to the high blocking potential of the microporous Si_3N_4 membrane towards the CO molecules in reaching towards the GaN sensing surface. The size-selective pore channels in Si_3N_4

membrane and a high BET specific surface area of 255 m^2 g^{-1} might have resulted in the preservation of the sensor signals towards H_2 for Si_3N_4-coated GaN sensors. A filtering effect of the membrane based on chemical activity (oxidation of CO gas) can be excluded because all experiments have been performed in an atmosphere without oxygen.

For ammonia-treated GaN based gas sensors also almost no sensing towards CO could be observed at 350 and 530 °C whereas towards H_2 exposure the resistance is dramatically reduced. This unusual behaviour of ammonia-treated GaN is quite surprising because GaN powder itself is synthesized by treating Ga_2O_3 commercial powder under ammonia at 900 °C. Hence a big question arises: *Why do gas sensors based on GaN powder synthesized from Ga_2O_3 with nitridation at 900 °C and the same synthesized GaN powder after its re-treatment under ammonia at 800 °C show completely different behaviours towards CO sensing*?

To clarify this, XRD measurements and elemental analysis of untreated- and ammonia-treated-GaN powders (from as-synthesized and commercial powders) are done. No significant differences in the X-ray diffraction patterns (Figure 6.23) could be observed between the untreated- and ammonia-treated-GaN-s powders. Although there is a difference in oxygen wt.% is found by the elemental analysis (Table 6.9). As-synthesized GaN powder at 900 °C shows a contamination of about 2.8 wt.% of oxygen which is reduced to about 1.6 wt.% of oxygen after treating it in ammonia at 800 °C. This difference could be due to the surface oxidation of as-synthesized GaN powder after storing it for a longer period under air at room temperature. In our case as-synthesized GaN powder has been stored for about six months before its re-treatment under dry ammonia at 800 °C.

In the case of commercial GaN powder, difference between the XRD patterns of untreated and ammonia-treated powders can be easily seen. Low intense peaks of Ga_2O_3 are observed for commercial GaN powder (see Figure 6.23). This indicates incomplete transformation of Ga_2O_3 to GaN after nitridation using the conditions applied by the manufacturer for the synthesis of commercial GaN powder. Oxygen contamination of about

4.9 wt.% is measured in as-received commercial GaN powder which is reduced to 2.4 wt.% after its nitridation at 800 °C (Table 6.9). Relatively higher oxygen contamination in commercial GaN compared to that in as-synthesized GaN powder could be attributed due to residual amount of Ga_2O_3 in commercial GaN powder.

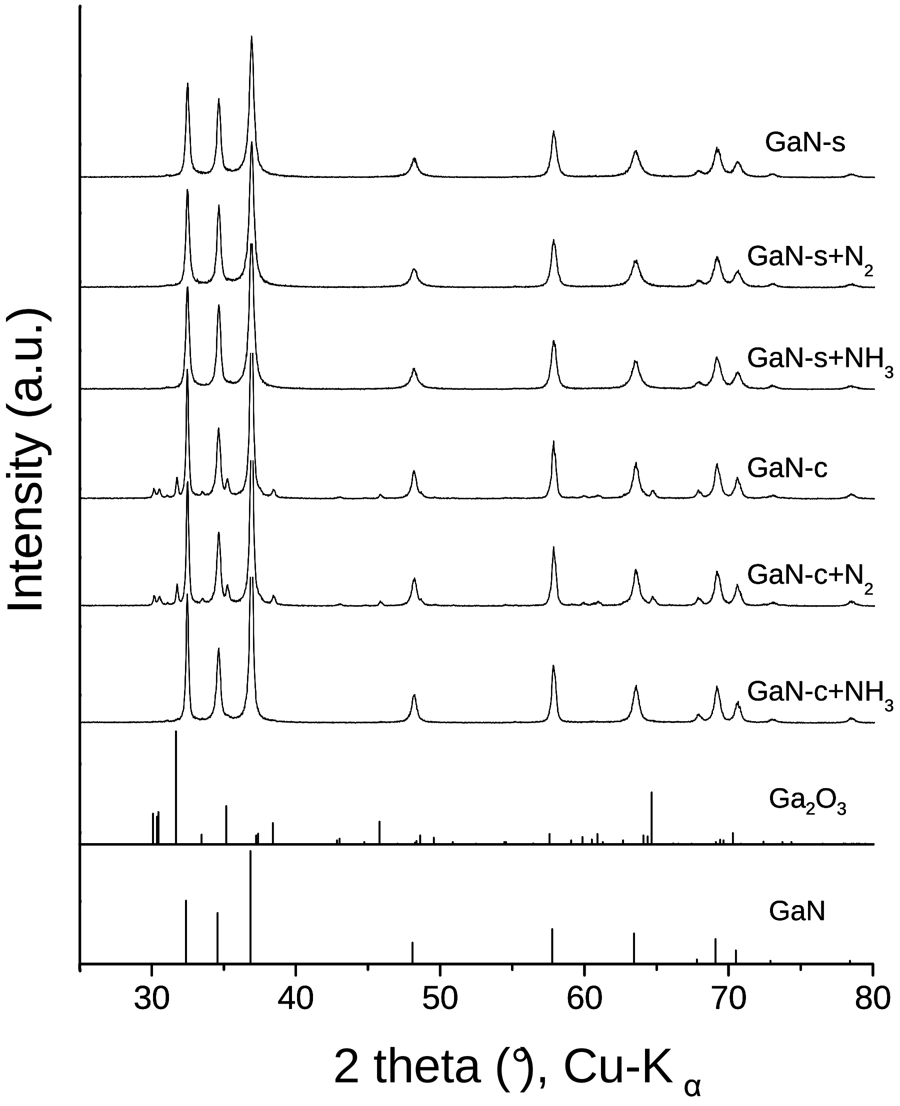

Figure 6.23. XRD patterns of as-synthesized GaN (GaN-s) and commercial GaN (GaN-c) powders and the powders obtained after treatment under nitrogen and ammonia {+N_2 indicates sample obtained after treatment under nitrogen using the same heating profile done for depositing screen-printed sensor material on sensor support (Chapter 2) and +NH_3 indicates samples treated under ammonia at 800 °C}.

Table 6.9. Elemental composition of the as-synthesized and commercial GaN powder obtained after treatment under nitrogen and ammonia.

Samples	**N (wt. %)**	**O (wt. %)**
GaN-s	14.9	2.81
GaN-s+N_2	15.0	2.65
GaN-s+NH_3	15.9	1.62
GaN-c	13.8	4.95
GaN-c+N_2	13.9	4.93
GaN-c+NH_3	15.0	2.42

Based on elemental analysis we can propose that surface oxidation of GaN powder creates an oxidative amorphous layer (which does not appear in XRD pattern) which provides the sites for the sensing towards CO. Treating this powder under dry ammonia at 800 °C destroys the oxidative layer (converting to nitride layers) and consequently the sensing performance towards CO is dramatically reduced for ammonia treated-GaN gas sensors. The conversion of oxide to nitride after nitridation at 800 °C could be confirmed by looking at XRD pattern of untreated and ammonia-treated commercial GaN powders (Figure 6.23). Residual Ga_2O_3 peaks vanish by ammonia treated of commercial GaN powder at 800 °C. The above assumption is supported by the observation of the TEM images.

TEM images of untreated and ammonia-treated as-synthesized GaN powders are taken which are shown in Figure 6.24. For both untreated and ammonia-treated GaN powders an amorphous layer can be observed. Surface particles could be seen for as-synthesized GaN powder (Figure 6.24A, B), whereas no such such particle is observed for ammonia-treated powder (Figure 6.24C, D). This could be due to removal of surface oxide layer after nitridation at 800 °C. We were not able to analyze surface particle due to the lack of stability of these samples under the beam. The particle became amorphous during observation, which will most probably change the chemical composition.

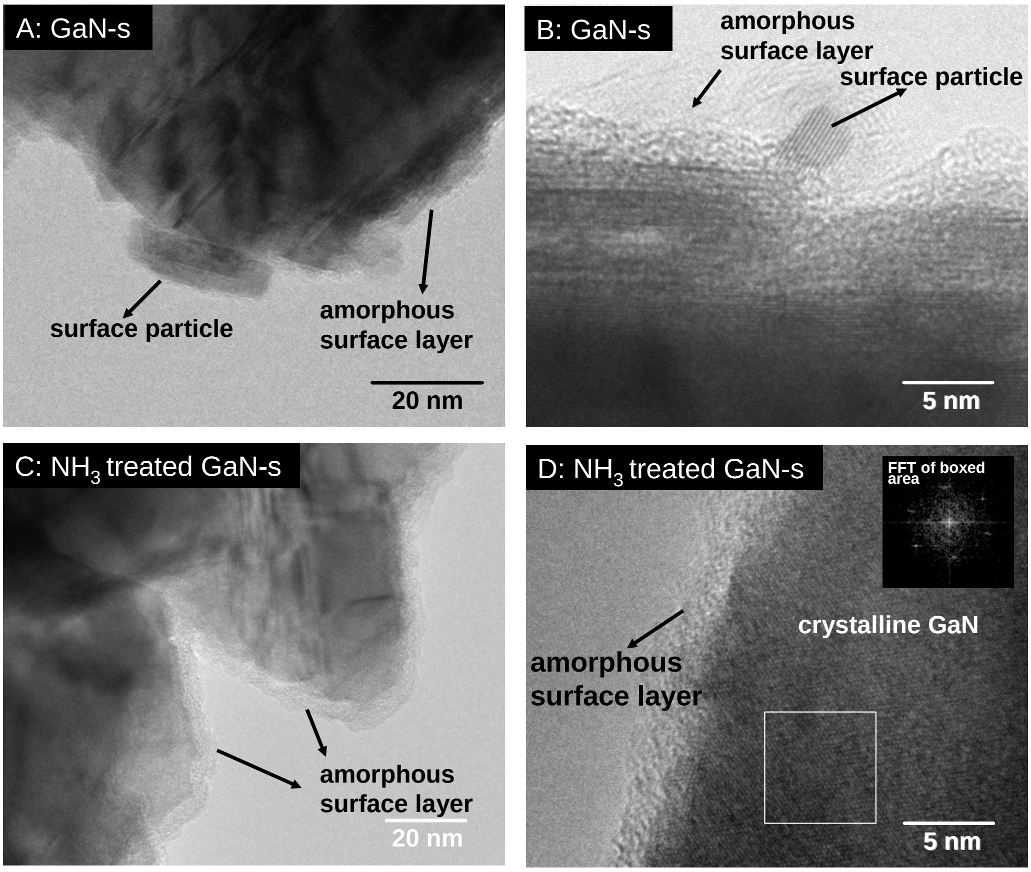

Figure 6.24. HRTEM images of (A,B) as-synthesized GaN powder and (C,D) ammonia treated as-synthesized treated powder at 800 °C.

Pyrolysis under ammonia to obtain Si_3N_4-coated GaN sensors could also lead to the nitridation of the slightly oxidized sensor surface which gives a “fresh” GaN. Therefore, in the case of Si_3N_4-coated GaN sensors both factors — size-selective microporous Si_3N_4 membrane and generation of fresh GaN during the deposition of Si_3N_4 on GaN sensors — could contribute to selective H_2 sensing.

The very different kinetics between CO and H_2 sensing (Figure 6.20 and Figure 6.21) and the fact that after the treatment with ammonia the detection of H_2 is still possible indicate that the reaction mechanism of the both gases should be different. As shown above a higher amount of contaminated oxygen is found for untreated GaN powders compared to ammonia-treated GaN powders, which can indicate that CO prefers to react with the residual lattice oxygen of GaN whereas H_2 reacts with both, lattice oxygen and also the lattice nitride. This would explain also the different kinetics in the recovery.

6.7. Perspectives for hydrogen separation and sensing

In summary, microporous Si_3N_4 ceramic has been synthesized by the ammonolysis of polysilazane HTT 1800 at 800 °C. Tubular γ-Al_2O_3/α-Al_2O_3 porous support is coated with microporous Si_3N_4 to evaluate its performance with respect to H_2/CO_2 permeance and permselectivity. Also Si_3N_4 layer is developed on screen printed GaN based sensor for H_2/CO detection and the effect of microporous Si_3N_4 membranes and ammonia treatment on screen printed GaN sensors has been investigated. The gas permeance measurements and gas-sensing of Si_3N_4-coated porous and sensor supports have demonstrated many interesting results.

The maximum H_2/CO_2 permselectivity of Si_3N_4/γ-Al_2O_3/α-Al_2O_3 membrane is found to be 4.60 at 200 °C which is in the range of pure Knudsen mechanism. No significant change in permeance value is observed for gases when permeance measurements are done at different temperatures (20–300 ºC), hence possibility of pure Knudsen diffusion mechanism for gas permeance through Si_3N_4/γ-Al_2O_3/α-Al_2O_3 membrane is ruled out. Cracks within Si_3N_4 membrane are seen. The reason behind crack formation could be due the thermal instability of the intermediate γ-Al_2O_3 porous layer and nitrogen doping of γ-Al_2O_3 under ammonia at 800 °C.

Transient response characteristics and sensor signals of uncoated GaN, 3 times Si_3N_4-coated and ammonia treated GaN sensors exposed to CO (10, 20 and 120 ppm) and H_2 (40, 400 and 900 ppm) in nitrogen at 350 and 530 °C are obtained. The uncoated GaN shows very high sensor signals towards CO in oxygen-free background whereas the microporous Si_3N_4 membrane coated and ammonia treated sensors show almost no signal to CO at 530 °C. The H_2 sensor signals are found to be still quite remarkable for Si_3N_4-coated GaN sensor confirming high permeance of H_2 through Si_3N_4 membrane compared to CO permeance due to size-selective transport of gases through the Si_3N_4 ceramic layers. Hence, a novel membrane/sensor integration using Si_3N_4 membrane layer on GaN sensor has been achieved which is highly selective/sensitive to H_2 and the interfering effect of CO is strongly reduced compared to the effect on uncoated GaN sensor. This clearly shows the potential of amorphous-microporous-Si_3N_4 coated GaN sensors to achieve high hydrogen selectivity/sensitivity in gas sensing applications. Also a completely new way of obtaining H_2 selective GaN sensor has been achieved by its treatment under dry ammonia.

6.8. References

[1] M. Horz, A. Zern, F. Berger, J. Haug, K. Muller, F. Aldinger, M. Weinmann, "Novel polysilazanes as precursors for silicon nitride/silicon carbide composites without "free" carbon," *Journal of the European Ceramic Society,* 25 (2005) 99-110.

[2] Q.D. Nghiem, J.K. Jeon, L.Y. Hong, D.P. Kim, "Polymer derived Si-C-B-N ceramics via hydroboration from borazine derivatives and trivinylcyclotrisilazane," *Journal of Organometallic Chemistry*, 688 (2003) 27-35.

[3] M.A. Schiavon, G.D. Soraru, I.V.P. Yoshida, "Synthesis of a polycyclic silazane network and its evolution to silicon carbonitride glass," *Journal of Non-Crystalline Solids,* 304 (2002) 76-83.

[4] N.R. Dando, A.J. Perrotta, C. Strohmann, R.M. Stewart, D. Seyferth, "Methylhydridopolysilazane and its pyrolytic conversion to Si_3N_4/SiC Ceramics," *Chemistry of Materials*, 5 (1993) 1624-1630.

[5] A. Kojima, S. Hoshii, T. Muto, "Characteristics of polysilazane compound and its application as coating for carbon material," *Journal of Materials Science Letters,* 21 (2002) 757-760.

[6] K.S.W. Sing, D.H. Everett, R.A.W. Haul, L. Moscou, R.A. Pierotti, J. Rouquerol, T. Siemieniewska, "Reporting physisorption data for gas solid systems with special reference to the determination of surface-area and porosity (Recommendations 1984)," *Pure and Applied Chemistry,* 57 (1985) 603-619.

[7] J.L. Wan, M.J. Gasch, A.K. Mukherjee, "In situ densification behavior in the pyrolysis consolidation of amorphous Si-N-C bulk ceramics from polymer precursors," *Journal of the American Ceramic Society*, 84 (2001) 2165-2169.

[8] S. Kaskel, K. Schlichte, B. Zibrowius, "Pore size engineering of mesoporous silicon nitride materials," *Physical Chemistry Chemical Physics*, 4 (2002) 1675-1681.

[9] G.T. Burns, G. Chandra, "Pyrolysis of preceramic polymers in ammonia - Preparation of silicon-nitride powders," *Journal of the American Ceramic Society,* 72 (1989) 333-337.

[10] D. Farrusseng, K. Schlichte, B. Spliethoff, A. Wingen, S. Kaskel, J.S. Bradley, F. Schuth, "Pore-size engineering of silicon imido nitride for catalytic applications," *Angewandte Chemie-International Edition*, 40 (2001) 4204-4207.

[11] Y. Iwamoto, "Precursors Derived Ceramic Membranes," E-MRS Spring Meeting, Strasbourg, 2004.

[12] D.S. Lee, J.H. Lee, Y.H. Lee, D.D. Lee, "GaN thin films as gas sensors," *Sensors and Actuators B: Chemical*, 89 (2003) 305-310.

[13] F. Yun, S. Chevtchenko, Y.T. Moon, H. Morkoc, T.J. Fawcett, J.T. Wolan, "GaN resistive hydrogen gas sensors," *Applied Physics Letters*, 87 (2005) -.

[14] M. Kerlau, O. Merdrignac-Conanec, P. Reichel, N. Barsan, U. Weimar, "Preparation and characterization of gallium (oxy)nitride powders - Preliminary investigation as new gas sensor materials," *Sensors and Actuators B: Chemical*, 115 (2006) 4-11.

Chapter 7. Unconventional route to synthesize microporous carbon-rich SiCN ceramics

This chapter is directed towards the synthesis, pore structure characterization and specific surface area determination of carbon-rich silicon carbonitride (C-rich SiCN) ceramic materials derived from poly(diphenylsilylcarbodiimide). Poly(diphenylsilylcarbodiimide), namely $–[Ph_2Si\text{-}NCN]_n–$, are reported to be suitable precursors for high-temperature stable C-rich SiCN polymer-derived ceramics [1].

The concept of the present work is explained in section 7.1. Section 7.2 gives short summary of poly(diphenylsilylcarbodiimide) derived ceramic which is basically the main conclusion from the work of Mera et al. [1]. High temperature thermogravimetric analysis, pore-size and specific surface area measurements, and microstructural analysis of the samples obtained at different intermediate temperatures between 1500–2000 °C are described in sections 7.3–7.5.

7.1. Concept

Polymer-derived SiCN ceramics have unique properties, such as high-temperature stability, oxidation, and corrosion resistance [2]. Earlier studies have demonstrated that resistance to crystallization of PDCs is enhanced when the ceramics contain high amounts of excess carbon [3-4]. In our group Mera et al. have recently synthesized C-rich SiCN ceramics obtained by pyrolysis of poly(diphenylsilylcarbodiimide) [1]. They have reported that the samples annealed at 1500–1700 °C contain relatively high amounts of carbon of about 60–70 wt.%. The high quantity of phenyl side chains in the precursor polymer results in the ceramic having a high percentage of excess free carbon. They have observed formation of graphite-like structure (graphene layers) at 1700 °C and turbostratic carbon at 2000 °C.

Graphene, an allotrope of carbon, is a monolayer of carbon atoms arranged in a two-dimensional honeycomb structure. *Graphite (Hexagonal graphite, h-graphite)* consists of sp^2

carbon hexagonal networks of carbon atoms with covalent bonding between carbon atoms within a plane and a weak van der Waals interaction between planes. The bonding force between graphene layers is much weaker than that of intra layers. *Turbostratic carbon (t-carbon)* is regarded as a variant of h-graphite [1]. Both the h-graphite and t-carbon are stacked up by graphene layers with a regular spacing but different stacking ordering degree. The hexagonal network of graphite layers is stacked in the direction perpendicular to the layer plane (c-axis) in an AB stacking arrangement. In turbostratic carbon there is no stacking order between adjacent layers and the interlayer space (> 0.342 nm) is larger than that for crystalline graphite (0.335 nm) [6].

Carbon molecular sieve membrane is primarily prepared by carbonizing polymeric films at high temperature in vacuum or in inert atmosphere [7]. This kind of carbon molecular sieving material is amorphous and formed by disordered stacking of aromatically turbostratic carbon [2], but the stability of carbon membranes is limited to 300–400 °C. The unique combination of properties — high temperature thermal stability due to high carbon amount and formation of turbostratic carbon — in C-rich SiCN ceramics derived from poly(diphenylsilylcarbodiimide) has motivated us to investigate more about the microstructural development at high temperature between 1500 and 1700 °C.

7.2. Poly(diphenylsilylcarbodiimide)-derived ceramics

Poly(diphenylsilylcarbodiimide) has been synthesized by the reaction of diphenyldichlorosilane with bistrimethylsilylcarbodiimides using pyridine as catalyst [1]. Polysilylcarbodiimides are generally air and moisture sensitive polymers. By insertion of bulky aromatic substituents at silicon, the air sensitivity massively decreases. Some of the important conclusions extracted from the previous work done by Mera et al. on poly(diphenylsilylcarbodiimide) derived SiCN ceramics are as follows [1, 9]:

- ✓ It has been proposed that high carbon contents (graphene layers) in C-rich SiCN ceramics seal the a-Si_3N_4 (amorphous silicon nitride) and prevent the out diffusion of N_2 gas and therefore increase the stability of Si_3N_4 clusters which leads to an enhanced thermal stability of the SiCN ceramic against crystallization.
- ✓ C-rich SiCN proves to be more temperature resistant than the reported SiCN ceramics with lower carbon content. Crystallization of poly(diphenylsilylcarbodiimides) has been found to occur at 50 °C higher than that of SiCN ceramics derived from other polysilylcarbodiimides [10].
- ✓ Phenyl-substituted polysilylcarbodiimide C-rich SiCN ceramics have been found to be nanostructured ceramics consisting of nanodomains of amorphous silicon nitride (a-Si_3N_4), amorphous silicon carbide (a-SiC) and amorphous carbon (a-C) up to 1450 °C, as revealed by SAXS and MAS NMR studies.
- ✓ It has been observed that C-rich SiCN ceramics crystallize directly to α- and β-SiC without being converted to Si_3N_4.

7.3. Polymer to ceramic transformation

Low temperature thermogravimetric (TG) analysis of poly(diphenylsilylcarbodiimide) up to 1400 °C has already been reported by Mera et al. [1]. Ceramic yield of about 40.12 % by mass has been obtained at 1400 °C. Release of trimethylchlorosilane and its decomposition products has been observed between 180 and 400 °C. Nitriles HCN (m/z=27), hydrogen (m/z=2), cyanogen C_2N_2 (m/z=52) have been found to eliminate between 400 and 600 °C. Above 1000 °C, a small mass loss has been attributed to the release of hydrogen and nitrogen. Major mass loss has been observed between 500 and 600 °C, but complete ceramic formation has not been observed in this temperature range. A mass loss of about 10 % has been observed between 600 and 1100 °C. The ceramic formation has been found to complete above

1100 °C. Here onwards **S1** denotes for poly(diphenylsilylcarbodiimide) pre-ceramic precursor.

In Figure 7.1, the high temperature thermogravimetric curve of **S1** (pre-pyrolyzed at 1100 °C) in flowing helium is presented. A mass loss of about 6.5 % could be observed between 1000–1400 °C, mainly due to the evolution of nitrogen and hydrogen. For the temperature range 1400–2000 °C a mass loss of about 19.5 % is observed (Figure 7.1) due to the loss of nitrogen. This high amount of nitrogen loss is attributed to carbothermal reaction as explained further below.

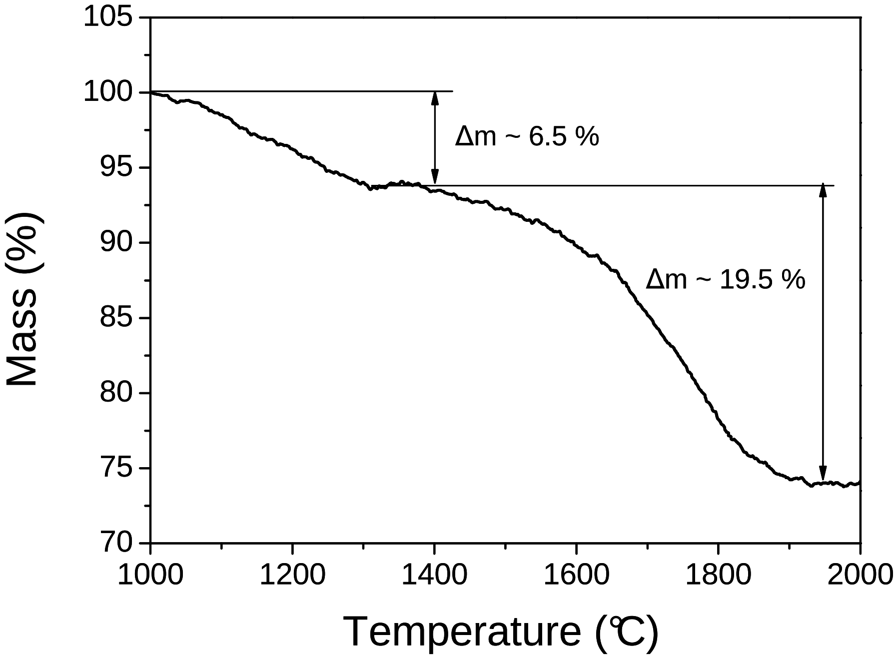

Figure 7.1. High temperature thermogravimetric analysis (HT-TGA) of pyrolyzed sample obtained at 1100 °C derived from poly(diphenylsilylcarbodiimide) performed in flowing He at a heating rate of 2 °C min^{-1}.

One single phase amorphous SiCN ceramic can be obtained by thermal decomposition of polysilazanes at 1100 °C [2, 11]. The polysilazane-derived ceramics contain mixed bonds where silicon is bonded to both nitrogen and carbon at the same time, as shown in Figure 7.2. Whereas the SiCN ceramics obtained by thermolysis of polysilylcarbidiimides at approximately 1100 °C is consisting of three types of nanodomains (1–3 nm in size) of amorphous silicon nitride (a-Si_3N_4), amorphous silicon carbide (a-SiC) and amorphous carbon (a-C) up to 1450 °C, , as revealed by SAXS and MAS NMR [9] (Figure 7.2). No mixed bonds have been found in this structure.

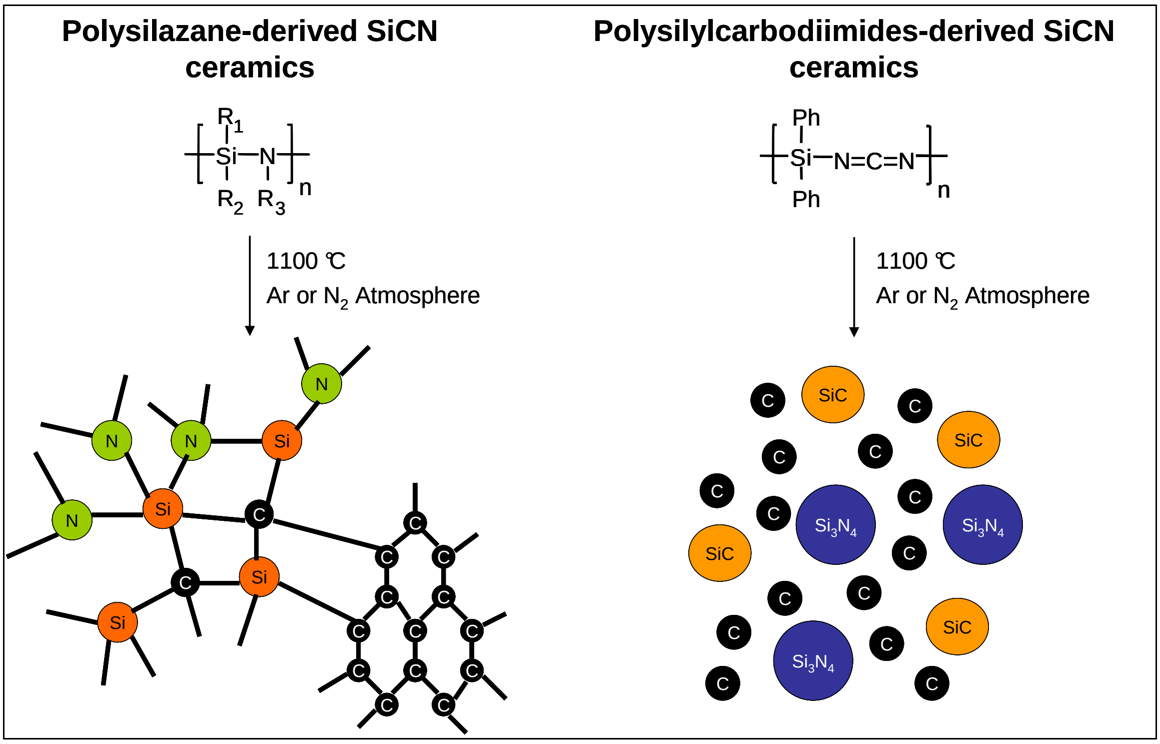

Figure 7.2. Comparison between the microstructure of SiCN ceramics derived from polysilazanes and polysilylcarbodiimides at and above 1100 °C, up to the temperature of carbothermal reaction (1450 °C).

Above 1450 °C a-Si_3N_4 reacts with carbon to form a-SiC (Eq. 7a and 7b) which transforms afterwards into α/ß-SiC.

$$\text{a-}Si_3N_4 + 3\text{a-C} \longrightarrow 3\text{a-SiC} + 2N_2\uparrow \qquad (7a)$$
$$\text{a-SiC} \longrightarrow \alpha/\text{ß-SiC} \qquad (7b)$$

$$\text{a-}Si_3N_4 + 3\text{a-C} \longrightarrow 3\alpha/\text{ß-SiC} + 2N_2\uparrow \qquad (7c)$$ [**Carbothermal reaction**]

Nitrogen evolution which is mainly correlated with loss of nitrogen during carbothermal reaction (Eq. 7c) could lead to the formation of porous structure in these ceramics above 1450 °C.

7.4. Porosity characteristics

In order to investigate if the gases released below 700 °C would have generated porous structure during polymer-ceramic transformation, pore-size analysis of the sample pyrolyzed at 700 °C is done. Unexpectedly the sample is found to be almost non-porous (with respect to micro- and mesopores). Absence of pores at 700 °C could be due to collapse of porous structure (those are generated during gas evolution below 700 °C, see low temperature TG discussion in section 7.3) because of high viscous flow in the material at higher temperatures.

Samples pyrolyzed at 1100 and 1500 °C are also found to be non-porous. Nitrogen sorption isotherm curve of the sample annealed at 1700 °C for 2 h shows a combination of type I and type IV curve (a hysteresis loop), in Figure 7.3a4, which is characteristic of a porous material with micro- and mesopores. Pore-size analysis of this sample shows a narrow pore-size distribution centered around 4 nm along with some microporosity, as shown in Figure 7.3b4. BET specific surface area of this sample is found to be about 337 m^2/g. Presence of mesopores and small amount of micropores indicates that micropores could have formed either at temperature below 1700 °C or by annealing for shorter time at 1700 °C, according to Ostwald ripening in porous ceramic materials [12].

To investigate the conditions of micropore formation in C-rich SiCN samples, several specimens have been annealed over different times at the temperatures corresponding to the regime of the carbothermal reaction (see Table 7.1). A relatively short annealing time of the samples pre-annealed (**2**, at 1500 °C) and heat-treated at intermediate temperatures (**3** and **4**, at 1600 and 1650 °C, respectively) leads not only to a significant increase in the SSA of the samples, up to 440 and 568 $m^2\ g^{-1}$, respectively, but also changes the pore-size distribution. N_2-adsorption isotherm of both specimens are type-I isotherms which are related to the microporous nature of the materials (Figure 7.3a1-a2). The carbon-rich SiCN ceramics exposed to the carbothermal reaction at 1650 °C develop a SSA as high as 568 $m^2\ g^{-1}$ with a micropore volume of 0.22 $cm^3\ g^{-1}$.

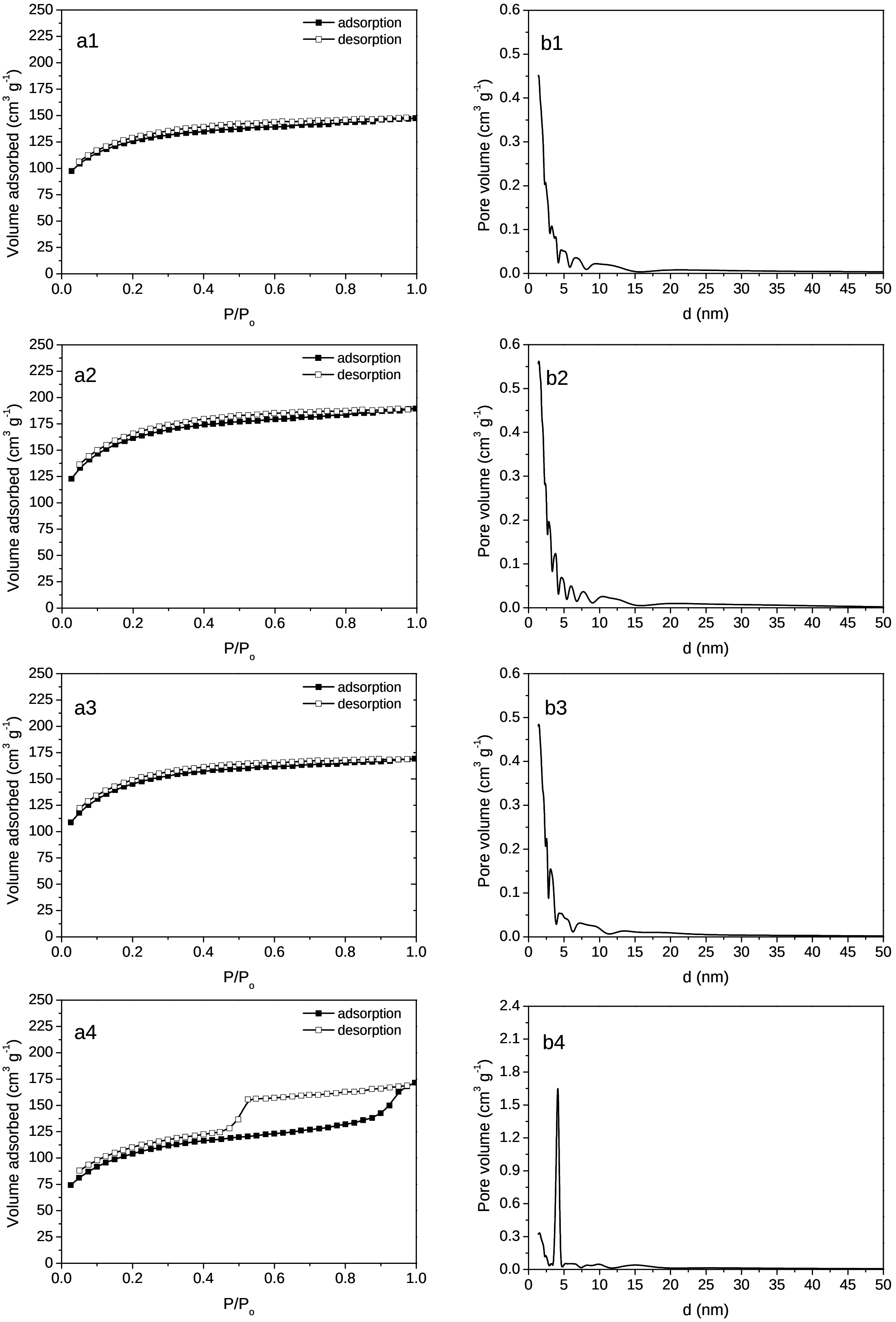

Figure 7.3. N_2-sorption isotherms (a1–a4) and pore-size distributions (b1–b4) of C-rich SiCN-ceramics pyrolyzed at (1) 1600 °C for 30 min (sample **3**), (2) 1650 °C for 30 min (sample **4**), (3) 1700 °C for 1 h (sample **5**), and (4) 1700 °C for 2 h (sample **6**). (P/P_o: relative pressure, d: pore diameter)

Table 7.1. Preparation, BET specific surface area (SSA), pore-size characteristics of samples **1-7** obtained by pyrolysis of **S1** at different temperatures between 1100 and 2000 °C (in the case of the samples **3-5**, the sign plus (+) indicates that two annealing steps have been used).

Sample	**Preparation conditions**		**BET SSA (m^2 g^{-1})**	**Micro-pore vol. (cm^3 g^{-1})[a]**	**Micro-/ Mesoporosity**
	Temp. (°C)	**Dwelling time (h)**			
1	1100	2	< 1	-	nonporous
2	1500	2	3	-	nonporous
3	1500 + 1600	2 + 0.5	440	0.18	mainly microporous
4	1500 + 1650	2 + 0.5	568	0.22	mainly microporous
5	1500 + 1700	2 + 1	513	0.20	mainly microporous
6	1700	2	337	0.07	meso-/microporous
7	2000	2	28	-	nonporous

[a] t-method [13]

From 1650 to 2000 °C, the average pore size increases but micro-pore volume fraction decreases as the pyrolysis temperature is increased. As reported in the case of other polymer-derived ceramics [14-15], this thermodynamically favorable decrease in specific surface area appears to occur due to a viscous flow process of the residual amorphous phase.

In order to understand how the annealing time influences the specific surface area and pore-size distribution, another is prepared at 1700 °C using annealing time of 1 h (sample **5**) with intermediate annealing step at 1500 °C. By comparing pore-size distribution and specific surface area (Table 7.1) of this sample with the sample annealed at 1700 °C for 2 h (sample **6**), it can be observed that shorter annealing time causes a higher specific surface area and also has an important role on the pore size distribution of the material. The sample synthesized by annealing for 2 h at 1700 °C generates ceramics with a mixture of micro- and mesopores (Figure 7.3b4). By decreasing the annealing time to 1 h, only microporosity (pore size < 2 nm) is observed as shown in Figure 7.3b3. Increasing the temperature to 2000 °C (sample **7**), the material becomes more compact with a low specific surface area of 28 m^2/g due to sintering, as shown in Table 7.1.

7.5. Microstructural analysis of carbon-rich SiCN ceramics

7.5.1 XRD characterization

XRD patterns of the samples prepared for pore-size analysis between 1100 and 2000 °C are depicted in Figure 7.4. It could be observed that ceramics obtained up to 1500 °C remain amorphous. Samples start to transform into crystalline β-SiC at $T \geq 1600$ °C. Small fraction of α-SiC is also found. Surprisingly no crystalline Si_3N_4 is formed as found in earlier studies of other polysilycarbodiimides with low carbon content [16]. Resistance to crystallization at T ~1500 °C could be due high amount of carbon as reported elsewhere [17]. At 2000 °C turbostratic carbon reflex is also detected.

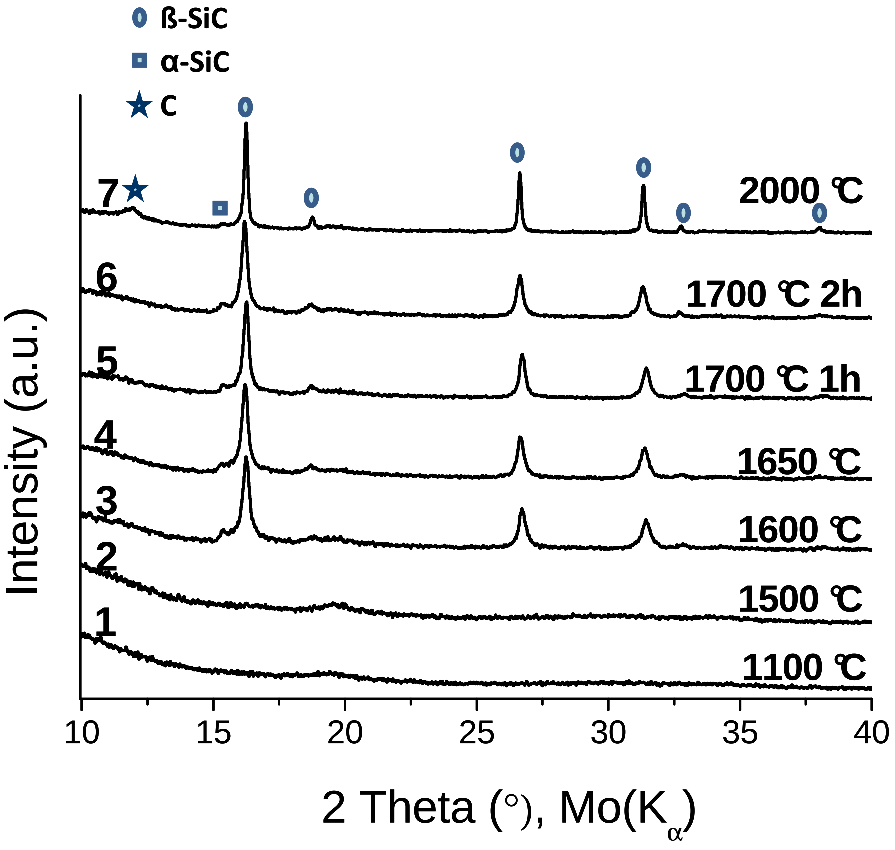

Figure 7.4. X-ray diffraction patterns of samples **1–7**, obtained by the pyrolysis of **S1** at different temperatures between 1100 and 2000 °C.

7.5.2 Elemental analysis

Elemental composition of the samples obtained by pyrolysis of **S1** pre-ceramic precursor at different temperatures and using different annealing conditions between 1100 and 2000 °C are presented in Table 7.2.

Table 7.2. Elemental composition of samples **1–7** obtained by the pyrolysis of **S1** at different temperatures between 1100 and 2000 °C.

Sample	**Composition (wt.%)**				**Empirical formula**
	Si	**C**	**N**	**O**	
1	21.80	60.90	16.70	0.60	$Si_1C_{6.52}N_{1.53}O_{0.05}$
2	24.05	60.19	17.47	0.29	$Si_1C_{5.84}N_{1.29}O_{0.02}$
3	30.41	62.07	5.99	1.52	$Si_1C_{4.76}N_{0.39}O_{0.08}$
4	32.53	64.25	1.93	1.28	$Si_1C_{4.60}N_{0.11}O_{0.07}$
5	31.02	66.93	0.67	1.37	$Si_1C_{5.03}N_{0.43}O_{0.07}$
6	22.69	76.92	0.35	0.04	$Si_1C_{7.91}N_{0.03}$
7	24.06	75.66	0.28	0.00	$Si_1C_{7.34}N_{0.02}$

Elemental analysis indicates that as the pyrolysis temperature is increased the relative carbon content slightly increases while nitrogen content in the ceramics is drastically decreased and ceramics are almost nitrogen free above 1700 °C. The decrease in nitrogen content in the ceramics above 1500 °C is attributed to the carbothermal reaction (Eq 7c). The sample pyrolyzed at 1100 °C (sample **1**) containing 16.7 wt. % N has low specific surface area. When the sample is synthesized at 1650 °C (sample **4**) with additional intermediate annealing step at 1500 °C for 2 h, the nitrogen content is diminished to 1.93, forming a microporous material with a high specific surface area of about 568 m^2/g (from Table 7.1).

A strong correlation between the nitrogen content and the specific surface area of the samples is observed (Figure 7.5) which indicates that the key factor in the formation of the porous structure is the evolution of nitrogen gas during carbothermal reaction. The carbon content (from Table 7.2) in the ceramic samples remains almost constant for those samples which have shown high specific surface area with micro- and mesoporous structure.

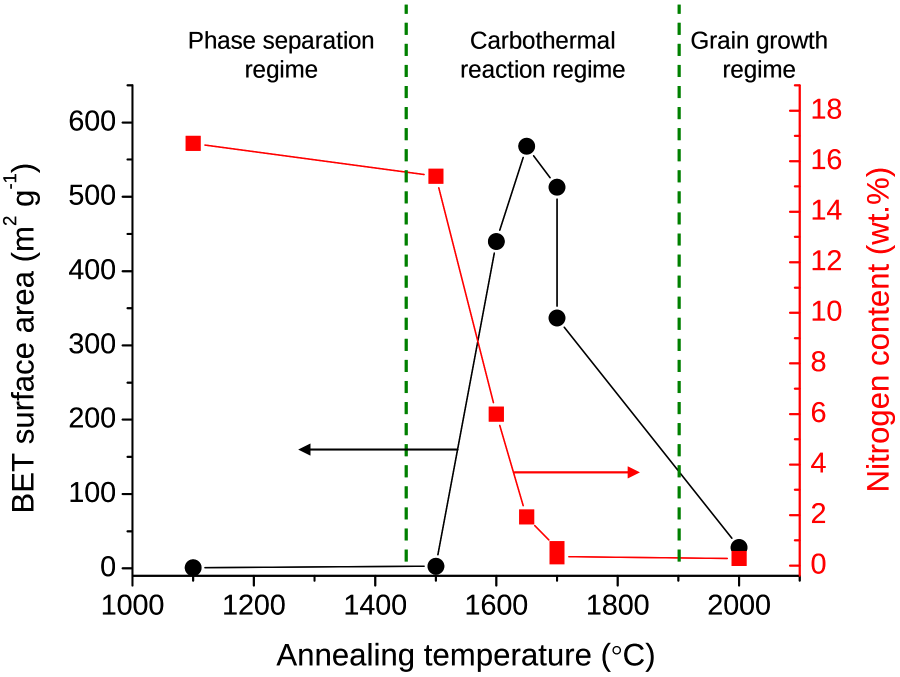

Figure 7.5. Correlation between BET specific surface area and nitrogen content and the corresponding annealing temperatures of 1100 °C (sample **1**), 1500 °C (sample **2**), 1600 °C (sample **3**), 1650 °C (sample **4**), 1700 °C (sample **5** and **6**), and 2000 °C (sample **7**).

7.5.3 Raman spectroscopy

To investigate the structural evolution of the free carbon phase in the samples obtained by pyrolysis at different temperatures at and above 1100 °C, raman spectroscopic measurements are done. Raman spectra of samples **1–7** are presented in Figure 7.6.

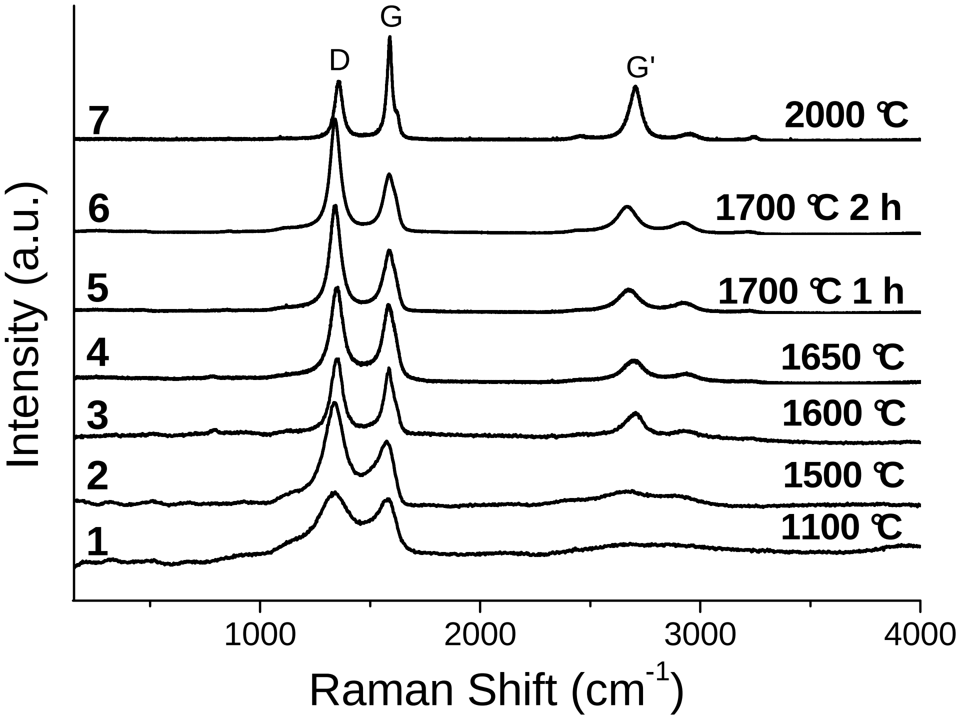

Figure 7.6. Micro-Raman spectroscopy measurements of the samples **1–7** obtained by the pyrolysis of **S1** at different temperatures between 1100 and 2000 °C (wavelength λ = 514.5 nm).

Samples synthesized at 1100 and 1500 °C show broad and overlapped signals. It indicates the presence of significant amount of structural disorder of the free carbon phases in these samples. These spectra are typical for sp^2 structure of carbon – D and G bands characteristic for such structure [18]. The D band is due to the breathing modes of sp^2 atoms in rings. The D band is known as the disordered or defect mode. Development of the D band indicates disordering of graphite [19]. The G band is a tangential shear mode of carbon atoms that corresponds to the stretching mode in the graphite plane [20]. Samples **3–7** obtained at T ≥ 1600 °C exhibit distinct and narrower D and G bands. Narrow bands indicate the presence of relatively ordered graphene like structure.

G' band is not clearly visible for the samples synthesized up to 1500 °C, indicates high degree of structural disorder in carbon phase. It is found to appear in the range of 2600–2800 cm^{-1} for the samples which are obtained at T ≥ 1600 °C. The G' band is observed in defect-free samples and is very sensitive to the stacking ordering of the graphene sheets along the c-axis [6]. In our case, with the increase of pyrolysis temperature and/or annealing time, the intensity of G' band is also increased due to an increase in the organization of the free carbon phase. Hence, we should expect enhancement in the structural organization of the free carbon phase in these temperature range. Increased ordering in a-C increases the intensity of G' band and shifts peak G upwards.

At 2000 °C, the integral intensity of the G band is increased with respect to the D band, i.e. I(G)/I(D) > 1. This evidenced formation of high amount of turbostratic carbon phase at 2000 °C (also appeared in the XRD pattern, Figure 7.4).

7.5.4 TEM characterization

TEM studies have been performed to perceive visibly the local organization of graphene layers and porous structure of synthesized ceramics. The micro/nanostructure of the samples prepared at 1100 (sample **1**), 1650 (sample **4**), 1700 (sample **5** and **6**) and 2000 °C (sample **7**) were characterized by high-resolution transmission electron microscopy (HRTEM), as shown in Figure 7.7a–f.

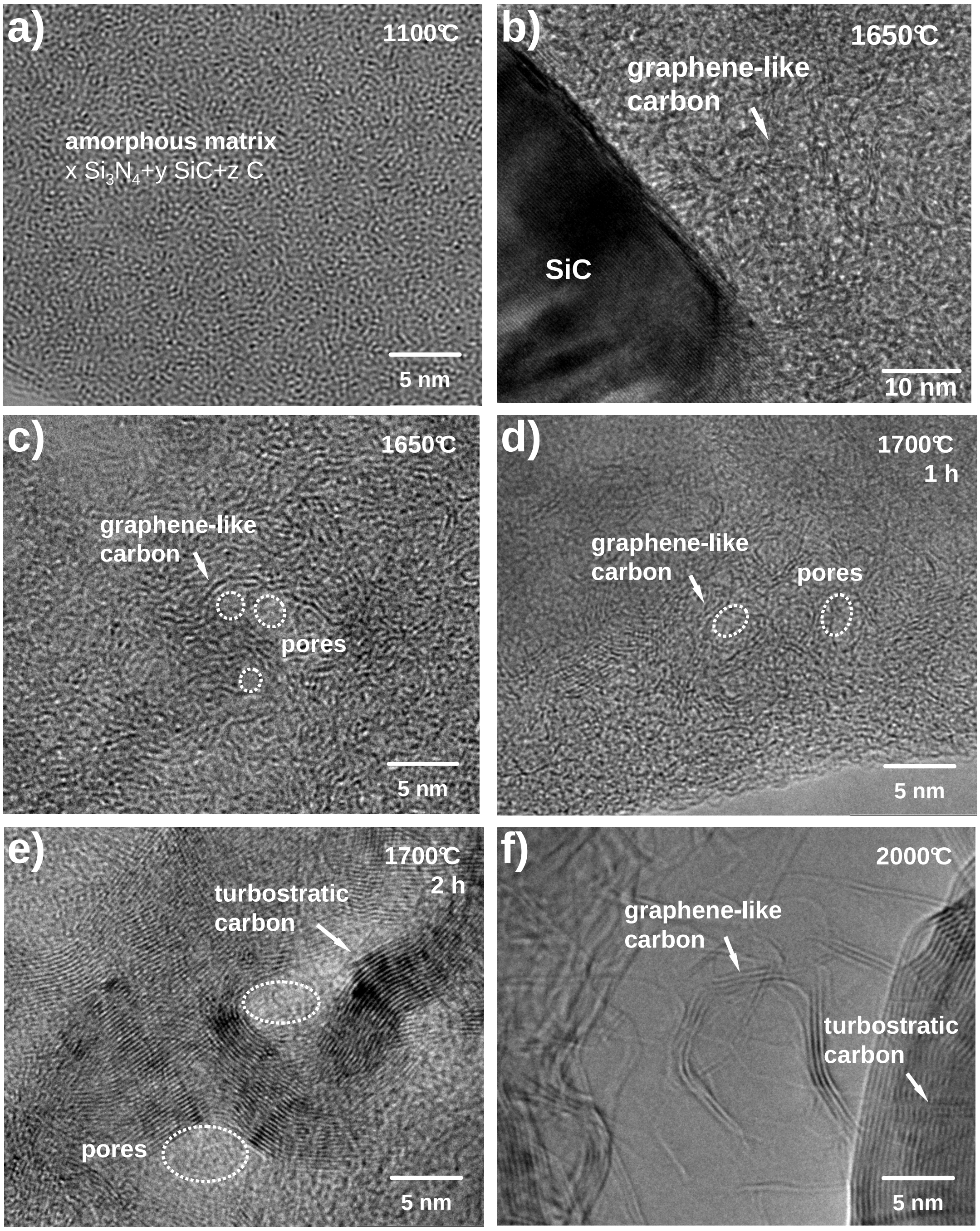

Figure 7.7. High resolution TEM images revealing the microstructure of samples annealed at (a) 1100 °C (sample **1**), (b, c) 1650 °C (sample **4**), (d) 1700 °C for 1h (sample **5**)**,** (e) 1700 °C for 2h (sample **6**), and (f) 2000 °C (sample **7**)**.**

The sample **1** at 1100 °C shows no indication of any crystalline phase (Figure 7.7a). The sample with the highest surface area of 568 m^2 g^{-1} (sample **4**) obtained via annealing at 1650 °C for 30 minutes is composed of α/ß-SiC crystallites, homogeneously dispersed throughout the matrix as shown in Figure 7.7b. The latter solely consists of graphene-like carbon, which, as a consequence, yields the high specific surface area monitored for this material. Since graphene-like carbon is structurally disorganized, and it can allow the formation of a high pore volume between the wound graphene stacks.

High-Resolution TEM images of the samples prepared at 1700 °C, but with different annealing times of 1 h (sample **5**) and 2 h (sample **6**) are shown in Figure 7.7d and Figure 7.7e, respectively. In the carbon phase of sample **5** small micropores can be distinguished (Figure 7.7d). In the case of sample **6**, the carbon phase is turbostratic. Meso-pores of diameter about 4 nm are clearly visible in Figure 7.7e enclosed within the turbostratic carbon phase. The increase in the size of the pores from micro- to mesopores seems to be correlated to the increase in the number of graphene layers. A low number of graphene layers can accommodate small micropores between the stacks (samples **4** and **5**) and large number of graphene layers like in turbostratic phase (more than 10 layers graphene) lodge large mesopores between the stacks (sample **6**). The diameter of the pores and the number of graphene layers increase with increasing the dwelling time.

At 2000 °C, only large SiC crystallites surrounded by two types of carbon phase (not shown here), namely graphene-like and turbostratic, can be observed. Due to the integral nature of micro-Raman spectroscopy, the presence of graphene-like carbon was not possible to be identified by this method. It is assumed that the bands corresponding to graphene phase perfectly overlapped with the ones of turbostratic carbon. Another problem is the nature of the second-order G' band. In the case of turbostratic carbon, there is no stacking order between adjacent layers and therefore there is a very weak interaction between the graphene planes so that turbostratic carbon can be considered to be 2D graphite, similar to a graphene layer.

At 2000 °C, the carbothermal reaction is finished and the micro- and mesopores are not observed anymore. Figure 7.7f presents the differences between the graphene-like carbon in sample **7** with 1–4 layers graphene and the turbostratic carbon phase with 10–20 layers of graphene.

HRTEM analysis reveals that the micro- and mesopore structures are located only in the carbon phase, as shown schematically in Figure 7.8. The diameter of pores could be related to the number of graphene layers.

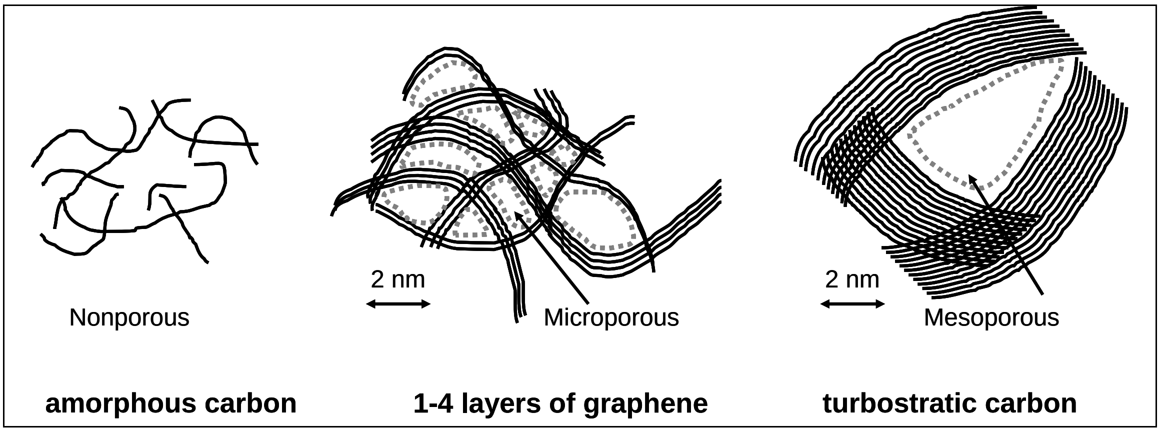

Figure 7.8. Schematic representation of the dependence of pore size on the number of graphene layers and their organization.

7.6. Limitations of poly(diphenylsilylcarbodiimide)-derived ceramics

It is already shown in Chapter 4 that macroporous α-Al_2O_3 supports are not stable at 1100 °C and intermediate mesorporous γ-Al_2O_3 layer also loses its mesoporous structure above 800 °C. Pore-size analysis of **S1** derived ceramics (from Table 7.1) indicates that microporous C-rich SiCN ceramics are formed at $T \geq 1600$ °C and at such high temperature porous γ-Al_2O_3/α-Al_2O_3 supports do not retain porosity. Crack-free membrane formation by the deposition/pyrolysis of **S1** at $T \geq 1600$ °C would be feasible only for those macroporous support and mesoporous intermediate layer which can do not loose porosity in the temperature range of 1600–1700 °C. To the best of our knowledge until today no such macroporous support or intermediate mesoporous ceramics are available. The main problem of coating **S1** preceramic precursor on SnO_2 coated sensor support is the melting point of SnO_2 (T_m ~1630 °C) which is the limiting temperature region where we have observed formation of microporous C-rich SiCN ceramics. Because of these limitations coatings of microporous C-rich SiCN ceramic layers have not been done on porous- and sensor-supports to study hydrogen separation / sensing performance.

In summary, C-rich SiCN ceramics with a very high specific surface area and defined pores size have been synthesized by means of simple pyrolysis of carbon-rich polysilylcarbodiimide-based precursor, varying the thermolysis parameters, namely temperature, annealing time and utilizing additional annealing steps. The thermal decomposition of SiCN ceramics is correlated with the carbothermal reaction of amorphous SiCN with excess carbon. Carbothermal reaction affects the BET specific surface area and also the pore-size distribution. The samples annealed at 1600, 1650 °C for 30 min each and at 1700 °C for 1 h are mainly microporous. The micropore ceramics obtained at 1650 °C develop a BET specific surface are of about 568 $m^2 g^{-1}$. The sample annealed at 1700 °C for 2 h transform to mesoporous ceramic, which is attributed to the formation pore space enclosed by organized grapheme layers. This correlation is valid only for the temperature range in which the carbothermal reaction occurs. HRTEM confirmed that the micro/nanostructure is composed of SiC homogeneously dispersed in graphene-like carbon matrix and the pores are associated with the carbon phase.

7.7. References

[1] G. Mera, R. Riedel, F. Poli, K. Muller, "Carbon-rich SiCN ceramics derived from phenyl-containing poly(silylcarbodiimides)," *Journal of the European Ceramic Society,* 29 (2009) 2873-2883.

[2] R. Riedel, G. Mera, R. Hauser, A. Klonczynski, "Silicon-based polymer-derived ceramics: Synthesis properties and applications - A review," *Journal of the Ceramic Society of Japan*, 114 (2006) 425-444.

[3] H.J. Kleebe, Y.D. Blum, "SiOC ceramic with high excess free carbon," *Journal of the European Ceramic Society*, 28 (2008) 1037-1042.

[4] G. Gregori, H.J. Kleebe, Y.D. Blum, F. Babonneau, "Evolution of C-rich SiOC ceramics - Part II. Characterization by high lateral resolution techniques: electron energy-loss

spectroscopy, high-resolution TEM and energy-filtered TEM," *International Journal of Materials Research*, 97 (2006) 710-720.

[5] Z.Q. Li, C.J. Lu, Z.P. Xia, Y. Zhou, Z. Luo, "X-ray diffraction patterns of graphite and turbostratic carbon," *Carbon*, 45 (2007) 1686-1695.

[6] M.A. Pimenta, G. Dresselhaus, M.S. Dresselhaus, L.G. Cancado, A. Jorio, R. Saito, "Studying disorder in graphite-based systems by Raman spectroscopy," *Physical Chemistry Chemical Physics*, 9 (2007) 1276-1291.

[7] A.F. Ismail, L.I.B. David, "A review on the latest development of carbon membranes for gas separation," *Journal of Membrane Science*, 193 (2001) 1-18.

[8] B. Zhang, T.H. Wang, S.L. Liu, S.H. Zhang, J.S. Qiu, Z.G. Chen, H.M. Cheng, "Structure and morphology of microporous carbon membrane materials derived from poly(phthalazinone ether sulfone ketone)," *Microporous and Mesoporous Materials*, 96 (2006) 79-83.

[9] G. Mera, A. Tamayo, H. Nguyen, S. Sen, R. Riedel, "Nanodomain structure of carbon-rich silicon carbonitride polymer-derived ceramics," *Journal of the American Ceramic Society*, 93 (2010) 1169-1175.

[10] J.F. Klebe, J.G. Murray, "Organosiliconcarbodiimide polymers and process for their preparation," United States Patent 3352799, 1967.

[11] P. Colombo, G. Mera, R. Riedel, G.D. Soraru, "Polymer-derived ceramics: 40 years of research and innovation in advanced ceramics," *Journal of the American Ceramic Society*, 93 (2010) 1805-1837.

[12] V.V. Slezov, J. Schmelzer, J. Moller, "Ostwald ripening in porous materials," *Journal of Crystal Growth*, 132 (1993) 419-426.

[13] F. Schuetz, K.S.W. Sing, J. Weitkamp, *Handbook of Porous Solids*, wiley-VCH Verlag GmbH, Weinheim, 2002.

[14] J. Lipowitz, J.A. Rabe, L.K. Frevel, R.L. Miller, "Characterization of nanoporosity in polymer-derived ceramic fibers by X-ray-scattering techniques," *Journal of Materials Science*, 25 (1990) 2118-2124.

[15] J.L. Wan, M.J. Gasch, A.K. Mukherjee, "In situ densification behavior in the pyrolysis consolidation of amorphous Si-N-C bulk ceramics from polymer precursors," *Journal of the American Ceramic Society*, 84 (2001) 2165-2169.

[16] Y. Iwamoto, W. Volger, E. Kroke, R. Riedel, T. Saitou, K. Matsunaga, "Crystallization behavior of amorphous silicon carbonitride ceramics derived from organometallic precursors," *Journal of the American Ceramic Society*, 84 (2001) 2170-2178.

[17] C. Turquat, H.J. Kleebe, G. Gregori, S. Walter, G.D. Soraru, "Transmission electron microscopy and electron energy-loss spectroscopy study of nonstoichiometric silicon-carbon-oxygen glasses," *Journal of the American Ceramic Society*, 84 (2001) 2189-2196.

[18] J. Robertson, "Amorphous Carbon," *Advances in Physics*, 35 (1986) 317-374.

[19] A.C. Ferrari, J. Robertson, "Interpretation of raman spectra of disordered and amorphous carbon," *Physical Review B*, 61 (2000) 14095-14107.

[20] L.J. Xue, W.Z. Li, G.G. Hoffmann, J.G.P. Goossens, J. Loos, G. de With, "High-resolution chemical identification of polymer blend thin films using tip-enhanced raman mapping," *Macromolecules*, 44 (2011) 2852-2858.

Chapter 8. Conclusions and outlook

In this thesis high temperature hydrogen separation and sensing performance of polymer-derived microporous ceramic membranes has been studied. Three different classes of ceramics (SiBCN, Si_3N_4 and SiCN) have been synthesized and deposited on porous tubular γ-Al_2O_3/α-Al_2O_3 supports and on gas sensors using a dip-coating method. Gas transport mechanisms and permeation behavior of the membranes deposited on porous supports were investigated. Potential applications of microporous ceramic coated gas sensors for H_2 sensing under harsh reducing conditions and with enhanced selectivity of H_2 with respect to CO are explored.

As a first step, laboratory-scale gas permeation set-up has been designed and realized. The experimental method of the realized set-up for gas permeance measurement is based on constant volume manometric method. The gas permeation properties of a membrane can be tested between room temperature (RT) and 450 °C under moisture-free condition with a feed pressure of 1 atm. The experimental set-up is capable of measuring permeation of single (Ar, He, N_2, CO_2, Kr) as well as mixed gas (H_2 and CO in N_2) permeances by employing a micro gas chromatograph as a detector.

The porous supports — on which ceramic membranes are deposited — used in the present work, have been provided by Noritake Company limited, Japan and Fraunhofer Institute for Ceramic Technologies and Systems (IKTS), Hermsdorf, Germany. The thermal stability of tubular macroporous α-Al_2O_3 supports (received from Noritake Company limited, Japan) is evaluated by measuring phase composition and pore-size distribution (using mercury porosimeter) before and after treating the supports under various atmospheres (air, argon and ammonia) at 800 °C. The phase composition and porosity of α-Al_2O_3 supports remains unaffected irrespective of treatments under air/argon/ammonia up to 800 °C, indicating the suitability of the as-received porous supports for the coating of intermediate mesoporous γ-Al_2O_3 and top microporous membrane coating. The phase transformation from γ- to δ-Al_2O_3

at temperatures above 1000 °C results in a decreased BET SSA. XRD, SEM and pore-size characterizations of the as-received α-Al_2O_3 supports indicate an average pore diameter of 0.64 µm in the base α-Al_2O_3 support tube (layer thickness ~6 mm) as well as a mean pore diameter of about 0.045 µm in the intermediate α-Al_2O_3 layer (layer thickness ~50 µm). Intermediate mesoporous γ-Al_2O_3 layer is deposited on macroporous tubular α-Al_2O_3 supports by dipping the supports in a boehmite colloidal dispersion with subsequent calcination at 800 °C for 2 h. The thickness of the formed γ-Al_2O_3 layer is found to be about 1 µm after single-fold coating/calcination step. The pore-size distribution of the γ-Al_2O_3 ceramic powder obtained after calcination at 800 °C shows a mean pore-size of about 8 nm with BET specific surface area (SSA) of 144 $m^2\ g^{-1}$. The composite porous supports, γ-Al_2O_3/α-Al_2O_3, obtained as described above are chosen for the deposition of a top microporous membrane.

(1) The first microporous ceramic which is synthesized in the present work is a polymer-derived SiBCN ceramic. The performance of the SiBCN ceramics have been studied in terms of H_2/CO selectivity and as a protective coating for widely used SnO_2 based gas sensors under harsh reducing conditions. Two pre-ceramic polymers, namely polyborotrisilazane and polyborotetrasilazane have been synthesized by the hydroboration of 1,3,5-trivinyl-1,3,5-trimethyl-cyclosilazane and 1,3,5,7-tetravinyl-1,3,5,7-tetramethyl-cyclosilazane, respectively, with borane dimethylsulphide. The structures of the resulting polymers are studied by solid-state NMR and ATR-IR spectroscopic methods, which confirm polymerization via hydroboration. Thermal analysis of the synthesized polymers shows ceramic yields of about 63 and 65 % by mass for polyborotrisilazane and polyborotetrasilazane, respectively, obtained at 1000 ºC under flowing argon. As confirmed by XRD and HR-TEM, the resulting SiBCN ceramics are amorphous. Pore-size characteristics of the unsupported SiBCN ceramic obtained by pyrolysis of both polymers at 800 ºC are evaluated by N_2-sorption isothermal analysis, however, microporous nature is found only for the ceramic derived from polyborotrisilazane. Therefore, the

polyborotrisilazane polymer has been selected for the deposition on γ-Al_2O_3/α-Al_2O_3 porous supports.

SiBCN membranes with thickness of about 2.8 µm were deposited on γ-Al_2O_3/α-Al_2O_3 porous supports by three-fold dip-coating/pyrolysis steps. The gas permeation properties of the multilayered SiBCN / γ-Al_2O_3/ α-Al_2O_3 membranes are evaluated by mixed gas and single gas permeation measurements. These membranes show a H_2/CO selectivity of about 10.5 and a H_2 permeance of about 1.05×10^{-8} mol m^{-2} s^{-1} Pa^{-1} at 440 °C. The transport of gas molecules through the SiBCN membranes is found to be governed by both activated and Knudsen diffusion. H_2 permeation through SiBCN membranes is activated at high-temperatures which indicate the presence of molecular sieves (pore-size ~0.3 nm) in the amorphous SiBCN matrix. Interconnection of large micropores (0.68-0.73 nm) present in the amorphous SiBCN layers and micropore channel defects, allows for H_2 and CO transport by the Knudsen diffusion mechanism. Very few works have been done in the field of polymer-derived microporous ceramic membranes and especially in the direction of H_2/CO separation. The results obtained in this work show a higher H_2 permeance of 1.05×10^{-8} mol m^{-2} s^{-1} Pa^{-1}, however, a lower H_2/CO selectivity of about 10.5 compared to that of a polysilazane (PSZ)-derived SiO_2 membrane (Figure 8.1).

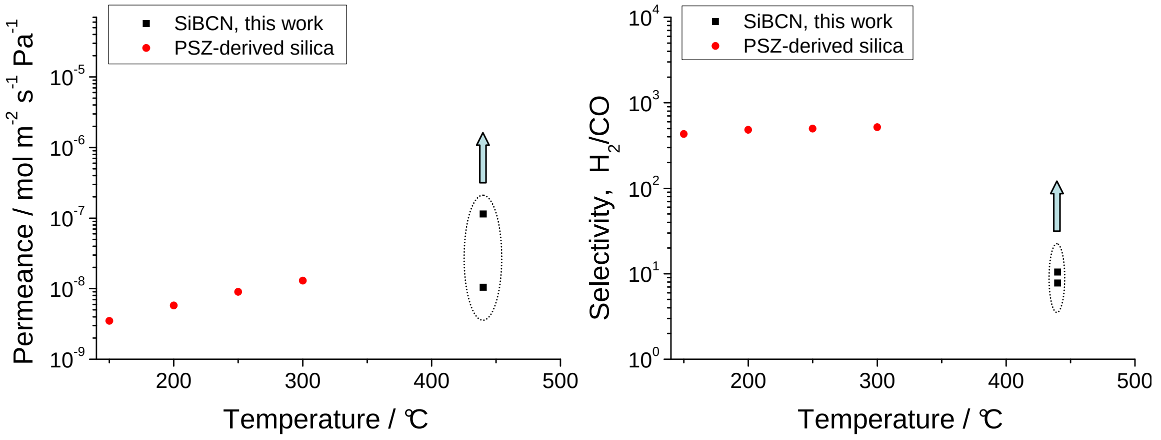

Figure 8.1. Performance (H_2 permeance and H_2/CO selectivity) for SiBCN/γ-Al_2O_3/α-Al_2O_3 multilayer membranes in comparison to that of a polysilazane-derived microporous ceramic membrane (data taken from reference number [32], chapter 5). The arrows indicate the goals to be achieved to obtain pure H_2.

By increasing the number of SiBCN coating layers, the CO permeance is decreased by a larger extent due to decrease in the number of micropore channel defects if compared to that of H_2 that results in an enhanced H_2/CO selectivity. Because of these tunable permeance properties as well as high temperature stability, the multilayer SiBCN/γ-Al_2O_3/α-Al_2O_3 membranes are appeared to be interesting candidates for hydrogen separation under high-temperature conditions.

(2) In the second part of the work related to microporous SiBCN ceramics, the membranes were integrated into chemiresistors and the effect of a molecular sieve filter on the classical SnO_2-sensors' stability and sensing characteristics have been investigated. The deposition of SiBCN membranes on SnO_2 sensors is performed by dip-coating of the SnO_2-sensor into pre-ceramic polymer solutions followed by the subsequent pyrolysis in argon at 800 ºC for 2 h. Transient response characteristics and sensor signals of uncoated SnO_2, three-fold and five-fold SiBCN-coated SnO_2 sensors exposed to CO (10, 20 and 120 ppm) and H_2 (40, 400 and 900 ppm) in nitrogen — under oxygen-free conditions — at 350 and 530 °C are obtained. All sensors show reversible resistance changes towards CO exposure at both temperatures. However, the uncoated SnO_2 sensor is reduced at 530 ºC in H_2 to tin while the SiBCN coated SnO_2 sensors remain stable and show a reversible resistance change suitable for the detection of H_2 and CO under the oxygen-free conditions.

The Si_3N_4 ceramics, the second type of material studied in the present work, is synthesized by the ammonolysis of commercially available polysilazane (KiON HTT 1800). Thermogravimetric analysis of the polymer shows a yield of about 51 % by mass at 1000 °C after pyrolysis in dry ammonia. The amorphous Si_3N_4 ceramic is completely microporous with a BET SSA of 255 $m^2 g^{-1}$ and reveals a micropore volume of 0.11 $cm^3 g^{-1}$ (measured by N_2-sorption analysis). Si_3N_4 membranes are developed by coating of a diluted polysilazane on the inner wall of γ-Al_2O_3/α-Al_2O_3 supports (provided by IKTS, Hermsdorf, Germany) followed by ammonolysis at 800 °C. Single gas permeance measurements of the multilayer $Si_3N_4/\gamma\text{-}Al_2O_3/\alpha\text{-}Al_2O_3$ membrane indicate that the gas permeance through the membrane follows Knudsen diffusion mechanism. No significant decrease in the permeances of the gases (He, H_2, N_2, CO_2, and O_2) is measured between 20 and 200 °C. This transport behavior has been attributed to a crack formation on the surface of the $Si_3N_4/\gamma\text{-}Al_2O_3/\alpha\text{-}Al_2O_3$ membrane due to the instability of the $\gamma\text{-}Al_2O_3$ intermediate layer under ammonia at 800 °C. The pronounced crack formation within the Si_3N_4 membrane results in a poor H_2/CO_2 permselectivity.

The microporous Si_3N_4 ceramics have been applied to screen printed GaN based sensors to improve their selectivity towards H_2. Gas sensing properties of three sensors — uncoated GaN, Si_3N_4 coated- and ammonia treated-GaN sensors in oxygen-free conditions — are studied at 350 and 530 °C under different H_2 (40-900 ppm) and CO (10-120 ppm) concentrations. Uncoated GaN shows high sensor signals towards H_2 and CO whereas the microporous Si_3N_4 coated- and ammonia treated-GaN sensors show almost no signals to CO at 350 and 530 °C. The H_2 sensor signals for Si_3N_4 coated-GaN sensors are found to be slightly reduced confirming reasonable permeance of H_2 through the Si_3N_4 membrane due to size-selective transport. Surprisingly, the gas sensing behaviour of ammonia treated-uncoated GaN sensors towards H_2 and CO are found to be similar to that of ammonia treated-Si_3N_4 coated-GaN sensors. The reason behind the loss of CO sensing for ammonia treated-GaN sensors has been attributed to the removal of a surface oxide layer during ammonia treatment resulting in fresh GaN surface. As a result, novel H_2 selective gas sensors have been developed by (i) coating of microporous Si_3N_4 layer on GaN sensor, and (ii) ammonia treatment of GaN sensors.

(3) The last part of the present thesis deals with the synthesis of SiCN ceramics with high specific surface area and tunable micro- and mesoporosity by the thermal decomposition of carbon-rich polymer-derived SiCN ceramics. The carbon-rich SiCN ceramics are

synthesized by the pyrolysis of a carbon-rich poly(diphenylsilylcarbodiimide) precursor under argon and by varying thermolysis parameters (temperature, annealing time, and additional annealing step). The ceramic synthesized at 1650 °C for 30 min with an additional intermediate annealing step at 1500 °C for 2 h results in the formation of a microporous ceramic with high specific surface area of about 568 m^2 g^{-1}, whereas, a mesoporous ceramic (pore-size ~4 nm) is obtained by annealing at 1700 °C for 2 h. HRTEM investigation reveals that the annealing conditions affect the organization of graphene-like carbon layers (free carbon) and the micro- and mesopores are enclosed within these layers. The synthesized novel high surface SiCN ceramics are chemically inert and can be used as catalyst supports for high temperature and hydrogen storage applications.

The experimental results achieved within the framework of the present studies allows for the following recommendations for future research work:

i) *Improving the set-up for characterization of gas permeances*: The set-up realized in this work feeds gas-mixture to the feed-side at a pressure of 1 atm, therefore, gases permeate through the membrane under a pressure gradient of about 1 atm and the whole permeance measurement takes longer time. By introducing back-pressure valve at the retentate-end, the feed-side pressure can be increased which will increase the pressure gradient; hence, the permeance characteristics will be achieved in shorter time.

ii) *Improving the hydrothermal stability of polymer-derived microporous membranes*: Stability of different layers of multilayered membranes under hydrothermal condition (under a stream at 400-500 °C) is an important requirement for their application at the hydrogen production and separation site in the membrane reactor. The present work was not focused in this direction; the results of this work are a proof-of-concept demonstration of the suitability of polymer-derived ceramics for high temperature H_2

separation and purification applications. Therefore, the hydrothermal stability of polymer-derived microporous ceramic materials needs to be examined for the future development of materials for H_2 purification. Also, the hydrothermal stability of the intermediate mesoporous layer materials should be tested and future experimental investigations for the development of hydrothermally stable mesoporous ceramics could be a field of future research. Following candidate materials have the potential for high hydrothermal stability: (i) polymer-derived microporous silicon oxycarbide (SiOC) and silicon carbide (SiC) ceramics and (ii) $MgAl_2O_4$ as an intermediate mesoporous layer.

iii) *Exploring novel supports*: Three microporous ceramic materials (SiBCN, Si_3N_4 and carbon rich SiCN) studied in the present work are Si-based ceramics, whereas the porous supports on which these ceramics layers are deposited are Al_2O_3-based ones. The difference in the thermal expansion coefficients between membrane and porous supports can lead to crack formation at their interface. In this regard, the SiC-based macroporous supports and mesoporous intermediate layers can be explored to eliminate the problems related to thermal mismatch.

iv) *Exploring the mechanism of gas detection*: As demonstrated in the present work that ammonia treated GaN sensors show high sensor signals towards H_2 and almost no sensing signals to CO, whereas untreated GaN sensors detect both H_2 and CO. The exact mechanism of this peculiar behavior could be verified by careful microstructural characterization of GaN especially with respect to the behavior of amorphous surface oxide layer. The difference in the H_2 and CO sensing mechanisms of untreated- and ammonia treated-GaN sensors needs to be studied under operando conditions by using surface specific spectroscopic techniques like Diffuse Reflectance Infrared Fourier Transform (DRIFT) spectroscopy.

v) *Improving membrane-sensor integration*: In the present work the membrane-sensor integration is achieved by the coating of microporous ceramic layer on the top of screen-printed planar sensors. Further studies can be done for slightly modified filter-sensor integration system by introducing an intermediate mesoporous layer between the microporous ceramic layer and the gas sensing layer. A sharp thickness gradient between the sensing layer and the sensor support, due to the thickness (~50 µm) of the sensing layer, exists at the edges of a screen-printed sensing layer which can result in cracks within the membrane layer. Therefore, an intermediate mesoporous layer can provide a smooth porous surface between the sensing layer and the top microporous ceramic coating and hence eliminate in this way the crack formation.

List of Abbreviations

ATR-IR	Attenuated Total Reflection Infrared Spectroscopy
BSE	Back Scattered Electron
CP	Cross-Polarization
CVD	Chemial Vapor Deposition
DEPT	Distortionless Enhancement by Polarization Transfer
DFT	Density Functional Theory
DSC	Differential Scanning Calorimetry
EA	Elemental Analysis
EDX	Energy Dispersive X-ray Spectroscopy
EELS	Electon Energy Loss Spectroscopy
FFT	Fast Fourier Transform
FT-IR	Fourier Transform Infrared Spectroscopy
FWHM	Full Width at Half Maximum
IR	Infrared
MAS	Magic Angle Spinning
MS	Mass Spectrometry
NMR	Nuclear Magnetic Resonance
PDC	Polymer-Derived Ceramic
ppm	Parts Per Million
RT	Room Temperature
SAED	Selected Area Electron Diffraction
SAXS	Small Angle X-ray Scattering
sccm	Standard Cubic Centimeter per Minute
SE	Secondary Electron
SEM	Scanning Electron Microscopy
STA	Simultaneous Thermal Analysis
TEM	Transmision Electron Microscopy
TGA	Thermogravimetric Analysis
XRPD	X-ray Powder Diffraction

Eidesstattliche Erklärung

Hiermit erkläre ich an Eides statt, dass ich die vorliegende Dissertation selbständig und nur mit den angegebenen Hilfsmiteln angefertigt habe. Von mir wurde weder an der Technischen Universität Darmstadt noch einer anderen Hochschule ein Promotionsversuch unternommen.

Darmstadt, den 26. April 2012

Ravi Mohan Prasad

Curriculum Vitae

Personal data

Name: Ravi Mohan Prasad

Date and place of birth: 06.06.1981, Jamshedpur (India)

Nationality: India

Contact email-ID: Ravimohan.prasad@gmail.com

Education & professional experience

11/2011–till date	Research associate at FG Disperse Feststoffe, FB Material- und Geowissenschaften, Technische Universitaet Darmstadt, Germany
Since 08/2007	Ph.D. in Materials Science, Technische Universitaet Darmstadt, Germany
07/2005–06/2007	M.Tech. in Metallurgical and Materials Engineering at Indian Institute of Technology (IIT) Kharagpur, Kharagpur, India
07/1999–06/2003	B.Tech. in Metallurgical Engineering at Indian Institute of Technology (IIT) Madras, Chennai, India

List of publications:

Related to thesis

[1] **R.M. Prasad**, A. Gurlo, R. Riedel, M. Hübner, N. Barsan, U. Weimar, "Microporous ceramic coated SnO_2 sensors for hydrogen and carbon monoxide sensing in harsh reducing conditions," *Sensors and Actuators B: Chemical*, 149 (2010) 105-109

[2] **R.M. Prasad**, Y. Iwamoto, R. Riedel, A. Gurlo, "Multilayer amorphous-Si-B-C-N/gamma-Al_2O_3/alpha-Al_2O_3 membranes for hydrogen purification," *Advanced Engineering Materials*, 12 (2010) 522-528 *(cover publication)*

[3] **R.M. Prasad**, G. Mera, K. Morita, M. Mueller, H.-J. Kleebe, A. Gurlo, C. Fasel, R. Riedel, "Thermal decomposition of carbon-rich polymer-derived silicon carbonitrides leading to ceramics with high specific surface area and tunable micro- and mesoporosity," *Journal of the European Ceramic Society*, 32 (2012) 477-484

[4] **R.M. Prasad**, A. Gurlo, R. Riedel, M. Hübner, O.M. Conanec, N. Barsan, U. Weimar, "Influence of oxygen contamination in GaN based gas sensors on CO/H_2 selectivity" *(to be submitted)*

[5] **R.M. Prasad**, M. Hübner, A. Gurlo, O.M. Conanec, R. Riedel, N. Barsan, U. Weimar, "Microporous Si_3N_4 ceramic coated GaN sensors for high hydrogen selectivity with respect to carbon monoxide" *(to be submitted)*

Other publications

[6] M. Hojamberdiev, **R.M. Prasad**, K. Morita, Y. Zhu, M.A. Schiavon, A. Gurlo, R. Riedel, "Template-free synthesis of polymer-derived mesoporous SiOC/TiO_2 and SiOC/N-doped TiO_2 ceramic composites for application in the removal of organic dyes from contaminated water," *Applied Catalysis B: Environmental*, 115-116 (2012) 303-313

[7] M. Hojamberdiev, **R.M. Prasad**, K. Morita, M.A. Schiavon, R. Riedel, "Polymer-derived mesoporous SiOC/ZnO nanocomposite for the purification of water contaminated with organic dyes," *Microporous and Mesoporous Materials*, 151 (2012) 330-338

Conferences presentations:

[1] **R. M. Prasad**, A. Gurlo, R. Riedel, M. Huebner, N. Barsan, U. Weimar, Microporous ceramic membranes for H_2/CO separation and sensing, *VI International Workshop on Semiconductor Gas Sensors — SGS 2008*, 14-19 September, 2008, Zakopane, Poland *(Poster presentation)*

[2] **R.M. Prasad**, A. Gurlo, Y. Iwamoto, R. Riedel, Thermoresistant amorphous ceramic membranes for hydrogen purification, *High temperature Materials Chemistry (HTMC)-13*, September 14-18, 2009, Davis, USA *(Oral presentation)*

[3] **R.M. Prasad**, G. Mera, A. Gurlo, R. Riedel, High-surface area carbon-rich SiCN polymer-derived ceramics with tunable micro- and mesoporous structure, *Materials Science and Engineering (MSE) 2010*, August 24-26, 2010, Darmstadt, Germany *(Poster presentation)*

[4] **R.M. Prasad**, M.S. Bazarjani, R. Riedel, A. Gurlo, Polymer-derived ceramics with tunable micro- and mesoporous structure for hydrogen separation, *3rd International Congress on Ceramics (ICC)*, November 14-18, 2010, Osaka, Japan *(Invited talk)*

[5] **R.M. Prasad**, M. Hübner, O. Merdrignac-Conanec, A. Gurlo, R. Riedel, N. Barsan, U. Weimar, Characterization of membranes for hydrogen purification applying a membrane/gas-sensor combination, *MRS Spring meeting*, April 25-29, 2011, San Francisco, USA *(Poster presentation)*

[6] M.S. Bazarjani, **R.M. Prasad**, C. Schitco, A. Gurlo, R. Riedel, A fundamental design approach towards microporous polymer derived nanocomposites for gas separation applications, *12th International Conference on Inorganic Membranes*, July 9-13, 2012, Enschede, Netherland (*Oral presentation*)

[7] **R.M. Prasad**, A. Gurlo, R. Riedel, O. Merdrignac-Conanec, M. Hübner, N. Barsan, U. Weimar, Influence of oxygen impurities on the CO/H_2 selectivity of GaN based gas sensors, *IMCS 2012 - The 14th International Meeting on Chemical Sensors*, May 20-23, 2012, Nürnberg, Germany (*Oral presentation*)